



INVESTIGATION OF RADIO FREQUENCY DISCHARGES AND  
LANGMUIR PROBE DIAGNOSTIC METHODS IN A FAST FLOWING  
ELECTRONEGATIVE BACKGROUND GAS

DISSERTATION

Nathaniel P. Lockwood

AFIT/DS/ENP/DSP-04J

**DEPARTMENT OF THE AIR FORCE  
AIR UNIVERSITY**

***AIR FORCE INSTITUTE OF TECHNOLOGY***

---

**Wright-Patterson Air Force Base, Ohio**

APPROVED FOR PUBLIC RELEASE; DISTRIBUTION UNLIMITED

The views expressed in this thesis are those of the author and do not reflect the official policy or position of the United States Air Force, Department of Defense, or the United States Government.

AFIT/DS/ENP/DSP-04J

INVESTIGATION OF RADIO FREQUENCY DISCHARGES AND LANGMUIR  
PROBE DIAGNOSTIC METHODS IN A FAST FLOWING ELECTRONEGATIVE  
BACKGROUND GAS

DISSERTATION

Presented to the Faculty

Graduate School of Engineering and Management

Air Force Institute of Technology

Air University

Air Education and Training Command

in Partial Fulfillment of the Requirements for the

Degree of Doctor of Philosophy

Nathaniel P. Lockwood, BS, MS

Dec 2007

APPROVED FOR PUBLIC RELEASE; DISTRIBUTION UNLIMITED.

INVESTIGATION OF RADIO FREQUENCY DISCHARGES AND LANGMUIR  
PROBE DIAGNOSTIC METHODS IN A FAST FLOWING ELECTRONEGATIVE  
BACKGROUND GAS

Nathaniel P. Lockwood, BS, MS

Approved:

\_\_\_\_\_  
William F. Bailey (Chairman)

\_\_\_\_\_  
Date

\_\_\_\_\_  
Gary B. Lamont (Dean's Representative)

\_\_\_\_\_  
Date

\_\_\_\_\_  
David E. Weeks (Member)

\_\_\_\_\_  
Date

\_\_\_\_\_  
Robert B. Greendyke (Member)

\_\_\_\_\_  
Date

\_\_\_\_\_  
Keith L. Cartwright (Member)

\_\_\_\_\_  
Date

Accepted:

\_\_\_\_\_  
M. U. Thomas  
Dean, Graduate School of  
Engineering and Management

\_\_\_\_\_  
Date

**Abstract**

Discharges in a flowing background gas are used to produce charged and excited atomic and molecular species for numerous applications including etching semiconductors, pumping gas discharge lasers, and a variety of other applications (Pinhero and others, 1998). The effect of a flowing background gas on the charged and excited neutral species generation by an RF discharge in a flow tube and the diagnostics of the resulting plasma with a Langmuir probe have been investigated for pressures between 0.001 to 1 Torr and flow velocities up to 1000 m/s. This investigation was performed using a fluid plasma model based on the approach developed by Boeuf, 1987, and Boeuf and Pitchford, 1995 which was coupled to a chemical kinetic model. For lower pressures, a hybrid Particle-In-Cell/Monte Carlo Collision modeling method based on the approach of Cartwright and others, 2000, was used. In the presence of a flowing  $O_2(X)$  or  $N_2(X) - O_2(X)$  background gas, the RF discharge simulation results showed that the time averaged sheath length of an RF discharge is decreased due to the removal of detaching excited neutral species from the discharge volume. A factor of two reduction in the sheath length was realized for an increase in flow velocity from 25 m/s to 500 m/s, resulting in a doubling of the peak electric field at the sheath edge and in the bulk plasma. This resulted in an increased average ionization rate and a factor of ten increase in positive and negative ion densities, while the electron densities remained approximately constant. An increase in ion densities combined with a moderate electron density downstream due to detachment make an  $O_2(X)$  RF discharge in a fast flowing background gas an excellent means of supplying charged species downstream to a

secondary discharge to enhance the production of neutral excited species such as  $O_2(^1\Delta_g)$ .

The current collected and the appropriate analysis methods used for Langmuir probe current voltage characteristics in a flowing electronegative plasma vary depending on pressure. The simulation results indicated that standard electronegative probe analysis methods for stationary plasmas can be used for determining the ion density of a moderate electronegative,  $\alpha \approx 1 - 4$ , 0.001 Torr plasma at sub-thermal ion flow velocities. At 0.01 Torr, the analysis method for the diffusion-convection regime developed by Clements and Smy, 1976, was shown to produce nearly identical positive ion currents and hence ion density measurements for the same plasma conditions. At even higher pressures of 1 Torr, the ion convection current collected by a probe in an electronegative plasma was shown to be less for a given bias than the current collected in an electropositive plasma. The decrease in the ion current collection is caused by the compression of the upstream collecting radius resulting from the negative ions being “pushed” into the pre-sheath region. The compression of the collecting radius was due to frequent collisions of the flowing gas with the negative ions. The reduced ion current collected by the probe in an electronegative flowing plasma was shown to cause the standard convection limited regime probe analysis method for a flowing plasma to underestimate the positive ion density of the flowing electronegative plasma by up to 50% for a given probe bias. The combined use of a convective RF discharge and probe model make a powerful analysis tool for both predicting and measuring the charged and neutral species densities produced by a RF discharge in a flowing background gas.

## **Acknowledgements**

I wish to thank Prof Bill Bailey for suggesting this wonderfully interesting topic and for his encouragement and mentorship during my research and his devotion and hard work in getting me to the finish line. In addition, I would like to thank Prof Bob Greendyke, Dr. Keith Cartwright, and Prof David Weeks for their excellent support and guidance with my dissertation topic. I would also like to thank my parents, my Grandmother, Brother and Sister, and my Uncle for their loving support and encouragement. And last, but far from least, I want to thank my wife for her patience, loving devotion and for helping me keep my sanity during the long years that it took to perform this research.

Nathaniel P. Lockwood

## Table of Contents

	Page
Abstract .....	iv
Acknowledgements .....	vi
Table of Contents .....	vii
List of Figures .....	x
List of Tables .....	xvi
 I. Introduction .....	 1
Motivation .....	1
Overview .....	3
Objectives .....	4
Background Theory .....	7
RF Discharge Background Theory .....	7
Langmuir Probe Theory .....	13
Single Langmuir Probe Theory .....	18
Double Langmuir Probe Theory .....	20
Langmuir Probe Sheath Theory .....	24
One Dimensional Cylindrical Sheath Model .....	33
Solutions of the One Dimensional Sheath Model .....	36
Langmuir Probe Diagnostic Methods for a Flowing Plasma .....	41
 II. Development of the Plasma Fluid Model .....	 44
Plasma Fluid Model Overview .....	46
Plasma Fluid Model Background Theory .....	48
One Dimensional Solution to the Plasma Fluid Equations .....	56
Linearizing the Plasma Fluid Equations .....	60
Two Dimensional Solution to the Plasma Fluid Equations .....	62
Plasma Fluid Model Boundary Conditions .....	65
Plasma Fluid Model Algorithm Outline .....	70
Plasma Fluid Model Numerical Issues .....	75
Numerical Acceleration Techniques .....	76
Ion Density Rate of Change Acceleration Technique .....	80
Acceleration Techniques for Neutral Excited Species .....	86



	Page
III. Plasma Chemical Kinetic Model .....	89
Overview of the Plasma Chemical Kinetic Model .....	89
Electron Impact Reaction Modeling .....	90
Excited Neutral Species Modeling .....	91
Molecular Vibrational State Modeling .....	94
Losses of Neutral Excited Species to the Wall .....	97
Background Gas Chemical Kinetic Models .....	98
Oxygen Chemical Kinetic Model .....	98
Nitrogen and Oxygen Chemical Kinetic Model .....	102
IV. RF Discharge in a Fast Flowing Electronegative Gas .....	107
RF Discharge Model Set-Up .....	108
RF Discharge Model Comparisons .....	111
One Dimensional Electropositive Discharge Comparison .....	112
Two Dimensional Helium GEC RF Discharge Comparison .....	116
One Dimensional RF Discharge Results .....	120
One Dimensional $O_2(X)$ RF Discharge Results .....	121
Electropositive $O_2(X)$ RF Discharge Results .....	122
Electronegative $O_2(X)$ RF Discharge Results .....	131
$O_2(X)$ RF Discharge in a 25 m/s Flow .....	140
$O_2(X)$ RF Discharge in a 150 m/s Flow .....	145
One Dimensional $N_2(X)$ and $O_2(X)$ Gas Mixture RF Discharge Results .....	154
$N_2(X)$ - $O_2(X)$ RF Discharge in a Stationary and 250 m/s Flow .....	155
$N_2(X)$ - $O_2(X)$ RF Discharge in a 50 m/s Flow .....	159
$N_2(X)$ - $O_2(X)$ RF Discharge at greater than 250 m/s Flow .....	160
Two Dimensional RF Discharge Results in a Flow Tube .....	171
Electronegative $O_2(X)$ RF Discharge with Flow .....	175
$O_2(X)$ and $N_2(X)$ - $O_2(X)$ RF Discharge with Excited Neutrals .....	179
V. Langmuir Probe in a Flowing Electronegative Plasma .....	191
Langmuir Probe Model Using a PIC-MCC Method .....	192
Hybrid PIC-MCC Model .....	196
Hybrid PIC-MCC Langmuir Probe and Sheath Model Comparison .....	201
Langmuir Probe Model Setup .....	206
Hybrid PIC-MCC Langmuir Probe Model Results at Low Pressures .....	210
Probe in a Stationary and Flowing, Collisionless Electronegative Plasma .....	211
Fluid Langmuir Probe Model Results at Moderate Pressures .....	241
Conclusions .....	270
Recommendations .....	278

	Page
Appendix A. Two Dimensional Extension of the Fluid Equations .....	280
Appendix B. Oxygen Reactions and Rate Coefficients .....	282
Appendix C. Nitrogen and Oxygen Reactions and Rate Coefficients .....	285
Appendix D. Neutral Species Densities in a Nitrogen-Oxygen Mixture .....	293
Bibliography .....	295

## List of Figures

Figure	Page
1.1 Parallel Plate Capacitively Driven RF Discharge Diagram .....	10
1.2 Diagram of Characteristic Lengths of a Plasma and Langmuir Probe.....	15
1.3 Parameter Dependent Representation of Various Probe Operation Regimes in a Plasma .....	16
1.4 CVC for the Collisionless Regime.....	22
1.5 CVC for the Collisional Continuum Regime.....	29
2.1 RF Discharge in a Flowing Background Gas Geometry .....	66
2.2 Plasma Fluid Model Flow Diagram.....	71
2.3 Fluid Equation SBLOR Solver .....	74
2.4 RF Discharge in a Flowing Background Gas Geometry .....	79
2.5 Time Averaged Positive Ion and Electron Fluxes .....	82
4.1 Top Down View of Flow Tube.....	109
4.2 Ar RF Discharge with 200V Applied Voltage Time Averaged.....	113
4.3 Ar RF Discharge with 200V Applied Voltage Time Dependent .....	115
4.4 He GEC Reactor RF Discharge Geometry .....	116
4.5 Electron Density Profile in a 1 Torr He RF Discharge.....	118
4.6 Cycle Averaged Electron Energy Profile in a 1 Torr He RF Discharge.....	119
4.7 Cycle Averaged Potential Profile in a 1 Torr He RF Discharge.....	119
4.8 Electropositive $O_2(X)$ RF Discharge Time Averaged Results .....	124

Figure	Page
4.9 Comparison of the Time Averaged Mean Electron Energy.....	125
4.10 Comparison of the Time Averaged Species Current Densities .....	126
4.11 Electropositive $O_2(X)$ RF Discharge Time Averaged Results .....	128
4.12 Electropositive $O_2(X)$ RF Discharge Time Dependent Profiles for a 1000V .....	129
4.13 Electropositive $O_2(X)$ RF Discharge at a 1000V .....	131
4.14 RF Discharge with Electrode Sheath and Ambipolar Field.....	133
4.15 Electronegative $O_2(X)$ RF Discharge at 1000V without Neutral Excited Species.....	134
4.16 Time Averaged Electric Field in an Electronegative $O_2(X)$ RF Discharge at 1000V without Detachment .....	135
4.17 Chemical Kinetic Rates in Pure $O_2(X)$ .....	136
4.18 (a) Time Dependent Electric Field and (b) Time Averaged Production Rates in $O_2(X)$ RF Discharge .....	137
4.19 Cycle Dependent Ionization in an Electronegative $O_2(X)$ RF Discharge .....	139
4.20 $O_2(X)$ RF Discharge at 1000V with Chemical Kinetics and a 25 m/s Flow .....	141
4.21 Comparison of the Current Density in $O_2(X)$ RF Discharge.....	145
4.22 $O_2(X)$ RF Discharge at 1000V with Chemical Kinetics in a 150 m/s Flow.....	147
4.23 Production Rates for (a) Charged Species (b) Neutral Excited Species in an $O_2(X)$ RF Discharge .....	149
4.24 $O_2(X)$ RF Discharge (a) Charged Species Densities (b) Peak Bulk Electric Field .....	150
4.25 Neutral Excited Species Densities for an $O_2(X)$ RF Discharge .....	151
4.26 Time Averaged Charged Species Densities in a $N_2(X)$ - $O_2(X)$ RF Discharge .....	156
4.27 Densities of $N_2(X)$ Vibrational States .....	158

Figure	Page
4.28 Time Averaged Ion and Electron Flux in a $N_2(X)$ - $O_2(X)$ RF Discharge.....	161
4.29 Time Dependent Electron Current Density in a $N_2(X)$ - $O_2(X)$ RF Discharge.....	163
4.30 Average Charged Species Production Rates in a Flowing $N_2(X)$ - $O_2(X)$ Gas.....	164
4.31 Charged Species Densities in a $N_2(X)$ - $O_2(X)$ .....	165
4.32 Neutral Excited Species Production Rates in a $N_2(X)$ - $O_2(X)$ Flowing Gas .....	167
4.33 Neutral Excited Detaching Species Densities in a $N_2(X)$ - $O_2(X)$ Flowing Gas.....	168
4.34 Densities in a 2-D $O_2(X)$ RF Discharge in a Stationary Gas.....	173
4.35 (a) Charged Species Densities (b) Ambipolar Field of an $O_2(X)$ RF Discharge.....	174
4.36 Charged Species Densities of an $O_2(X)$ RF Discharge in a 250 m/s Flow .....	177
4.37 Ambipolar Electric Field in a $N_2(X)$ - $O_2(X)$ RF Discharge in a 250 m/s Flow .....	179
4.38 Species Densities of an $O_2(X)$ RF Discharge in a 250 m/s Flow .....	180
4.39 $O_2(X)$ Species Densities in an RF Discharge in a 250 m/s Flow .....	181
4.40 Mean Electron Energy of $N_2(X)$ - $O_2(X)$ RF Discharge in a 250 m/s Flow .....	183
4.41 Production Rates of a $N_2(X)$ - $O_2(X)$ RF Discharge in a 250 m/s Flow .....	184
4.42 Charged Species Densities in a $N_2(X)$ - $O_2(X)$ RF Discharge in a 250 m/s Flow .....	185
4.43 $O_2(X)$ Species Densities in a $N_2(X)$ - $O_2(X)$ RF Discharge in a 250 m/s Flow .....	186
4.44 $N_2(X)$ Species Densities in a $N_2(X)$ - $O_2(X)$ RF Discharge in a 250 m/s Flow.....	188
5.1 Comparison of (a) Potential Difference and (b) Standard Deviation Profiles .....	203
5.2 Comparison of the 1-D Sheath, Pre-Sheath and Hybrid PIC-MCC Models.....	204
5.3 Comparison of Density Profiles between the Hybrid PIC-MCC and Sheath Model.....	205
5.4 Langmuir Probe in a Flowing Background Gas Geometry .....	207
5.5 Langmuir Probe in a 0.001 Torr Non-Flowing Oxygen Plasma.....	212

Figure	Page
5.6 Mid-Section Slice of the (a) Potential and Radial Ion Velocities .....	214
5.7 Radial Current Density Comparisons along the Probe Length .....	216
5.8 Langmuir Probe in a 0.001 Torr Oxygen Plasma Flowing at 200 m/s .....	217
5.9 (a) Potential and Positive Ion Velocity Profiles Normalized to the Probe Bias and Electronegative Bohm Velocity .....	218
5.10 (a) Potential and (b) Positive Ion Velocity Comparison of 400 m/s, 200 m/s and No Flow Cases .....	219
5.11 Positive Ion Velocity Vector Plot Near Downstream Tip of the Probe with Probe Center at 3 cm .....	221
5.12 Negative Ion Density Around a Probe in a 0.001 Torr Oxygen Plasma Flowing at 200 m/s .....	222
5.13 Negative Ion Velocity Vectors Downstream of the Probe in a 200 m/s Flow at 0.001 Torr with Center of Probe at 3 cm .....	223
5.14 Negative Ion Velocity Vectors at the Upstream Tip of the Probe in a 200 m/s Flow at 0.001 Torr with Center of Probe at 3 cm .....	224
5.15 Probe Sheath in a 0.001 Torr 200 m/s Flow .....	226
5.16 Langmuir Probe in a 0.01 Torr 200 m/s Flowing Oxygen Plasma .....	228
5.17 Langmuir Probe in a 0.01 Torr Stationary Oxygen Plasma .....	230
5.18 Comparison of the Radial Ion Velocity and Sheath Radius .....	231
5.19 Contour Plot of Potential Around the Probe Tip in a 200 m/s Flow at 0.01 Torr with Probe Center at $z = 3$ cm .....	232
5.20 Drop in Potential Over the Pre-Sheath at $r=0.2$ cm .....	233

Figure	Page
5.21 Negative Ion Velocities Near the Tip of the Probe in a 200 m/s Flow at 0.01 Torr with Probe Center at $z = 3$ cm.....	234
5.22 Net Charge Density Around a Probe .....	235
5.23 Mid Sectional Profile of the Charge Density Around a Langmuir Probe in a 200 m/s Flow .....	236
5.24 Radial Current Density Comparisons Along the Probe Length at 0.01 Torr.....	238
5.25 Comparisons of Hybrid PIC-MCC Probe Model and Convection Diffusion Theory at 0.01 Torr .....	240
5.26 Langmuir Probe Fluid Model Set-up .....	242
5.27 Ion Flux and the Divergence of the Ion Flux in a Sourceless 1-D O <sub>2</sub> Probe Model with the Sheath Edge Determined using the Quasi-Neutrality Condition .....	246
5.28 Contour Plot of the Positive Ion Density Around a Probe.....	249
5.29 Contour Plot of the Positive Ion Density Around a Probe.....	250
5.30 Contour Plot of the Potential Difference Around a Probe .....	251
5.31 Electric Field at the Tip of the Probe .....	253
5.32 Charged Species Densities at the Tip of the Probe ( $z = 2.5$ cm) .....	255
5.33 Comparison of (a) Net Charge and (b) Potential Profiles at the Probe Tip .....	256
5.34 Negative Ion Velocity Vector Plot Near Probe Tip .....	257
5.35 Comparison of Radial (a) Potential Profiles and (b) Net Charge .....	258
5.36 Positive Ion Collecting Radius.....	260
5.37 Langmuir Probe Collection Radius for Ions Flowing into the Sheath Region .....	261
5.38 Comparison of the Probe CVC in a Non-Flowing and Flowing Gas .....	262

Figure	Page
5.39 Estimated Positive Ion Density Based on Simulated Current Collection .....	263
5.40 Radial Electric Field Near the Upstream Collecting Radius .....	264
5.41 Average Path of the Positive Ions Collected by the Probe .....	265
5.42 Radial Current Density Comparisons along Length of the Probe.....	266
5.43 Comparison of the Collected Current by a Probe .....	268
5.44 Comparison of the Probe CVC in a 1 Torr Non-Flowing and Flowing Background Gas .....	269
D.1 Time Dependent Current Densities in a $N_2(X)$ - $O_2(X)$ RF Discharge at 1000V in (a) Stationary (b) 250 m/s Flow Conditions .....	293
D.2 Density Profiles of Excited Neutral Species Produced in a $N_2(X)$ - $O_2(X)$ RF Discharge	294



## List of Tables

Table	Page
4.1 Comparison of Discharge Structure for Limiting Cases.....	140
4.2 Comparison of $O_2(X)$ RF discharge Cases.....	148
4.3 Primary Reactions that Result in Gains and Losses of Neutral Excited Species.....	152
B.1 Oxygen Chemical Kinetic Reactions in the PFM .....	282
C.1 Nitrogen Chemical Kinetic Reactions in the PFM.....	285
C.2 Nitrogen, Oxygen, and Nitrous Oxide Chemical Kinetic Reactions in the PFM.....	287
C.3 References for Tables C.1 and C.2.....	290
C.4 Wall Loss Probabilities in a Nitrogen – Oxygen Mix.....	292

# INVESTIGATION OF RADIO FREQUENCY DISCHARGES AND LANGMUIR PROBE DIAGNOSTIC METHODS IN A FAST FLOWING ELECTRONEGATIVE BACKGROUND GAS

## I. Introduction

### Motivation

Discharges in a flowing background gas are used to produce charged and excited atomic and molecular species for growing high quality compound materials, sterilizing surgical equipment, etching semiconductors, pumping gas lasers, and a variety of other applications (Pinhero and others, 1998). The Air Force is currently developing the Electric Chemical Oxygen Iodine Laser (ElectriCOIL) system to replace the liquid chemistry  $O_2(^1\Delta_g)$  generator currently used in the Air Borne Laser (ABL) system (Zimmerman and others, 2003). The ElectriCOIL system produces  $O_2(^1\Delta_g)$  in a radio frequency (RF) or microwave discharge in a flowing pure or molecular oxygen noble gas mixture. Downstream of the discharge, the  $O_2(^1\Delta_g)$  is mixed with  $I(^2P_{3/2})$  to create the population inversion necessary for lasing (Pitz and others, 2004). Improving the yield and reducing the quenching rate of  $O_2(^1\Delta_g)$  as it is convected downstream is critical to improving the performance of the ABL system. The use of a second non-self sustained discharge operating at a lower power downstream of the first discharge to boost the yield of  $O_2(^1\Delta)$  was investigated (Hicks and others, 2006). Being able to predict and measure the plasma density convected downstream by the first discharge is essential to maintaining the second non-self sustained discharge due to supplying an electron source.

RF discharges are also used in a flowing electronegative background gas to dissociate molecular oxygen and nitrogen. Nitrogen and oxygen atoms have been shown to be very beneficial in the growth of semi-conductor materials. However, ions produced by RF discharges create point defects on impact with the growing film, rendering them useless (Mantis, 2006). Placing the semi-conductor film downstream far enough that the ion density is negligible is a common approach to avoiding this problem.

Accurately predicting the neutral excited species and plasma density produced by an RF discharge in a flowing oxygen and oxygen-nitrogen background gas and understanding the effect that a flow has on a RF discharge is essential to improving the excited atomic and molecular species yield for both applications. In addition, performing diagnostics of the plasma density convected downstream using a Langmuir probe is also critical to monitoring performance of the RF discharge and determining the placement of the second RF discharge or semiconductor film.

The objectives of this research are to first, develop a Langmuir probe diagnostic technique for determining ion density in a moderate to low pressure (0.001 to 1.0 Torr) electronegative plasma downstream of a discharge. The secondary objective is to examine plasma and excited neutral densities generated by a RF discharge in a fast flowing electronegative gas and study the subsequent decrease in density of the charged and neutral excited species downstream.

## Overview

The first chapter provides a more detailed statement of the objectives of the study and describes the general approach taken to achieve those objectives. The last part of the first chapter provides background information on basic Langmuir probe and RF discharge theory.

Chapter II summarizes the drift-diffusion-convection plasma fluid model that was developed for this research to investigate electronegative plasma generation and Langmuir probe diagnostics. Background theory and assumptions associated with the fluid equations and drift-diffusion-convection approximation of the momentum equation are presented. The development of the approach to solve the fluid equations numerically and several computational issues associated with the numerical method are discussed. Finally, methods for accelerating the convergence of the fluid equation solutions are developed and discussed.

Chapter III provides an overview of the plasma chemical kinetics model used in conjunction with the plasma fluid model to determine the loss and gain rates for the charged and excited neutral species. The specific details used to model the electron kinetics and neutral species chemical kinetic reactions used in the RF discharge model for pure  $O_2(X)$  and an  $N_2(X) - O_2(X)$  gas mixture are also reviewed and discussed.

In chapter IV, results of the plasma fluid model for an electropositive RF discharge model are examined and compared to other computer models and expanded to an electronegative RF discharge. The model setup of a RF discharge in a flow tube for one and two dimensions is presented. Results of the RF discharge model for  $O_2(X)$  and  $N_2(X) - O_2(X)$  background gases at a variety of flow rates and voltages are then

presented. Conclusions are drawn on the effect of a flowing background gas on charged and neutral species production and the structure of the RF discharge.

Chapter V summarizes the development of the hybrid Particle-in-Cell-Monte Carlo Collision (PIC-MCC) method used to reduce convergence time of the simulation and overcome numerical issues associated with modeling a Langmuir probe. The methodology used to model a Langmuir probe in a flowing plasma is described and model results are compared to established sheath models and other Langmuir probe diagnostic approaches. Results from the computer simulations of the Langmuir probe are examined, trends in the ion current collection for low and moderate pressure flowing plasmas are analyzed, and a method is proposed for analyzing a plasma in a moderate pressure flowing electronegative plasma. Finally conclusions are drawn about the effect of a flowing electronegative plasma on the sheath and current collection of a Langmuir probe.

## **Objectives**

The overall goal of this research is to develop plasma kinetic models to investigate plasma generation and probe diagnostic methods in a flowing electronegative background gas. The first objective of this study is to assess the accuracy of current Langmuir probe methods for determining the positive ion densities of an electronegative plasma in a fast flowing background gas. The second objective is to determine the effect of a fast flowing background gas on a RF discharge using a combined plasma fluid and chemical kinetic approach to quantitatively explore: the generation of the plasma and

excited neutral species, the effects of the neutral gas flow on the discharge sheath structure, and the decay of plasma and excited species downstream of the discharge.

Langmuir probes have been used previously to perform diagnostics in fast flowing gases (Clements and Smy, 1969); however, the combined effect of negative ions, intermediate gas pressures and flow on the probe sheath and the resulting current measured by the probe have not been investigated either theoretically or computationally. Using a hybrid PIC-MCC and a plasma fluid model approach, the effects of these parameters on the probe sheath are studied and a method is developed for determining the positive ion density from a Langmuir probe current measurement. For the low pressure regime ( $P \sim 1 - 10$  mTorr), a hybrid PIC-MCC model was used and for the moderate pressure regime ( $P \sim 1$  Torr), a fluid model was developed. The PIC-MCC model is valid for any pressure regime, however, the computational overhead associated with the Monte Carlo Collision model make it impractical for use at higher pressures. The two models developed for this study are used to investigate the response of the probe sheath in both the collisionless and transitional collisional regimes of a background gas with a uniform density and flow velocity. Based on the results of the modeling, an approach for analyzing the Current Voltage Characteristic (CVC) of the Langmuir probe is developed and compared to the flowing plasma Langmuir probe diagnostic techniques developed by Clements and Smy, 1969.

RF discharges in flowing, electronegative background gases at moderate pressures have been shown to be sensitive to flow velocities as low as 5 mps (Sato and Shida, 1999). Stoeffels and others, 1995, have said that “particular attention must be paid to the behavior of the charged species since they determine both the physical and chemical

features of the plasma such as RF power dissipation, the structure of the plasma sheath, and the fluxes of reactive molecules reaching the surface.“ This study addresses issues that have not been answered in previous studies to include: the effect of a fast flowing electronegative background gas on charged and neutral species densities, the decay of charged and neutral species densities downstream of the discharge, and the effects of excited neutral species on the RF discharge structure. To investigate the impact of flow on a RF discharge, a fluid model of a RF discharge in a fast flowing background gas was developed. One dimensional modeling of a RF discharge in argon and molecular oxygen in non-flowing conditions were performed to bolster the understanding of the effects of molecular gas and negative ions on the RF discharge structure and fields. One dimensional RF discharges in both a  $O_2(X)$  and  $N_2(X)-O_2(X)$  mixture were then used to approximately model plasma and excited neutral species production in a large diameter tube in a flowing background gas. From the one dimensional  $O_2(X)$  and  $N_2(X)-O_2(X)$  RF discharge models, the change in the plasma and neutral densities in the discharge region due to changes in flow velocity were examined. A two dimensional fluid model was then employed to examine the decay of the charged and excited neutral species densities downstream from the discharge. The potential for using a RF discharge in a fast flowing electronegative gas to convect charge downstream to a second microwave discharge is then discussed.

To understand the physics of an RF discharge and Langmuir probe in a flowing plasma, it is useful to understand what is currently known about RF discharges and Langmuir probes in a stationary and flowing background gas. The next sections provide

background information on standard RF discharge operation and Langmuir probe diagnostic techniques.

## **Background Theory**

### **RF Discharge Background Theory**

RF discharges in electropositive and electronegative gases have been extensively studied both computationally Graves, 1987, Paranjpe, 1992, Boeuf, 1987, Lymberopoulos and Economou, 1992, Ellaisi and others, 2006 and experimentally by Nakano and others, 1994, Katsch and others, 1999, Stoffels and others, 1995. The operation of an RF discharge in a variety of background gases and pressures is well understood. The background gas for an RF discharge can be either electropositive or electronegative in nature. A plasma in an electropositive gas, such as *He*, *Ar*, or  $N_2(X)$ , exhibits negligible electron attachment rates to neutral molecules, therefore the plasma is only composed of electrons, positive ions and neutral molecules or atoms. An electronegative gas, such as  $O_2(X)$  or  $SF_6$ , has a high electron affinity and hence negative ions are also present in the RF discharge generated plasma.

RF discharges operate at frequencies between 100 kHz and 100 MHz and can be capacitively or inductively coupled with the generated plasma. This study is concerned exclusively with parallel plate capacitively coupled discharges which are characterized by parallel electrodes immersed in a background gas. Typical pressures of operation for RF discharges are in the range of 10-100 mTorr and power densities are between 0.1 and 1 W/cm<sup>2</sup> (Raizer, 1994). At low frequencies (<50 kHz), the discharge is referred to as an alternating current (AC) discharge essentially operates similar to a direct current (DC) discharge, except that the electrodes switch roles as the cathode and anode during the



oscillatory half cycle. At frequencies greater than 50 kHz, the differences of a DC discharge from an RF discharge become apparent due to the current density through the discharge being directly proportional to the discharge frequency. The proportionality of the discharge current to the frequency is due to displacement current caused by the time varying electric fields in the sheath region. At frequencies greater than 50 kHz, electron conduction current, however, still dominates in the bulk plasma in RF discharges (Raizer 1994). At these lower frequencies secondary electron emission due to ions impacting the electrodes is still required to sustain the discharge. At higher frequencies of approximately 10 MHz, the electron currents and subsequent Joule heating result in ionization rates that are adequate to sustain the discharge without secondary electron emission (Boeuf and Pitchford, 1995). An RF discharge operating without secondary electron emission is referred to as being in the alpha mode, while an RF discharge with high enough discharge currents to induce secondary electron emission is referred to as operating in the gamma discharge mode. At these higher frequencies, the electron energy relaxation time is greater than the RF cycle time for noble background gases, so the electrons remain energetic during the entire RF cycle (Boeuf, 1993). The time varying electric field of the RF discharge transferring energy to the electrons in the bulk plasma makes the RF discharge more efficient than DC discharges at sustaining a high plasma density. For non-noble electropositive gases, such as molecular nitrogen and methane, electron energy relaxation time is much less than the RF cycle time, so the electrons relax in energy quickly resulting in excitation waves along with the movement of the electrons and time varying electric fields near the plasma-sheath edge (Graves, 1988). At frequencies greater than 100 MHz, the electrons oscillate without experiencing collisions,

which results in the electron current lagging in phase with respect to the discharge electric field. This situation results in very weak collisional coupling between the electrons and the background gas resulting in low ionization rate and current densities (Paranjpe, 1998).

Plasmas created by RF discharges are generally separated into two spatial regions referred to as the quasi-neutral bulk plasma and the sheath region. The bulk plasma in an electropositive RF discharge is characterized by small electric fields. For an electropositive plasma, quasi-neutral implies

$$n_i = n_e \quad (1.1)$$

while for an electronegative plasma

$$n_i = n_e + n_n \quad (1.2)$$

where

$n_e$  - Electron number density

$n_i$  - Positive ion number density

$n_n$  - Negative ion number density

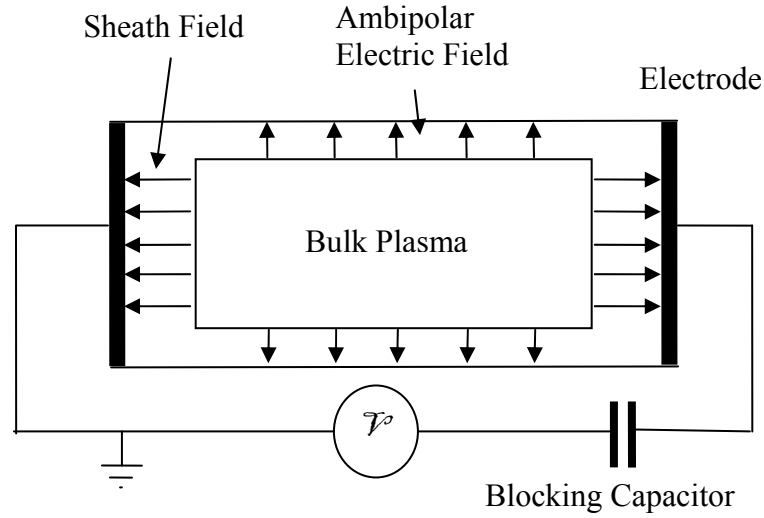


**Figure 1.1 Parallel Plate Capacitively Driven RF Discharge Diagram**

The time varying sheaths near the electrodes are characterized by high electric fields and a loss of the quasi-neutrality in the plasma. The sheath region is non-quasi-neutral because negatively charged species are generally accelerated away from the electrode due to the sheath electric field. However, the positive ions are accelerated towards the electrode due to the electric field in the sheath. Time varying sheaths are formed in a RF discharge near the electrodes due to the oscillating electrons being lost very quickly when closely approaching the electrode. During that time, the instantaneous sheath electric field collapses to a near zero value linearly with time, allowing a large electron current to the electrode (Boeuf, 1987). The relatively massive ions, however, only respond to the average electric field and hence a low ion current to the electrode is present during the entire RF cycle. The continuous presence of positive ions in the sheath region results in a net positive space charge in the sheath when the densities of the electrons and ions are averaged over an RF cycle. The net positive charge in the sheath

produces a large time averaged electric field in the sheath directed towards the electrodes as shown in Figure 1.1.

Plasmas generated by RF discharges at frequencies greater than 10 MHz in an electropositive gas typically have electron number densities of  $10^8 - 10^{11} \text{ cm}^{-3}$ , high temperature electrons ( $T_e \approx 1 - 10 \text{ eV}$ ), and ions with near neutral gas temperatures due to high collisional coupling with the background gas (Raizer, 1994). The density of an electropositive plasma is determined by ionization rates, ambipolar diffusion losses transverse to the discharge, recombination of charged species, and losses of charged species to the electrodes. Ionization primarily occurs at the edge of the sheath region due to a near exponential dependence on the electric field and a moderately high number of electrons in that region. The density of an electronegative plasma is additionally influenced by the rate of bulk processes such as attachment and detachment with neutral species in the background gas. In highly electronegative gases, negative ion densities are generally one to two orders of magnitude greater than the electron densities due to fast attachment rates. Studies have shown that the rates of these bulk processes can be strongly influenced by the densities of atoms and excited molecules produced in RF discharges (Shibata and others, 1994).

If the current and voltage on the electrodes continue to grow in the alpha mode, the discharge eventually contracts so that the current density at the electrodes rises by an order of magnitude. Externally the transition from the alpha to the gamma mode can be observed by the bulk plasma at the gap center becoming much brighter due to larger numbers of excited neutral species being produced. There are many internal differences between the alpha and gamma mode discharge sheath structure and charge production

mechanisms. The electrode sheath is smaller in the gamma mode resulting in a higher electric field,  $E \approx V / d_\gamma$ , where  $d_\gamma$  is the gamma mode sheath length. The reduction in the sheath thickness and hence increase in sheath field is optimal for electron multiplication and as a result electrons, created by ions impacting with the electrode, multiply in the sheath region due to ionization. The high plasma density associated with the gamma discharge mode is due to the intense electron multiplication in the electrode sheath. In the positive column, ionization levels are determined by the processes occurring in the sheaths and since large amounts of ionization occur in the sheaths in the gamma mode, very little ionization occurs in the positive column (Raizer, 1994). The alpha and gamma RF discharge modes both have normal current density modes, however,  $J_{n\gamma} \gg J_{n\alpha}$ , where  $J_{n\gamma}$  is the normal current density in the gamma mode and  $J_{n\alpha}$  is the normal current density in the alpha mode.  $J_{n\gamma}$  is larger than  $J_{n\alpha}$  due to a larger electron density and displacement current in the sheaths (Raizer, 1994). Like the alpha mode, the characteristics of the gamma discharge mode are altered in different pressure regimes. In moderate pressure gamma discharges, the bulk plasma processes are responsible for the fairly high electron temperature,  $T_e$ , which is close to the  $T_e$  of the alpha discharge. In a low pressure discharge, the bulk plasma  $T_e$  of the gamma mode is much lower than that of the alpha discharge mode resulting in secondary electron emission supplying the majority of the electrons in the discharge (Raizer, 1991).

Choosing to operate the RF discharge in one mode or the other depends on the intended application of the discharge. For etching applications, the alpha mode is generally preferred because the hotter plasma and more energetic ions of the gamma mode tend to destroy the substrate being etched. For producing high yields of excited

molecular species the alpha mode is also preferable due to the high  $T_e$  values in the bulk plasma. To create high yields of atomic species from the higher energy dissociation processes, the gamma mode is some times more desirable due to the high energy electrons near the sheath edge. However sputtering of metal off of the electrode surface which occurs in the gamma mode contaminates the plasma and lowers the discharge stability. The contamination results in less uniformity in the production of excited species and usually makes this mode of operation undesirable for materials processing. For this investigation of the charged and excited neutral species produced by an RF discharge, the focus is on the alpha mode of operation for RF discharges. This is due to the sensitivity to uniformity associated with the semi-conductor growing processes and the need to produce lower energy electrons resulting in high yields of  $O_2(^1\Delta)$  and  $O_2(^1\Sigma)$  states for pumping the oxygen-iodine laser with an RF discharge (Hicks, 2006). In the next section, the theory of Langmuir probes is reviewed. This theory provides a basis for the development of a method of analyzing Langmuir probes in a flowing, moderately collisional electronegative plasma.

### **Langmuir Probe Theory**

The Langmuir probe method is unique from other diagnostic techniques in its ability to determine the spatial distribution of density and temperature in a plasma. A Langmuir probe is a metal conductor which is usually coated with insulation almost to the tip. Probe shapes are generally spherical, cylindrical, planar, or elliptical, with the most common shape being cylindrical. The exposed metal portion of the Langmuir probe is usually less than 1 mm in diameter and in many cases is only a tens of micrometers in diameter and under many conditions, results in only small disturbances in the plasma

(Cenian and others, 2004) and (Lieberman and Lichtenberg, 1994). The modeled Langmuir probe radius used in this investigation is 0.5 mm, which is on the larger side for a Langmuir probe. To perform diagnostics with a Langmuir probe, the surface of the probe is placed in contact with the plasma. The probe potential, which is referenced with respect to either an electrode, grounded metal wall, or another probe, is systematically varied by a potentiometer to obtain a current-voltage characteristic (CVC). Analysis of the CVC enables determination of the density and temperature of a plasma (Raizer, 1991).

Langmuir probe techniques for measuring the plasma density and temperature have existed for nearly eighty years (Tonks and Langmuir, 1929). Existing theories for determining electron density and temperature using single and double probe CVCs in a non-flowing, electropositive plasma have been studied extensively for collisionless (Mott-Smith and Langmuir, 1926) and collisional plasmas (Kiel, 1969). Relevant parameters for determining the appropriate regime for analyzing a Langmuir probe are shown in Figure 1.2. The Debye length,  $\lambda_D$ , is the shielding length of the plasma and is related to the length of the probe sheath and  $\lambda_i$  is the ion mean free path between collisions with the background gas.

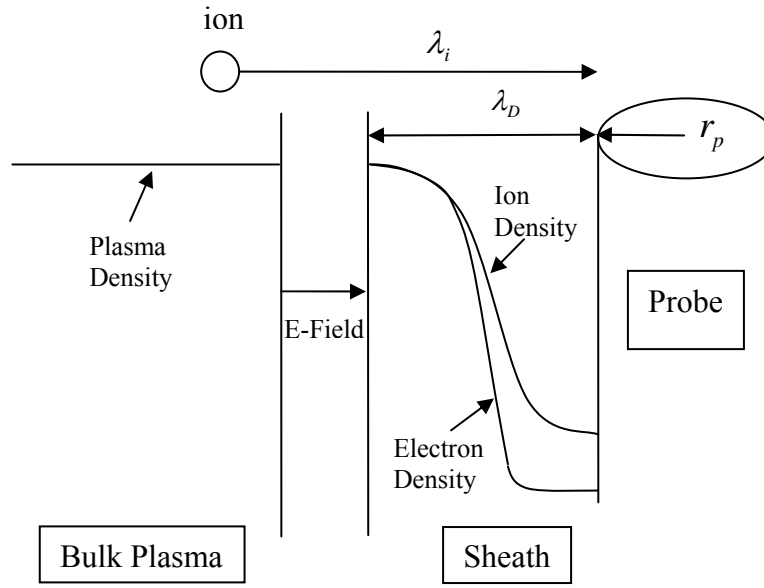


**Figure 1.2 Diagram of Characteristic Lengths of a Plasma and Langmuir Probe for Determining Appropriate Analysis Theories for a Probe CVC**

The collisionless regime, shown in Figure 1.3, is defined by  $\lambda_i \gg \lambda_D$  which indicates that almost no collisions occur while an ion is traversing the probe sheath. The collisional regime is defined by  $\lambda_D \gg \lambda_i$  which indicates that the ions experience many collisions while traversing the probe sheath. Langmuir probe theory is further divided up into thin sheath theory defined by  $r_p \gg \lambda_D$  and thick sheath theory defined by  $r_p < \lambda_D$  where  $r_p$  is the probe radius. A probe being in the thick or thin sheath regime is relevant for determining if the probe sheath length is large enough that its determination is required for performing the analysis of the ion current collected by the probe to establish the density of the plasma.



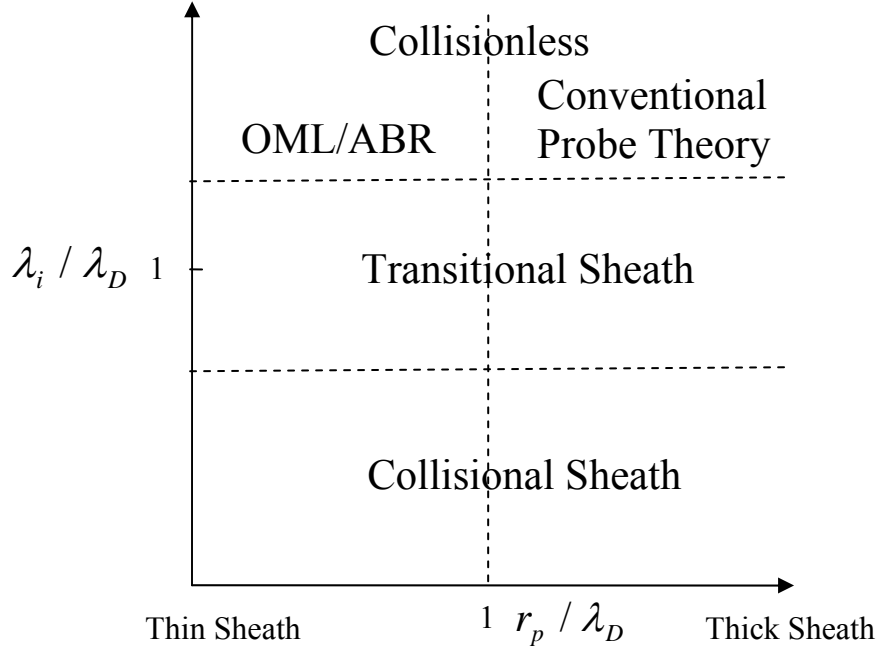


**Figure 1.3 Parameter Dependent Representation of Various Probe Operation Regimes in a Plasma**

A variety of well developed theories by Mott-Smith and Langmuir, 1926, Chen, 1965, Bernstein and Rabinowitz, 1966, Sonin and others, 1966, Lamframboise, 1966, et. al., exist for analyzing the CVC of a non-flowing, electropositive, collisionless plasmas in the Orbital Motion Limited (OML) regime. Recently modifications to OML theory have been made by Sternovsky, Lampe, and others to account for increased ion current to the probe created by weak ion-neutral collisions and charge exchange in the sheath (Sternovsky and others, 2004). Allen, Boyd, and Reynolds (ABR) developed the Radial-Motion theory also known as ABR theory for the collisionless, thin sheath regime in the limit of cold ions ( $T_i / T_e = 0$ ) (Allen and others, 1957). These approaches were later modified by Chen, 1965, using an iterative method for determining the ion density of a probe with a thick sheath. Shih and Levi, 1971, investigated ABR theory for the sheath in the presence of a few ion-neutral collisions and found that ABR theory reduced to

Chen's theory with slight modifications. Amemiya, 1999, made further modification to ABR theory to account for the presence of negative ions using an iterative method that determined the sheath radius by matching the predicted CVC curve with the measured CVCs. Su and Lam, 1963, Kiel, 1969, and many others have developed theories to analyze electrostatic probes in a non-flowing, electropositive, collisional plasma with thin and thick sheaths respectively. However, for the transitional regime, where  $\lambda_D \approx \lambda_i$ , none of the treatments described above are valid and no complete theory exists for analyzing probe CVCs. Theories do not exist due to the complexity associated with the coincidence of two transitions in the characteristic lengths that define the sheath and as a result there is no simple analytic sheath description (Franklin, 2003).

In addition, work has been done in the case of flowing plasmas, however, it is mostly centered around collisional, collisionless, thin, and thick electropositive plasmas. Lam developed the foundational theory for the ion convection current collected by an arbitrary object with a small viscous boundary layer in a flowing plasma (Lam, 1964). Clements and Smy noted a two order of magnitude difference in ion current collected between probe measurements in a stationary and flowing electropositive, high pressure plasmas and applied Schulz and Brown's theory and Lam's theory to develop an analysis for thin and thick sheath cylindrical probes respectively to account for the increase in ion convection current (Clements and Smy, 1969 and 1970). Andrews and Swift-Hook, 1971, developed a slight analytic modification to collisionless ABR theory to account for increases in floating point potential caused by cold ions flowing into the collisionless pre-sheath of the plasma. Kanal, 1964, and Hoegy and Wharton, 1973, developed analytic predictions for the current collected by a cylinder for a warm, flowing, collisionless

plasma in the OML case. Recently, McMahon and others have modeled finite temperature, flowing electropositive collisionless plasmas using a variant of Parker's "outside-in" method (McMahon and other, 2005). Hutchinson has recently investigated a spherical probe in a drifting, collisionless, non-zero Debye length plasma using a modified Particle-in-Cell approach (similar to the method reported in Chapter V). However, currently there is no established theory that describes the sheath of a Langmuir probe in a transitional collisional regime in the presence of a fast flowing electronegative plasma. In this study, we develop a modified version of Clement and Smy's theory to analyze the CVC of a probe in an electronegative, transitional regime plasma and assess the accuracy of already established probe analysis techniques for analyzing probe CVCs. In the next section, the basic theories for interpreting probes in the various regimes are reviewed to help interpret the results of the models presented in Chapter V.

### **Single Langmuir Probe Theory**

A single probe is commonly used to measure the electron density and temperature of a DC discharge because a steady reference is provided by an electrode at a constant potential. The experimentally measured probe current and potential can be described by the following expressions

$$I_m = I_e - I_i \quad (1.3)$$

$$V = V_p + V_s \quad (1.4)$$

where

$I_m$  - Total electronic and ionic current

$I_i$  - Positive ion current

$I_e$  - Electron current

$V_p$  - Probe potential with respect to the plasma

$V_s$  - Plasma potential

If the probe is unbiased relative to ground then  $V = V_s$ , which is the floating point of the curve, and the charged species are collected by the probe due to their thermal velocity. Since, the electron thermal velocity is much greater than the ion thermal velocity, the probe collects mostly electron current. For a positively biased probe relative to the plasma potential such that  $V > V_s$ , ions are repelled by the probe and electrons are attracted and for  $V < V_s$ , electrons are repelled by the probe and ions are attracted. When  $V > V_s$  or  $V < V_s$ , a sheath forms around the probe screening the potential of the probe from the rest of the plasma. At a distance from the probe larger than the sheath radius the plasma is quasi-neutral and free of electric fields. The charged species in the quasi-neutral regime that come into contact with the sheath are then either attracted to the probe surface or repelled depending on the charge of the species and the bias of the probe.

The vast majority of current collected by the probe when  $V \geq V_s$  is electron current. Assuming the electron velocity distribution is Maxwellian, the electron current to the probe can be expressed as

$$I = I_{e,sat} \text{Exp}(eV_p / kT_e) \quad (1.5)$$

where

$$v_{e,th} = \sqrt{\frac{8kT_e}{\pi m_e}} \text{ - Electron thermal velocity}$$

$$I_{e,sat} = S(en_e \bar{v}_{e,th} / 4)$$

$I_{e,sat}$  - Electron saturation current

$S$  - Surface area of the sheath

$e$  - Fundamental unit of charge

The plasma is analyzed by plotting the current collected by the probe versus the potential bias of the probe. The electron temperature and saturation current can be determined from the single probe CVC by recasting Equation 1.5 into the form

$$\ln \frac{I}{I_{e,sat}} = eV_p / kT_e \quad (1.6)$$

The plot of  $\ln I$  versus  $V_p$  can be fit using standard techniques. The slope of the fit line is equal to  $e / kT_e$  and the y intercept is  $-\ln I_{e,sat}$ . From these measured values, the plasma density is then calculated from the electron saturation current using the equation

$$n_e = \frac{I_{e,sat}}{S(ev_{e,th} / 4)} \quad (1.7)$$

where the sheath radius is considered to be small compared to the probe radius and is therefore assumed to be equal to the probe radius (Raizer, 1991). Measuring the electron saturation current, however, is not realizable in many cases due to the large currents that are developed by the highly mobile electrons which disturb the plasma and produce errors in probe measurements. As a result, most plasma density measurements are made using the ion saturation current, which is the current collected by the probe when the electrons are completely repelled by the negative probe bias. However, measuring the ion saturation current commonly requires a more sophisticated analysis approaches which will be discussed in the next sections (Lieberman and Lichtenburg, 1994).

### **Double Langmuir Probe Theory**

Since there is no appropriate voltage reference for a single probe in an RF discharge, a double probe diagnostic method is typically used to determine the electron

temperature and density of the discharge (Malter and Johnson, 1950). Several methods have been developed for determining the ion density and electron temperature from a double probe CVC. Methods of calculating the electron temperature presented in this section were developed by Chen, 1965, Schott, 1968, and Menart, 2004. The first method for determining electron temperature is based on the assumption that the electrons are distributed according to a Maxwell-Boltzmann distribution and the current collected by the first probe is the same as the current collected by the second probe for a particular probe bias (Raizer, 1991). Using this assumption, we obtain the equation

$$I_m = I_{i,1}(V_{P1}) - I_{e1} \exp[eV_{P1} / kT_e] = -I_{i,2}(V_{P2}) + I_{e2} \exp[eV_{P2} / kT_e] \quad (1.8)$$

$$V_m - V_c = V_{P1} - V_{P2} \quad (1.9)$$

where

$I_m$  - Total electronic and ionic current on either probe 1 or 2

$I_{i,1}(V_{P1})$  - Ion current on probe 1

$I_{e1}$  - Electron saturation current on probe 1

$V_{P1}$  - Voltage on probe 1

$T_e$  - Electron temperature

$V_m$  - Voltage difference between probe 1 and probe 2

$V_c$  - Voltage offset for the zero current in the CVC.

Taking the derivative of equation 1.8 with respect to  $V_m$ , yields the electron temperature of the plasma

$$T_e = \frac{e}{k} \left( \frac{I_{i,1}}{\frac{dI_{i,1}}{dV_{p1}} - 2 \frac{dI_m}{dV_m}} \right) \quad (1.10)$$

Shown in Figure 1.4 is an example of a theoretical double probe CVC produced using Kiel's collisionless sheath theory to determine the ion saturation current to each probe (Chung, 1975). From equation 1.10, the electron temperature of the plasma can be determined by using the steep portion of the curve shown in Figure 1.4. This steep portion of the CVC is due to the current transitioning between ion saturation currents of the two probes.

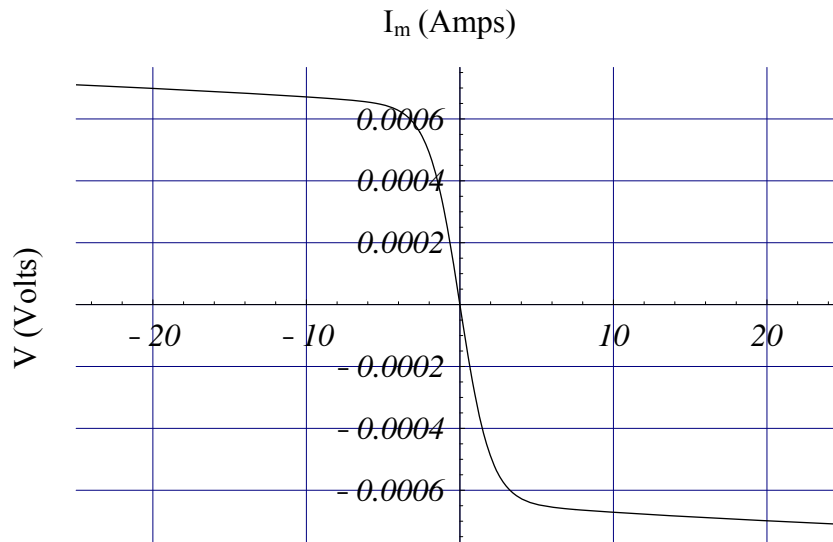


**Figure 1.4 CVC for the Collisionless Regime with  $T_e = 1$  eV,  $n_e = 10^{12}$  cm<sup>-3</sup>,  $r_p = 0.025$  cm**

A second method that is commonly employed to calculate the electron temperature from a double probe CVC is based on the same equations as the previous

method. This second method, however, has been shown to produce more precise results in the case of noisy CVCs. The zero current point in the CVC ( $I_m = 0$ ) implies that

$$I_{i,1}(V_{P1}) = I_{e1} \exp[eV_{P1} / kT_e] \Big|_{I_m=0} \quad (1.11)$$

$$I_{i,2}(V_{P2}) = I_{e2} \exp[eV_{P2} / kT_e] \Big|_{I_m=0} \quad (1.12)$$

using these relationships and equation 1.8, it can be shown that

$$\ln \left[ \frac{(I_{i,1} - I_{i,2}) \Big|_{I_m=0}}{I_m - I_{i,1}} + 1 \right] = -\frac{eV_m}{kT_e} + \ln \left[ \frac{I_{e2}}{I_{e1}} \right] \quad (1.13)$$

where the left hand side of equation 1.13 can be plotted for various values of  $I_{i,1}(V_m)$  and  $I_m(V_m)$  along the steep segment of the CVC shown in Figure 1.4. The left hand side of equation 1.13 results in a linear curve, which can be fitted using standard techniques.

Fitting the curve, results in the values for,  $-\frac{e}{kT_e}$  and  $\ln \left[ \frac{I_{e2}}{I_{e1}} \right]$ , which are the slope and the y intercept of the fit line (Raizer, 1991).

Menart also developed an equation based on the work of Schott to calculate the electron temperature starting from equations 1.8 and 1.9 (Menart, 2004). Menart's alteration to Schott's development was to relax the assumption that the CVC is symmetric or that the zero current point is located at the origin of the CVC. Menart's equation for determining the electron temperature is given by

$$T_e = \frac{e}{k} \left( \frac{I_{i,1} I_{i,2}}{(I_{i,2} + I_{i,1}) \frac{dI_m}{dV_m} + (I_{i,2} \frac{dI_{i,1}}{dV_m} - I_{i,1} \frac{dI_{i,2}}{dV_m})} \right). \quad (1.14)$$

This approach has been shown to be useful for analyzing double probes in a plasma with density gradients or differences in ion convection current (due to different flow velocities



of the background gas) to the two probes (Menart, 2002). It can be shown that equation 1.14 is the same as equation 1.10 if symmetry of the CVC about the origin is assumed.

To simplify the resulting equation, the additional approximation is made that

$$\frac{dI_{i,1}}{dV_m} \ll \frac{dI_m}{dV_m} \text{ and } \frac{dI_{i,2}}{dV_m} \ll \frac{dI_m}{dV_m} \quad (1.15)$$

which results in Schott's form of equation 1.14 given by

$$T_e = \frac{e}{k} \left( \frac{I_{i,1} I_{i,2}}{(I_{i,2} + I_{i,1}) \frac{dI_m}{dV_m}} \right) \quad (1.16)$$

In the next section, we review the classic sheath equations for the collisionless and continuum collisional regimes used for determining the sheath radius and hence ion density for either a single or double probe method.

### **Langmuir Probe Sheath Theory**

In this section we examine methods developed by Mott-Smith and Langmuir, Kiel, and Thorton for determining plasma densities in collisionless, continuum collisional, and transitional regimes, respectively. The first method considered is applicable for determining the plasma density for either a single or double probe in an electropositive plasma in the conventional thin sheath regime. The expression for the ion saturation current is modified slightly from a pure thermal flux to the probe due to the acceleration of the ions in the quasi-neutral transition region that smoothly connects the bulk plasma with the sheath. This transition region is commonly referred to as the pre-sheath region and was identified by Lam, 1967. The ion velocity increases due to the potential drop over the pre-sheath region until the ions reach a high enough energy that the electrons are repelled and quasi-neutrality no longer exists (Riemann, 2000). The ion

velocity at which this occurs under certain conditions is referred to as the ion sound speed or Bohm velocity and is given by the expression

$$u_B = \sqrt{\frac{kT_e}{M_i}} \quad (1.17)$$

where  $M_i$  is the mass of the ion (Bohm, 1949) and (Franklin, 2002). However, recently it has been shown by Riemann that the Bohm velocity only precisely determines the sheath edge in the asymptotic limit when  $\lambda_D / L \rightarrow 0$  where  $L$  is the scale length of the pre-sheath transition region (Riemann, 1997). For a collisionless plasma, the potential drop in the pre-sheath region can be determined by using conservation of the ion energy given by the equation

$$\frac{1}{2} M u_B^2 = eV_s \quad (1.18)$$

where  $V_s$  is the potential difference between the plasma potential and the boundary of the pre-sheath and sheath region. Substituting equation 1.17 into equation 1.18, solving for  $V_s$  and remembering that  $n_i = n_e = n_{e0} \exp\left(-\frac{eV_s}{kT_e}\right)$ . The ion current to the probe can then be expressed as

$$I_i = \exp(-0.5) S n_i \sqrt{\frac{kT_e}{M_i}} \quad (1.19)$$

where  $S$  is the surface area of the collection region. Using the result for the electron temperature obtained from equations 1.10 or 1.14 and the sheath radius (which in the thin sheath regime,  $\lambda_D / r_p \rightarrow 0$ , is the probe radius), the ion density can be determined (Lieberman and Lichtenberg, 1994). However, for probes in the thick sheath regime, the sheath radius is much larger than the probe radius and must be determined in order to

measure the ion density in a plasma. In a collisionless plasma, where the sheath radius is of non-negligible extent, the Bohm velocity is used as a criterion to define the “sheath edge” and hence the collecting surface area of the probe for most probe theory. In this regime, either ABR theory or OML theory (depending on the size of the probe and  $\lambda_D$ ) needs to be used to analyze the probe CVC.

Now we consider the collisional regime where the ion mean free path is much less than the Debye length,  $\lambda_i \ll \lambda_D$ , which introduces an additional parameter into theories for determining the positive ion current collected by a probe. A method developed by Kiel, based on the work done by Su, Lam, and Kiel, can be used to evaluate the plasma density in the continuum collisional regime (Kiel, 1966). The continuum collisional thick and thin sheath regimes are defined by  $r_s \gg \lambda_D \gg \lambda_i$  and  $\lambda_D \gg r_s \gg \lambda_i$  respectively, where the sheath radius,  $r_s$ , is thick or thin depending on the sheath radius value relative to the Debye length. Kiel uses expressions for the electron density, which were derived from the one-dimensional Poisson and continuity equations for electrons and ions. This system of equations was solved using the approximation that the plasma is quasi-neutral close to the edge of the sheath. The equation relating the plasma density and ion saturation current is given by

$$I_{i,1sat} = \frac{I_R}{\zeta_{1p}} (1 + \gamma_i) \quad (1.20)$$

where

$$I_R = 4\pi e D_i n_0 r_p \quad (1.21)$$

$$\gamma_i = \frac{T_e}{T_i}$$

$$\zeta_{1p} = \left( \frac{r_p}{L/2} \right) \ln(\pi L / 4r_p) \quad (1.22)$$

is a coefficient for cylindrical probe geometries and  $D_i$  is the ion diffusion coefficient.

The expression

$$\zeta_{1p} = 1 \quad (1.23)$$

is used for spherical probe geometries (Kiel, 1966). These equations are applicable in the cases where the region of quasi-neutrality extends very close to the collecting surface, such that the sheath radius can be approximated as the probe radius. The solution of Poisson's equation and the continuity equations assume that  $n_i = n_e = n_0$  at the boundary between the sheath and the quasi-neutral regions. Electron temperatures in this plasma regime can still be obtained via methods previously discussed and the ion temperature is assumed to be the same as the neutral gas temperature or is measured by some other means (Kiel, 1969).

Kiel also developed an equation that estimates the thickness of the sheaths based on Poisson's equation and the continuity equations. In developing the equations for thick sheaths, he assumes that the expression for the flux is given by the drift-diffusion form of the momentum equation given by

$$\Gamma_j = -D_j n_0 (\bar{\nabla} N_j - N_j \bar{\nabla} \phi_j) \quad (1.24)$$

and that

$$\bar{\nabla} n_j \ll n_j \bar{\nabla} \phi_j \quad (1.25)$$

where

$$\phi_j = \frac{-qV}{kT_j} - \text{Normalized potential} \quad (1.26)$$

$$N_j = \frac{n_j}{n_0} \text{ - Number density of species } j$$

$V$  - Potential difference

Equation 1.25 assumes the flux of all species is dominated by the electric field and very little flux results from number density gradients in the sheath. Kiel uses the boundary conditions

$$\begin{aligned}\phi_j(r_s) &= \phi_s = 0 \\ \nabla \phi_j(r_s) &= 0\end{aligned}\tag{1.27}$$

and also uses the relationship developed by Blank between the Debye length and sheath radius where

$$n_0 = (\lambda_D / r_s)^{2/3}\tag{1.28}$$

at the sheath-presheath boundary. Equation 1.28, however, is only valid for the case when  $\lambda_D / \lambda_i \gg 1$  (Blank, 1968) and according to Franklin, 2003,  $\lambda_D$  in equation 1.28 is the local Debye length which is applicable in this case since  $n_i = n_e = n_0$ . From these equations, Kiel develops an expression for the thick sheath radius of a cylindrical probe which is given by

$$\frac{r_s}{r_p} = 1 + 3650 \left( \left[ \frac{1}{n_0 (T_i + T_e)} \right]^{1/2} \frac{|V_p|}{r_p} \right)^{0.62}\tag{1.29}$$

where  $V_p$  is the probe potential. The value of the thick sheath radius,  $r_s$ , may be substituted for  $r_p$  in equation 1.22 allowing us to obtain a thick sheath estimate of the plasma density using a double or single Langmuir probe diagnostic technique (Kiel, 1969). According to equation 1.29 and Kiel's explanation, the sheath radius expands as

a result of the probe becoming more negatively biased resulting in more ions being required to shield the probe. However, the ions are slowed by ion-neutral collisions, therefore, the sheath increases in size, so that more ions are available to shield the probe. This results in the ion saturation current having a greater slope due to the collecting surface increasing with the increased negative bias of the probe. This relationship between current and voltage is shown in Figure 1.5, which features a double probe CVC produced from Kiel's continuum collisional probe theory given by Equation 1.29.

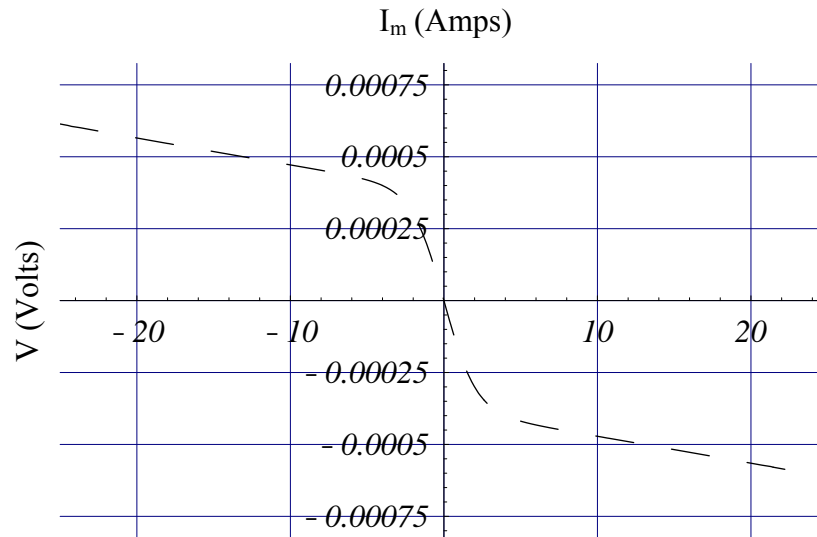


**Figure 1.5 CVC for the Collisional Continuum Regime with  $T_e = 1$  eV,  $n_e = 10^{12}$  cm<sup>-3</sup>,  $r_p = 0.025$  cm,  $\lambda_i = 0.019$  cm**

One main difference between the CVCs of the collisional and collisionless regimes, shown in Figures 1.4 and 1.5, is that the probe in the collisionless regime collects a larger ionic current due to the higher mobility of the ions at low pressures. This relationship suggests that the theories used to analyze ion current collected in the collisional and collisionless regime could be averaged to develop an analysis method for the transitional regime. Such an approach was developed by Thorton for the transitional

regime to provide an estimate of the CVC for conditions between the continuum collisional and the collisionless regime using a harmonic mean of the probe currents from the two limiting regimes (Thorton, 1971). This model was derived by matching Kiel's collisional and the collisionless, Langmuir probe models and links the currents associated with these limiting regimes using a harmonic mean given by the following expression

$$I_m = \frac{I_{nc} I_c}{I_c + I_{nc}} \quad (1.35)$$

$I_{nc}$  - Collisionless probe current

$I_c$  - Collisional probe current

Thorton's harmonic mean provides a guess at the current to the probe in the transitional regime, however, it has been shown by Franklin and Riemann that there exists no a priori sheath edge criterion when  $\lambda_D / \lambda_i \approx 1$ . Riemann, 1997, has shown that the transitional pre-sheath region scales in length on the "intermediate scale" which accounts for both collisions and space charge and is given by the expression

$l_m = \lambda_D^{4/5} \lambda_i^{1/5}$  in the low collisional case where  $\lambda_D / \lambda_i < 1$ . Riemann has also stated that, "there is no unambiguous definition of a sheath edge,  $r_s$ , for finite values of  $\lambda_D / \lambda_i$ ".

Riemann has however, shown that in the presence of low collisions,  $\lambda_D / \lambda_i \ll 1$ , the Bohm velocity is achieved by the ions close to the edge of the sheath. Franklin has also stated that the problem lies in having a coincidence of two "transitions" and there is no simple analytic expression for the plasma balance equation for this condition (Franklin, 2003). As a result of this theoretical problem, no definitive theories have been developed to estimate the probe sheath radius in a transitional collisional regime. However,  $r_s$ , is

not arbitrary and must be chosen within the range of the intermediate scale between 0 and  $(\lambda_D/\lambda_i)^{4/5}$  (Riemann, 1997).

All of the methods presented for measuring the plasma number density and electron temperature were derived based on the plasma being electropositive. However, the plasmas of interest to this study are generated in oxygen or an oxygen mix and are electronegative in nature. Since, negative ions have low mobility and the probe potential is negatively biased, a negligible number of negative ions reach the probe surface. The positive ion current to the probe, however is altered because the sheath radius and Bohm velocity are altered by the presence of negative ions. Franklin, 2003, and Chung, 2006, have determined trends between the electronegativity, ionization rate, collected current and the sheath length. Amemiya and others, 1999, have shown numerically that the collected ion current can increase in certain plasma conditions if negative ions are present in a plasma in either OML and ABR radial motion theory. Touryan and Chung, 1975, showed that the sheath density profile became increasingly steep and the sheath radius became narrower due to the presence of negative ions. In addition, Chung has developed a numerical model of the electronegative fluid equations and has shown that in an electronegative plasma with weak ionization that the sheath width decreases with increasing negative ion to electron ratios,  $\alpha_0$ , (also referred to as electronegativity) and ionization rate given by  $k_i n_{gas} n_e$  where  $k_i$  is the ionization coefficient and  $n_{gas}$  is the number density of the gas (Chung, 2006).

Allen and Braithwaite, 1988, developed an expression for the Bohm velocity in a three component plasma given by



$$u_s = \left[ \frac{eT_e}{M_i} \frac{(1 + \alpha_0 \exp(-(\gamma_n - 1)\phi_s))}{(1 + \alpha_0 \gamma_n \exp(-(\gamma_n - 1)\phi_s))} \right]^{1/2} \quad (1.36)$$

where

$$\gamma_n = T_e / T_n. \quad (1.37)$$

By balancing the kinetic and potential energy of the positive ions at the sheath edge using equation 1.18, we obtain the expression for the sheath edge potential given by

$$\phi_s = \frac{eT_e}{2M_i} \frac{(1 + \alpha_0 \exp(-(\gamma_n - 1)\phi_s))}{(1 + \alpha_0 \gamma_n \exp(-(\gamma_n - 1)\phi_s))} \quad (1.38)$$

The sheath edge potential from equation 1.38 can be solved using standard root finding techniques and is the same for planar, cylindrical, or spherical probes. Recently, it has been shown that  $\alpha_0$  and  $\gamma_n$  can be measured using a Langmuir probe by analytically fitting the measured CVC (Crespo and others, 2004). In addition, Crespo and others have developed a complex fitting scheme of the current collected at a particular probe bias and radius which is used to determine the sheath thickness and floating potential of a probe.

The fit to the positive ion current collected by a Langmuir probe is given by

$$\Gamma(x_p, \phi_p) = \sum_{i=0}^2 (a_i + b_i \phi_p^{1/2}) x_p^i \quad (1.39)$$

where  $a_i$  and  $b_i$  are constants that depend on  $\alpha_0$  and  $\gamma_n$  and  $x_p = r_p / \lambda_D$  (Crespo and others, 2004). The sheath radius is given by five fitting parameters and has the form

$$x_s = x_p + k_1(\phi_p) x_p^{0.2k} + k_2(\phi_p) x_p^{0.7} \quad (1.40)$$

where

$$k_1(y_p) = k_{10} + k_{11} \phi_p^{1/2} \quad (1.41)$$

$$k_2(y_p) = k_{20} + k_{21} \phi_p^{1/4} + k_{22} \phi_p^{1/2} \quad (1.42)$$

where  $k_{10}$ ,  $k_{11}$ ,  $k_{20}$ ,  $k_{21}$  and  $k_{22}$  depend on  $\alpha_0$  and  $\gamma_n$  and are provided in look up tables or can be calculated using a fitting method with  $k = 1$ , or 2 for planar or spherical probes respectively. Similar, to the sheath radius approximation of equation 1.29 developed by Kiel, Crespo's sheath radius is primarily dependent on the probe bias and probe radius. Crespo's analytic method allows the analysis of a collisionless, electronegative plasma completely by a Langmuir probe (Crespo and others, 2004).

Recently there have been several advances in the theory and numerical solutions of the electronegative pre-sheath and sheath equations in a collisional electronegative plasma. Numerical solutions of the full sheath model have been used before by Amemiya, Kono, Franklin, Chung, and others to analyze the CVCs of probes and study the behavior of the sheath and pre-sheath in an electronegative plasma. The next section highlights the pertinent features of a one dimensional cylindrical sheath model that was developed based on the theory produced by Allen and Braithewait, Palop, and Franklin using the approach taken by Kono. This limited model is used to validate the hybrid PIC-MCC model that is developed in Chapter V to analyze a cylindrical probe in a transitional, flowing, electronegative plasma.

### **One Dimensional Cylindrical Sheath Model**

In the one dimensional sheath model, only the first two moments of the Boltzmann equation are used with the assertion that the thermal energy of the electrons and ions is constant outside the sheath region. The electrons and negative ions are assumed to be in Boltzmann equilibrium according to standard sheath theory (Franklin, 2000). For the purposes of differentiating the quasi-neutral region from the non-quasi-neutral sheath region, we maintain the sheath and pre-sheath description despite the terms

being shown to be ambiguous in a collisional plasma by Riemann, 1997. The steady-state continuity equation is integrated over a cylindrical surface assuming that the source term in the continuity equation is insignificant. The integration of the current continuity equations results in the normalized form given by

$$n_i u x = i_0 \quad (1.43)$$

where  $u$  is the normalized mean ion velocity and  $i_0$  is the normalized ion current. The normalized time independent form of the ion momentum and Poisson's equation are given by

$$u \frac{du}{dx} = \frac{d\phi}{dx} + \frac{1}{\gamma_i n} \frac{dn_i}{dx} + \delta u \quad (1.44)$$

$$\frac{1}{x} \frac{d}{dx} \left( x \frac{d\phi}{dx} \right) = n_i - n_e - n_n \quad (1.45)$$

where the standard normalizations used by Riemann and Kono are applied to simplify the system of equations and reduce the parameter space

$$\begin{aligned} x &= \frac{r}{\lambda_D} & \phi &= -\frac{\Phi - \Phi_p}{T_e} & i_0 &= \frac{I_0}{2\pi\lambda_D n_{e0} l_0 u_s} \\ \alpha_0 &= \frac{n_{n0}}{n_{e0}} & \delta &= \frac{v_e \lambda_D}{u_s} & \gamma_n &= \frac{T_e}{T_n} \\ \gamma_i &= \frac{T_e}{T_i} & u &= \frac{v}{u_s} & \lambda_D &= \sqrt{\frac{kT_e}{4\pi e^2 n_{e0}}} \\ u_s &= \sqrt{\frac{T_e}{M_i}} \end{aligned}$$

$u$  - Positive ion velocity normalized by the electropositive Bohm velocity

$x$  - Radial distance normalized to the electron Debye length

$\Phi_p$  - Plasma potential

$\phi$  - Potential normalized to the electron temperature

$i_0$  - Normalized ion current

$I_0$  - Positive ion current to the probe

$\alpha_0$  - Negative ion to electron ratio

$\delta$  - Collision frequency normalized by the Debye length to the Bohm velocity

$\gamma_n$  - Ratio of electron and negative ion temperatures

$\gamma_i$  - Ratio of electron and positive ion temperatures

$v_{ith}$  - Ion thermal velocity

$\nu_c$  - Collision frequency

$\sigma$  - Elastic collision cross-section

The electrons and negative ions in Boltzmann equilibrium are given in their normalized form by the expression

$$n_e = n_{e0} \exp(-\phi) \quad (1.46)$$

$$n_n = n_{n0} \exp(-\gamma_n \phi) \quad (1.47)$$

To solve this set of fluid equations, we adopt an approach based on the method used by Kono, 2000. Using equations 1.43 and 1.45 and the normalized electron and negative ion densities presented previously, Poisson's equation can be recast as

$$\frac{1}{x} \frac{d}{dx} \left( x \frac{d\phi}{dx} \right) = \frac{i_0}{xu} - \exp(-\phi) - \alpha_0 \exp(-\gamma_n \phi) \quad (1.48)$$

In the pre-sheath region, quasi-neutrality is assumed and equation 1.48 becomes

$$\frac{1}{x} \frac{d}{dx} \left( x \frac{d\phi}{dx} \right) = 0 = \frac{i_0}{xu} - \exp(-\phi) - \alpha_0 \exp(-\gamma_n \phi) \quad (1.49)$$

Equations 1.43, 1.44, and 1.49 can be reduced to a relationship between the ion velocity and potential in the quasi-neutral pre-sheath given by

$$\left( u + \frac{\delta i_0}{uA(\phi)} \right) \frac{\partial u}{\partial \phi} = 1 + \frac{B(\phi)}{\gamma_i A(\phi)} + \frac{\delta i_0 B(\phi)}{A(\phi)^2} \quad (1.50)$$

where

$$A(\phi) = \exp(-\phi) + \alpha_0 \exp(-\gamma_n \phi) \quad (1.51)$$

$$B(\phi) = \exp(-\phi) + \alpha_0 \gamma_n \exp(-\gamma_n \phi) \quad (1.52)$$

Equation 1.50 describes the relationship between positive ion velocity and potential in the pre-sheath region and the solution of this equation can be used to obtain the density of the electrons, positive and negative ions from equations 1.46, 1.47 and 1.43. Equations 1.50, 1.43, 1.44, and 1.45 then form the solution of the entire sheath and pre-sheath region.

### **Solutions of the One Dimensional Sheath Model**

In the collisionless case,  $\delta = 0$ , equation 1.50 becomes

$$u \frac{\partial u}{\partial \phi} = 1 + \frac{B(\phi)}{\gamma_i A(\phi)} \quad (1.53)$$

using the initial condition,  $u(0) = 0$ , the solution to equation 1.53 is easily found to be

$$u(\phi) = \sqrt{\phi - \frac{1}{\gamma_i} \ln \left( \frac{\exp(-\phi) + \alpha_0 \exp(-\gamma_n \phi)}{1 + \alpha_0} \right)} \quad (1.54)$$

which is simply conservation of energy with finite temperature ions. Next, we examine the upper limit of velocity for  $u(\phi)$  in the pre-sheath region which is also known as the Bohm criterion. The Bohm criterion indicates the point where the quasi-neutrality of the pre-sheath breaks down and the initial stages of sheath formation begins in a collisionless

plasma (Allen and Braithwaite, 1988). The Bohm criterion in the plasma fluid equation treatment also corresponds to the electric field becoming infinite at the transition from the pre-sheath to the sheath region (Allen and others, 1957) and (Allen and Braithwaite, 1984). An additional criterion proposed by Braithwaite and Allen is also used which ensures that the sheath must correctly match the plasma such that

$$\frac{\partial \rho}{\partial \phi} = 0 \quad (1.55)$$

where  $\rho$  is the net charge density. Using equations 1.43 and 1.51 combined with Allen and Braithwaite's condition results in the equation

$$\left. \frac{\partial n_i}{\partial \phi} \right|_{\phi=\phi_S} + B(\phi) = 0 \quad (1.56)$$

which is always true in the pre-sheath region. Palop and others, 2002, have also shown that the transition from the pre-sheath to the sheath occurs at the maximum positive ion current density. This maximum in the positive ion current density occurs at the sheath edge potential and can be determined using the expression

$$\left. \frac{\partial J_i}{\partial \phi} \right|_{\phi=\phi_S} = \left. \frac{\partial J_i / \partial x}{\partial \phi / \partial x} \right|_{x=x_S} = 0 \quad (1.57)$$

where  $J_i$  is the positive ion current density (Palop, 2002). Equation 1.57 can be recast using the relationship

$$\left. \frac{\partial n_i}{\partial \phi} \right|_{\phi=\phi_S} = - \frac{n_i}{u} \left. \frac{\partial u}{\partial \phi} \right|_{\phi=\phi_S} \quad (1.58)$$

into

$$\left. \frac{\partial u}{\partial \phi} \right|_{\phi=\phi_S} = \frac{uB(\phi)}{A(\phi)} \quad (1.59)$$

using the quasi-neutral relationship of the pre-sheath. Substituting equation 1.50 into 1.59 and solving for the ion current density, we recover the electronegative Bohm velocity with finite temperature ions developed by Kouznetsov and others, 1999, and given by the expression

$$u_B(\phi) = \sqrt{\frac{1 + \alpha_0 \exp(-(\gamma_n - 1)\phi)}{1 + \gamma_n \alpha_0 \exp(-(\gamma_n - 1)\phi)}} + \frac{1}{\gamma_i} \quad (1.60)$$

Equation 1.60 is the same as equation 1.36 except with the addition of a  $1/\gamma_i$  term which results from the inclusion of the ion diffusion in equation 1.44 and is normalized by the electropositive Bohm velocity.

For  $\delta > 0$ , equation 1.50 can be solved numerically if the current to the probe and the initial velocity of the ions are specified. A solution for equation 1.50 does not exist for the initial condition  $u(0) = 0$  due to the ion current continuity equation, 1.43. To circumvent this problem in a low pressure ( $P \leq 0.01$  Torr) background gas, equation 1.54 provides a good initial condition for  $u(\phi)$  at a near zero initial  $\phi$  due to the collisional drag being smaller at lower velocities (Kono, 2000). To find the upper velocity limit for the pre-sheath region for the collisional case, we substitute equation 1.50 into 1.59 and solve for  $u$  obtaining equation 1.60 again, which suggests that the Bohm criterion represents the maximum current of the pre-sheath equation as a function of  $\phi$  that can be obtained in a collisional or collisionless regime. This result is consistent with Franklin's proof and model that there is no collisionally modified Bohm criterion (Franklin, 2003). What is modified by collisions is the potential at the edge of the pre-sheath region which changes the Bohm velocity achieved by the ions at the edge of the

quasi-neutral region. The sheath edge potential is usually obtained using a conservation of energy argument

The solution to the quasi-neutral pre-sheath equation, equation 1.50, does exist beyond the electronegative Bohm velocity. However, past the point where quasi-neutrality no longer exists (where  $u(\phi) > u_B(\phi)$ ) the solution to equation 1.50 does not provide a physically reasonable result (Kono, 2000). In the sheath region, the equations 1.43, 1.44, and 1.45, can be solved using a Runge-Kutta or other standard numerical techniques with the results of the solution to the pre-sheath equation being used as the initial conditions.

In the sheath, positive ions are accelerated to energies much higher than their thermal energy due to the large electric field present in the sheath. At low pressures, the ions at any point in the sheath have essentially the same velocity with little variation from the mean velocity. As a result the velocity distribution function of the ions can be approximated using a delta function and the collision frequency is then given by the expression

$$N_g \langle \sigma v \rangle \approx N_g \int_{-\infty}^{\infty} \sigma(v) v \delta(v - u) dv = N_g \sigma(u) u \quad (1.61)$$

which is consistent with Riemann's, 1997, constant mean free path case. Equation 1.44 combined with ion momentum equation and the equation 1.61 results in the expression

$$\left(u - \frac{1}{\gamma_i u}\right) \frac{du}{dx} = \frac{d\phi}{dx} + \frac{1}{\gamma_i x} + \frac{\lambda_D u^2}{\lambda_i} \quad (1.62)$$

There are two singularities in the full solution of the sheath equations that occur at the ion sound velocity (which is  $u_B(\phi)$ ) and at the ion thermal velocity given by  $u(\phi) = \sqrt{1/\gamma_i}$ .



To provide the initial conditions for the sheath model using the pre-sheath model, problems associated with the singularities of the sheath model and the absence of pre-sheath values at velocities greater than the Bohm velocity must be overcome. Riemann, 1997, and Palop and others, 2004, have developed methods to join the solution of the pre-sheath model to the sheath model across these singularities in a collisional regime. Riemann has shown that various other attempts to match the sheath and pre-sheath solutions across the singularities associated with the time independent fluid equation in a collisional regime were inconsistent without the use of the pre-sheath intermediate length scale,  $\lambda_D^{4/5} \lambda_i^{1/5}$ . Care must also be taken in any sheath/pre-sheath matching attempt using this approach to ensure that the spatial derivatives of the potential and the positive ion velocities match between the pre-sheath and sheath region according to equation 1.55 (Allen and Braithewaite, 1987). Also it has been shown by Allen and Braithewaite, 1987, that depending on the plasma parameters, two transitions from a quasi-neutral to a sheath region can occur (electronegative pre-sheath transition to a quasi-neutral electropositive halo and electropositive halo transition to the sheath solution). The potential for multiple transitions from quasi-neutrality to the sheath were predicted by Allen and Braithewaite and their presence makes the matching of the pre-sheath and sheath regions in an electronegative plasma very difficult. To ensure the validity of the PIC-MCC model in investigating the sheath of a Langmuir probe, the 1-D sheath/pre-sheath model presented previously is used to determine the accuracy of the PIC-MCC approach. However, due to the difficulties associated with sheath/pre-sheath matching in an electronegative plasma, a sheath/pre-sheath matching scheme was not used. As a result, the initial conditions for

the sheath model were obtained from the PIC-MCC model for the purposes of comparing the results of the two models.

### **Langmuir Probe Diagnostic Methods for a Flowing Plasma**

In this section, we review some common methods of determining the current density collected by a Langmuir probe in a flowing, electropositive plasma. Clements and Smy developed a simple method of determining the ion density of a flowing, collisional plasma using the asymptotic thick sheath probe analysis approach developed by Schulz and Brown, 1955. This approach is valid when the unitless electric Reynolds number

$$R = \frac{u_f L}{T_e \mu_i} > 1 \quad (1.63)$$

where  $L$  is the characteristic length of the probe,  $u_f$  is the flow velocity of the plasma, and  $\mu_i$  is the ion mobility. This condition is that the convection velocity of the ions to the probe sheath is greater than the diffusion velocity. The characteristic length of the probe is the length of the probe parallel to the direction of flow. The next condition that must be met is that

$$RX^2 \phi_p^2 \geq 1 \quad (1.64)$$

where

$$X = \frac{\lambda_D}{L} \quad (1.65)$$

$$\phi_p = \frac{eV_p}{kT_e} \gg 1 \quad (1.66)$$

Satisfying these conditions results in a thick sheath in the collisional continuum plasma compared to the probe radius. It is then assumed that all the convected ion current to the

edge of the sheath region is transported to the probe surface due to the sheath fields producing a much higher ion velocity than the flow velocity. Another condition that must be satisfied for this approach is that the viscous boundary layer around the probe is smaller than the probe sheath. According to Lam, the viscous boundary layer is approximately

$$r_b \approx \frac{L}{R_e^{1/2}} \quad (1.67)$$

$$R_e = \frac{u_f L}{\nu} \quad (1.68)$$

where  $R_e$  is the hydrodynamic Reynold's number and  $\nu$  is the kinematic viscosity. If the viscous boundary layer is much smaller (which is the case for most sub millimeter Langmuir probes) than the sheath radius then this simple probe analysis approach is valid.

Using the asymptotic thick sheath relation between probe bias and ion current produced by Shulz and Brown, 1955, for electrostatic probes in a collisional continuum plasma

$$V_p = \frac{I_i^{1/2} r_s}{(2\pi\mu_i\epsilon_0)^{1/2}} \log\left(\frac{r_s}{r_p}\right) \quad (1.69)$$

where  $l$  is the length of the cylindrical probe. The expression for the ion convection current to the sheath is then given by

$$I_i = A_s e n_i u_f \quad (1.70)$$

Using equation 1.70, the sheath radius can then be obtained and substituted into equation 1.69. For the case of a cylindrical Langmuir probe transverse to the flow (which is the

orientation of the probe used by Clements and Smy, 1969, in the development of the theory), the relationship between the ion current and the probe bias is given by

$$V_p = \frac{I_i^{3/2}}{(2\pi l^3 \mu_i \epsilon_0)^{1/2} (2n_i e u_f)} \log \left( \frac{I_i}{2n_i l e u_f r_p} \right). \quad (1.71)$$

In accordance with Kiel's thick sheath method for a collisional continuum plasma, the sheath radius increases with increasing probe bias (Kiel, 1963). The assumption made by Clements and Smy, 1969, that the ion drift velocity into the probe sheath is negligible, however, is not valid for the lower pressures of interest to this study of Langmuir probes and the effect of drift velocity on the ion current collected by the probe need to be included in the diagnostic method of Clements and Smy.

The thick sheath theory developed by Clements and Smy gives us an excellent starting point to launch our investigation into analyzing a probe CVCs in an electronegative plasma in the transitional collisional regime. In Chapter V, the theory presented in this section for flowing and non-flowing plasmas is compared to the results of the computational models developed for this investigation. Based on the comparison, the utility of the theory of Clements and Smy for analyzing probe CVCs in a flowing, electronegative plasma is assessed. In the next chapter, we present the development of the fluid model used to study both the Langmuir probe and the RF discharge, the limitations of the fluid approach, and acceleration methods used to speed the convergence of the plasma fluid model.

## II. Development of the Plasma Fluid Model

In this chapter, the theoretical development of the plasma fluid model used to study the RF discharge operation and the Langmuir probe sheath is presented. The theoretical development is based on the approach employed by Boeuf, 1987, Fiala and others, 1994, and Boeuf and Pitchford, 1995, to solve the time-dependent two component, three moment fluid equations. In addition, the limitations of the fluid approach and acceleration methods used to speed the model to a periodic state are presented. The following fluid model is also used in combination with a chemical kinetic model, presented in Chapter III, to investigate the effect that a flowing plasma has on the RF discharge structure and production rate of charged and excited neutral species.

A plasma fluid model generally consists of the self-consistent solution of the fluid equations for electrons, positive ions, and negative ions combined with field equations. The fluid equations represent simplified forms of the first three moments of the Boltzmann transport equation, which include the continuity, momentum, and energy balance equations for the electrons, and positive and negative ions. These equations are coupled to Poisson's equation in order to determine the electric fields which affect the transport of the charged species. The magnetic fields induced in the chamber by the time varying electric fields, have a negligible effect on electron and ion motion, therefore the full electromagnetic equations are not included in the model presented in this chapter.

Rates of various reactive kinetic processes involving electrons, such as ionization and attachment, form the source terms for the fluid equations. The rates of these reactions are generally determined by assuming a form for the electron energy

distribution function (EEDF), obtaining the cross section of the reactive process and integrating over energy. The EEDF in a fluid model approach is frequently assumed to be Maxwellian. This assumption, however, is not always valid, therefore, a kinetic method that determines the species velocity distribution function is required to model the discharge accurately. To start the plasma fluid model, charged species are given an initial spatial density and flux profiles in the simulation, and then the continuity, momentum, energy balance, and Poisson equations are solved self-consistently in time using appropriate spatial boundary conditions until a periodic solution is reached. In solving these equations, one obtains the temporal and spatial dependence of the charged species concentrations, the charged species fluxes, the electric field, scalar potential, the mean electron energy, and various chemical kinetic reaction rates (Graves, 1994).

To use the drift-diffusion form of the fluid equations, which neglect species inertia, the collision frequency within the plasma must be high enough that the plasma is approximately in a continuum collisional regime. Being in a continuum collisional regime implies that the mean free path for all charged species is shorter than the smallest characteristic dimension of the discharge such that  $\lambda_D \gg \lambda_e$  and  $\lambda_D \gg \lambda_i$ . Paranjpe states that this assumption can be made when pressures exceed 300 mTorr for most gases (Paranjpe, 1991). Another common approximation made in plasma fluid models is called the local field approximation. This approximation assumes that the electrons are in equilibrium with the local electric field, which implies that one can use the electron energy distribution function (EEDF), drift velocities, and species production rates measured in drift tube experiments. Instead of solving the electron energy balance equation many researchers use this approximation instead. However, the local field

approximation is not always applicable and fails in two notable cases. The first case being in very low pressures, where the EEDF may be modulated very strongly by the time varying electric field and as a result the electrons may not be in equilibrium with the field and hence do not have a stationary distribution. The local field approximation also fails in the sheath region, which has large electric fields, but a small Townsend ionization coefficient, due to electrons diffusing against the sheath field. In these instances the local field approximation should not be made, and the electron energy balance equation should be replaced with a solution to the space and time dependent Boltzmann equation (Paranjpe, 1991).

### **Plasma Fluid Model Overview**

The plasma fluid model is designed to determine the number densities, electron energy, potential, fluxes, and yields of excited atomic or molecular species in a one or two dimensional moderate pressure plasma. The capabilities of the plasma fluid model are provided in the list below.

1. 1-D or 2-D Cylindrical or Cartesian Geometry
2. Three fluid, three moment fluid model coupled with Poisson's equation
3. Grid generator using a ray tracing method with variable geometry
  - a. Homogenous or variable grid spacings
  - b. Electrodes or dielectric surfaces may be in the interior or exterior of the computational domain
4. Multiple background gas types modeled
  - a.  $Ar$ ,  $He$ ,  $N_2(X)$ ,  $O_2(X)$  and  $N_2(X) - O_2(X)$  mixture currently modeled

- b. Electropositive or electronegative gases
  - c. Complex background gas chemical kinetics using equilibrium field approximation
  - d. Chemical kinetic reaction analyzer
- 5. Multiple boundary conditions
  - a. Conductor, static and time dependent
  - b. Infinite dielectric
  - c. Dielectric coated electrodes
  - d. Continuous boundary conditions for flow modeling
  - e. Cylindrical axis
  - f. Secondary emission
  - g. Selective quenching of excited atomic and molecular states with the wall
- 6. Simplistic background gas flow model coupled with fluid equations
- 7. Time dependent transport of excited atoms and molecules via diffusion and convection
- 8. Acceleration of charged and neutral species transport
  - a. Ion sub-cycling
  - b. RF cycle averaging of neutral species density growth in time using an implicit time step
  - c. Charged species represented by a Boltzmann distribution

The charged species transport model developed for the plasma fluid model is based on theory developed by Boeuf, 1987, Boeuf and Pitchford, 1995, in the development of Kinema's RF-SIGLO 1-D and 2-D fluid models. The additional capabilities added to



Boeuf and Pitchford's modeling approach are centered on modeling an RF discharge and a Langmuir probe in a flowing background gas. In the next section, the theoretical approach developed by Boeuf and Pitchford for a three component fluid model and the solution methodology of the fluid equations is reviewed.

### Plasma Fluid Model Background Theory

To determine the characteristics of the plasma downstream of the RF discharge, a model based on the continuity, momentum, and energy fluid equations was employed. In this section, assumptions associated with the drift-diffusion form of the momentum and continuity fluid equations, the electron energy equation, and the local field approximation (used to determine the transport and production coefficients for the fluid equations) are reviewed in detail. The zeroth moment of the Boltzmann transport equation, the continuity equation, has the form

$$\frac{\partial n}{\partial t} + \vec{\nabla} \cdot (n\vec{v}) = S \quad (2.1)$$

where

$n$  – Species number density

$\vec{v}$  – Species average velocity

$S$  – Source term of species that are gained or lost.

The general form of the first moment of the Boltzmann transport equation, the momentum equation is

$$mn \left[ \frac{\partial \vec{v}}{\partial t} + (\vec{v} \cdot \vec{\nabla}) \vec{v} \right] = qn(\vec{E} + \vec{v} \times \vec{B}) - \vec{\nabla} \cdot \Pi + f|_c \quad (2.2)$$

where

$m$  - Mass of the species

$q$  - Charge of the species

$\Pi$  -- Pressure dyad

$\vec{E}$  -- Electric field

$\vec{B}$  -- Magnetic field

$f|_c$  -- Rate of momentum transferred due to collisions.

Since a collisional regime is modeled, the momentum equation may be simplified by making the following assumptions. The first assumptions are that the species do not constitute a viscous fluid and behave like an ideal gas. Hence the pressure dyad can be diagonalized

$$\Pi = \begin{pmatrix} P & 0 & 0 \\ 0 & P & 0 \\ 0 & 0 & P \end{pmatrix} \quad (2.3)$$

and using the ideal gas law to relate pressure to density,

$$P = nkT \quad (2.4)$$

the following expression is obtained for the divergence of the pressure dyad

$$\vec{\nabla} \cdot \Pi = \vec{\nabla}(nkT) \quad (2.5)$$

Next, the collisions with the background gas are approximated using the Krook collision operator given by

$$f|_c = M_{\alpha\beta} n v_c (\vec{v}_\alpha - \vec{u}_f) \quad (2.6)$$

where

$M_{\alpha\beta}$  - Reduced mass of the charged species and neutral species

$\nu_c$  - Collision frequency with neutral species

$\vec{v}_\alpha$  - Charged species average velocity

$\vec{u}_f$  - Neutral species average velocity.

For the pressure regime that is modeled, the neutral collision frequency is large enough that the charged species experiences several collisions every spatial grid step. At the low energies of an RF discharge, each collision results in a nearly isotropic scattering of the charged species, hence the momentum obtained by the particle from being accelerated by the electric field over a distance is dissipated. Therefore, the inertia and acceleration terms in the momentum equation for all charged species is neglected as shown in the expression

$$\frac{mn}{M_{\alpha\beta}\nu_c} \left[ \frac{\partial \vec{v}}{\partial t} + (\vec{v} \cdot \vec{\nabla}) \vec{v} \right] \approx 0 \quad (2.7)$$

The currents in the discharges that are modeled are insufficient to generate a substantial magnetic field, hence the magnetic field term is also neglected. Substituting the approximations of equations 2.5, 2.6, and 2.7 into equation 2.2 and rearranging the terms results in the following drift-diffusion-convection form of the species momentum given by the equation

$$\vec{\Gamma}_\alpha = n\vec{v}_\alpha = qn\mu_\alpha \vec{E} - \vec{\nabla}(D_\alpha n) + n\vec{u}_f \quad (2.8)$$

where

$$D_{\alpha} = \frac{qT_{\alpha}}{M_{\alpha\beta}v_c} \text{ - Diffusion coefficient}$$

$$\mu_{\alpha} = \frac{q}{M_{\alpha\beta}v_c} \text{ - Mobility coefficient}$$

where  $v_c$  is a function of  $E/N$  for the electrons. If we assume that the neutral species velocity distribution is isotropic then  $\vec{u}_f = 0$ . This assumption is used for the initial development of the plasma fluid model to reduce the complexity of the presentation.

To determine the thermal energy of the charged species, a common form of the energy equation is used (Lieberman and Lichtenberg, 1994):

$$\frac{\partial(n\varepsilon)}{\partial t} + \vec{\nabla} \cdot \left( \frac{5}{3} (n\varepsilon)\vec{v} + \vec{Q} \right) = \vec{J} \cdot \vec{E} - nNk_L(\varepsilon) \quad (2.9)$$

where

$\vec{Q}$  - Heat flow vector

$\vec{J} \cdot \vec{E}$  - Joule heating

$k_L(\varepsilon)$  - Energy loss coefficient due to collisions

$N$  - Neutral species number density

$\varepsilon$  - Electron mean energy

By dividing equation 2.9 by the fundamental charge,  $e$ , we obtain the electron energy equation where  $\varepsilon$  is in units of electron volts:

$$\frac{\partial(n\varepsilon)}{\partial t} + \vec{\nabla} \cdot \left( \frac{5}{3} (n\varepsilon)\vec{v} + \frac{\vec{Q}}{e} \right) = -\vec{\Gamma} \cdot \vec{E} - nNk_L(\varepsilon) \quad (2.10)$$

In the power and pressure ranges considered for this model, RF discharges only heat the background gas (either argon, oxygen, or nitrogen) by a few hundred degrees

Kelvin (Boeuf and Pitchford, 1995). The fast flow of the background gas through the modeled parallel plate RF discharge, results in the convection of both the thermal energy of the ions and neutrals out of the discharge region. The resulting fast convection losses or reduced residence time of the ions and neutral species results in negligible heating of both the positive and negative ions and the background gas. Therefore, only the heating and cooling of the electrons by Joule heating, electron energy loss by collisions, and the divergence of the electron energy density flux in the RF discharge is considered.

To close the continuity, momentum, and energy equations for the electrons, the thermal energy of the electrons is equated to the electron mean energy according to the local equilibrium assumption discussed previously. This assumption implies that the transport and production coefficients at a particular position or time in the discharge can be equated to the coefficients calculated under a uniform and constant electric field (Boeuf, 1987). In the high collisional regime, the force due to the electric field and the momentum loss due to collisions is much larger than the inertia terms for electrons (same approximation as used in equation 2.7). The electron energy and momentum relaxation frequency is the sum of the elastic and inelastic collision frequencies given by the expressions

$$\frac{\nu_e}{P} = \frac{2m_e}{M} \frac{\nu_{MT}}{P} + \sum_k \frac{\nu_k}{P} \quad (2.11)$$

$$\frac{\nu_m}{P} = \frac{\nu_{MT}}{P} + \sum_k \frac{\nu_k}{P} \quad (2.12)$$

where  $\nu_e$  is the energy relaxation frequency,  $\nu_{MT}$  is the elastic momentum transfer collision frequency,  $\nu_k$  is the collision frequency of a particular inelastic collision, and

$\nu_m$  is the momentum relaxation frequency. If this frequency is much greater than the RF discharge field frequency then it has been shown by Winkler and others that the isotropic portion of the Electron Velocity Distribution Function (EVDF) follows the time varying field with little temporal variation (Winkler and others, 1985). In the case of a molecular gas such as nitrogen or oxygen, where  $\nu_e, \nu_m \sim 10^9$  Hertz/Torr, the condition is more than satisfied for the RF field frequencies and pressures of interest in this investigation (Boeuf, 1987). The electron energy distribution is calculated by a solution of the time independent Boltzmann transport equation by balancing the electron heating due to a uniform electric field with the energy lost by the electrons due to collisions with the background gas. The time independent Boltzmann transport determines the EEDF based on the measured cross-sections of a specific type of gas from which the diffusion, mobility, and production rate coefficients are obtained in steady state. The uniform electric field required to generate an EEDF is commonly divided by the background gas number density and becomes the reduced field,  $E/N$ . By using the local equilibrium assumption, more accurate transport and rate coefficients for inelastic collision frequencies used in equation 2.13 are obtained than assuming the form of the EEDF and integrating the cross-section of the collision type over the entire energy range as has been done in other fluid models (Boeuf, 1987). The local equilibrium approximation, however, does not completely treat the electrons in the high energy tail of the electron energy distribution correctly because they are not necessarily in collisional equilibrium with the electric field. These high energy electrons can be energetic enough that the electron elastic and inelastic cross-sections are reduced and the electrons also have

enough energy to pass through the finite potential drop of the sheath. Not accounting for this reduction in the cross-sections or the penetration of the high energy electrons through a finite potential drop sheath and their resulting ionization mean free path can produce significant error in the calculation of the ionization rate especially in DC discharge simulations (Donkó and others, 2006). To properly simulate the high energy tail of the EEDF in a DC discharge, a kinetic or fluid-kinetic hybrid approach, such as a PIC-MCC method, must be adopted (Donkó and others, 2006). However, comparisons between fluid and kinetic PIC-MCC models simulating a RF discharge have shown that for pressures greater than 100 mTorr, the effect on the ionization rate due to the high energy electrons penetrating the sheath is minor and the two modeling approaches produce very similar results. (Nitschke and Graves, 1994)

The energy loss coefficient is given by the expression

$$k_L(\varepsilon) = \sum_i \frac{\delta\varepsilon_i \nu_i}{N} \quad (2.13)$$

where

$\delta\varepsilon_i$  - Energy lost due to the  $i^{\text{th}}$  inelastic collision process

$\nu_i$  - Collision frequency for the  $i^{\text{th}}$  inelastic collision process

$N$  - Neutral background gas density

To simplify the numerical technique, the electron energy equation 2.10 with some mathematical manipulation can be recast in to a form very similar to the continuity equations given by

$$\frac{\partial(n_e \varepsilon)}{\partial t} + \frac{5}{3} \vec{\nabla} \cdot \vec{\Phi}_\varepsilon = S_\varepsilon \quad (2.14)$$

$$S_\varepsilon = -e\vec{\Gamma}_e \cdot \vec{E} - k_L(\varepsilon)n_\varepsilon N \quad (2.15)$$

$$\vec{\Phi}_\varepsilon = -(n_e\varepsilon)\mu_e\vec{E} - D_e\vec{\nabla}(n_e\varepsilon) \quad (2.16)$$

where

$\Phi_\varepsilon$  - Electron energy flux

$\vec{\Gamma}_e$  - Electron flux

$S_\varepsilon$  - Electron energy density source term

These approximations result in the following system of equations that are solved to determine the charged species densities, potential, and electron thermal energy in an RF discharge given by

$$\frac{\partial n_e}{\partial t} + \vec{\nabla} \cdot \vec{\Gamma}_e = S_e \quad (2.17)$$

$$\frac{\partial n_i}{\partial t} + \vec{\nabla} \cdot \vec{\Gamma}_i = S_i \quad (2.18)$$

$$\frac{\partial n_n}{\partial t} + \vec{\nabla} \cdot \vec{\Gamma}_n = S_n \quad (2.19)$$

$$\vec{\Gamma}_j = n_j \vec{v}_j = sn_j \mu_j \vec{E} - D_j \vec{\nabla} n_j + n_j u_f \quad (2.20)$$

$$\nabla^2 \Phi = -\frac{e}{\varepsilon_0} (n_i - n_e - n_n) \quad (2.21)$$

$$\frac{\partial (n_e \varepsilon)}{\partial t} + \frac{5}{3} \vec{\nabla} \cdot \vec{\Phi}_\varepsilon = S_\varepsilon \quad (2.22)$$

where  $s$  is the sign of the charged species and  $j$  represents either an electron, ion, or negative ion species. The solution of this system of non-linear equations forms the basis of the fluid model developed to investigate a RF discharge and Langmuir probe in an



electronegative plasma. In addition, understanding the approximations associated with the drift-diffusion form of the fluid equation allow us to avoid using the plasma fluid model in regimes where the equations are not valid.

### **One Dimensional Solution to the Plasma Fluid Equations**

In this section, the temporal and spatial techniques used to solve the time-dependent drift-diffusion fluid equations and the electron energy equation, based on the previous assumptions, are reviewed in detail. The approach taken to solve the fluid equations is based upon the methods used by Boeuf and Pitchford to develop the fluid model RF-SIGLO (Boeuf and Pitchford, 1995). Equations 2.17 – 2.22 are solved using a Newton-Raphson root finding method combined with a Crank-Nicholson implicit time step technique. The Newton-Raphson method is one of the more common approaches employed in solving non-linear differential equations (Eastwood and Hockney, 1988). Linear differential equations can be discretized directly both spatially and temporally using standard methods (such as finite difference, finite volume, Crank-Nicholson, etc.) such that the equation can be represented by a simple linear system of equations. The Newton-Raphson method linearizes a non-linear differential equation,  $\delta(\phi^{k+1})$ , using a Taylor series expansion to find the solution,  $\phi^{k+1}(x)$ , at the  $k + 1$  iteration using the equation

$$\delta(\phi^{k+1}(x)) = \delta(\phi^k(x) + \Delta\phi(x)) = \delta(\phi^k(x)) + \frac{\partial\delta(\phi^k(x))}{\partial\phi^k(x)} \Delta\phi(x) + h.o.t \quad (2.23)$$

where

$$\Delta\phi(x) = \phi^{k+1}(x) - \phi^k(x)$$

Ignoring terms higher order than  $(\Delta\phi(x))^2$  in equation 2.23 and setting  $\delta(\phi^{k+1}(x)) = 0$ , which assumes the  $k + 1$  iteration is the solution to  $\delta(\phi^{k+1})$ , results in the following equation

$$\frac{\partial\delta(\phi^k(x))}{\partial\phi^k(x)}\phi^{k+1}(x) = -\delta(\phi^k(x)) + \frac{\partial\delta(\phi^k(x))}{\partial\phi^k(x)}\phi^k(x) \quad (2.24)$$

The Newton-Raphson method requires an initial guess to the solution,  $\phi^0(x)$ , to begin the iterative solution process described by equation 2.24. The iterative solution process continues until a tolerance condition is met and then the solution is considered converged. The convergence criterion used in this study is the L infinity norm which is the maximum relative change in the number density or voltage given by

$\zeta_\beta = \text{Max}(|\Delta\phi(x)|/|\phi^{ik}(x)|)$  (Horn, 1990). The Newton-Raphson technique is considered to be converged when  $\zeta_\beta < 10^{-5}$  criterion is met. This method converges quadratically if the initial starting condition is chosen appropriately, however, convergence is not guaranteed for all initial conditions (Hockney and Eastwood, 1988). This method forms the basis of the numerical approach used for the plasma fluid model and the derivations of the equations used in the calculations.

Due to the form of the energy and continuity equations being essentially the same, they are discretized and solved for using equation 2.24 in a similar fashion with only the need to change the source term to account for the various chemical kinetic processes that occur for a particular type of charged species. Discretizing equation 2.22 using a Crank-Nicholson implicit time scheme in one spatial dimension results in the following equation

$$\frac{(n_e \varepsilon)_i^{k+1,m+1} - (n_e \varepsilon)_i^{k,m}}{\Delta t} + \frac{5}{3} \left( \frac{1}{2} \right) \left( \frac{\vec{\Phi}_{\varepsilon,i+1/2}^{k+1,m+1} - \vec{\Phi}_{\varepsilon,i-1/2}^{k+1,m+1}}{\Delta x} + \frac{\vec{\Phi}_{\varepsilon,i+1/2}^{k,m} - \vec{\Phi}_{\varepsilon,i-1/2}^{k,m}}{\Delta x} \right) = \quad (2.25)$$

$$- e E_i^{k,m+1} \Phi_{e,i}^{k,m+1} - k_L(\varepsilon)_i^{k+1,m+1} n_{e,i}^{k,m+1} N_0$$

where the superscript k is the previous Newton iteration and k+1 is the current Newton iteration, m is the previous time step and m + 1 is the current time step, and the subscript i is the spatial step in the x direction. The discretized flux is defined on the half node point to accommodate the Scharfetter and Gummel, 1969, weighting scheme between two nodes and also so that a central differencing scheme may be used (Boeuf and Pitchford, 1995). For small changes in electron energy flux and hence the voltage, electron density, and mean energy, we can apply a Newton linearization scheme to equation 2.25, where

$$\Phi_{\varepsilon,i+1/2}^{k+1,m+1} = \Phi_{\varepsilon,i+1/2}^{k,m+1} + \delta \Phi_{\varepsilon,i+1/2}^{k,m+1} \quad (2.26)$$

$$\Phi_{\varepsilon,i-1/2}^{k+1,m+1} = \Phi_{\varepsilon,i-1/2}^{k,m+1} + \delta \Phi_{\varepsilon,i-1/2}^{k,m+1} \quad (2.27)$$

$$(n_e \varepsilon)_i^{k+1,m+1} = (n_e \varepsilon)_i^{k,m+1} + \delta (n_e \varepsilon)_i^{k,m+1} \quad (2.28)$$

$$k_L(\varepsilon)_i^{k+1,m+1} = k_L(\varepsilon)_i^{k,m+1} + \delta k_L(\varepsilon)_i^{k,m+1} \quad (2.29)$$

Substituting equations 2.26, 2.27, 2.28 and 2.29 into equation 2.25 results in the following

$$\delta (n_e \varepsilon)_i^{k,m+1} + \frac{5}{3} \frac{\Delta t}{2 \Delta x} \left( \delta \vec{\Phi}_{\varepsilon,i+1/2}^{k,m+1} - \delta \vec{\Phi}_{\varepsilon,i-1/2}^{k,m+1} \right) + \delta k_L(\varepsilon)_i^{k,m+1} n_{e,i}^{k,m+1} N_0 =$$

$$\Delta t \left( - e E_i^{k,m+1} \Phi_{e,i}^{k,m+1} - k_L(\varepsilon)_i^{k+1,m+1} n_{e,i}^{k+1,m+1} N_0 \right) - \quad (2.30)$$

$$\frac{5}{3} \frac{\Delta t}{2 \Delta x} \left( \vec{\Phi}_{\varepsilon,i+1/2}^{k,m+1} - \vec{\Phi}_{\varepsilon,i-1/2}^{k,m+1} + \vec{\Phi}_{\varepsilon,i+1/2}^{k,m} - \vec{\Phi}_{\varepsilon,i-1/2}^{k,m} \right) - \left( (n_e \varepsilon)_i^{k,m+1} - (n_e \varepsilon)_i^{k,m} \right)$$

Using the Scharfetter-Gummel weighting scheme for the energy flux results in the expression

$$\bar{\Phi}_{\varepsilon,i+1/2} = \frac{1}{\Delta x} \left( \frac{Z_{i+1} (n_e \varepsilon)_i D_{e,i} e^{Z_{i+1}}}{e^{Z_{i+1}} - 1} - \frac{Z_{i+1} (n_e \varepsilon)_{i+1} D_{e,i+1}}{e^{Z_{i+1}} - 1} \right) \quad (2.31)$$

$$\bar{\Phi}_{\varepsilon,i-1/2} = \frac{1}{\Delta x} \left( \frac{Z_i (n_e \varepsilon)_{i-1} D_{e,i-1} e^{Z_i}}{e^{Z_i} - 1} - \frac{Z_i (n_e \varepsilon)_i D_{e,i}}{e^{Z_i} - 1} \right) \quad (2.32)$$

where

$$Z_{i+1} = -s \frac{\mu_{e,i+1/2}}{D_{e,i+1/2}} (V_{i+1} - V_i) \quad (2.33)$$

$$Z_i = -s \frac{\mu_{e,i-1/2}}{D_{e,i-1/2}} (V_i - V_{i-1}) \quad (2.34)$$

and

$V_i$  - Potential at the  $i_{th}$  spatial step

$\mu_{e,i+1/2}$  - Electron mobility at the half integer spatial step

$s$  - Is -1 for electrons and negative ions and +1 for positive ions

The Scharfetter-Gummel weighting scheme results from the analytic integration of the combined continuity and momentum equations between two grid points with the assumption that the mobility and diffusion coefficients are constant. This is a very stable technique because it is exact in the limit of both a zero electric field (diffusion dominated flux) and a high electric field (drift) dominated flux (Boeuf, 1987). For  $Z < 1.0 \times 10^{-4}$ , the PFM switches to the diffusion limited form of equations 2.31 and 2.32 and for  $Z > 1.0 \times 10^2$  the PFM switches to the

drift limited form of equations 2.31 and 2.32 to avoid the singularities and computational overhead associated with those equations.

### Linearizing the Plasma Fluid Equations

The energy flux given by equation 2.31 is only a function of the electron energy density and voltage at the  $i$  and  $i + 1$  grid point

$$\bar{\Phi}_{\varepsilon,i+1/2}^{k,m+1} = \bar{\Phi}_{\varepsilon,i+1/2}^{k,m+1}((n_e \varepsilon)_{i+1}, (n_e \varepsilon)_i, V_{i+1}, V_i) \quad (2.35)$$

The Taylor series expansion of equation 2.35 is given as

$$\begin{aligned} \delta \bar{\Phi}_{\varepsilon,i+1/2}^{k,m+1} = & \left( \frac{\partial \bar{\Phi}_{\varepsilon,i+1/2}^{k,m+1}}{\partial (n_e \varepsilon)_{i+1}} \right) \delta (n_e \varepsilon)_{i+1}^{k,m+1} + \left( \frac{\partial \bar{\Phi}_{\varepsilon,i+1/2}^{k,m+1}}{\partial (n_e \varepsilon)_i} \right) \delta (n_e \varepsilon)_i^{k,m+1} + \\ & \left( \frac{\partial \bar{\Phi}_{\varepsilon,i+1/2}^{k,m+1}}{\partial V_{i+1}} \right) \delta V_{i+1}^{k,m+1} + \left( \frac{\partial \bar{\Phi}_{\varepsilon,i+1/2}^{k,m+1}}{\partial V_i} \right) \delta V_i^{k,m+1} \end{aligned} \quad (2.36)$$

From equation 2.36 the energy flux is only a function of the electron energy density and voltage at the  $i$  and  $i - 1$  grid point

$$\bar{\Phi}_{\varepsilon,i-1/2}^{k,m+1} = \bar{\Phi}_{\varepsilon,i-1/2}^{k,m+1}((n_e \varepsilon)_i, (n_e \varepsilon)_{i-1}, V_i, V_{i-1}) \quad (2.37)$$

$$\begin{aligned} \delta \bar{\Phi}_{\varepsilon,i-1/2}^{k,m+1} = & \left( \frac{\partial \bar{\Phi}_{\varepsilon,i-1/2}^{k,m+1}}{\partial (n_e \varepsilon)_i} \right) \delta (n_e \varepsilon)_i^{k,m+1} + \left( \frac{\partial \bar{\Phi}_{\varepsilon,i-1/2}^{k,m+1}}{\partial (n_e \varepsilon)_{i-1}} \right) \delta (n_e \varepsilon)_{i-1}^{k,m+1} + \\ & \left( \frac{\partial \bar{\Phi}_{\varepsilon,i-1/2}^{k,m+1}}{\partial V_i} \right) \delta V_i^{k,m+1} + \left( \frac{\partial \bar{\Phi}_{\varepsilon,i-1/2}^{k,m+1}}{\partial V_{i-1}} \right) \delta V_{i-1}^{k,m+1} \end{aligned} \quad (2.38)$$

and the discretized electron energy loss term is given by

$$\delta \mathcal{K}_L(\varepsilon)_i^{k,m+1} = \frac{1}{n_{e,i}} \left( \frac{\partial \mathcal{K}_L(\varepsilon)_i^{k,m+1}}{\partial \varepsilon_i} \right) \delta (n_e \varepsilon)_i^{k,m+1} \quad (2.39)$$

$$\begin{aligned} \delta k_L(\varepsilon)_i^{k,m+1} &= \left( \frac{\partial \varepsilon_i}{\partial (n_e \varepsilon)_i} \right) \left( \frac{\partial k_L(\varepsilon)_i^{k,m+1}}{\partial \varepsilon_i} \right) \delta (n_e \varepsilon)_i^{k,m+1} + \\ &\left( \frac{\partial (n_e)_i}{\partial (n_e \varepsilon)_i} \right) \left( \frac{\partial k_L(\varepsilon)_i^{k,m+1}}{\partial (n_e)_i} \right) \delta (n_e \varepsilon)_i^{k,m+1} \end{aligned} \quad (2.40)$$

These terms are then substituted into equation 2.30 to complete the linearization of the electron energy equation 2.22 in terms of  $n_e \varepsilon$  and  $V$ . The derivatives of equations 2.35 and 2.37 evaluated at values from the previous Newton iteration produces the value of the matrix coefficients used to solve for  $\delta (n_e \varepsilon)_i^{k,m+1}$  and  $\delta (V)_i^{k,m+1}$ .

$$\begin{aligned} A_i &= \frac{\Delta t}{2\Delta x} \left( \frac{\partial \vec{\Phi}_{\varepsilon,i+1/2}^{k,m+1}}{\partial V_{i+1}} \right) \\ B_i &= \frac{\Delta t}{2\Delta x} \left\{ \left( \frac{\partial \vec{\Phi}_{\varepsilon,i+1/2}^{k,m+1}}{\partial V_i} \right) - \left( \frac{\partial \vec{\Phi}_{\varepsilon,i-1/2}^{k,m+1}}{\partial V_i} \right) \right\} \\ C_i &= -\frac{\Delta t}{2\Delta x} \left( \frac{\partial \vec{\Phi}_{\varepsilon,i-1/2}^{k,m+1}}{\partial V_{i-1}} \right) \\ D_i &= \frac{\Delta t}{2\Delta x} \left( \frac{\partial \vec{\Phi}_{\varepsilon,i+1/2}^{k,m+1}}{\partial (n_e \varepsilon)_{i+1}} \right) \\ E_i &= 1 + \frac{\Delta t}{2\Delta x} \left\{ \left( \frac{\partial \vec{\Phi}_{\varepsilon,i+1/2}^{k,m+1}}{\partial (n_e \varepsilon)_i} \right) - \left( \frac{\partial \vec{\Phi}_{\varepsilon,i-1/2}^{k,m+1}}{\partial (n_e \varepsilon)_i} \right) \right\} + \left( \frac{\partial k_L(\varepsilon)_i^{k,m+1}}{\partial \varepsilon_i} \right) N_0 \\ F_i &= -\frac{\Delta t}{2\Delta x} \left( \frac{\partial \vec{\Phi}_{\varepsilon,i-1/2}^{k,m+1}}{\partial (n_e \varepsilon)_{i-1}} \right) \end{aligned}$$

Once the coefficients are substituted into equation 2.30, the energy equation can be recast into a matrix form such that

$$\langle A_1 \rangle \overrightarrow{\delta V} + \langle B_1 \rangle \overrightarrow{\delta (n_e \varepsilon)} = \overrightarrow{b_1} \quad (2.41)$$

where  $b_1$  is obtained from the right hand side of equation 2.30 and the matrices are given by

$$\langle A_1 \rangle = \begin{pmatrix} B_1 & A_1 & 0 & 0 \\ C_2 & B_2 & A_2 & 0 \\ 0 & \ddots & \ddots & \ddots \\ 0 & 0 & C_n & B_n \end{pmatrix} \quad (2.42)$$

$$\langle B_1 \rangle = \begin{pmatrix} E_1 & D_1 & 0 & 0 \\ F_2 & E_2 & D_2 & 0 \\ 0 & \ddots & \ddots & \ddots \\ 0 & 0 & F_n & E_n \end{pmatrix} \quad (2.43)$$

Similar matrix systems are formed for electron, positive and negative ion continuity equations and Poisson's Equation

$$\begin{aligned} \langle A_2 \rangle \delta V + \langle B_2 \rangle \delta(n_e) &= b_2 \\ \langle A_3 \rangle \delta V + \langle B_3 \rangle \delta(n_i) &= b_3 \\ \langle A_4 \rangle \delta V + \langle B_4 \rangle \delta(n_n) &= b_4 \\ \langle A_5 \rangle \delta V - \delta(n_e) - \delta(n_n) + \delta(n_i) &= b_5 \end{aligned} \quad (2.44)$$

This system of equations is then solved using a modified tri-diagnol solver. The sub-matrices are a matrix of the coefficients at each node and its adjacent nodes (i+1 and i-1 nodes) and are inverted to find the values for  $V_i$ ,  $n_e$ ,  $n_i$  and  $n_n$ .

### Two Dimensional Solution to the Plasma Fluid Equations

The one dimensional method can easily be extended to two dimensions by determining the matrix coefficients due to the divergence of the flux by including y component of the derivative. The two dimensional energy flux term at the half step, i+1/2, j+1/2, can be written as

$$\vec{\Phi}_{\varepsilon, i+1/2, j+1/2}^{k, m+1} = \vec{\Phi}_{\varepsilon, i+1/2, j+1/2}^{k, m+1} \left( (n_e \varepsilon)_{i+1, j}, (n_e \varepsilon)_{i, j+1}, (n_e \varepsilon)_{i, j}, V_{i+1, j}, V_{i, j+1}, V_{i, j} \right) \quad (2.45)$$

where the  $i$  index corresponds to the  $x$  direction and the  $j$  index corresponds to the  $y$  direction. The Taylor series expansion for the two dimensional energy flux term at the  $i+1/2, j+1/2$  spatial step is performed and included in the two dimensional energy equation 2.30. The resulting coefficients are provided in appendix A for completeness. The linearized energy equation can then be written for each node in the computational mesh such that

$$A_{i,j}\delta V_{i+1,j} + (B_{i,j} + H_{i,j})\delta V_{i,j} + C_{i,j}\delta V_{i-1,j} + D_{i,j}\partial(n_e \mathcal{E})_{i+1,j} + (E_{i,j} + K_{i,j})\partial(n_e \mathcal{E})_{i,j} + F_{i,j}\partial(n_e \mathcal{E})_{i-1,j} + G_{i,j}\delta V_{i,j+1} + I_{i,j}\delta V_{i,j-1} + J_{i,j}\partial(n_e \mathcal{E})_{i,j+1} + L_{i,j}\partial(n_e \mathcal{E})_{i,j-1} = b_{i,j} \quad (2.46)$$

To solve equation 2.46, the successive block line over-relaxation (SBLOR) iterative method is used (Benson and Evans, 1972). As a result, another iterative index is introduced where  $n$  is the previous SBLOR iteration and  $n+1$  is the current SBLOR iteration

$$A_{i,j}\delta V_{i+1,j}^{n+1} + (B_{i,j} + H_{i,j})\delta V_{i,j}^{n+1} + C_{i,j}\delta V_{i-1,j}^{n+1} + D_{i,j}\partial(n_e \mathcal{E})_{i+1,j}^{n+1} + (E_{i,j} + K_{i,j})\partial(n_e \mathcal{E})_{i,j}^{n+1} + F_{i,j}\partial(n_e \mathcal{E})_{i-1,j}^{n+1} = b'_{i,j} \quad (2.47)$$

where

$$b'_{i,j} = b_{i,j} - G_{i,j}\delta V_{i,j+1}^n - I_{i,j}\delta V_{i,j-1}^{n+1} - J_{i,j}\partial(n_e \mathcal{E})_{i,j+1}^n - L_{i,j}\partial(n_e \mathcal{E})_{i,j-1}^{n+1}$$

A similar approach can be used to discretize the ion and electron continuity and momentum equations and the resulting system of equations can be recast into a matrix form similar that of equation 2.44. The solution method used in the SBLOR method is similar to that of a standard successive line over relaxation (SLOR) method except that it solves a system of linear equations simultaneously (Kinema, 1995). In the SLOR and SBLOR methods, the 2-D grid is divided into a series of 1-D grids in the  $x$  or  $y$  coordinate (the  $x$  coordinate is chosen to simplify the discussion). The solution of the



system of equations starts next to the upper or lower boundary condition in the y coordinate and the system of 1-D plasma fluid equations is solved using a modified tri-diagonal matrix solver. Since, we are solving equations 2.18 through 2.24 simultaneously; each element of the tri-diagonal matrix for the line is composed of a matrix based on equation 2.44. The  $j+1$  and  $j-1$  terms from equation 2.46 are taken from the  $n$ th iteration of the SBLOR method and are added to the source terms  $b_1 - b_5$  in equation 2.44 according to equation 2.47. After a solution is obtained for a line, the  $j$  subscript in equation 2.47 is incremented by 1 and a solution is obtained for the next line. This process is repeated until convergence is achieved based on the criterion,

$$\text{Max} \left( \left| \delta N_{i,j}^{n+1} - \delta N_{i,j}^n \right| / N_{i,j}^n \right) < 1.0 \times 10^{-4}.$$

To begin a solution using the present method an initial condition must be provided to the model. Three different starting profiles of the number density were used to begin the model including a constant profile, cosine profile, and Gaussian number density profile. Attempts to accelerate the convergence of the model to steady state by starting the discharge simulation using a profile based on an estimated charge density and potential profile did not reduced the time required to achieve convergence of the simulation. This was due to the estimate being different enough from the final solution that the sheath region would be reformed and no time savings resulted. The time required to achieve cyclic convergence of an RF discharge model varies greatly based on a great number of factors which include number of mesh points, number ion species, size of the discharge region, voltage amplitude, pressure, closeness of the initial guess to the converged solution, etc. The majority of the time required to achieve a cyclically

converged solution was due to the slow moving positive and negative ions redistributing within the bulk plasma region of the discharge. The equations developed in this section provide the core of the plasma fluid model and can be used to model a variety of plasma transport problems. In the next section, the boundary conditions used to complete the plasma fluid model are presented.

### **Plasma Fluid Model Boundary Conditions**

In the plasma fluid model, five different boundary conditions for charged species transport are modeled. The boundary conditions model electrodes, an infinite dielectric, dielectric coated electrodes, and a continuous boundary condition for an RF discharge in flow tube shown in Figure 2.1. Secondary electron emission is also modeled for electrodes, infinite dielectrics, or dielectric coated electrodes. For the electrons, the normal flux boundary condition is given by the thermal flux of the electrons near the wall to a perfectly absorbing wall plus secondary emission caused by energetic ions striking the wall

$$\vec{\Gamma}_{e,w} = \frac{n_e v_{th}}{4} - \gamma \cdot \vec{\Gamma}_{i,w} \quad (2.48)$$

where

$n_e$  - Electron density near the wall

$\gamma$  - Secondary emission coefficient

$v_{th}$  - Electron thermal velocity

$\vec{\Gamma}_{e,w}$  - Electron flux normal to the wall

$\vec{\Gamma}_{i,w}$  - Ion flux normal to the wall

The electron density used near the wall for flux calculations is based on the electron density at the grid point adjacent to the wall using the potential difference and electron characteristic temperature, where  $T_{e,c} \equiv D_e / \mu_e$ , which is altered according to the Boltzmann equation (Nitschke and Graves, 1994). This is done in order to achieve an accurate loss rate of the electrons to the wall that accounts for both drift and diffusion losses across the node nearest the wall. For the positive ions, the diffusive flux is negligible compared to the drift flux in the sheath region near a wall, hence the ion flux normal to the wall is approximated as the ion drift flux given by

$$\vec{\Gamma}_{i,w} = \mu_i n_i \vec{E} \quad (2.49)$$

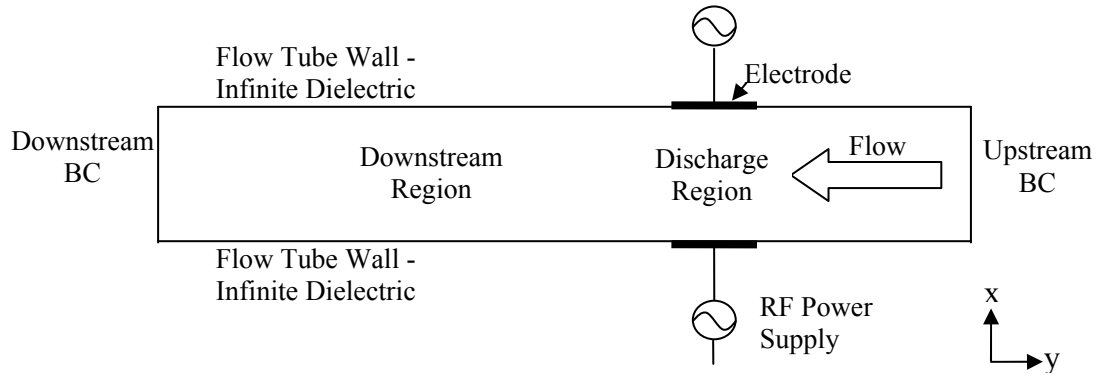


**Figure 2.1 RF Discharge in a Flowing Background Gas Geometry**

A negligible number of negative ions have enough thermal energy to overcome the electric field in the sheath near a wall, therefore the negative ion flux normal to the wall is approximated as

$$\vec{\Gamma}_{n,w} = 0 \quad (2.50)$$

Equations 2.48, 2.49, and 2.50 form the flux boundary conditions for all charged species in the PFM, next we will review the potential boundary conditions for the various materials in the PFM.

The time dependent potential boundary condition for a RF driven electrode is given by

$$V(t) = V_0 \cos(2\pi ft + \phi) \quad (2.51)$$

where

$V_0$  - Potential Amplitude

$f$  - RF frequency

$\phi$  - RF phase

The amplitude, frequency and phase are specified as inputs into the PFM simulation to simulate the applied RF voltage. The flow tube wall shown in Figure 2.1 is approximated as an infinite dielectric. The boundary condition used for the infinite dielectric is derived from basic electromagnetic theory boundary conditions for electric field perpendicular to the surface of a linear dielectric

$$\hat{n} \cdot (\epsilon_0 \vec{E}_1 - \epsilon_2 \vec{E}_2) = \sigma \quad (2.52)$$

where

$\vec{E}_1$  - Electric field at the plasma-dielectric interface in the plasma

$\vec{E}_2$  - Electric field at the plasma-dielectric interface in the dielectric

$\epsilon_2$  - Permittivity of the dielectric

$\sigma$  - Surface charge density at plasma-dielectric interface

No free charge is present in a dielectric, therefore,  $E_2$  can be expressed approximately as

$$E_{2,n} = -\frac{(V_1 - V_0)}{\Delta} \quad (2.53)$$

where

$E_{2,n}$  - Electric field normal to plasma-dielectric interface in the dielectric

$\Delta$  - Dielectric thickness

$V_1$  - Potential at the dielectric-plasma interface

$V_0$  - Potential on the dielectric surface exterior to simulation

Therefore for an infinite dielectric, as  $\Delta \rightarrow \infty$  then  $\vec{E}_2 \rightarrow 0$ , hence the electric field at the boundary of the infinite dielectric is given by the expression

$$\hat{n} \cdot \vec{E}_1 = \frac{\sigma}{\epsilon_o} \quad (2.54)$$

The dielectric coated electrode boundary condition is found by using equations 2.52 and 2.53, however,  $V_0$  is now the potential at the metal electrode surface and the dielectric thickness is not infinite. In the plasma near the dielectric surface, the electric field normal to the dielectric surface,  $E_{1,n}$ , can be approximated as

$$E_{1,n} = -\frac{(V_2 - V_1)}{h} \quad (2.55)$$

where

$h$  - Cell length

$V_2$  - Potential at the first grid point interior to the plasma

$V_1$  - Potential at plasma-dielectric interface

Substituting equation 2.55 and 2.53 into equation 2.52, the potential boundary condition on a dielectric coated electrode is found to be

$$-V_2 + (1 + \frac{h\varepsilon_2}{\varepsilon_o\Delta})V_1 = \frac{h}{\varepsilon_o}(\sigma + \frac{\varepsilon_2V_0}{\Delta}) \quad (2.56)$$

The surface charge density,  $\sigma$ , used in equations 2.54 and 2.56 on a dielectric surface in a plasma is calculated by summing the total charged species flux incident upon the dielectric surface using the equation

$$\frac{d\sigma}{dt} = e(|\Gamma_{i,w}| - |\Gamma_{e,w}| - |\Gamma_{n,w}|) \quad (2.57)$$

Equation 2.57 is numerically integrated using a modified Euler technique during each time step, resulting in the surface charge density value which is used for the electric field boundary conditions in equations 2.54 and 2.56 on the next time step (Boeuf and Pitchford, 1995).

For the geometry shown in Figure 2.1, the boundary conditions upstream or downstream of the RF discharge represent an end to the simulated domain, but not the end of the plasma. The boundary conditions either upstream or downstream of the RF discharge should not have any effect on the local plasma density or the potential in the plasma at the boundary due to a divergence of the flux across the boundary. To ensure the component of the divergence normal to the downstream or upstream boundary is zero the following flux condition is used for each charged species

$$\Gamma_{y,i+1} = \Gamma_{y,i} \quad (2.58)$$

which results in the derivative of the density in the normal direction being zero at the boundary such that

$$\frac{dn}{dy} = 0 \quad (2.59)$$

This boundary condition ensures that the y component of the species diffusive flux is zero and the y component of the convective flux is constant. Equations 2.54 and 2.57 are used to determine the potential boundary condition at the downstream and upstream boundary. Once a steady flow of quasi-neutral plasma has been established at the boundary, then  $\sigma \rightarrow 0$  and as a result  $E \rightarrow 0$ , and the drift and diffusion fluxes at the boundary go to zero resulting in only a convection flux across the boundary. This results in zero divergence of the species fluxes and no local increase or decrease in the charged species densities near the boundary.

### **Plasma Fluid Model Algorithm Outline**

A general outline of the logical flow and calculation order of the plasma fluid model is shown in Figure 2.2. The Plasma Fluid Model (PFM) was written in Fortran 90 using the Compaq Visual Fortran compiler and environment. User inputs to the PFM are provided using Fortran namelist input files. The input file provides all the geometric, numerical, and simulation parameters, while the chemistry data file along with pre-calculated results from a Boltzmann transport equation solver provides the data for modeling the background gas.

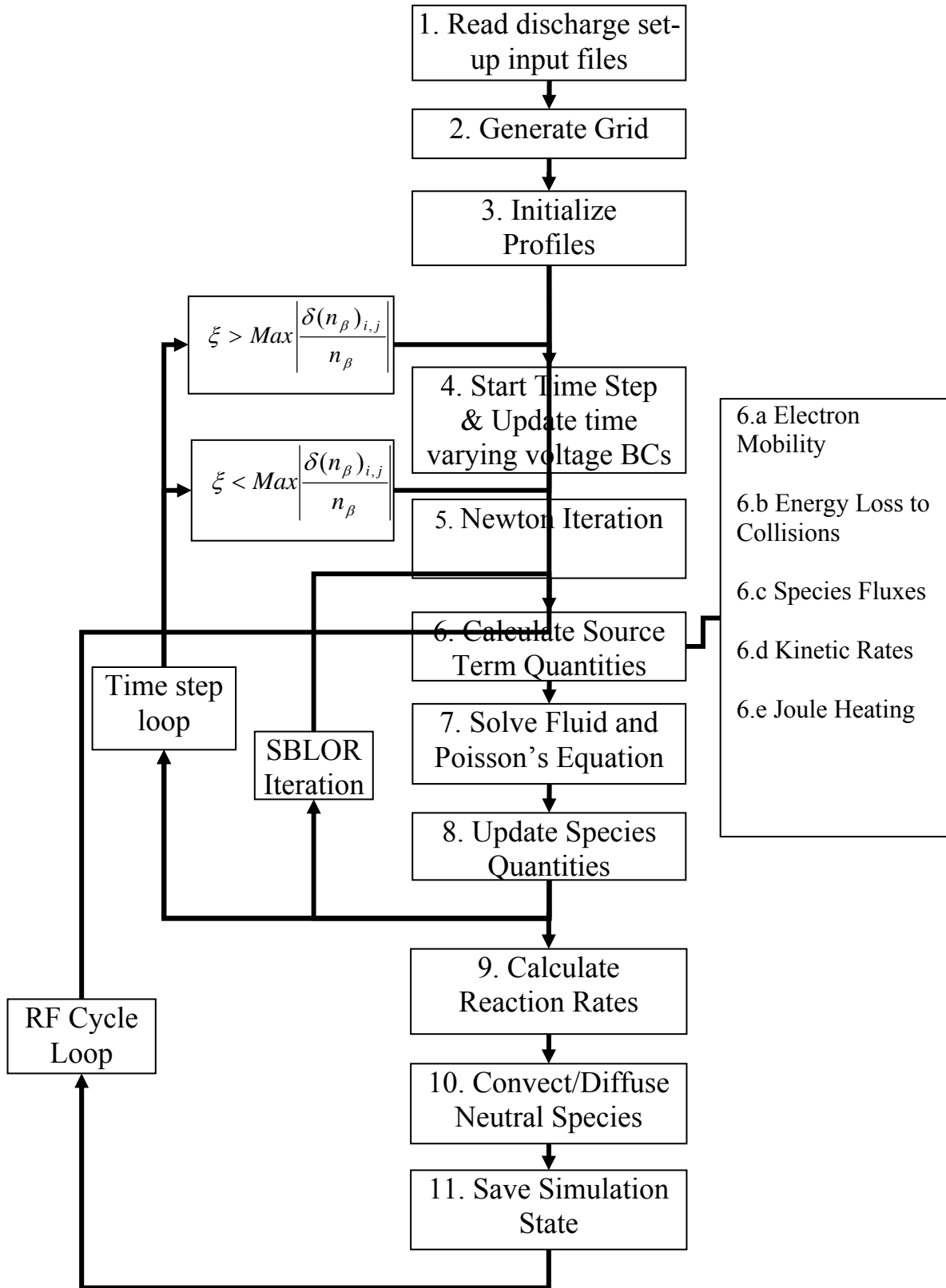


Figure 2.2 Plasma Fluid Model Flow Diagram



The following outline is a description of the blocks shown in the algorithm outlined in Figure 2.2 which is used in the PFM. Bullet numbers correspond to numbers in the algorithm blocks.

1. Read discharge set-up and chemistry data input files
  - a. Three files are read into the PFM
    - i. Discharge geometry and parameter PFM set-up file
    - ii. Background gas heavy species chemical kinetic data
    - iii. Electron chemical kinetic reaction rates versus  $E/N$  from time independent Boltzmann transport equation
2. Set-up computational grid using ray tracing method based on 1-D or 2-D geometry specified in PFM set-up file
3. Specify initial density or potential profile of plasma
  - a. Constant density or potential profile
  - b. Cosine density or potential profile
  - c. Import user specified density and potential profile
4. Start initial or next time step
  - a. If the Newton-Raphson solution of fluid equations converged start next time step
  - b. Update species densities and potentials
  - c. Update time varying voltages on boundaries
  - d. Update surface charge density on surfaces using equation 2.57
5. Start or continue Newton-Raphson iterative solution to fluid equations
  - a. If Newton-Raphson solution did not achieve convergence criterion perform another iteration

- b. Start Newton-Raphson using initial plasma densities and potential
6. Calculate source term quantities, such as ionization, detachment, electron energy loss coefficient, using updated densities, potential, and electron energy from previous Newton-Raphson iteration
  - a. Electron mobility
  - b. Chemical kinetic rates that produce charged species
  - c. Electron energy loss coefficient (equation 2.14)
  - d. Species fluxes (equations 2.32 and 2.33)
  - e. Joule heating (equation 2.16)
7. Solve linearized fluid equations with coefficients using SBLOR method
  - a. Update matrix coefficient terms used in equations 2.43 and 2.44 based on results of previous Newton-Raphson iteration
  - b. Begin SBLOR solution loop and assemble  $\langle A \rangle$  for line  $j$
  - c. Apply BCs and  $j \pm 1$  line change in density, energy, and potential quantities to equation 2.44  $\vec{b}$  vector
  - d. Add species source terms (ionization, attachment, etc.) to  $\vec{b}$  vector
  - e. Solve linear system  $\langle A \rangle \cdot \vec{x} = \vec{b}$  for line  $j$  then move to next line
  - f. Once, solution of each line complete check for convergence
8. Update changes in the species densities, energy, and potential
9. Calculate neutral species chemical kinetic reaction rates—this is sub-cycled
10. Solve the convection and diffusion equations for each species—this is sub-cycled
11. Save the state of the simulation for restart purposes

Shown in Figure 2.3 is a more detailed overview of the SBLOR matrix solving method

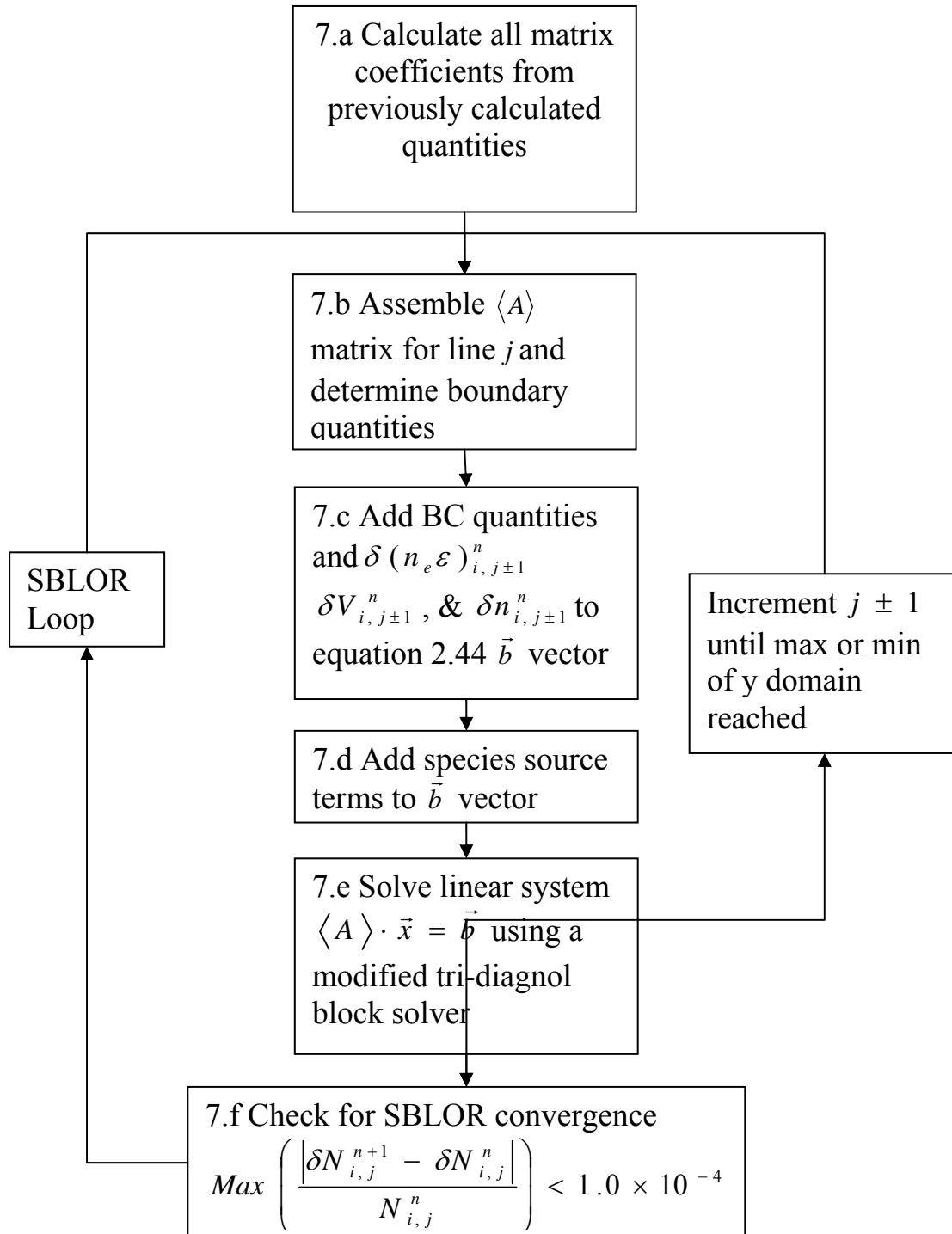


Figure 2.3 Fluid Equation SBLOR Solver

## Plasma Fluid Model Numerical Issues

The time steps used in plasma fluid simulations are governed by two constraints; the dielectric relaxation time and the Courant, Friedrichs, Lewy (CFL) condition. The spatial steps are also constrained by the requirement that the error due to the finite differencing approximation is small and the practical consideration that the sheath region of the discharge be adequately resolved with enough computational nodes to accurately simulate the rapidly changing electron density profile and the non-uniform electric field.

In order for the time-dependent moments of the Boltzmann transport equation to converge to a solution, the simulation time step must be less than the dielectric relaxation time and CFL condition given by the following equations (Boeuf, 1987):

$$\Delta t_d = \frac{\epsilon_o \vec{E}}{\vec{J}_{drift}} = \frac{\epsilon_o}{q(\mu_e n_e + \mu_i n_i + \mu_n n_n)} \quad (2.53)$$

$$\Delta t_{CFL} = \frac{\Delta x}{v_c} \quad (2.54)$$

where

$\Delta t_d$  - Dielectric time step

$\Delta t_{CFL}$  - CFL time step limit

$\vec{J}_{drift}$  - Total drift current density

$v_c$  - Maximum characteristic velocity

$\Delta x$  - Grid length

The dielectric relaxation time governs the time that it takes the charged species to respond to a disturbance in the charge density (Föll, 2006). The electrons usually

influence the dielectric relaxation time the most due to their high mobility. The CFL condition provides a constraint on the maximum time step relative to the computational cell size and the maximum characteristic velocity in the simulation. The CFL time constraint keeps the simulation from allowing species to pass over a computational cell within a time step, which would result in the simulation violating the continuity equation. In a plasma fluid simulation, the electrons move with the largest velocity due to their low mass. The maximum electron diffusion velocity that can be achieved is the electron thermal velocity for the case of electrons moving from a region of finite electron density to a region with no electron density. The electric field in the bulk plasma region required to generate an electron velocity greater than the electron thermal velocity in a collisional plasma is given by

$$\vec{E} = \frac{v_{th}}{\mu_e} \quad (2.55)$$

However, this large of an electric field is never encountered in the bulk plasma for conditions considered here. Near the sheath region, the electron drift and diffusion velocities are almost always in opposite directions near the sheath (the exception occurs only at low electric field values in electronegative discharges) and hence the net velocity of the electrons in the sheath is not as large as the electron thermal velocity. Therefore, the characteristic velocity used for the CFL condition to determine the largest time step is the electron thermal velocity.

### **Numerical Acceleration Techniques**

The need to resolve each RF cycle, the high computational demands of implicit time dependent methods, and the requirement that the explicit simulation time steps

satisfy the dielectric relaxation time and CFL conditions, result in the simulation of an RF discharge in a flowing background gas taking several hours to converge in one dimension and several days to converge in two dimensions for a large computational domain.

Therefore, three numerical acceleration techniques were developed to decrease runtime. The first technique is specific to accelerating the convection of a plasma downstream of an RF discharge in a flowing background gas and involves developing a guess to the decay profile of the charged species downstream of the RF discharge. The second acceleration technique is based on an approach developed by Ventzek and others, 1992, which accelerates the simulation to convergence by determining the rate of change of the time averaged positive ion densities and projects that change forward in time. The third method is an ion and chemical kinetic reaction sub-cycling scheme, which results from the low mobility of the ions compared to the electrons. In addition, the chemical kinetic reactions presented in Chapter III can also be sub-cycled based on if the reaction directly changes the gain or loss of a charged species or is only responsible for producing neutral species due to the difference in the plasma versus chemical kinetics rates.

Starting with the time independent form of the continuity equations and eliminating the drift and diffusive fluxes results in the following equation:

$$u_f \frac{dn_b(y)}{dy} = \alpha(y) - \beta(y)n_b(y) \quad (2.56)$$

where

$$\alpha(y) = \sum_r k_r(y)n_a(y)n_b(y)$$

$$\beta(y) = \sum_r k_r(y)n_c(y) + \frac{D_a}{\Lambda^2}$$

$\alpha(y)$  - Gain rate of the species

$\beta(y)$  - Loss frequency of the species

$k_r(y)$  - Reaction coefficient of reaction r

$n_b(y)$  - Number density of species a

$D_a$  - Electronegative ambipolar diffusion coefficient

$\Lambda^2 = \left( \frac{a_x}{\pi} \right)^2$  - Geometry coefficient for the tube

$a_x$  - Width of the tube.

This system of equations determines the convection and decay or growth of any species type in the simulation. The gain and loss coefficients in equation 2.56 are given as a function of position due to their dependence on the electron energy and density which changes downstream of the RF discharge. As a result, the integration of equation 2.56 is done numerically using a trapezoid method for the positive and negative ions and excited neutral species. The electron density downstream is not estimated using this approach because of the high mobility of the electrons and their dependence on the correct sheath structure near the walls (which has not developed downstream of the discharge yet). Once the density of the ions and excited neutral species has been estimated downstream, the electrons quickly drift downstream and are produced due to detachment to form a quasi-neutral bulk plasma. In order to provide an initial density to equation 2.56 for the charged and excited neutral species requires that the RF discharge simulation is run for approximately 200 or more cycles with no flow to establish the plasma sheath near the electrodes. Once the sheath is established, the simulation is run for another 200 RF

cycles with flow to establish the upstream profile of the RF discharge. Upon establishing the upstream density profile, a cross-section of the density profiles near the RF discharge in the x direction, see Figure 2.4, is chosen to provide the starting density for each species across the discharge. The y position of the cross-section is placed after the ambipolar electric field transverse to the RF discharge of the ion and excited species density profiles. Equation 2.56 is then numerically integrated in the y direction for each grid point in the x direction starting from the cross-sectioning line in the discharge region to the downstream boundary condition to determine the density of the species downstream of the RF discharge.

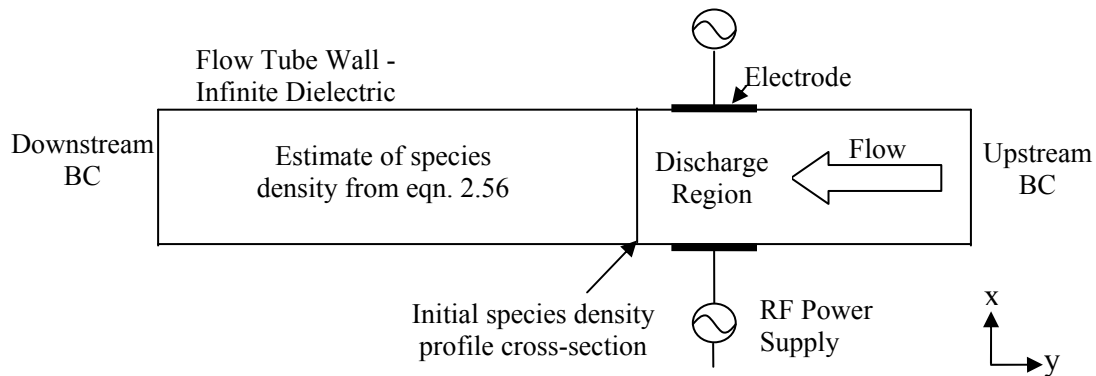


**Figure 2.4 RF Discharge in a Flowing Background Gas Geometry**

The previously described algorithm preserves the shape of the sheath in the RF discharge, which is important for keeping the model from diverging shortly after the acceleration is performed. The numerical integration of equation 2.56 is done successively for each species starting with the neutral species. Since, the electron energy and density is not estimated downstream, the change in the ionization and disassociation rates cannot be determined accurately in equation 2.56. As a result, the additional accuracy obtained by solving for all the species densities downstream simultaneously is



unwarranted. Due to the dependence of each species' density on the densities of the other species, this acceleration approach must be repeated several times to provide a reasonable estimate for the downstream densities of all species. The species density profiles calculated downstream using this method are usually close enough that convergence occurs within a few thousand cycles for oxygen and ten's of thousand of cycles for a nitrogen-oxygen mix due to the differences in process rates and number of chemical kinetic reactions in the gases.

### **Ion Density Rate of Change Acceleration Technique**

The second acceleration technique is useful in speeding up convergence of any RF discharge simulation. The acceleration scheme used in the PFM is similar to an acceleration scheme used by Ventzek and others, 1992, which accelerates the discharge simulation convergence by calculating the cycle averaged change in the density at each grid point for each charged species using a first order Taylor series approximation of the density

$$\overline{n(x, t + \Delta t_a)} = \overline{n(x, t)} + \delta \frac{d\overline{n(x, t)}}{dt} \Delta t_a \quad (2.57)$$

where

$\Delta t_a$  - Acceleration time step

$\delta$  - Damping coefficient

The damping coefficient,  $\delta$ , is modified to keep the number density at time  $t + \Delta t_a$  from being an unphysical value after the acceleration step. The number densities of the charged species are then normalized to maintain the quasi-neutral nature of the discharge in the center (Ventzek and others, 1992). Ventzek's method is effective at accelerating

the convergence of the discharge simulation, but the near zero values of the negative ions and electrons in the sheath region require that the damping coefficient be much less than one when the number density in the sheath is decreasing. This requirement effectively reduces the acceleration time step and effectiveness of the method. This method also does not necessarily keep the time averaged flux of the charged species to the electrode constant which can also result in the instability of the model, hence a more robust acceleration scheme was developed for this investigation.

The following derivation is done to determine the spatial damping coefficient that maintains a constant ion flux to either a dielectric or electrode boundary. For this derivation we focus on a one dimensional development, however, the method can easily be extended to multiple dimensions. The positive ion flux in the sheath and pre-sheath for most plasma conditions is dominated by the drift flux, therefore we approximate the flux as

$$\Gamma_i(x, t) \approx \mu_i n_i(x, t) E(x, t) \quad (2.58)$$

Averaging the ion flux over one RF cycle at each grid point in the sheath and pre-sheath from  $t - t_c$  to  $t$  results in the expression

$$\overline{\Gamma_i(x, t)} \approx \overline{\mu_i n_i(x, t) E(x, t)} \quad (2.59)$$

The time averaged positive ion flux in the sheath at  $t + \Delta t_a$  is given by

$$\overline{\Gamma_i(x, t + \Delta t_a)} \approx \overline{\mu_i n_i(x, t + \Delta t_a) E(x, t + \Delta t_a)} \quad (2.60)$$

Next we assume that the time averaged electric field between  $t$  and  $t + \Delta t_a$  does not change between cycles such that

$$\overline{E(x, t)} \approx \overline{E(x, t + \Delta t_a)} \approx \overline{E(x)} \quad (2.61)$$

Performing a Taylor series expansion of the positive ion density in equation 2.60 results in the expression

$$\overline{\Gamma_i(x, t + \Delta t_a)} \approx \mu_i(\overline{n_i(x, t)} + \frac{d\overline{n_i(x, t)}}{dt} \Delta t_a) \overline{E(x)} \quad (2.62)$$

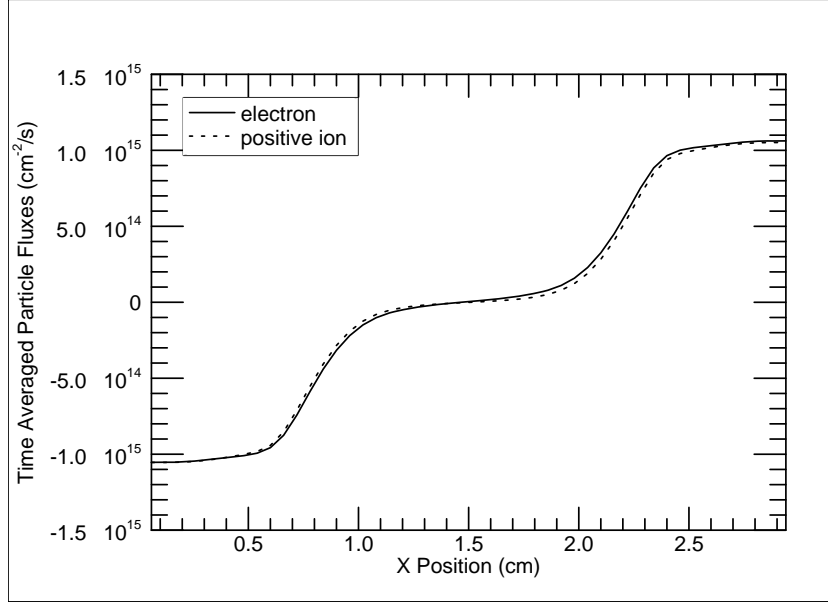


**Figure 2.5 Time Averaged Positive Ion and Electron Fluxes in a 1-D  $N_2(X)$ - $O_2(X)$  discharge**

From Figure 2.5, we notice that the positive ion flux is approximately constant throughout the sheath ( $X < 0.6$  cm). Letting  $x_s$  be the position of the sheath edge ( $\sim 0.60$  cm) and  $x_0$  be any position inside the sheath such that for the left side of the discharge where  $x_0 \leq x_s$  the expression for the ion flux at  $x_0$  is given by

$$\Gamma_0 = \overline{\Gamma_i(x_0, t + \Delta t_a)} \approx \overline{\mu_i n_i(x_0, t + \Delta t_a) E(x_0)} \approx \overline{\mu_i n_i(x_s, t + \Delta t_a) E(x_s)} \quad (2.63)$$

At the sheath edge the time averaged electric field has a minimum value compared to any other point in the sheath and since  $\Gamma_0$  is constant in the sheath, therefore

$$\overline{n_i(x_s, t + \Delta t_a)} = \frac{\Gamma_0}{\mu_i E(x_s)} \quad (2.64)$$

We develop a spatially dependent damping coefficient for equation 2.57, to avoid reducing the ion species densities to unphysical values while maintaining ion current continuity and a constant net charge. To accomplish this purpose,  $\chi(x_0)$ , is chosen to be the ratio of the ion density at any point in the sheath to the ion density at the sheath edge given by

$$\chi(x_0) = \frac{\overline{n_i(x_0, t + \Delta t_a)}}{\overline{n_i(x_s, t + \Delta t_a)}} = \frac{\overline{E(x_s)}}{\overline{E(x_0)}} = \frac{\overline{n_i(x_0, t)}}{\overline{n_i(x_s, t)}} \leq 1 \quad (2.65)$$

From equation 2.64, we note that the ratio of the ion density in the sheath to the ion density at the sheath's edge is approximately constant over the acceleration time step due to the electric field and ion flux being constant. At the sheath edge, equation 2.57 with  $\delta = 1$  is given by

$$\overline{n_i(x_s, t + \Delta t_a)} = \overline{n_i(x_s, t)} + \frac{d\overline{n_i(x_s, t)}}{dt} \Delta t_a \quad (2.66)$$

By multiplying both sides of equation 2.66 by  $\chi(x_0)$  at any position within the sheath, we obtain an expression for the ion density at  $x_0 \leq x_s$  based on the ion density rate of change at the sheath edge

$$\overline{n_i(x_0, t + \Delta t_a)} = \overline{n_i(x_0, t)} + \chi(x_0) \frac{d\overline{n_i(x_s, t)}}{dt} \Delta t_a \quad (2.67)$$

Outside of the sheath region, we are able to project the ion density forward in time without any damping coefficient such that for  $x > x_s$  we set  $\chi(x) = 1$

$$\overline{n_i(x, t + \Delta t_a)} = \overline{n_i(x, t)} + \frac{d\overline{n_i(x, t)}}{dt} \Delta t_a \quad (2.68)$$

The change in the density of the negative ions is altered such that the difference between positive and negative ion densities is maintained after the acceleration technique at every point in the discharge to maintain quasi-neutrality

$$\Delta n(x) = \overline{n_i(x, t)} - \overline{n_n(x, t)} \quad (2.69)$$

$$\overline{n_n(x, t + \Delta t_a)} = \overline{n_i(x, t + \Delta t_a)} - \Delta n(x) \quad (2.70)$$

The electron density remains unchanged over the acceleration time step to maintain the same net charge and hence the same electric field consistent with the approximation made in equation 2.61. Due to the time required to achieve cyclic convergence (defined by  $\text{Max} \left( \left| n(t)_{i,j} - n(t + t_c)_{i,j} \right| / n(t)_{i,j} \right) < 1.0 \times 10^{-8}$ ) of the RF discharge simulation depending mostly on the slow moving ions, there is no need to accelerate the change in density of the electrons. Since  $n_i(x_0, t) \gg n_n(x_0, t)$  in the sheath region, the negative ions are the limiting species to the acceleration time step. If an overly large acceleration time step is chosen such that the negative ion density at any grid point becomes less than 1% of its initial value at any point in the sheath, then the damping coefficient is reapplied such that

$$\overline{n_i(x, t + \Delta t_a)} = \overline{n_i(x, t)} + \delta\chi(x) \frac{d\overline{n_i(x, t)}}{dt} \Delta t_a \quad (2.71)$$

where

$$\delta = \left| \frac{0.99 \cdot \overline{n_n(x,t)}}{\chi(x) \frac{dn_i(x,t)}{dt} \Delta t_a} \right|. \quad (2.72)$$

which does not let the negative ion density reduce to less than 1% of its density before the acceleration time step. This limiting approach resulted in a more stable technique than merely requiring that the negative ions have a non-negative number density.

Using the previously described method to accelerate the change in the positive and negative ion densities insured that the ion flux is spatially constant in the sheath region. This is consistent with the time independent continuity equation if the species source terms are negligible in the sheath region such that

$$\vec{\nabla} \cdot \vec{\Gamma}_i = 0 \rightarrow \vec{\Gamma}_i = I_0 / e \quad (2.73)$$

where  $I_0$  is the ion current to the electrode. This approximation is true for most of the RF cycle due to the source of positive ions being primarily ionization by electrons and the electrons are repulsed by the high fields of the sheaths near the electrodes. This acceleration method also negates the effects of numerical error in the ion cycle averaged rate of change term,  $\overline{dn_i(x_0,t)} / dt$ , in the sheath region. This term can be less accurate in the initial stages of the sheath evolution due to the low electron densities which can disrupt the constant time averaged ion flux in the sheath. In a 1-D Argon RF discharge at 1 Torr, acceleration time steps of  $\Delta t_a = 250t_c$  were typically attainable versus Ventzek's method which only allowed  $\Delta t_a = 100t_c$ . Maximum acceleration time steps of  $\Delta t_a = 160t_c$  were realizable in a pure oxygen discharge with chemistry versus Ventzek's original approach which only allowed  $\Delta t_a = 20t_c$ . In 2-D flow simulations with

electronegative plasmas and chemical kinetic reactions, the maximum acceleration time step was reduced to  $\Delta t_a = 60t_c$  due to the low sheath fields downstream of the RF discharge being very sensitive to small changes in net charge densities and hence asymmetries were easily introduced into the charged species density profiles. This acceleration method made possible the execution of the 1-D RF discharge models in a nitrogen-oxygen mix in approximately 12 hours on an AMD Opteron 250 CPU using the Portland Group Fortran 90 compiler.

### **Acceleration Techniques for Neutral Excited Species**

Another problem in modeling both plasma transport and the subsequent chemical kinetics processes that ensue (such as interactions between excited electronic and vibrational states) is that the evolution of the excited states of the background gas occurs over a much longer time scale than the plasma transport. Since, excited states of the background gas change the gain and loss rates of the charged species, the discharge cannot achieve a steady state until the densities of the excited species in the background gas also achieve a steady state. A method very similar to the previously presented method (section *Ion Density Rate of Change Acceleration Technique*) for accelerating charged species changes was used to accelerate the evolution of the neutral excited species in the computational region. Since maintaining flux continuity of the neutral species at the boundaries is not essential to the stability of the neutral species density calculations, the refinements in the sheath region developed previously for charged species are unnecessary. Therefore, to accelerate the evolution of the neutral species densities, the changes in their density over a RF cycle are averaged to calculate

$\overline{dn_\alpha(x_0, t)} / dt$  for equation 2.57. Since, the change in excited species densities over the time of a RF cycle is small,  $\Delta t_a$  can be set to 200 times the RF cycle time or greater for molecular gas like pure oxygen or much greater for a noble gas like Argon. The limit to the length in the acceleration time step is due to the stiffness of the rate equations governing chemical kinetics of the background gas. The maximum acceleration time step for a large number of rate equations such as in the nitrogen-oxygen mix can generally only be found through experimentation and any  $\Delta t_a$  greater than 60 generally caused the simulation to diverge.

Finally, the third method of accelerating the cyclic convergence of the plasma fluid model is to subcycle the calculation of the negative and positive ion transport. Since, the mobility and density of the electrons is the primary limiter of the explicit simulation time step from equation 2.53 and ion densities only fluctuate by a small amount (less than 1%) during an RF cycle, therefore simulation time can be reduced by calculating the movement of the ions every few electron time steps. Through experiment with the model, it was found that simulating positive and negative ion transport every 10 electron time steps resulted in no difference in simulation results. It is important to note that the ion sub cycling acceleration method should only be applied once the simulation has adequately setup the sheath (moved away from the initial starting conditions) and has started slowly evolving towards the cyclic steady state solution. This is due to the sheath not being established which allows asymmetries to develop in the net charge density from unphysical transport of the ions.



Combining the drift-diffusion-convection form of the fluid model presented in this chapter with a chemical kinetic model (presented in the next chapter) enables us to determine the density of the plasma and excited species that can be produced by a RF discharge in a flowing electronegative background gas. In Chapter IV, the excited neutral species densities calculated using the chemical kinetic model are found to play a very important role in determining the gain and loss rates of the charged species in the RF discharge. The neutral species are also found to be essential to determining the sheath length and other aspects of the discharge structure and maintaining a significant electron density downstream of the RF discharge in an electronegative background gas.

### III. Plasma Chemical Kinetic Model

#### Overview of the Plasma Chemical Kinetic Model

The plasma chemical kinetic model in conjunction with the solution to the electron energy equation determines the ionization, attachment, recombination and detachment rates for the charged species continuity equations of the plasma fluid model as well as the rates for the production and loss of excited species which are also generated in the plasma. The calculation of the gains and losses of charged species is required to close the continuity equations of the plasma fluid model by providing the source term for a particular species. The creation of excited species from the background gas species is modeled in detail because large quantities of excited species significantly increase the detachment of negative ions and the rate of step-wise ionization. The presence of excited neutral species also alters the EEDF, which affects the rates of all chemical kinetic processes in the plasma. As a result, changes in the detachment rate caused by the removal of neutral excited species by a flowing background gas are shown to significantly alter the RF discharge sheath structure and excited neutral and charge species production rates.

Researchers have shown that significant quantities of  $O_2(^1\Delta_g)$ ,  $O_2(^1\Sigma_g)$  and  $O(^3P)$  can be produced by electric discharges in oxygen (Pitz and others, 2004). Fujii, 1994, has reported a yield of 17% of  $O_2(^1\Delta_g)$  with a RF discharge. Studies by Braginsky and others, 2006, have shown that significant percentages, between 10% to

16%, of  $O_2(^1\Delta_g)$  can be produced in oxygen RF discharges with pressures on the order of 10 to 15 Torr if atomic oxygen is removed downstream using mercury oxide coating on the flow tube walls. Schmiedberger and others, 2001, reported a 32% yield of  $O_2(^1\Delta_g)$  at low pressure (0.43 Torr) using an RF discharge. Verdeyen, and others, 2002, obtained an  $O_2(^1\Delta_g)$  yield of 16% in a flowing RF discharge at a pressure of 2 Torr. Aleksandrov and others, 1984, have shown that  $O_2(^1\Delta_g)$  detaches negative ions formed in molecular oxygen discharges at a rate comparable to the attachment rate. Ivanov and others, 1999, have stated, “Detachment processes on  $O(^3P)$  atoms and  $O_2(^1\Delta_g)$  molecules strongly influence the discharge electrodynamics and determine the electric field in a wide range of pL parameters”. Models by Shibata and others, 1995, have shown that detachment by  $O_2(^1\Delta_g)$  can alter sheath dimensions in a moderate pressure, multi-temperature oxygen RF discharge. Franklin, 2001, has theoretically investigated the effects of dissociative attachment and detachment on a discharge and concluded for 1 Torr pressures that an  $O_2(X)$  discharge is dominated by these loss and gain mechanisms. This chapter provides an overview of the methodology used to calculate the losses and gains of all species types, the specific rates of various processes, and considerations of the chemistry models of  $O_2(X)$  and a  $N_2(X)$ - $O_2(X)$  gas mixture.

### **Electron Impact Reaction Modeling**

To determine the electron impact reaction rates for processes such as ionization, electron impact excitation, and dissociation, a Boltzmann transport equation solver developed by Bennett and based on the theory developed by Rockwood, 1973, and

Bennett, 1997, was used. Bennett's Boltzmann transport equation solver balances the Joule heating due to a homogenous electric field with the electron energy losses due to inelastic collisions. Bennett used a two term Lorentz approximation to separate the Boltzmann transport equation into the isotropic and anisotropic portions of the EEDF. The electron impact cross-sections required by the Boltzmann transport equation solver to calculate the EEDF were either obtained from experiments or theory depending on the type of background gas and inelastic collision.

Electron impact reaction rates as a function of E/N and pre-calculated by the Boltzmann transport equation solver, are imported into the plasma fluid model. For each E/N value, there is a corresponding electron mean energy. The electron thermal energy, calculated using equation 2.14, is equated to the electron mean energy using a linear interpolation scheme. By equating the thermal and mean energy according to the local field equilibrium approximation, the electron reaction rates are also determined at every grid point in the simulation. Using this approach the source terms, for both charged and neutral excited species, are determined for the continuity equations used in the PFM.

### **Excited Neutral Species Modeling**

The plasma chemical kinetic model determines the excited and neutral species densities by solving the time-dependent continuity equation combined with the time-independent momentum equation which includes diffusive and convective fluxes and results in the equation

$$\frac{dn}{dt} - D\nabla^2 n + \vec{\nabla} \cdot (n\vec{U}_{flow}) = S \quad (3.1)$$

The solution to equation 3.1 is determined using a Crank-Nicholson time integration technique combined with a Newton-Raphson technique for calculating the spatial portion of the differential equation and a SLOR technique is used to solve the resulting matrix. Equation 3.1 is solved for each neutral excited species density successively since their densities do not change greatly over the time step used (which is on the order of the RF cycle time). The source term in equation 3.1 is calculated using a set of chemical reactions for a particular gas type. The coefficients of the electron impact reactions are determined using the method described in the section *Electron Impact Reaction Modeling* on page 91. For general reactions between heavy neutral species, the reaction equations and rate coefficients are provided by a chemical kinetic data file using the reactions specified in appendices B and C. The reaction equations are automatically turned into a system of equations which constitute the source term for equation 3.1. The reaction rate coefficients used in the modeling of the heavy species reactions as a function of the background gas temperature are calculated using an Arrhenius form (Capitelli and others, 2000) for the reaction rate given by

$$k = A\left(\frac{T_g}{C}\right)^D \text{Exp}\left(\frac{T_g}{B}\right) \quad (3.2)$$

$T_g$  - Background gas temperature

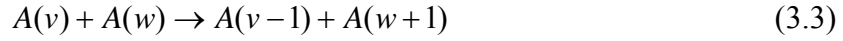
The coefficients A, B, C, and D are specified by the user in the chemical data file for a particular reaction type. If the rate coefficient is not exponentially dependent on temperature then setting the B coefficient to zero removes that dependence from the rate coefficient. The Arrhenius form of the reaction rate given by equation 3.2 is used to model detachment rates, electronic-electronic (E-E), electronic-vibrational (E-V), and

electronic-translational (E-T) energy exchanges between atoms and molecules (Gordiets and others, 1995). These energy exchange mechanisms are found to be significant mechanism for changing the density of the excited neutral species and hence the detachment rate of negative ions by the background gas.

For some molecular background gases, such as a  $N_2(X) - O_2(X)$  mixture, the population of vibrationally excited states maybe significant and an important source of detachment (Aleksandrov, 1984) and (Gordiets and others, 1995). Therefore, the chemical kinetic model also calculates the non-equilibrium vibrational state population through a system of rate equations that determine the population of a particular vibrational state. The transport of the vibrationally excited species is determined by solving equation 3.1 for the number density of each vibrationally excited state. The reaction rates for the direct electron excitation of a vibrational state of a molecule are determined using the Boltzmann solver described in the section *Electron Impact Reaction Modeling* on page 91. The excitation of molecular rotational states by electron impact is also included in the Boltzmann solver for the purposes of determining the electron energy losses, however, the population densities of rotationally excited molecules are not tracked for any gas type in this investigation. This is due to the rotational excited states not having a high enough energy or population density to play a significant role in exchanging energy with electronic (E-R) or vibrational (V-R) excited states and therefore these energy exchange mechanisms have been omitted from the plasma fluid model (Capitelli and others, 2000).

## Molecular Vibrational State Modeling

The vibrational-vibrational (V-V) energy exchange processes have the general reaction form:



The V-V rate coefficient for exchanging vibrational state energy between molecules has been estimated using experimental results and calculated using a trajectory method and the Schwartz-Slawsky-Herzfeld (SSH) theory (Gordiets and others, 1995) and (Capitelli and others, 2000). To determine the general rate coefficient of V-V exchange for arbitrary values of  $v$  and  $w$ , a scaling function based on SSH theory of vibrational relaxation times is introduced and has the general form for  $N_2(X)$  and  $O_2(X)$  of

$$k_{v,v-1}^{w,w+1} = k_{1,0}^{0,1} \frac{(v+1)}{(1-\chi_e v)} \frac{(w+1)}{(1-\chi_e w)} \exp(-\delta_{VV} |v-w|) \left[ \frac{3}{2} - \frac{\exp(-\delta_{VV} |v-w|)}{2} \right] \quad (3.4)$$

$$k_{1,0}^{0,1} = C \left( \frac{T_g}{300} \right)^\eta \quad (3.5)$$

$$\delta_{VV} \cong \frac{4\Delta E}{3E_{1,0}} \gamma_0 \equiv 0.427 \Delta E L \sqrt{\frac{\mu}{T_g}} \quad (3.6)$$

$\chi_e$  - Anharmonicity of the molecule

$\Delta E$  - The anharmonic transition energy in Kelvin

$$\gamma_v = 0.32 E_{v+1,v} L \sqrt{\frac{\mu}{T_g}}$$

$E_{v+1,v}$  - The energy of the vibrational transition  $v+1 \rightarrow v$  in Kelvin

$L$  - The characteristic parameter of the short-range repulsive potential

in Angströms such that  $U(r) \approx \exp(-r/L)$

where the energies of the vibrational states are found from the anharmonic Morse oscillator and are given by  $E_v \equiv \hbar\omega[(v + 0.5) - \chi_e(v + 0.5)^2]$  and  $\Delta E \equiv \hbar\omega(1 - 2\chi_e)$ .

The vibrational-translational (V-T) relaxation process for a vibrationally excited molecule is given by the general form



where

$M$  - Neutral collision partner in the background gas

The V-T relaxation rate coefficients for diatomic molecules found in a  $N_2(X)$ - $O_2(X)$  mixture are determined using empirical fits, based on SSH theory, to experimental results (Capitelli and others, 2000). The rate coefficient of the V-T relaxation of a vibrational state from  $v = 1 \rightarrow v = 0$  can be described by the following approximation

$$k_{1,0} = AT^n \exp\left\{-\frac{B}{T^{1/3}} + \frac{C}{T^m}\right\} \times \left[1 - D \exp\left\{-\frac{E_{1,0}}{T}\right\}\right]^{-1} \quad (3.8)$$

where

$E_{1,0}$  - Energy of the vibrational transition from  $v = 1 \rightarrow v = 0$

Values of the fitting parameters  $n$ ,  $m$ ,  $A$ ,  $B$ ,  $C$ , and  $D$  in equation 3.8 have been tabulated by Capitelli and others, 2000, for both  $N_2(X)$  and  $O_2(X)$ . To accurately model the vibrational population requires that the V-T relaxation from vibrational state  $v + 1 \rightarrow v$  is calculated for all vibrational states. The V-T rate coefficient for the relaxation of vibrationally excited molecules by two or more vibrational levels is optically unallowed (Bernath, 1995) and as a result is insignificant and can be ignored



(Capitelli and others, 2000). The V-T rate coefficients can be calculated using SSH theory and approximations from the anharmonic Morse oscillator model to obtain  $\Delta E$  and  $E_{v+1,v}$ , similar to V-V exchange, resulting in the following expression for the scaling function for the quenching of state  $1 \rightarrow 0$  rate coefficient given by

$$k_{v+1,v} = k_{1,0} \frac{(v+1)(1-\chi_e)}{1-(v+1)\chi_e} \exp(\delta_{VT}v) \quad (3.9)$$

where for  $\gamma_v < 20$

$$\delta_{VT} \cong \frac{4\Delta E}{3E_{1,0}} \gamma_0 \equiv 0.427 \Delta EL \sqrt{\frac{\mu}{T_g}} \quad (3.10)$$

and for  $\gamma_v > 20$

$$\delta_{VT} \cong \frac{4\Delta E}{E_{1,0}} \gamma_0^{2/3} \equiv \frac{1.87 \Delta EL^{2/3} \mu^{1/3}}{E_{1,0}^{1/3} T_g^{1/3}} \quad (3.11)$$

$$\gamma_v = 0.32 E_{v+1,v} L \sqrt{\frac{\mu}{T_g}} \quad (3.12)$$

The rate coefficient  $k_{v+1,v}$  increases with  $v$  and for higher vibrational levels, its value is highly dependent on  $\delta_{VT}$ , therefore, care should be taken in selecting the  $L$  parameter as well as insuring that the background gas temperature is not below 300K. The magnitude of  $k_{v+1,v}$  also should not exceed the electron energy loss coefficient,  $k_L(\varepsilon)$ , or the assumptions made with SSH theory which are used in developing this model do not hold and the V-T rate coefficient given by Equation 3.9 for higher vibrational states is inaccurate (Capitelli and others, 2000). Due to the limitation of SSH theory, this model should be used with caution for transitions involving high-lying vibrational levels

( $v > 15$ ) regardless of the value of  $\delta_{VT}$  (Cacciatore and Billing, 1992). As a result of this known limitation, only the densities of the vibrational states for  $v \leq 15$  were tracked in the Plasma Fluid Model for a nitrogen gas. In order to ensure the validity of the vibrational model, a Boltzmann vibrational distribution must be obtained for the higher vibrational states in both stationary and flowing conditions.

### **Losses of Neutral Excited Species to the Wall**

To obtain boundary conditions for Equation 3.1 on the wall ( $x = X_0$ ), consider a wall layer,  $\lambda_{wall} < \lambda_\alpha$ , with thickness approximately equal to  $\lambda_\alpha$ , which is the mean free path of the species (Capitelli and others, 2000). Since collisions do not occur within  $\lambda_{wall}$ , under stationary conditions the following expression is obtained for the neutral species flux to and from the wall

$$\Gamma_- = (1 - \kappa)\Gamma_+ \quad (3.13)$$

where

$\Gamma_-$  - Species flux away from the wall

$\Gamma_+$  - Species flux toward the wall

$\kappa$  - Wall deactivation or recombination coefficient.

From diffusion theory of species in a Boltzmann distribution scattering isotropically in collisions with the background gas and off of the wall (Stoffels and others, 1995), the expression for the flux away and toward the wall is given by

$$\Gamma_- = \frac{Nv_{th}}{4} \Big|_{x=X_0} - \frac{1}{2}D \frac{\partial N}{\partial x} \Big|_{x=X_0} \quad (3.14)$$

$$\Gamma_+ = \frac{Nv_{th}}{4} \Big|_{x=X_0} + \frac{1}{2} D \frac{\partial N}{\partial x} \Big|_{x=X_0} \quad (3.15)$$

Substituting equations 3.14 and 3.15 and the definition of the approximate diffusion coefficient,  $D = v_{th} \lambda_{mfp} / 3$ , into equation 3.13 results in the following boundary condition for a neutral species given by

$$D \frac{\partial N}{\partial x} \Big|_{x=X_0} = \frac{2\kappa}{2 - \kappa} \frac{Nv_{th}}{4} \Big|_{x=X_0} . \quad (3.16)$$

Using equation 3.16, allows the plasma fluid model to determine the excited species deactivation or recombination rate at the wall depending on the incident species.

For this study, three background gases were modeled:  $Ar$ ,  $O_2(X)$ , and  $N_2(X)$  -  $O_2(X)$  gas mixture. The background gases were modeled in order of complexity to provide insight into RF discharges with and without a flow for electropositive, electronegative, and electronegative gases with complex chemistry. The following sections provide an overview of the specific species, rate coefficients, and assumptions used to model each of the background gases used in this study.

## Background Gas Chemical Kinetic Models

### Oxygen Chemical Kinetic Model

Pinhero and others, 1998, have shown that the excited and dissociated species present in an oxygen discharge are important in calculating the plasma density and electrode sheath length. As a result the oxygen plasma chemical kinetic model tracks the local densities of  $O_2(X)$  and its excited species  $O_2(^1\Delta_g)$  or  $O_2(a)$ ,  $O_2(^1\Sigma_g)$  or

$O_2(b)$  and also densities of ground state atomic oxygen  $O(^3P)$  and its first excited state  $O(^1D)$  as well as ozone  $O_3$ . The excited states of  $O(^1S)$ ,  $O(3s^5S^0)$ ,  $O(3s^3S^0)$ ,  $O(3p^5P)$ ,  $O(3p^3P)$  atomic oxygen do not exist in high densities due to either rapid collisional de-excitation and/or a high radiative decay rate and therefore their densities are not tracked in the plasma model, but their cross-sections are included in the Boltzmann solver to determine the EEDF. The oxygen chemical kinetic model of electron interactions includes the electron rates for the direct excitation of excited states of molecular and atomic oxygen as well as the super-elastic quenching of those excited states combined with the dissociation of molecular oxygen which are calculated by a self-consistent solution to the Boltzmann equation. The cross-sections for the electron excitation and dissociation of ground state molecular oxygen were measured in several different experiments, the results of which were compiled by Phelps, 1985. A listing of all electron impact and heavy species processes are included in appendix B.

For certain discharge conditions a significant percentage of  $O_2(a)$  and  $O(^3P)$  (typically ~10% to 20% for discharges specifically used to generate  $O_2(a)$  and 5% for  $O(^3P)$ ) is generated, therefore the direct ionization, attachment, dissociation and excitation of  $O_2(a)$  and  $O(^3P)$  by electron impact must also be calculated to obtain the correct densities of the excited states. Another consideration is also the effect on the EEDF of electron collisions with  $O_2(a)$  and  $O(^3P)$ . Results of Bennett's Boltzmann equation solver indicated that large percentages of  $O_2(a)$  had minimal effect on the EEDF, while the same is not true for  $O(^3P)$ . The influence  $O(^3P)$  has on the EEDF is

due to large inelastic excitation cross-sections with the largest cross-section being the excitation of  $O(^1D)$  whose excitation threshold is 1.96 eV.

Once the percentages of  $O_2(a)$  and  $O(^3P)$  are approximately known they are used in the Boltzmann solver to determine the modified EEDF and rates for electron impact reactions. Cross-sections for the electron excitation of atomic oxygen were obtained from Laher and Gilmore, 1990, who reported numerical fits to measured cross-section data. For  $O_2(a)$ , a cross-section for the excitation of  $O_2(a) \rightarrow O_2(b)$  was measured by Hall and Trajmar, 1975, at 4.5 eV and the form of the cross-section over a range of electron energies was suggested by Fournier, 1984. Also the cross-section of the disassociative attachment of  $O_2(a)$  was measured by Burrow, 1973. Both of these cross-sections were used in this study to calculate the excitation and disassociative attachment rate of  $O_2(a)$ . However, few other experimental measurements for the excitation and dissociation of  $O_2(a)$  exist, therefore the cross-sections of  $O_2(a)$  were approximated to be the same as cross-sections for  $O_2(X)$  except that the electron energy required of a certain cross-section value was reduced by the excitation threshold energy of  $O_2(a)$  such that

$$\sigma_{O_2(a)}(\varepsilon - \varepsilon_{th}) = \sigma_{O_2(X)}(\varepsilon) \quad (3.17)$$

where

$$\varepsilon_{th} = 0.97 \text{ eV} - \text{Excitation threshold energy of } O_2(a)$$

This approximation is reasonable because the potential energy well binding the two  $O$  atoms in the  $O_2(X)$  and  $O_2(a)$  states are very close in shape with the only difference

being due mainly to the offset of the threshold energy of  $O_2(a)$  (Graves, 1992). The minimum energy level of the potential well also occurs at nearly the same equilibrium bond radius, so any transitions from  $O_2(a)$  to any other state via electron impact would represent the same change in momentum as a transition from the  $O_2(X)$  state. Also in studying the cross-section of dissociative attachment of  $O_2(X)$  and  $O_2(a)$ , Burrows, 1973, found their cross-sections to be very similar. It was also shown by Burrows, 1973, that the electron impact cross-sections of  $O_2(X)$  and  $O_2(a)$  are similar for exciting electronic states and dissociation of molecular oxygen.

To model attachment of electrons in low energy regions of the plasma (outside the discharge region), three body attachment was included in the set of rate equations for electron interactions. A median rate coefficient was taken from the swarm experiments of McCorkle and used for electrons with mean energies less than 1 eV (Christophorou, 1984). For electron mean energies greater than 1 eV, the rate coefficient was set to zero reflecting the extremely low rate of the three-body attachment at higher electron energies.

Due to the fast V-T relaxation of the vibrational states of oxygen due to collisions with  $O(^3P)$ , the vibrational temperature of molecular oxygen is approximately the same as the thermal temperature of the molecular and atomic oxygen in a discharge. Therefore, the density of the excited vibrational states can be estimated using detail balance. Results of the detailed balance calculation indicate that the density of vibrationally excited oxygen is fairly low (for RF discharges that do not heat the background gas significantly). As a result the densities of vibrationally excited molecular oxygen are not tracked in the oxygen chemical kinetic model, however, the energy lost by

electrons due to impact excitation of vibrational states of  $O_2(X)$  is used in the calculation of the EEDF.

### Nitrogen and Oxygen Chemical Kinetic Model

The  $N_2(X) - O_2(X)$  chemical kinetic model includes all the chemical reactions and species of the oxygen model as well as excited species of  $N_2(X)$  and ground state atomic nitrogen,  $N(^4S)$ , that exist in high densities in an RF discharge. It has been shown by Aleksandrov, 1984, that the electronic and vibrationally excited and dissociated species present in a  $N_2(X) - O_2(X)$  gas mixture discharge are important in calculating the detachment of  $O^-$ . As a result the  $N_2(X) - O_2(X)$  plasma chemical kinetic model tracks the densities of the same species as the oxygen chemical kinetic model with the addition of  $O(^1S)$ ,  $NO(X)$ , excited states of molecular nitrogen  $N_2(X, v = 1 - 15)$ ,  $N_2(^1\Sigma_u^-)$  or  $N_2(a^1)$ ,  $N_2(B^3\Pi_g)$  or  $N_2(B)$ ,  $N_2(C^3\Pi_u)$  or  $N_2(C)$ ,  $N_2(A^3\Sigma_u^+)$  or  $N_2(A)$ ,  $N_2(a''^1\Sigma_g^+)$  or  $N_2(a'')$  and ground state atomic nitrogen  $N(^2P)$  and its excited states  $N(^2D)$  and  $N(^4S)$ . Electron impact cross-sections for other excited states of  $N_2(X)$ ,  $O_2(X)$  and  $O(^3P)$  which include:  $N_2(W^1\Delta_u)$  or  $N_2(W^1)$ ,  $N_2(W^3\Delta_u)$  or  $N_2(W^3)$ ,  $N_2(B'^3\Sigma_u^-)$  or  $N_2(B')$ ,  $N_2(A')$  or  $N_2(A'^5\Sigma_g^+)$ ,  $N_2(E'^3\Sigma_g^+)$  or  $N_2(E^3)$ ,  $N_2(a'^1\Sigma_u^-)$  or  $N_2(a')$ ,  $N_2(a'^1\Pi_g)$  or  $N_2(a)$ ,  $N_2(w^1\Delta_u)$  or  $N_2(w^1)$ ,  $O_2(A^3)$ ,  $O_2(C^3)$ ,  $O_2(A)$ ,  $O_2(C)$ ,  $O_2(c)$ ,  $O(5p^3P^0)$ ,  $O(3p^3P^0)$ ,  $O(3s^3S^0)$ ,  $O(5s^3S^0)$  have been included in the Boltzmann solver to determine the EEDF, however, these states are short lived either due to auto-dissociation, radiative decay, or quenching by inelastic collisions. The

states  $O_2(A)$ ,  $O_2(C)$ , and  $O_2(c)$  all auto-dissociate to  $O(^3P)$ , the states  $N_2(W)$  and  $N_2(B')$  quickly decay to  $N_2(B)$  and  $N_2(w)$  decays to  $N_2(a')$  (Gordiets and others, 1995). The  $N_2(X)-O_2(X)$  gas mixture model of electron interactions includes the electron rates for the direct excitation of  $O_2(X)$ ,  $O_2(a)$ ,  $O(^3P)$ ,  $N_2(X)$ ,  $N_2(X,v)$ , and  $Ar$  as well as the super elastic quenching of those excited states combined with the dissociation of molecular oxygen and nitrogen which are calculated by a self-consistent solution to the Boltzmann equation. A listing of all the electron impact processes in the model is included in appendix C.

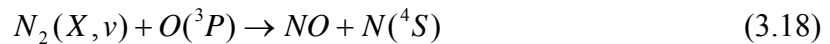
A highly detailed chemical kinetic model of the heavy species reactions occurring in a  $N_2(X)-O_2(X)$  discharge was developed by Nahorny and others, 1993, which included over 400 heavy species chemical kinetic processes. Many of those processes were shown by Gordiets and others, 1995, to be insignificant in producing species important to the plasma discharge and hence a subset of the most important chemical reactions was produced. The heavy species processes in the  $N_2(X)-O_2(X)$  model are mostly based on the subset of processes used by Gordiets and others, 1995. A listing of all the heavy species processes in the  $N_2(X)-O_2(X)$  model are included in appendix C.

The vibrational states of  $N_2(X)$  are included in the model because the vibrational states  $N_2(X, v \geq 6)$  detach  $O^-$  and  $O_2^-$  (Aleksandrov, 1978), exchange energy with electronic states of  $N_2(X)$ , and are dissociated due to electron impact at a much greater rate than  $N_2(X)$  (Capitelli and others, 2000). Due to the Vibrational-Electronic (V-E) energy exchanges, which excite vibrational states to higher vibrational states,  $N_2(X)$  has



been found to have vibrational temperatures much larger than the translational temperature of  $N_2(X)$  which is consistent with the results of Gordiets and others, 1995, Guerra and others, 1998, and Capitelli and others, 2000. To calculate the vibrational population densities, the processes of electron-vibrational (e-V), V-V, V-T, and V-E energy exchange, as well as, single vibrational energy exchange in collisions with the wall have been included and are listed in appendix C (Gordiets and others, 1995). Due to the high density of vibrationally excited nitrogen, both inelastic and superelastic collisions of electrons with  $N_2(X, \nu > 0)$  have been included in the Boltzmann equation solver. Vibrationally excited  $O_2(X)$  and  $NO(X)$  are also included in the model, but only for vibrational levels  $\nu = 0$  and  $\nu = 1$ . The first vibrational levels of  $O_2(X)$  and  $NO(X)$  are included in the model due to resonant reactions with  $N_2(X, \nu = 28, 27)$  and the  $N_2(X, \nu = 15, 14)$ , respectively due to the change in the energy between the corresponding states being roughly the same. Higher vibrational levels of  $O_2(X)$  and  $NO(X)$  are not included in the model because they are efficiently relaxed in V-T energy exchanges with  $O(^3P)$  atoms. Rate coefficients for V-V and V-T energy exchange processes with  $N_2(X, \nu \leq 15)$ ,  $O_2(X, \nu \leq 1)$ ,  $NO(X, \nu \leq 1)$ ,  $O(^3P)$ , and  $N(^2P)$  were calculated using equations 3.5, 3.6, and 3.9 with parameters provided in appendix C, Table 2 (Gordiets and others, 1995).

Other notable reactions involving vibrationally excited nitrogen in a  $N_2 - O_2$  mix include the reaction



which has been cited by several authors as the most important reaction affecting the upper levels of vibrationally excited nitrogen and is also crucial in the formation of  $NO$  and  $N(^4S)$  (Gordiets and others, 1995). The rate coefficient of process 3.18 is given by

$$k(\nu) = k_0 \exp\left[-\frac{E_a}{T} + \frac{\beta E_\nu}{T}\right] \quad (3.19)$$

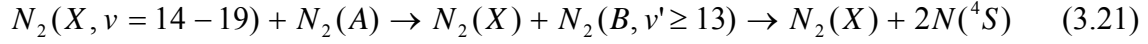
where  $E_a$  is the activation energy and has a value of  $38,000K$ .  $E_\nu$  is the vibrational energy of  $N_2(X, \nu)$ , which is commonly approximated by the energy of the anharmonic Morse oscillator which is given by

$$E_\nu = \hbar\omega[(\nu + 1/2) - \chi_e(\nu + 1/2)^2] \quad (3.20)$$

The parameter  $\beta$  is a multiplier associated with a decrease in the activation energy of the reaction due to the anharmonicity of higher vibrational energies of  $N_2(X, \nu)$ . Due to the large activation energy of reaction 3.18, the reaction rate is insignificant except with higher vibrational values.

Atomic nitrogen is also a major detacher of  $O^-$  and  $O_2^-$  negative ions as well as a major quencher of vibrationally excited nitrogen, therefore dissociation of molecular nitrogen was modeled in detail. Included in the model are the dissociation of  $N_2(X)$  and  $N_2(X, \nu)$  by electron impact as well as dissociation by the reaction of excited species of nitrogen. A study by Cacciatore and others, 1982, showed that the dissociation cross-section of  $N_2(X, \nu = 5)$  is two hundred times greater than the dissociation cross-section of ground state nitrogen. The dramatic increase in dissociation cross-section of vibrationally excited nitrogen combined with a lower threshold energy of dissociation result in a large contribution of electron dissociation of vibrationally excited nitrogen to

the overall dissociation rate of nitrogen. An additional reaction involving vibrationally excited nitrogen that significantly contributes to dissociation is



where a reaction rate of  $2 \times 10^{-11} \text{ cm}^3/\text{s}$  is reported as a reasonable value, but the true value of the rate coefficient is not known to a high level of accuracy (Guerra and others, 2003). These dissociation reactions, equation 3.18 and 3.21, of vibrationally excited  $N_2(X)$  were added to Gordiets and others, 1995, chemical kinetic model due to ground state dissociation of  $N_2(X)$  not being able to account for the higher measured densities of  $N(^4S)$  (Guerra and others, 2003). A complete listing of the reactions included in the  $N_2(X) - O_2(X)$  chemical kinetic model is presented in appendix C.

Using the presented chemical kinetic model, coupled with the RF discharge plasma fluid model enables a detailed study of the effect of flow on both the RF discharge structure and the charged and neutral species production rates. The loss of neutral excited species out of the discharge region is shown to have a large impact on the spatial structure of the discharge by increasing the electronegativity of the discharge. Also the neutral excited species play an important role in maintaining an electron density downstream of the RF discharge through detachment of the negative ions.

#### IV. RF Discharge in a Fast Flowing Electronegative Gas

To provide an estimate of the density of charged and excited neutral species produced by an RF discharge in a fast flowing background gas, the PFM and the chemical kinetic model developed in Chapters II and III are used.  $O_2(X)$  and  $N_2(X)$  and  $O_2(X)$  mixture RF discharges are modeled in both one and two dimensions at a pressure of 1 Torr. As a preliminary step, the results of a one dimensional  $Ar$  RF discharge model are examined to first establish the validity of the PFM through comparisons with a verified model and later to contrast those results with a RF discharge in an electronegative background gas under stationary and flowing conditions. To provide additional verification of the model results in two dimensions, the PFM was compared to the results of Salabas and others, 2002, who modeled the standard Gaseous Electronic Conference (GEC) reactor using a two dimensional solution method for the fluid equations. Next, we examine an  $O_2(X)$  RF discharge neglecting negative ions and neutral excited species to examine the effect of a molecular versus a noble gas on the RF discharge structure. We then examine an  $O_2(X)$  RF discharge with and neglecting negative ions and neutral excited species to determine the effect of negative ions and neutral excited species on the discharge sheath structure and the production of charged species. The  $O_2(X)$  RF discharge is then examined in a variety of flow conditions to determine neutral and charged species densities and production rates in a flowing background gas for the purpose of supplying charge to a non-self sustaining discharge

downstream. A mixture of  $N_2(X)$  and  $O_2(X)$  is then used as the background gas of an RF discharge to investigate the generation of charged and neutral species, such as  $N(^4S)$ ,  $N_2(A)$ ,  $O(^3P)$ ,  $O_2(b)$ , at different flow velocities for plasma material processing purposes. In the one dimensional  $N_2(X)$  and  $O_2(X)$  RF discharge model, the change in the plasma and neutral densities in the discharge region due to changing flow velocity are examined. Finally, a two dimensional fluid model is employed to examine the decay of the plasma density and excited neutral species downstream of the RF discharge. Results of the simulations indicate that a RF discharge in a fast flowing electronegative gas produces high positive and negative ion densities which decay slowly downstream. A reasonably high density of electrons can also be realized in a flowing  $O_2(X)$  or  $N_2(X) - O_2(X)$  background gas due to the detachment caused by neutral excited species downstream of the RF discharge. In addition, from the one and two dimensional RF discharge model results, the plasma densities used in the Langmuir probe model are also established.

### **RF Discharge Model Set-Up**

The two dimensional geometry of the flow tube, from a top down view, is shown in Figure 4.1. The one dimensional model represents the cross section of the flow tube through an electrode in the x direction. In the simulations described in this chapter both electrodes are driven and the background gas flow is parallel to the electrode surface.

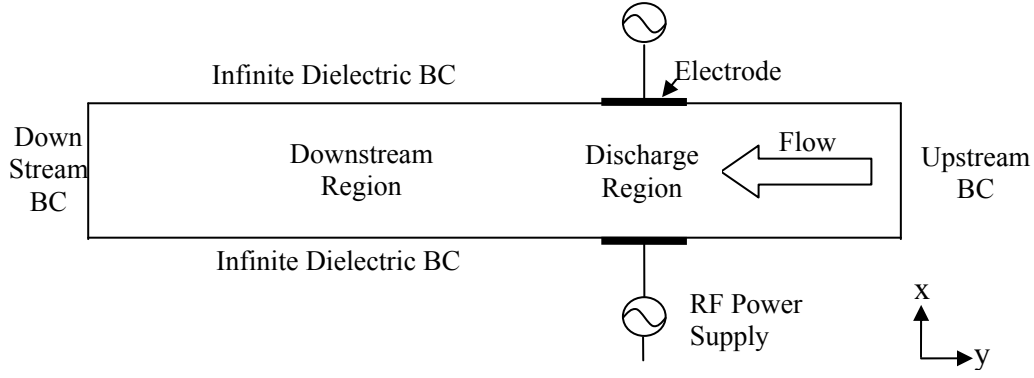


**Figure 4.1 Top Down View of Flow Tube**

The electrodes in the simulation are uncoated conductors with an applied voltage on both electrodes given by

$$V(t) = \frac{V_{rf}}{2} \sin(2\pi ft + \phi) \quad (4.1)$$

where

$V_{rf}$  - Total applied RF voltage

$f$  - Voltage frequency

$\phi$  - Phase shift

For simulation results presented in this chapter, the voltage oscillates at  $f = 13.56$  MHz and there is a phase shift in the voltage of 180 degrees between the electrodes.

The gas flow results in the removal of species generated in the active volume of the RF discharge. In the one dimensional model, the flow losses are estimated using the equation

$$\nu_{flow} = \frac{U_{flow}}{\delta} \quad (4.2)$$

where

$\nu_{flow}$  - Flow loss frequency

$\delta$  - Length of species excitation region

$U_{flow}$  - Flow velocity

which follows the approach taken by Raizer, 1991. In addition, the assumption is made that the boundary layer near the walls of the tube is small due to the low pressures and high flow velocities of the background gas as discussed in Chapter I. As a result the boundary layer has little effect on the plasma generated by the RF discharge and therefore the flow velocity across the electrode gap is made constant to reduce the complexity of the modeling. Also due to the high flow velocities in the flow tube, the small discharge region, and moderate power levels, the heating of the background gas by the RF discharge has been found to be low in other studies at similar pressures and flow velocities (Zimmerman and others, 2003). As a result, heating of the background gas has been ignored in this study.

The one dimensional electropositive *Ar* discharge was modeled using 50 evenly spaced grid points and the simulation achieves cyclic convergence in 250 RF cycles with a wall clock time of 8 minutes. The cyclic convergence criterion for both one and two dimensions is obtained by comparing the ion density at the same point in two consecutive RF cycles such that

$$Max\left(\frac{|n_i^k - n_i^{k-1}|}{n_i^{k-1}}\right) < 10^{-7} \quad (4.3)$$

The exact number of RF cycles required to achieve convergence was highly dependent on the closeness of the initial starting density to the final converged density of the RF

discharge. Using the acceleration techniques described in Chapter II, the total convergence time for a one or two dimensional simulation could be reduced by a factor of 4 or higher. The electronegative RF discharge models without chemical kinetics took longer to converge (nearly a 1000 RF cycles) due to the sheath profiles used for the initial conditions being significantly different from the converged sheath profiles. For an electronegative RF discharge, the simulation tended to reform the sheaths regardless of how well the initial condition densities matched the converged solution densities. As a result little time savings was realized by using closer approximations to the final converged density of the RF discharge. The electronegative RF discharge models with chemical kinetics took substantially longer to converge due to the neutral excited species densities evolving on a much slower time scale than the charged species densities.

### **RF Discharge Model Comparisons**

In this section, we compare the results of a one dimensional *Ar* RF discharge modeled in the PFM to the model results of RF-Siglo and Lymberopoulos and Economou, 1992. RF-SIGLO and Lymberopoulos and Economou's model have been verified with experimental results. Results of RF-SIGLO and PFM agreed to within a relative error at all points of 0.01% or less in the time averaged electron and ion densities. This exceptional agreement was primarily due to the modeling method used in PFM being based on the RF-SIGLO numerical modeling method and a consistent set of reaction rate coefficients. In light of this agreement, the results of the two models are presented as single data sets.



### **One Dimensional Electropositive Discharge Comparison**

*Ar* is one of the simplest and best studied gases due to its chemically inert and electropositive nature. *Ar* is commonly used in many plasma processing applications as a buffer gas due to its well known properties and behavior. The *Ar* RF discharge simulation for this investigation is performed in a Cartesian geometry with the electrodes being separated by 3 cm. The effect of secondary electron emission from the electrodes is neglected. The background gas is maintained at 1 Torr and any heating of the gas due to collisional coupling with the plasma is also neglected.

During an RF cycle, the electrons are pushed to and from the electrode surface due to the potential difference between the electrode and the bulk plasma. The “pushing” of the electrons results in the cooling and heating of the electrons as they are incident upon or exit the sheath region, respectively. The primary source of electron and ion production in the *Ar* discharge in the alpha mode is from direct impact ionization and the primary loss mechanisms are due to current losses to the electrodes and ambipolar diffusion transverse to the discharge direction (Paranjpe, 1992). Simulation results, shown in Figure 4.2, indicate that the majority of ionization occurs at the sheath/pre-sheath region of the time dependent active sheaths. Peaks in the ionization profile result as the sheath electric fields gradually build from a near zero value (highest density of electrons) and push the electrons out of the sheath region (Boeuf, 1987). This small portion of the RF cycle (approximately 1/6 of the cycle) produces the majority of the ionization due to a sufficient number of electrons being available along with a substantial electric field. The combination of these two conditions results in a maximum Joule heating of the electrons and ionization rate near the sheath edge as shown in Figure 4.2d.

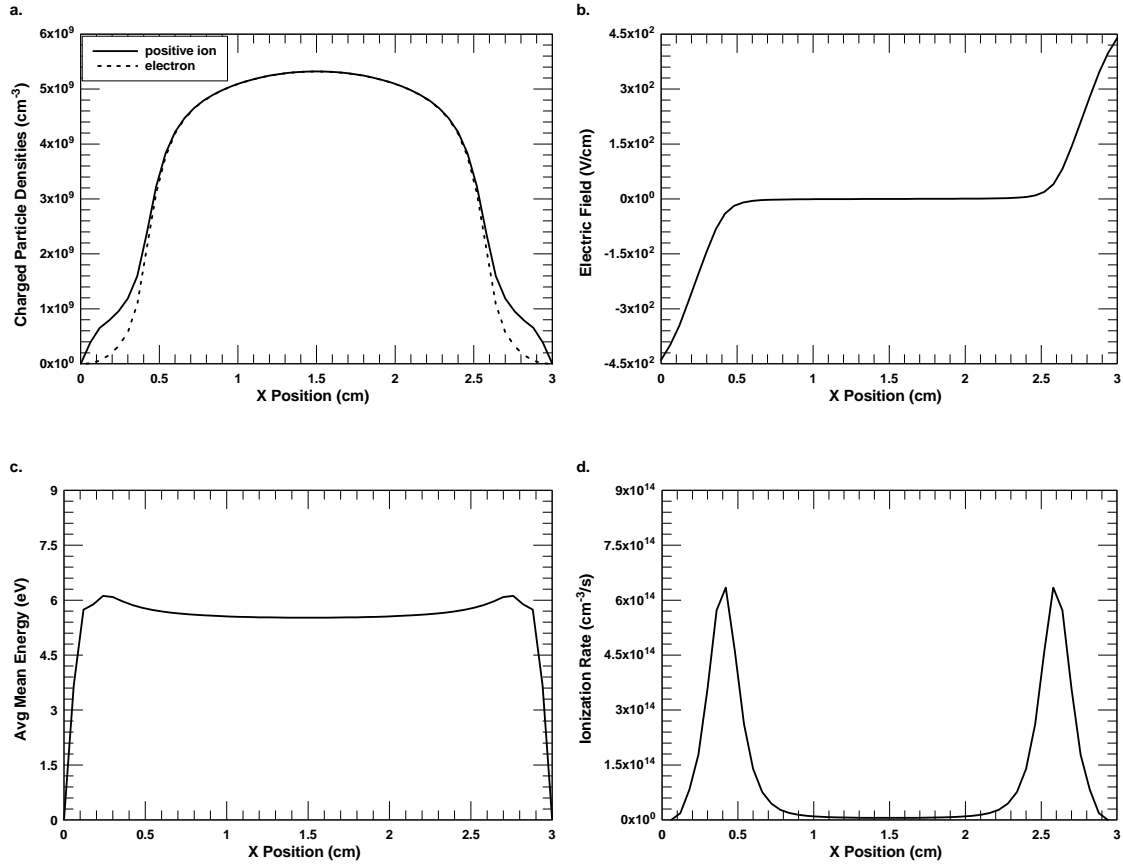


**Figure 4.2 Ar RF Discharge with 200V Applied Voltage Time Averaged (a) Electron and Ion Density (b) Electric Field (c) Electron Mean Energy and (d) Ionization Rate for a 3 cm Separation Between Electrodes, 1 Torr Pressure, and Asymmetrically Driven Electrodes**

The peak plasma density,  $n_i = 5.3 \times 10^9 \text{ cm}^{-3}$ , of the Ar RF discharge was within 10.4% of the peak density,  $n_i = 4.8 \times 10^9 \text{ cm}^{-3}$ , obtained by the model developed by Lymberopoulos and Economou, 1992. Both discharges were modeled under the same conditions of frequency, voltage, and pressure and a discharge length of 2.54 cm (Referring to Lymberopoulos and Economou's results without the inclusion of meta-stable Ar atomic states). The amplitude of the total current density determined by the PFM for the Ar RF discharge is  $2.3 \text{ mA/cm}^2$  (shown in Figure 4.3), which was identical to the results of RF-Siglo and within 12% of the results of Lymberopoulos and

Economou at  $2.07 \text{ mA/cm}^2$ . In addition, the electron mean energy values,  $5.92 \text{ eV}$ , and profiles calculated by the PFM are within 2% of the mean energies reported by Lymberopoulos and Economou, 1992.

The time dependent electric fields and current densities for the *Ar* RF discharge are shown in Figure 4.3. In Figure 4.3a, the time dependent electric fields vary symmetrically over an RF cycle, achieving a maximum value at one electrode, while simultaneously having a minimum value at the other electrode. The time dependent electric field also varies primarily near the electrodes with only a small electric field present in the bulk plasma. This result is consistent with the observations of Raizer, who noted that small electric fields in the bulk plasma region is a characteristic of an RF discharge in an electropositive noble gas such as *Ar* (Raizer, 1994). Since, the RF discharge is essentially a complex resistor in a circuit, current continuity must be maintained through out the discharge. The majority of the current density in the bulk plasma region is due the drift and diffusion of electrons. In the sheath region, however, the dominant current is displacement current for most of the RF cycle. The ion current to the electrodes counts for a very small portion of the current at anyone time during the cycle as shown in Figure 4.3b. However, the ion current is always directed towards the electrodes in accordance with the average electric field in the sheath. The electrons have a much larger current due to their much higher mobility, however, they are repelled by the sheath electric fields for the majority of the RF cycle. As a result, the electron current to the electrodes occurs mostly in pulses when the time dependent electric field has a minimum value near the electrodes. The resulting cycle averaged current densities, however, are the same for both electrons and ions.

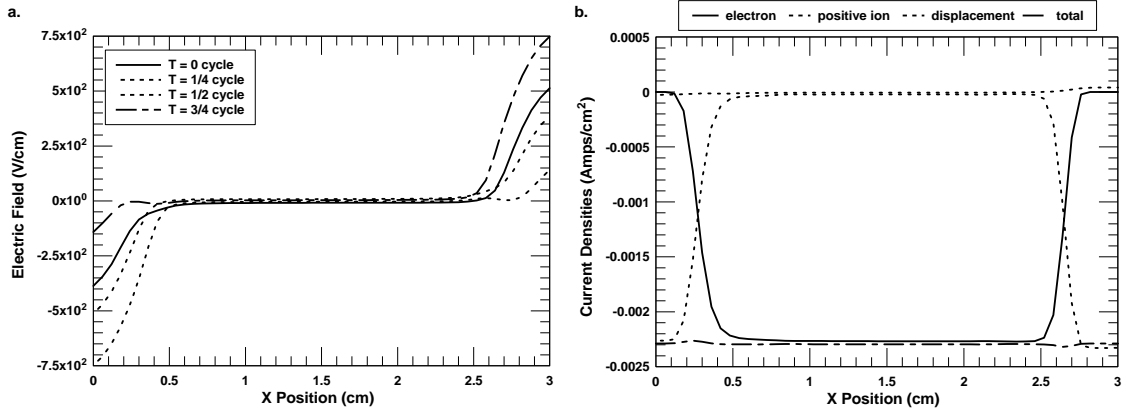


**Figure 4.3 Ar RF Discharge with 200V Applied Voltage Time Dependent (a) Electric Field (b) Current Density at 3 cm Separation of Electrodes, 1 Torr, and Asymmetrically Driven**

These results for the *Ar* discharge were presented mainly to validate the accuracy of the plasma transport model and provide a basis for comparing the *Ar* electropositive discharge with an electronegative discharge in a complex molecular gas. The differences in the discharge sheath structure of an electropositive noble and molecular gas, which has a faster electron energy relaxation rate, are very relevant in determining the effect of flow on the discharge structure. The differences in the RF discharge structure of noble and molecular gas RF discharges will be examined in greater detail in the *One Dimension  $O_2(X)$  RF Discharge Results* section. In the next section, we compare the results of the PFM against the standardized Gaseous Electronics Conference (GEC) reactor. The plasma densities produced by the GEC reactor have been exhaustively investigated making it an excellent experimental set-up to compare RF discharge simulations against.

## Two Dimensional Helium GEC RF Discharge Comparison

To provide additional verification that the results of the PFM are valid, the model was compared to the results of Salabas and others, 2002. Their simulation is based on a different solution method for the fluid equations. The model results of Salabas were shown to compare well to the measured values of peak plasma density and average mean energy obtained from of the *He* GEC discharge. The GEC RF discharge is composed of both a driven and grounded electrode configuration with a maximum RF amplitude of 217 Volts. Secondary electron emission from the electrodes is neglected and a blocking capacitor is placed in series with the driven electrode resulting in a DC bias of -61.8 Volts. The background gas for the simulation is *He* and is held at a constant pressure of 1 Torr through out the simulation region. The simulation geometry of the GEC reactor is shown in Figure 4.4

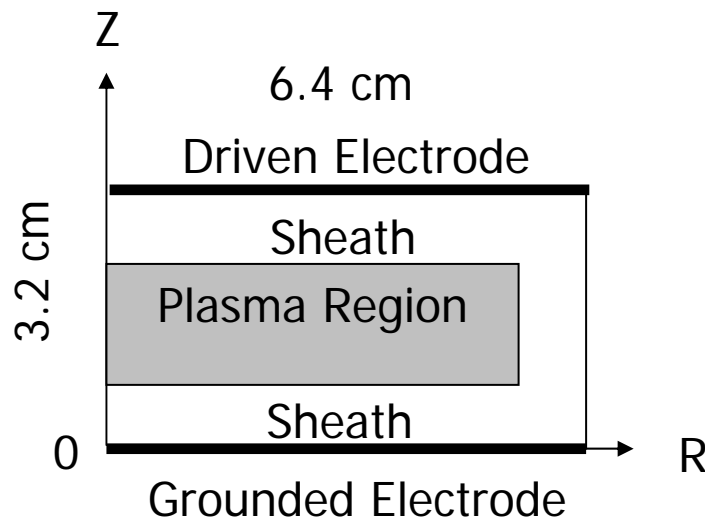
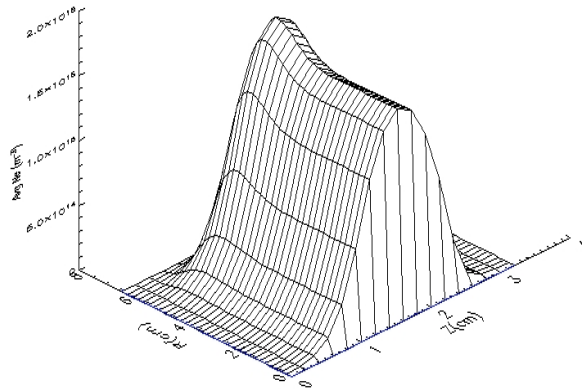


Figure 4.4 *He* GEC Reactor RF Discharge Geometry

The *He* GEC reactor is modeled in a cylindrical  $r, z$  coordinate system assuming that the discharge is symmetric about the  $z$ -axis. The simulation is performed using a 32 by 16 node grid with a 100 simulation time steps used to resolve each RF cycle (which matches the fidelity used by Salabas in simulating the GEC reactor). The simulation was run until the relative change in the ion density from RF cycle to RF cycle was less than  $10^{-7}$ . The results of Salabas' simulation were compared to results of the PFM. The results of the two simulations compared favorably in peak density and mean electron energy with largest difference being in the peak mean electron energy of the simulations. Peak electron and ion densities of the two simulations were both  $2.0 \times 10^9 \text{ cm}^{-3}$  and the fall off in density of electrons in the sheath region, shown in Figure 4.5, was similar though only a side-by-side comparison was possible. The electron density profile is asymmetric and is displaced away from the electrode at  $z = 3 \text{ cm}$  due to the bias voltage of  $-61.8 \text{ V}$  introduced at the electrode using a blocking capacitor.



**Figure 4.5 Electron Density Profile in a 1 Torr He RF Discharge at 217 V in a GEC Reactor Geometry**

The cycle averaged electron energy and potential difference profiles, Figures 4.6 and 4.7, were within 10% in value through the discharge region as well. However, a more pronounced spike in the average energy profile was observed in the results of Salabas and others, 2002, at the corner of the driven electrode and the outer wall of the reactor chamber shown in Figure 4.6. This spike in the cycle averaged electron energy produces the peak that is observed in the electron density shown in Figure 4.5. The less pronounced spike observed in the PFM output may result from the different collision cross-sections used in the two models. The different cross-sections used in Salabas' fluid model versus the PFM, would produce a lower electron energy relaxation rate at higher electric fields resulting in a higher peak in the electron energies. The peak average

electron energies of 15 eV and 23 eV were observed for the PFM and Salabas' fluid model respectively.

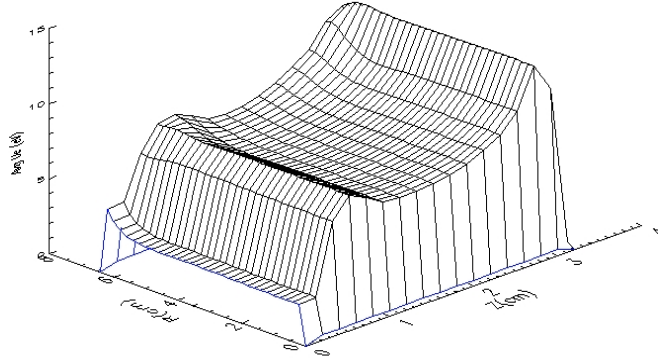


**Figure 4.6 Cycle Averaged Electron Energy Profile in a 1 Torr *He* RF Discharge at 217V in a GEC Reactor Geometry**

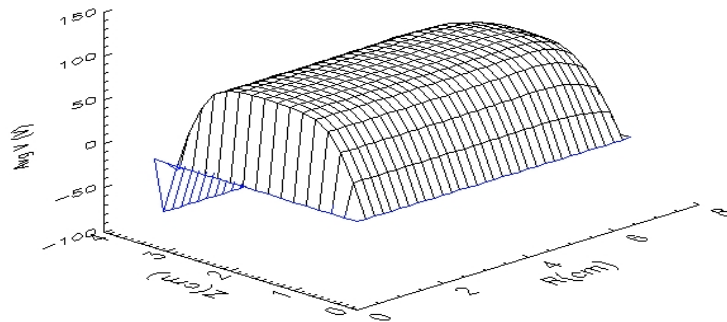


**Figure 4.7 Cycle Averaged Potential Profile in a 1 Torr *He* RF Discharge at 217 V in a GEC Reactor Geometry with -61.8V DC Bias**



The comparison of the PFM results with the model results of Salabas and others, 2002, suggest that the solution of Poisson's equation and the drift-diffusion fluid equations used by both fluid models are reasonably similar. Differences between the electron collision cross-sections used by the two models most likely account for the majority of the differences observed in the peak mean energy. Having compared the PFM to models verified by experimental results, the PFM is next used to investigate the effect of negative ions, chemical kinetics and a flowing background gas on the sheath structure, charged particle density, and neutral species production in an  $O_2(X)$  RF discharge.

### **One Dimensional RF Discharge Results**

The investigation of  $O_2(X)$  and  $N_2(X) - O_2(X)$  RF discharges are first performed in one dimension to examine the effects of flow in the discharge region only. All one dimensional simulations of the  $O_2(X)$  RF discharge presented in this section were performed on a 100 node grid. The smaller grid size was used to resolve the smaller electronegative sheaths associated with an  $O_2(X)$  RF discharge. Time steps for all  $O_2(X)$  and  $N_2(X) - O_2(X)$  RF discharge simulations were kept to less than the dielectric relaxation time, which resulted in about 600 time steps per RF cycle. Similar to the  $Ar$  RF discharge, the primary source of electrons and positive ions of an  $O_2(X)$  RF discharge operating in the alpha mode is electron impact ionization of ground state molecular oxygen (Raizer, 1994).

## One Dimensional $O_2(X)$ RF Discharge Results

The chemical kinetics of the  $O_2$  background gas vary significantly from those of the noble gases  $Ar$  and  $He$ . Important differences in the RF discharge structure result from the electronegative nature of  $O_2$  and its' fast electron energy relaxation rate. These chemical kinetic differences significantly alter the  $O_2$  discharge sheath structure, production rates of excited and charged species, electron and ion densities, and electron mean energy.  $O_2$  RF discharge characteristics and sheath structure in a stationary background gas have been investigated extensively using both experiment and models (Nakano and others, 1994, Stoffel's and others, 1995, Shiabata and others, 1995, Ivanov and others, 1998, and Elaissi and others, 2006). Therefore, this investigation primarily focuses on the effect of a flowing background gas on the  $O_2$  RF discharge sheath structure and plasma characteristics. To help examine the effects that a flowing gas has on various aspects of the  $O_2$  chemical kinetics of the discharge, we break the analysis up into two limited chemical kinetic cases. These cases isolate the effects of negative ions, inelastic electron energy losses and detaching neutral excited species on the sheath structure and charged and neutral species densities. The cases are: the electropositive case, which neglects the effect of attachment and excited neutral species, and the electronegative case, which only neglects the effect of excited neutral species. Once the effect of negative ions on the charged particle density and RF discharge structure is established, the effect of low and high flow velocities are investigated with an emphasis on the density of excited neutral species, which alter the ratio of negative ions to electrons or  $\alpha$  value of the discharge. The electropositive and electronegative  $O_2(X)$

RF discharge cases represent the bounding cases for the effect that flow velocity has on the RF discharge. For an  $O_2(X)$  RF discharge in a stationary or low flow velocity background gas, very high densities of detaching neutral species are achieved. Therefore, the limiting case is the electropositive  $O_2(X)$  RF discharge where detachment has reduced the  $\alpha$  value of the discharge to less than 1. At very high flow velocities, the density of the detaching species is low and hence the  $\alpha$  value of the discharge becomes much greater than one and the limiting case for high flow velocities is the electronegative  $O_2(X)$  RF discharge case.

### **Electropositive $O_2(X)$ RF Discharge Results**

In the first limited chemical kinetic case, we examine the characteristics of an  $O_2(X)$  RF discharge in the absence of negative ions to better understand the effect of negative ions and fast electron energy relaxation rates on the RF discharge structure. The electropositive  $O_2(X)$  RF discharge simulation used the same transport and ionization coefficients as the full chemical kinetic  $O_2(X)$  RF discharge model. The disassociative attachment reaction, which is responsible for the majority of the negative ion production, is treated as just an inelastic collision that does not produce a negative ion species. The electropositive  $O_2(X)$  RF discharge is investigated at the applied voltages of 200V and 1000V to study the effect of increased voltage on the discharge and enable the comparison of the electropositive  $O_2(X)$  RF discharge to the *Ar* discharge in the previous section. The 1000V of applied voltage is of interest to this study in order to allow the production of large densities of charged and excited neutral species by the RF discharge. However, the *Ar* RF discharge would transition to the gamma discharge mode

if operated at a 1000V, therefore a 200V RF electropositive  $O_2(X)$  RF discharge was also simulated in order to compare the results of the two simulations.

The time averaged profiles of the  $Ar$  and  $O_2(X)$  RF discharges, shown in Figures 4.2 and 4.8, are quite different due to the differences in the transport properties, energy relaxation, and ionization rates of the two gas types. The peak time averaged electron and ion density profiles are both narrower and lower in density in the electropositive  $O_2(X)$  versus  $Ar$  RF discharge. The narrower density profile in the  $O_2(X)$  RF discharge is related to the larger sheath lengths and the peaks of the average ionization occurring closer to the center of the discharge. The lower cycle averaged mean energy, shown in Figure 4.9, is due to the larger electron energy losses caused by inelastic collisions with lower threshold energies in  $O_2(X)$ . This reduction in mean energy is consistent with the results of Ellaisi and others, 2006, for an  $O_2(X)$  RF discharge. The faster energy relaxation rates associated with  $O_2(X)$  result in a lower average electron densities caused by the lower average mean electron energies and hence lower ionization rates. The faster energy relaxation rate also results in a dip in the center of the average mean electron energy profile, shown in Figure 4.9a. The observed dip occurs at the point of lowest average electric field shown in Figure 4.8b. The lower average electric field occurs in the center of the discharge due to the shielding of the positively charged sheath by the electrons.

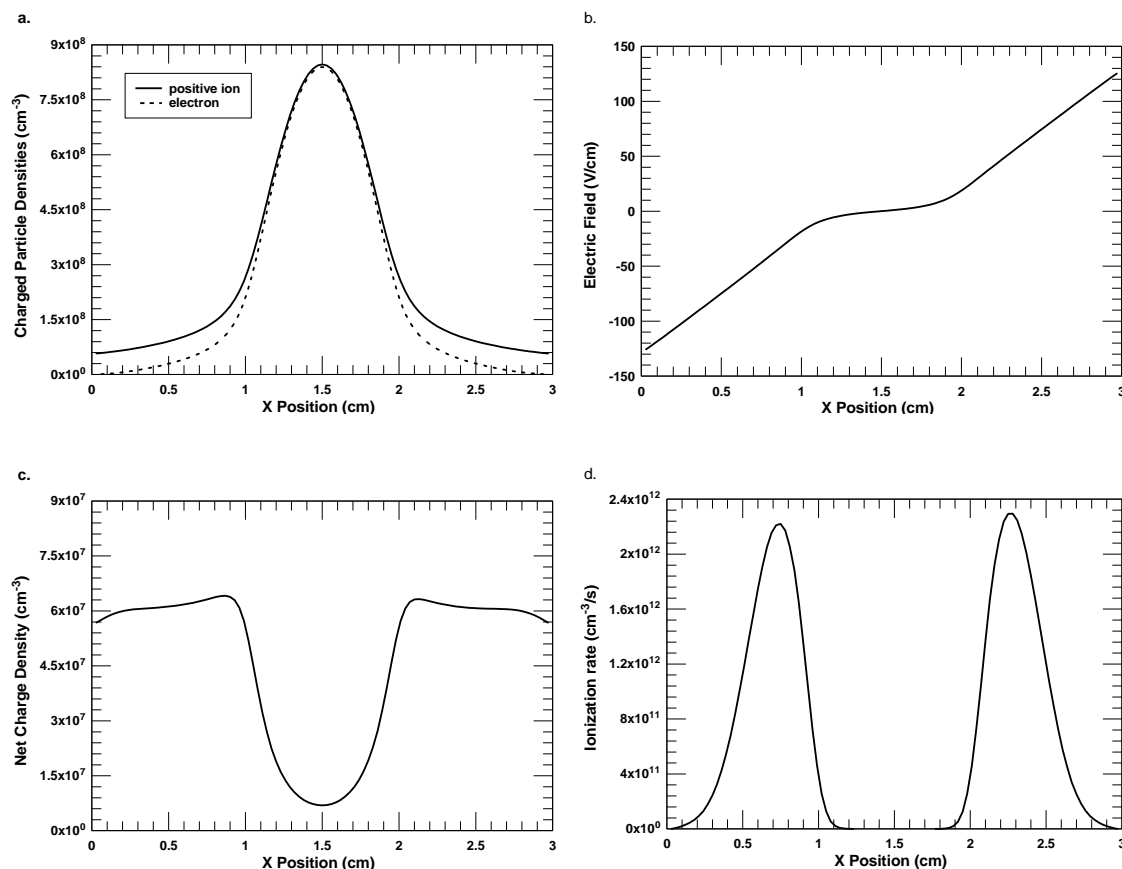


**Figure 4.8 Electropositive  $\text{O}_2(X)$  RF Discharge Time Averaged Results for a 200V Applied Voltage and 1 Torr Background Gas (a) Charge Species Densities (b) Electric Field (c) Net Charge Density (d) Ionization Rate**

The average net charge density, shown in Figure 4.8c, indicates that for these discharge conditions, a quasi-neutral bulk plasma region does not exist on average. The lack of a time averaged quasi-neutral region results from the sheaths associated with the electrodes overlapping; resulting in a non-negligible time averaged electric field through out the discharge region. A non-negligible average electric field in the bulk plasma region of an electropositive discharge is a characteristic of a molecular electropositive discharge and is not usually observed in RF discharges with a noble background gas when the gap between the electrodes is large in length (Graves, 1988). As a result of the large sheath

lengths, the peaks in the ionization rate (which occur at the sheath edge due to the larger electric fields) are closer to the center discharge than in an *Ar* RF discharge with the same discharge parameters. Now we will examine the effect of increased applied voltage on ionization rate and the RF discharge structure.

Increases in RF voltage for an *Ar* discharge (assuming that the discharge stays in the alpha mode) does not result in a significant change in the sheath length or structure and only results in an increase in ionization rate and plasma density in the ~1 Torr pressure regime (Boeuf, 1987). Boeuf's result for a noble gas like *Ar*, however, does not apply to a complex molecular electropositive RF discharge background gas such as  $N_2(X)$  as shown by Graves, 1988. Increasing the applied voltage in the electropositive  $O_2(X)$  RF discharge to 1000V increases the cycle averaged mean electron energy in the center and near the electrodes of the RF discharge as shown in Figure 4.9b.

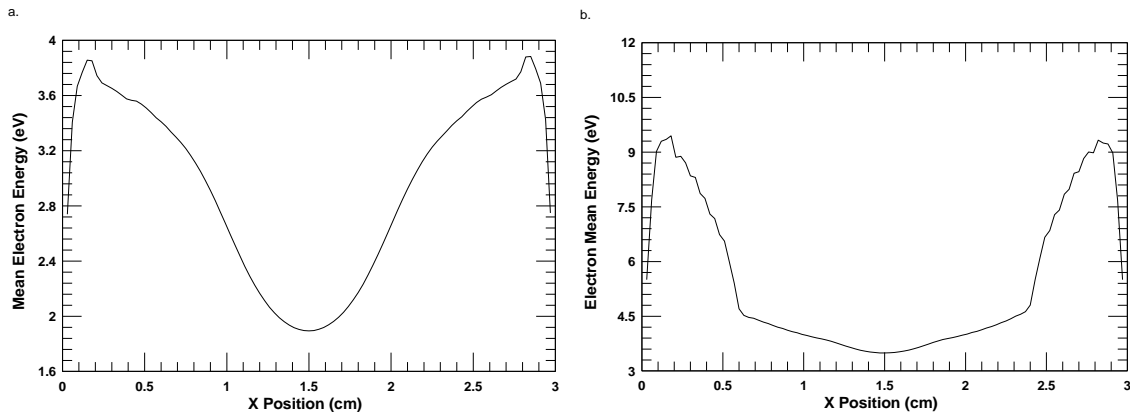


**Figure 4.9 Comparison of the Time Averaged Mean Electron Energy for (a) 200 V and (b) 1000 V Electropositive  $O_2(X)$  RF Discharge in a 1 Torr Pressure Background Gas with a 3 cm Electrode Separation**

Shown in Figure 4.10 are the cycle averaged particle current densities, which are the same for electrons and ions on a time averaged basis. The electrons and ions achieving the same cycle averaged current to the electrodes is necessary for the

discharge to maintain a constant space charge and hence achieve a cyclic steady state. As discussed in the section *Ion Density Rate of Change Acceleration Technique* on page 81, the ion particle current is constant in the sheath region near the electrodes due to the lack of ionization (the electrons are repelled by sheath electric field). Towards the center of the discharge region, the ion currents decrease by over three orders of magnitude on average due to the low time averaged electric fields in the center of the discharge. The increase in the applied voltage and subsequent increase in electron mean energy result in a factor of 200 increase in the average ionization rate. As a result of the increase in ionization rate and the higher potential difference across the sheath, charged particle currents to the electrodes are increased by a factor of 61.

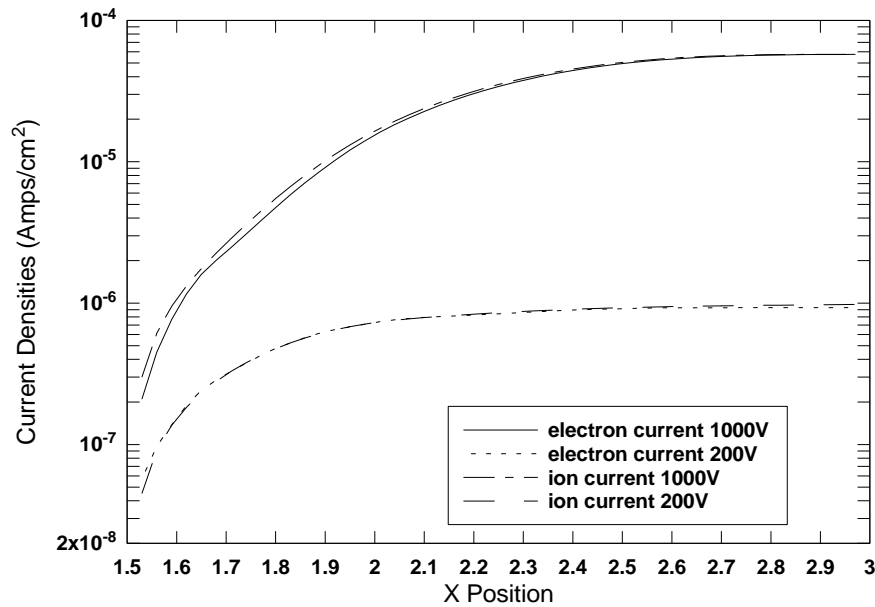


**Figure 4.10 Comparison of the Time Averaged Species Current Densities at (a) 200 V and (b) 1000V in an Electropositive  $O_2(X)$ RF Discharge in a 1 Torr Background Gas**

The time averaged discharge structure at 1000V, shown in Figure 4.11, is similar to the discharge structure at 200V shown in Figure 4.8. The explanations for the various features of the discharge structure, shown in Figure 4.11, are the same as in the 200 V case and will not be discussed further, however, there are a few notable differences. One observed difference is a 45% higher ion and electron density in the 1000V versus 200V case due to the higher electric fields and hence ionization rate. As a result of the increase in voltage and charged particle currents to the electrodes, the positive ion density in the sheath region, shown in Figure 4.11a, is much higher than the density of electrons, which are repelled to a greater extent by the larger sheaths. In addition, the peaks in the average ionization rate are moved even further towards the center of the discharge and become broader resulting in the majority of the ionization occurring near the middle of the discharge. The reason for the broadening of the average ionization rate profile is important to understanding the differences between an electropositive and an electronegative molecular discharge and requires further discussion.



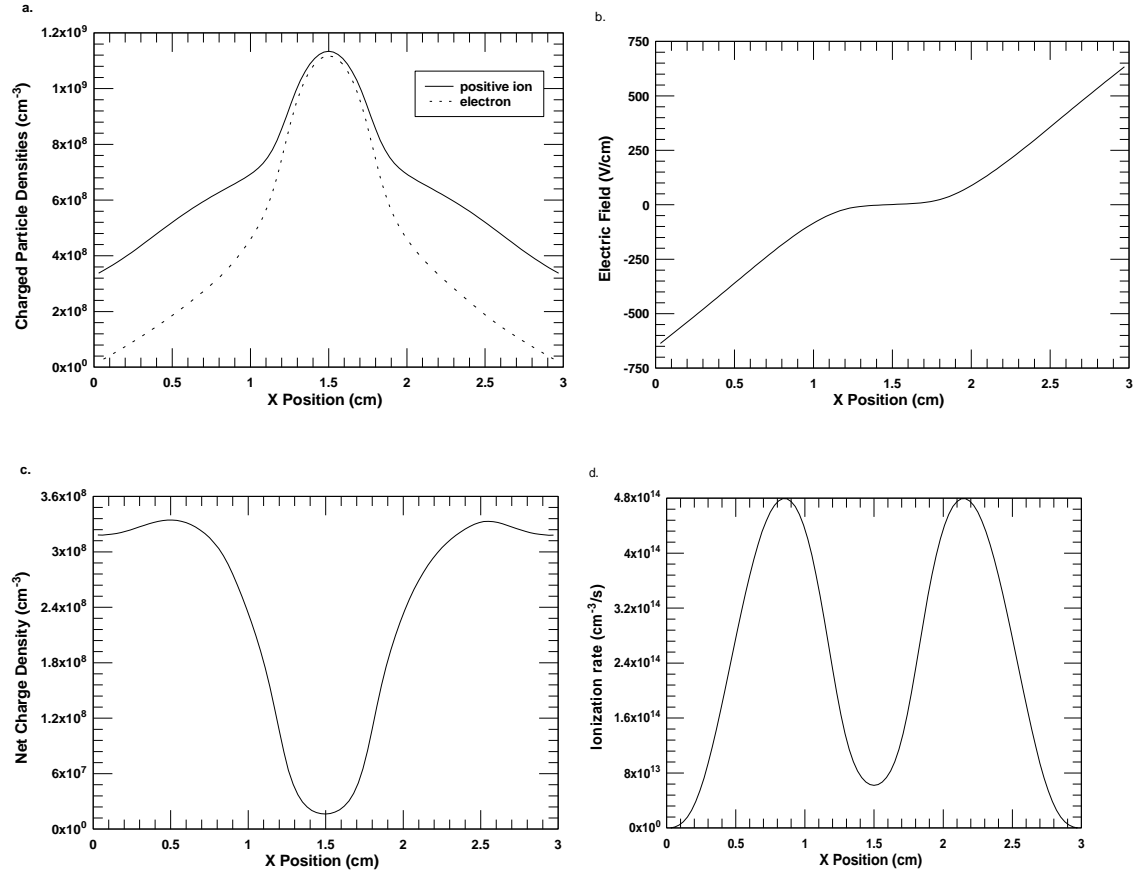


**Figure 4.11 Electropositive  $\text{O}_2(X)$  RF Discharge Time Averaged Results for a 1000V Applied Voltage and 1 Torr Background Gas (a) Charge Species Densities (b) Electric Field (c) Net Charge Density (d) Ionization Rate**

Due to the large extent of the sheath electric field within the discharge region, the electrons are moved substantially during each RF cycle as seen in Figure 4.12b. From Figure 4.12c, ionization occurs most prevalently at the time dependent plasma-sheath edge during the movement of the electrons where a substantial electron density and electric field exists. The coincidence of high electron density and electric field results in a local higher electron mean energy due to Joule heating (Graves, 1988). The maximum time dependent ionization rate from Figure 4.12c is achieved close to the mid point of the RF cycle where the simulation time is  $T = 0.52$  cycle and at a position of 0.75 cm from

the left electrode. At this time in the cycle, the electrons are being accelerated out of the left sheath by the increasing left electrode sheath field. As the electrons are “pushed” by the left electrode sheath into the right electrode sheath, the electrons incident on the right electrode field are “cooled” and by  $T = 0.76$  cycle, the ionization rate in the discharge becomes negligible.

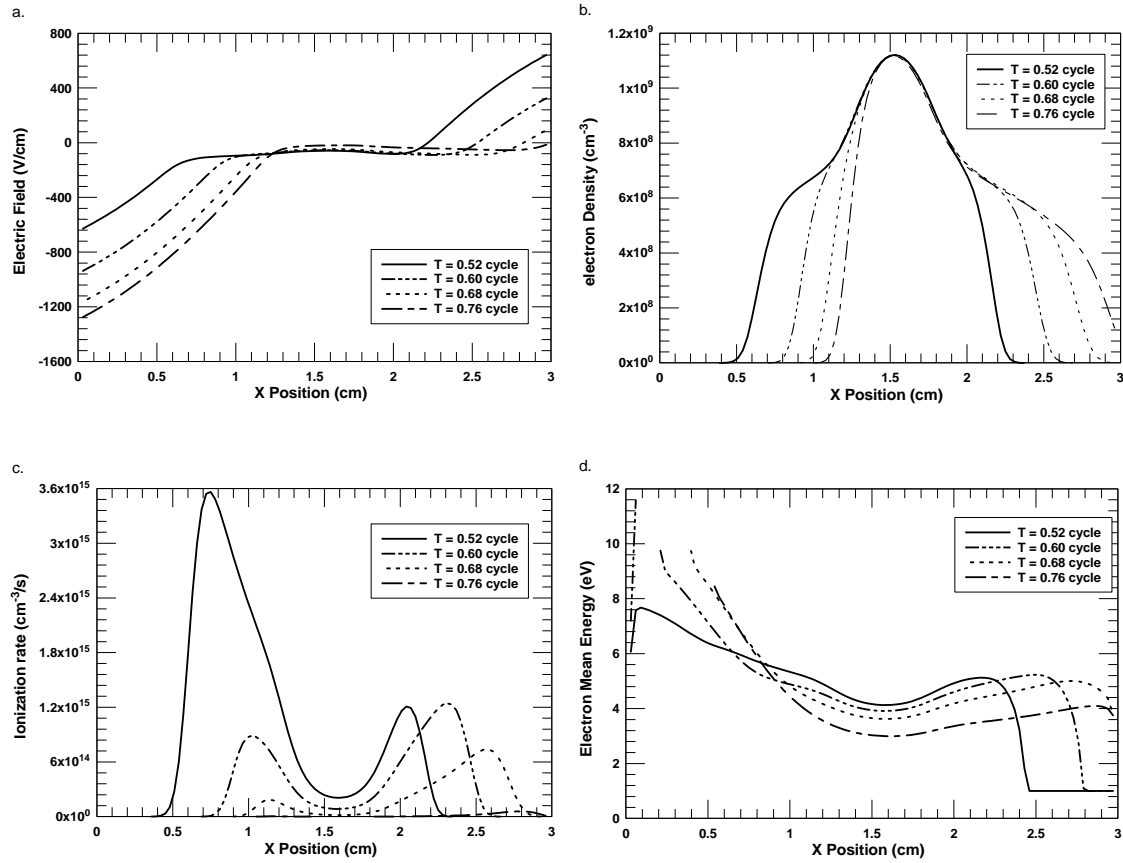


**Figure 4.12 Electropositive  $O_2(X)$  RF Discharge Time Dependent Profiles for a 1000V Symmetrically Driven 1 Torr Background Gas with 3 cm Electrode Separation (a) Charge Species Densities (b) Electric Field (c) Net Charge Density (d) Ionization Rate**

In the absence of a large electric field and substantial electron currents (i.e low Joule heating), the ionization rate and mean energy of the electrons relaxes very quickly due to the large collisional energy losses associated with the  $O_2(X)$  background gas.

The fast electron energy relaxation effect is seen at  $T = 0.76$  cycle in Figure 4.12d. As a result of the fast electron energy relaxation, the location of peak ionization in an  $O_2(X)$  RF discharge moves with the edge of the large electric field, as seen in Figure 4.12a, resulting in a “traveling excitation wave” (Graves, 1987). The broadening in the time averaged ionization peaks, seen in Figure 4.11d, is also a result of the traveling excitation wave and the larger sheaths (resulting in a longer excitation wave traveling distance) associated with the increased voltages in a molecular electropositive RF discharge. The movement and broadness of the peak in ionization rate with the large time varying electric fields results in the peak average ionization rate being much closer to the center of the discharge. The traveling nature of the ionization wave provides no set position for the ion and electron source and makes the sheath edge determination problematic which is consistent with the comments of Franklin, 2003 and Chung, 2006. Fast energy relaxation, however, does not occur in an  $Ar$  RF discharge due to the high threshold energy for the inelastic collisions and therefore a traveling excitation wave is not observed in  $Ar$  or other noble gas RF discharges. The observation of the traveling excitation wave in the simulation is consistent with the model for an electropositive  $N_2(X)$  RF discharge at 0.8 Torr background gas operating at 28V and 1 mAmp/cm<sup>2</sup> in the alpha mode studied by Graves, 1987.

Examining the current density of the 1000V discharge, shown in Figure 4.13b, we see the majority of the current density in the bulk plasma region is due to the drift and diffusion of electrons and the dominant current in the sheath region for most of the RF cycle is the displacement current. In Figure 4.13a, we note that the time dependent electric field in the bulk region of the plasma is significant due to the lack of a time

averaged quasi-neutral plasma in the center of the discharge resulting from the sheaths of the electrodes overlapping. The total peak current density through the discharge is observed to increase by a factor of 6 from  $8.5 \times 10^{-4}$  amps/cm<sup>2</sup> to  $5.0 \times 10^{-3}$  amps/cm<sup>2</sup> between the 200V and 1000V cases respectively due to the higher electric fields (where displacement current density is nearly a factor of 100 greater than the species current density to the electrodes).

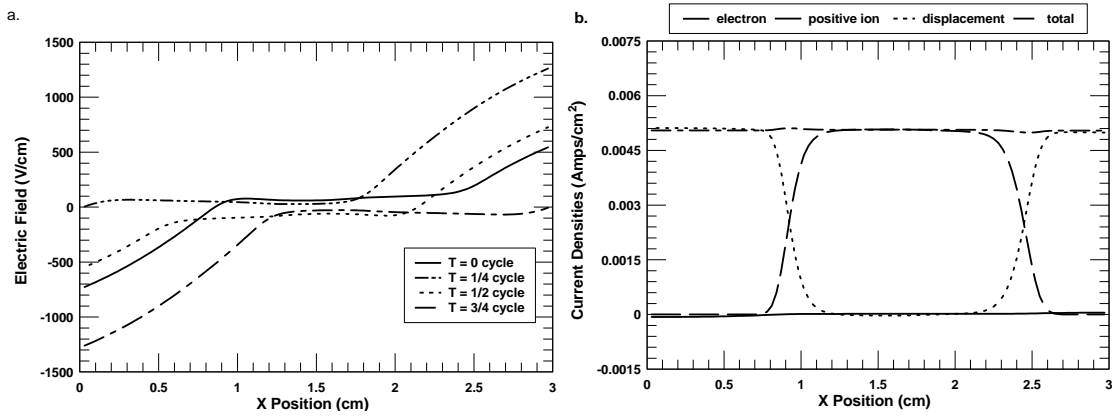


**Figure 4.13 Electropositive  $O_2(X)$  RF Discharge at a 1000V (a) Time Dependent Electric Field (b) Current Densities at the T = 0 Cycle Point**

### Electronegative $O_2(X)$ RF Discharge Results

Having examined some main characteristics of a molecular electropositive  $O_2(X)$  RF discharge which represents an  $O_2(X)$  RF discharge with high detachment rates; we now examine the other limiting case of a highly electronegative  $O_2(X)$  RF discharge with attachment and ion recombination, but neglecting detachment processes by excited neutral species. The electronegative  $O_2(X)$  RF discharge simulation is performed under the same simulation conditions as the 1000V electropositive  $O_2(X)$  RF discharge. The presence of negative ions in an  $O_2(X)$  RF discharge is due primarily to dissociative

attachment, reaction process 37 in appendix B, which results in the  $O_2(X)$  discharge having an electronegative characteristic (Shiabata and others, 1995). The  $\alpha$  value of an RF discharge significantly alters many aspects of the discharge such as the sheath structure and internal electric fields in the bulk region of the plasma (Elaissi and others, 2006). Due to the fast dissociative attachment rate in an  $O_2(X)$  RF discharge, which is dependent on the electric field amplitude, free electrons quickly attach to atomic oxygen resulting in a large  $\alpha$  value. In an RF discharge, the average electric field is directed towards the electrodes, trapping the negative ions within the bulk plasma resulting in a negligible negative ion flux to the electrodes. Transverse to the discharge, the ambipolar electric field also contains the negative ions seen in Figure 4.14. As a result, the negative ions cannot leave the discharge volume and their density is determined by the chemical kinetic processes in the RF discharge.

In moderate pressure discharges operating in the alpha mode, number density ratios of the charged species are established by the balancing of losses and gains of the charged species through bulk and sheath processes. The continuity equation for the determining the gains and losses of negative ions is given by

$$\frac{\partial n_n}{\partial t} + \bar{\nabla} \cdot \bar{\Gamma} = \nu_a n_e - k_r n_i n_n - \sum_d k_d n_n n_d . \quad (4.4)$$

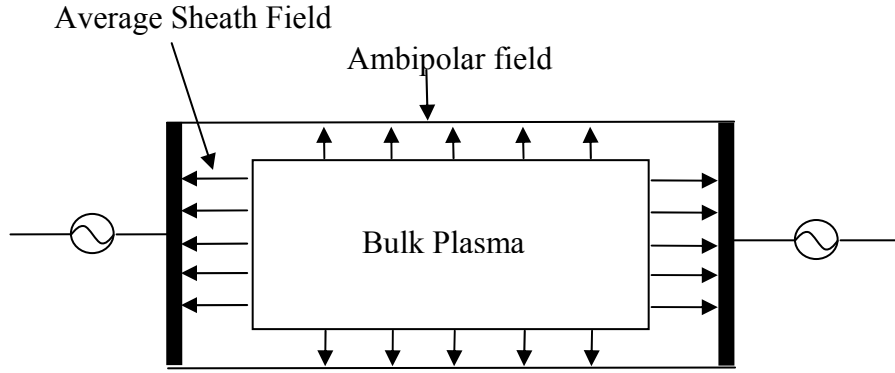


**Figure 4.14 RF Discharge with Electrode Sheath and Ambipolar Field**

The cycle averaged volumetric rates of equation 4.4 can be balanced because the negative ions are trapped within the discharge, resulting in the equation

$$\alpha = \frac{n_n}{n_e} = \frac{\nu_a}{k_r n_i + \sum_d k_d n_d} \quad (4.5)$$

If no detaching species,  $n_d$ , are present then  $\alpha$  is given by

$$\alpha = \frac{\nu_a}{k_r n_i} \quad (4.6)$$

Therefore, as the dissociative attachment frequency,  $\nu_a$ , increases the number of negative ions and the  $\alpha$  value of the discharge increases due to the recombination of positive and negative ion densities being the only loss mechanism of negative ions in a stationary plasma. The cycle averaged charged species densities of the electronegative  $O_2(X)$  RF discharge are presented in Figure 4.15. The discharge presented in Figure 4.15a has a  $\alpha$  value of 150, which is similar to the  $\alpha$  values observed in discharges with higher electronegative background gases such as  $SF_6$  and  $CF_4$  (Paranjpe, 1992) and (Soon-

Youl, and others, 1998). The sheath lengths in the electronegative  $O_2(X)$  discharge are 0.7 cm, where the sheath length is defined by the distance from the electrode where the net charge is negligible.

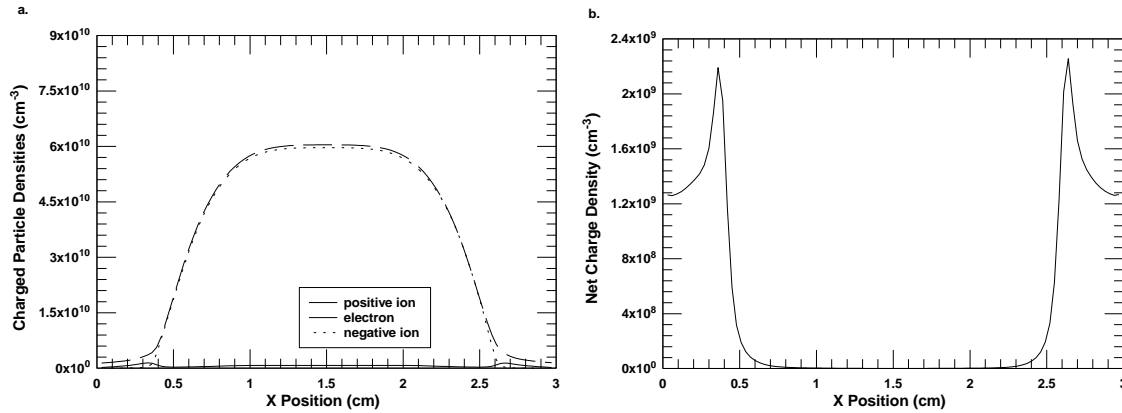


**Figure 4.15** Electronegative  $O_2(X)$  RF Discharge at 1000V without Neutral Excited Species or Detachment (a) Average Charged Species Densities (b) Net Charge Density

The compression of the sheath and the higher positive ion densities of the electronegative  $O_2(X)$  discharge compared to the electropositive  $O_2(X)$  discharge is due to the need for increased ionization rate to help sustain the discharge. The need for higher ionization rates results from the large loss rate of electrons to dissociative attachment. Chung has shown that for electronegative plasmas, an increase in ionization results in the decrease of the sheath width, allowing the quasi-neutrality condition to be achieved nearer to the surface (Chung, 2006). In addition, the decrease in the sheath width results in a higher potential drop over the pre-sheath region resulting in higher electric fields near the edge of the sheath (Chung, 2006). The result of a compressed sheath due to the presence of negative ions is also consistent with the observations in experiments and modeling that highly electronegative gases have thinner sheaths than electropositive gases in a time averaged fashion (Paranjpe, 1990) and (Nakano and

others, 1994). Since the sheath is compressed, the average electric field in the electronegative discharge is larger by nearly a factor of two throughout the sheath, Figure 4.16, than was observed in the electropositive  $O_2(X)$  RF discharge case.

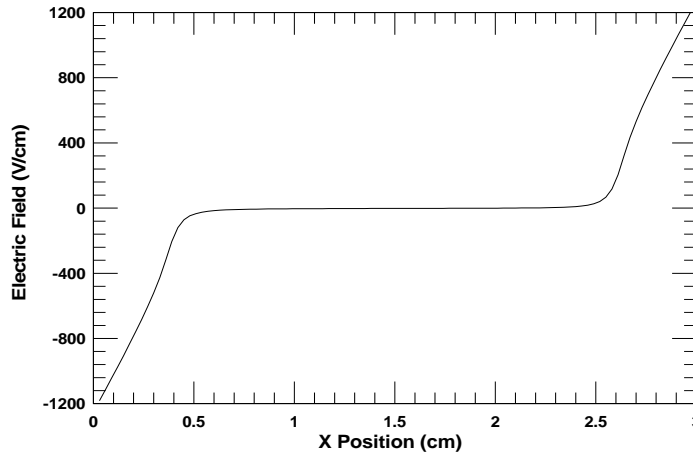


**Figure 4.16 Time Averaged Electric Field in an Electronegative  $O_2(X)$  RF Discharge at 1000V without Detachment**

The increased electric field in the sheath leads to a higher ionization rate. However, the dissociative attachment rate exhibits a weaker dependence on the reduced field (Figure 4.17b) and becomes essentially constant at 160 Td to 240 Td. Dissociative attachment mainly results from the lower amplitude time dependent electric fields present in the bulk plasma of an electronegative discharge (Raizer, 1994).



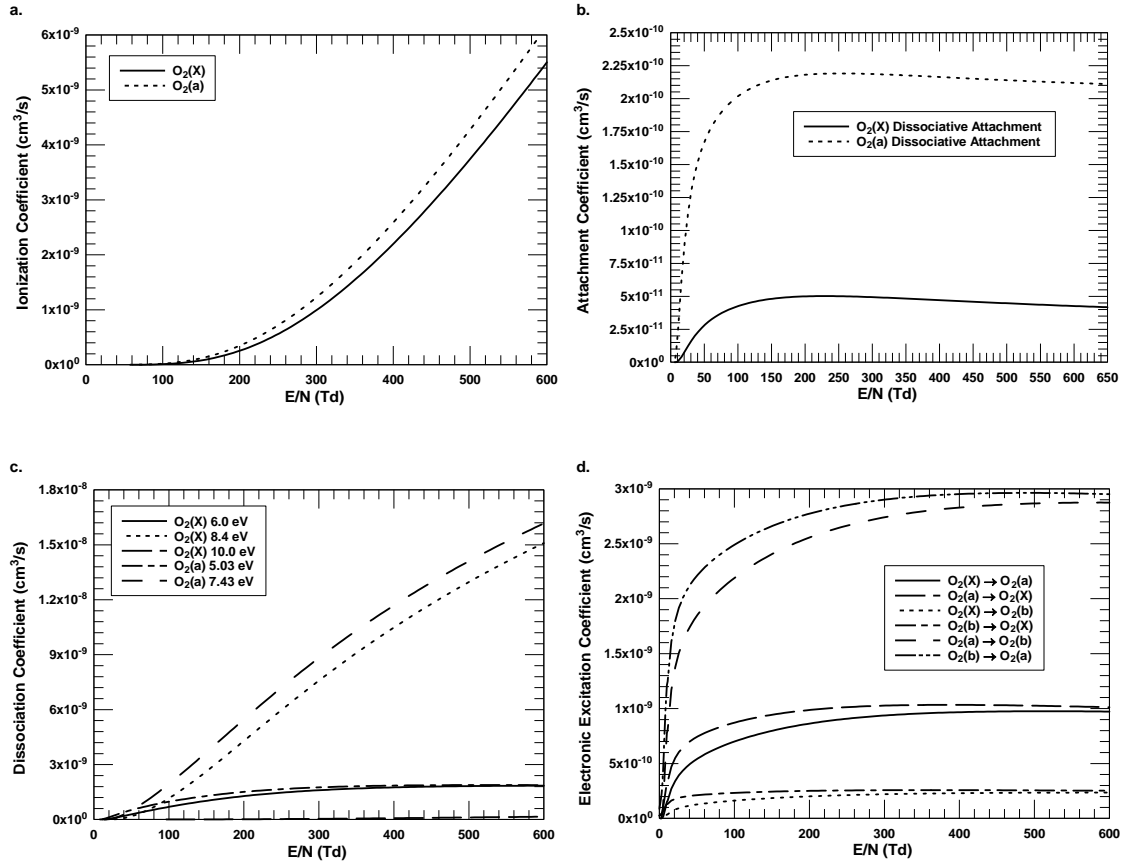


**Figure 4.17 Chemical Kinetic Rates in Pure  $O_2(X)$  (a) Ionization (b) Attachment (c) Dissociation of  $O_2(X)$  and (d) Excitation Rate of  $O_2(a)$**

Examining the time dependent electric field in Figure 4.18a, we observe that the electric fields are non-negligible in the bulk plasma for the electronegative  $O_2(X)$  RF discharge. The peak time dependent electric fields in the bulk plasma of the electronegative  $O_2(X)$  RF discharge, 305 V/cm, are also increased over the electric fields in the electropositive  $O_2(X)$  RF discharge, 105 V/cm, by nearly 300%. The large electric fields in the bulk plasma of an electronegative discharge are well known and have been described as a defining characteristic of an electronegative discharge (Raizer, 1994). The maximum in the dissociative attachment rate on a time dependent basis occurs primarily at the edge of

the electron density and the electric fields in the bulk plasma similar to the traveling excitation wave in an electropositive molecular RF discharge.

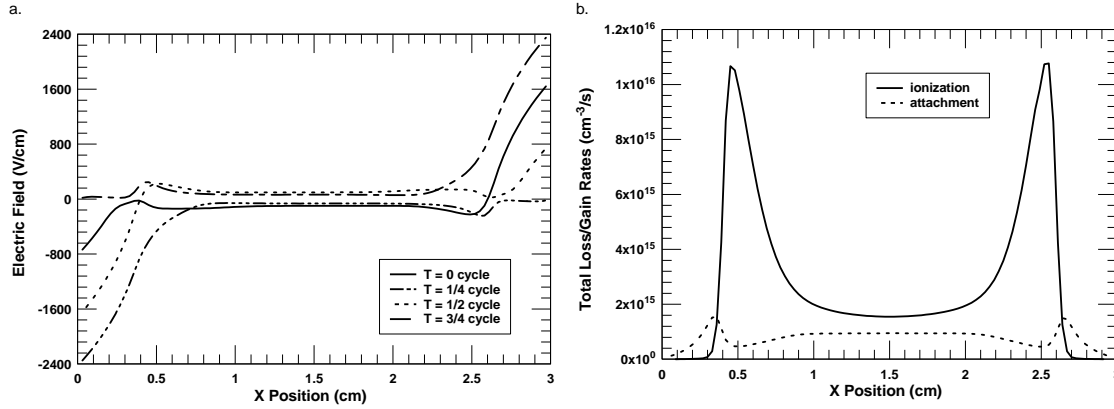


**Figure 4.18 (a) Time Dependent Electric Field and (b) Time Averaged Production Rates in  $O_2(X)$  RF Discharge at 1000V without Detaching Neutral Species**

Another difference observed between a highly electronegative and electropositive RF discharge are peaks in the time averaged electron densities shown in Figure 4.19b. These peaks occur in the sheath region and result from an electric field reversal, shown in Figure 4.18a, near the electrodes. The electric field reversal occurs at the point in the RF cycle when the electrons are pushed past the location where the negative ions start exponentially decreasing in density. This point, which occurs at about 4.5 mm from the electrodes on either side of the discharge, is shown in Figure 4.19b. The electric field reversal results from the net charge density being negative during a small period in the RF cycle when the electrons are pushed towards the electrode as the sheath of the opposite electrode reaches its maximum extent, seen in Figure 4.19a. The sheath upon which the electrons are incident acts to de-accelerate the electrons and repel them away from the electrode creating a large divergence in the flux, shown in Figure 4.19e. This results in an increase in the local density of the electrons at the stopping point on the right

side of the discharge in Figure 4.19b. The peaks observed in the average electron density produced by the PFM have also been observed in the computer model results of Elaissi and others, 2006, and Shibata and others, 1995.

In the electronegative  $O_2(X)$  RF discharge, the negative charge is predominately composed of negative ions. As a result, the space charge separation in the sheath on a time averaged basis is primarily due to the positive and negative ions near the sheath region. The positive and negative ions do not respond significantly to the time dependent fields in the RF discharge and hence the space charge separation associated with the ions is stationary. The ionization in the electronegative  $O_2(X)$  RF discharge, unlike the electropositive  $O_2(X)$  RF discharge case, mostly occurs as the electrons move into the more static sheath region formed by the stationary space charge of the positive and negative ions. The electric field reversal, discussed previously and shown in Figure 4.19a, combined with the electron current inbound on the time varying right sheath result in high levels of Joule heating and ionization at the sheaths edge near the electrode. Therefore, unlike the electropositive  $O_2(X)$  RF discharge, the time average and time dependent ionization occurs mainly near the electrodes. The charge separation created by the positive and negative ion densities acts to anchor the sheath edge and stops the excitation wave from traveling with the edge of the electric field and electron density as was seen in the electropositive  $O_2(X)$  RF discharge. Similar to the electropositive case, at lower electric fields, seen in Figures 4.19 b and d at  $T=0.88$ , the electron mean energy relaxes to a very low value within a fraction of an RF cycle which is consistent with the results of Elaissi and others, 2006.

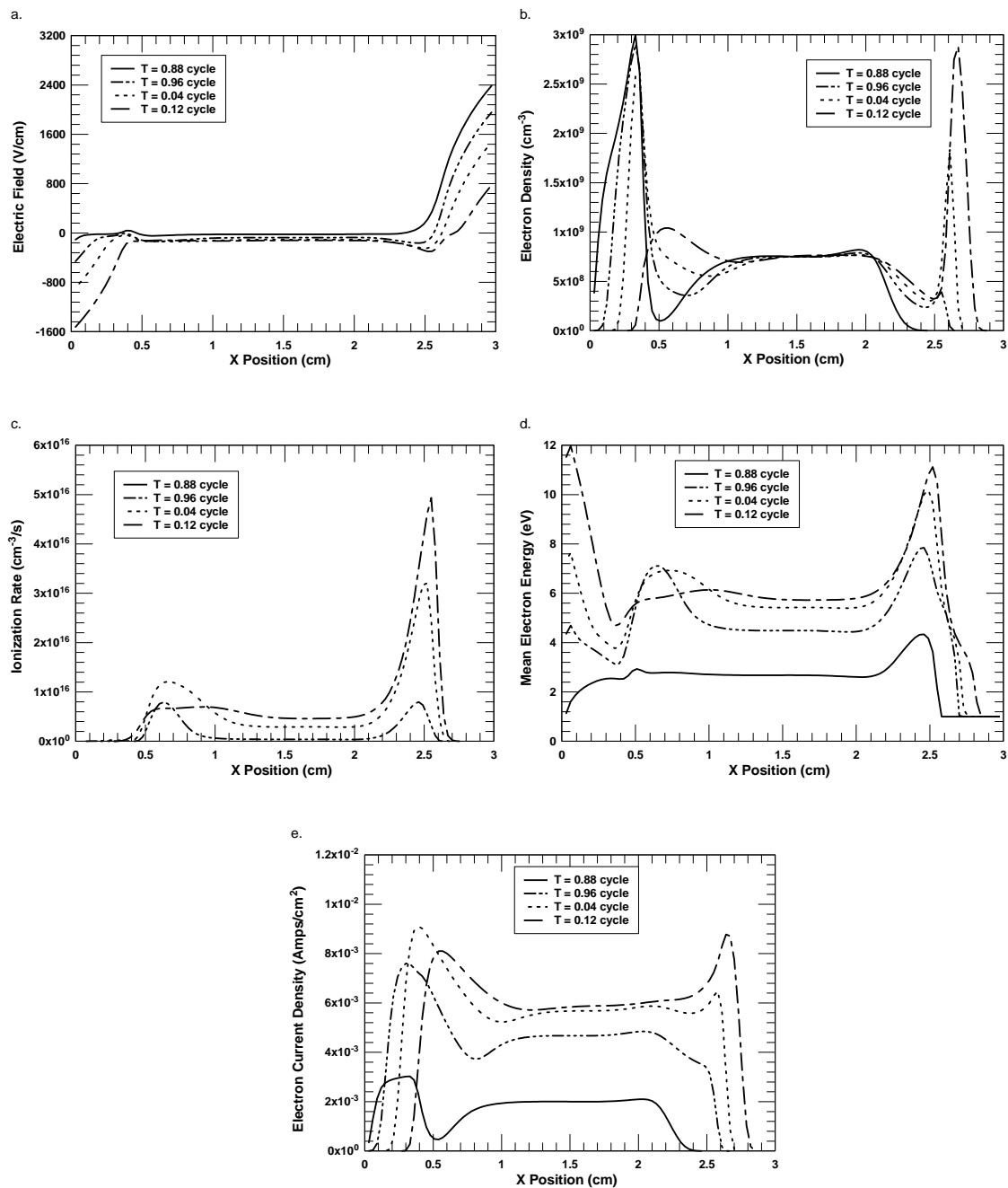


**Figure 4.19 Cycle Dependent Ionization in an Electronegative  $O_2(X)$  RF Discharge at 1000V without Detaching Neutral Species (a) Electric Field (b) Electron Density (c) Ionization Rate (d) Mean Energy (e) Electron Current Density**

In Table 4.1 is a summary comparison of the discharge characteristics of the electropositive and electronegative  $O_2(X)$  RF discharge. General results indicate that

the presence of large densities of negative ions significantly reduces the sheath length and increases the peak electric fields in an  $O_2(X)$  RF discharge. Next, we will investigate how neutral excited species and a flowing background gas influence the ratio of negative ions and the resulting effects on the discharge structure.

**Table 4.1 Comparison of Discharge Structure for Limiting Cases**

<u>Effect</u>	<u>Electropositive</u>	<u>Electronegative</u>
Negative ion /electron ratio	0	150
Peak Ion Density	$1.15 \times 10^9 \text{ cm}^{-3}$	$6.0 \times 10^{10} \text{ cm}^{-3}$
Sheath Length	1.5 cm	0.7 cm
Peak Sheath E-field	650 V/cm	1200 V/cm
Peak bulk E-field	105 V/cm	300 V/cm
Ionization position	Traveling	Stationary

### **$O_2(X)$ RF Discharge in a 25 m/s Flow**

In this section, we will examine an  $O_2(X)$  RF Discharge with the full chemical kinetic model for  $O_2(X)$  discussed in Chapter III. The discharge conditions are the same as the electropositive and electronegative  $O_2(X)$  RF Discharges except for the addition of a 25 m/s flow velocity. The inclusion of neutral excited species chemical kinetics into the  $O_2(X)$  RF discharge simulation primarily affects the rate at which electrons are detached from the negative ions. The species primarily responsible for detaching in an  $O_2(X)$  RF discharge are  $O_2(a)$ ,  $O_2(b)$ , and  $O(^3P)$ . At larger densities of the neutral excited species, the  $\alpha$  value of the discharge is reduced through detachment reactions

according to equation 4.5. The 25 m/s flow velocity reduces the neutral excited species densities such that an intermediate  $\alpha$  value of approximately 9 is obtained. This intermediate  $\alpha$  value results in the sheath expanding to 1.4 cm based on Figure 4.20c and the peak bulk electric field reducing from 305 V/cm for the electronegative case to 160 V/cm. The sheath length with detaching neutral excited species is approximately twice as wide as the electronegative case without detachment reactions. In a stationary  $O_2(X)$  RF discharge, the detachment of negative ions by excited neutral species is large enough that the  $\alpha$  value is less than 0.5 and the discharge structure shares more similarities with the electropositive  $O_2(X)$  RF discharge presented previously.

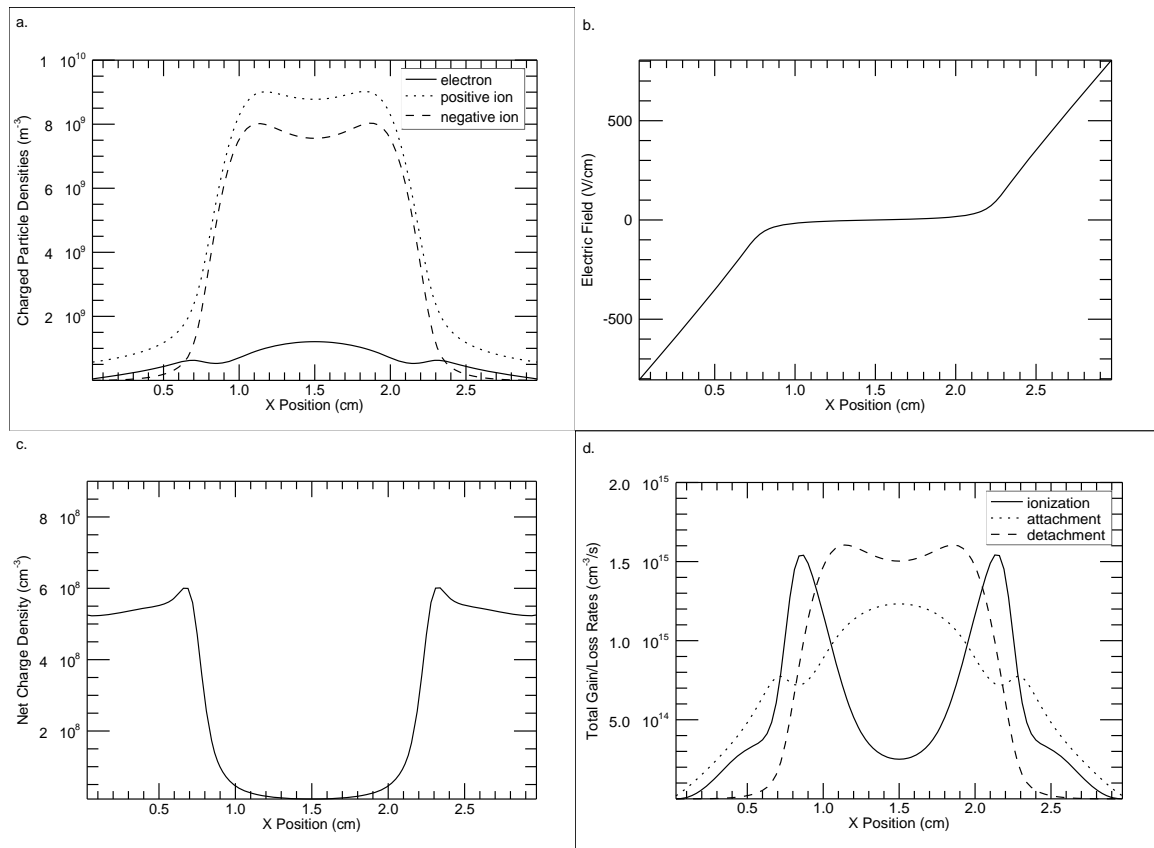


**Figure 4.20  $O_2(X)$  RF Discharge at 1000V with Chemical Kinetics and a 25 m/s Flow Transverse to the Discharge (a) Average Charge Density (b) Average Electric Field (c) Net Charge Density and (d) Loss and Gain Rates of Electrons**

Detachment by  $O_2(b)$  and  $O(^3P)$  occurs primarily in the center of the discharge due to neutral species diffusing into the center from the primary generation region. The main production location for  $O_2(b)$  and  $O(^3P)$  is nearer to the electrode due to their production rates being dependent on higher electron energy dissociation processes given by reactions 1, 3, and 41 in appendix B. However, due to quenching of the excited species by thermal diffusion to the electrodes, the density of the excited neutrals decreases towards the cathodes (Pinhero and others, 1998). The attachment rate of electrons and detachment rate of negative ions with  $O_2(a)$ ,  $O_2(b)$ , and  $O(^3P)$ , exceeds the ionization rate as shown in Figure 4.20d. This indicates the electrons and negative ions go through multiple attachment and detachment collisions before the electron is lost from the system. This result is consistent with the results of Gousset and others, 1991, who showed that detachment by  $O_2(a)$  and  $O(^3P)$  provided the main balance mechanism between electron and negative ion densities. Due to detachment reactions, the majority of the electrons are produced farther from the electrodes and the  $\alpha$  values of the  $O_2(X)$  RF discharge are reduced. As a result there is a lower density, but broader, time averaged net charge density in the sheath region and the average length of the sheath expands. This results in a reduction of the time averaged electric field amplitude, which is consistent with the analysis of Chung, 2006, and the electropositive  $O_2(X)$  RF discharge results. The sheath length, however, is not as large as the electropositive  $O_2(X)$  RF discharge case due to the presence of the negative ions and the spatially distributed source of electrons resulting from detachment in the center of the discharge. The

expansion of the sheath also influences the distance from the electrode at which ionization occurs during the cycle, shown in Figure 4.20d. This results in the peak of the average ionization rate moving towards the center of the discharge as was observed in the electropositive  $O_2(X)$  RF discharge. The expansion of the sheath results in greater production rates of lower energy metastable species  $O_2(a)$  and  $O_2(b)$  via direct electron excitation in the discharge due to the lowering of the internal bulk electric fields and mean electron energy in the RF discharge for reaction processes 37 and 35. The reduction in the internal bulk electric fields is due to a greater proportion of the negative charge in the bulk plasma being highly mobile electrons which shield the average space charge in the sheaths better than the negative ions. The production of substantial amounts of  $O(^3P)$  and  $O_2(b)$  still occurs due to the high electric fields near the sheath edge and fast deactivation of  $O(^1D)$  with  $O_2(X)$  in reactions 1 and 3 by higher energy electrons. In the 25 m/s flow case, reaction 1 is the main source of  $O_2(b)$  which is consistent with the model results of Pinhero and others, 1999. The expansion of the sheath due to increasing production of detaching species is also consistent with the results observed by Shibata and others, 1995. They observed that the sheath expanded with increased applied voltage from 75 V to 150 V due to higher densities of  $O(^3P)$  and negative ions creating higher rates of detachment.

In addition, a local minimum in the middle of the positive and negative ion densities shown in Figure 4.20a is also observed due to the high levels of detachment in the 25 m/s background gas flow. The inclusion of excited neutral species also results in the peaks in the electron density at the edge of the sheath region becoming less prominent



also seen in Figure 4.20a. This is due to the longer sheaths and lower electric fields in the bulk plasma region. The lower electric fields in the sheath reduces the stopping rate of the electrons as they move towards the electrode and hence lowers the divergence of the electron flux at the sheath edge.

With the inclusion of detaching neutral excited species, the increase in the sheath width also decreases the current to the electrodes. Hence the current across the RF discharge and the power required to sustain the discharge is reduced, as seen in Figure 4.21 a and b. The reduction in discharge current is mainly due to the reduced peak electric fields in the discharge resulting in a lower ionization rate (detachment provides the additional electron source to help maintain the discharge). Comparing the current composition between the  $O_2(X)$  RF discharge cases with and without neutral excited species, we notice that the total current density in the case with detaching species is half that of the electronegative case without detaching species. This is due to the electric fields in the sheath region being half that of the electronegative  $O_2(X)$  RF discharge case. The reduction in the sheath electric field also reduces the positive ion current to the electrodes (the main loss mechanism of the positive ions). Also, the positive and negative ion current contribution in the bulk plasma is significantly reduced in the case with detaching species due to the reduction in density of the positive and negative ions and the lower fields in the discharge region. In addition, the electron current now represents a larger proportion of the current in the bulk plasma similar to the electropositive  $O_2(X)$  RF discharge due to the lower electric fields in the bulk plasma.

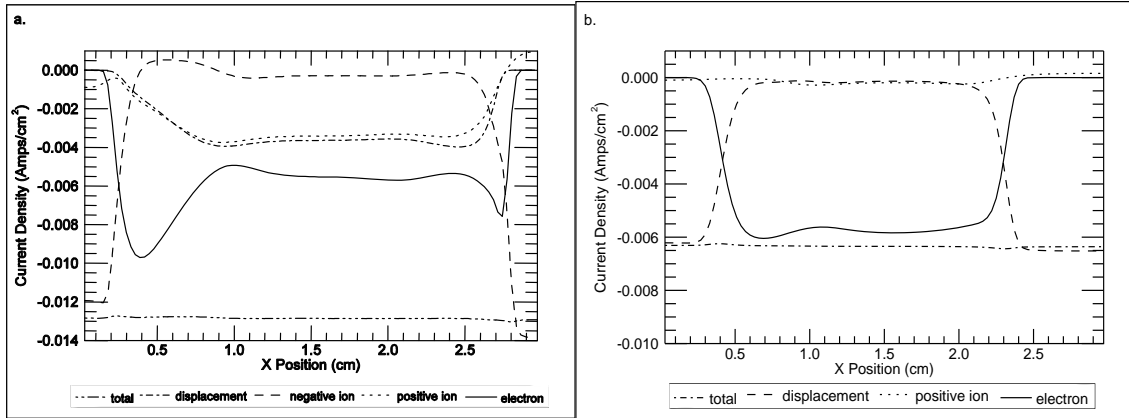


**Figure 4.21 Comparison of the Current Density in  $O_2(X)$  RF Discharge at 1000V at Peak Values (a) without Detaching Neutral Species and (b) with Detaching Neutral Species**

In summary, the addition of neutral excited species to the chemical kinetics of an  $O_2(X)$  RF discharge has the effect of reducing the  $\alpha$  value of the discharge. The reduction of the  $\alpha$  value in turn alters the discharge structure such that the sheath length and electric fields more resemble an electropositive rather than an electronegative  $O_2(X)$  RF discharge. In the next section, we will examine the effects of increased flow velocity on the neutral excited species densities and the discharge structure characteristics.

#### **$O_2(X)$ RF Discharge in a 150 m/s Flow**

The result of increasing the flow velocity to 150 m/s on the RF discharge sheath structure, while keeping all other parameters constant, is shown in Figure 4.22. Increasing the flow velocity through the RF discharge increases the convective loss rate of all the species in the simulation by the factor given by equation 4.2. The resulting average plasma densities and electric field profiles shown in Figure 4.22 now resemble the results of the electronegative  $O_2(X)$  RF discharge shown in Figure 4.15. In the higher flow velocity case, the  $\alpha$  value has increased from 9 to 38, the positive ion density

has increased by a factor of four due to a factor of five boost in ionization rate resulting from the time averaged sheath lengths being compressed to 0.9 cm. The increase in the  $\alpha$  value (where  $n_i = n_e(\alpha + 1)$  in the quasi-neutral bulk plasma and  $n_e$  remains the same between cases) reduces the ability of the electrons to shield the large positive charge of the sheath. This is due to the positive ion density in the sheath being much larger than the average electron density in the discharge region, which is shown in Figure 4.22a. As a result of the reduced shielding effectiveness of the electrons, the time dependent electric fields in the bulk plasma increase from a peak value of 160 V/cm to 245 V/cm when the flow velocity is increased from 25 m/s to 150 m/s respectively. From Figure 4.22, we note that the densities of  $O_2(a)$  have been reduced by a factor of 50 and the densities of  $O_2(b)$  and  $O(^3P)$  have been reduced by a factor of 10. This reduction in neutral excited species, however, only results in a net reduction in the detachment rate by a factor of two due to the dramatic increase in negative ion density in the 150 m/s versus 25 m/s flow velocity case.

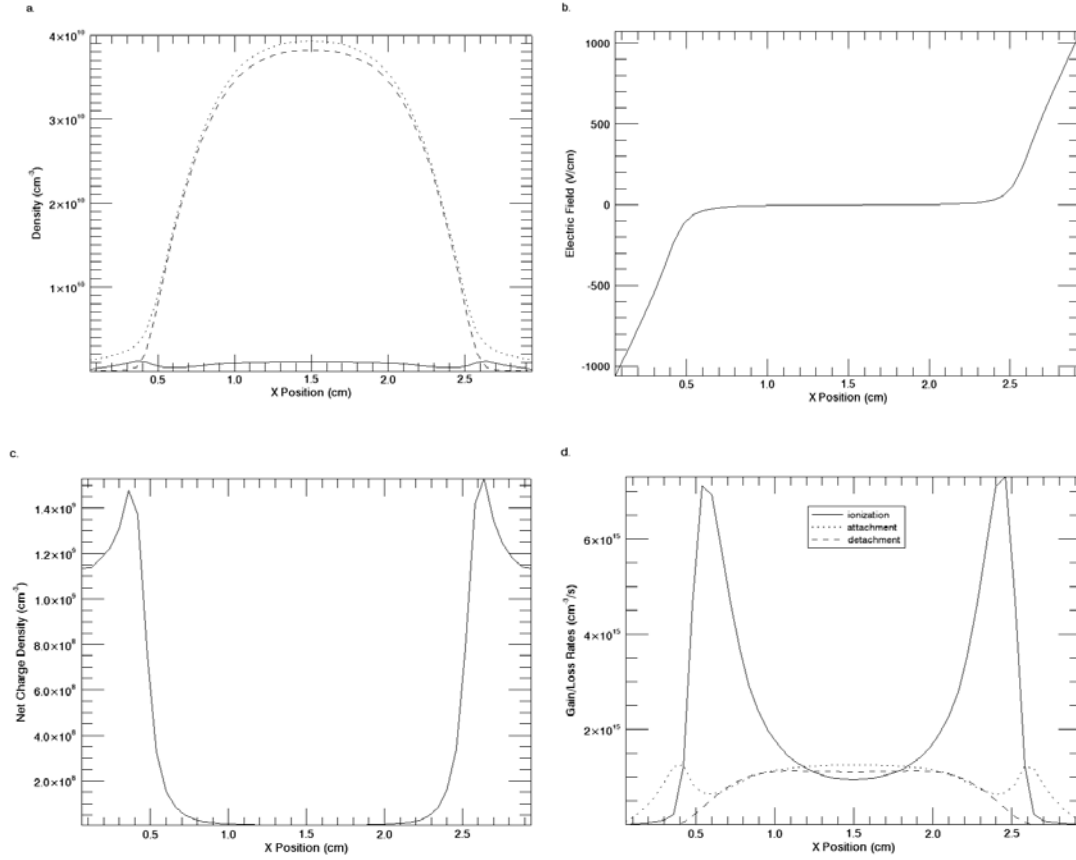


**Figure 4.22  $O_2(X)$  RF Discharge at 1000V with Chemical Kinetics in a 150 m/s Flow Transverse to the Discharge (a) Average Charge Density (b) Average Electric Field (c) Net Charge Density (d) Loss and Gain Rates of the Charged Species**

In Table 4.2 is a comparison of the discharge structure in the low and high flow velocity cases as well as the bounding cases which have been referred to as the electropositive and electronegative cases. The 150 m/s flow velocity case is more like the electronegative case in structure and ion densities due to the reduced density of the excited neutral species and hence a higher  $\alpha$  value. The 25 m/s flow velocity case is more like the electropositive limiting case due to the lower  $\alpha$  value of the discharge resulting from the larger density of excited neutral species.

**Table 4.2 Comparison of  $O_2(X)$  RF discharge Cases**

<b>Effect</b>	<b>Electropositive</b>	<b>Low Flow 25 m/s</b>	<b>High Flow 150 m/s</b>	<b>Electronegative</b>
Negative ion /electron ratio	0	8	38	150
Peak Ion Density	$1.15 \times 10^9 \text{ cm}^{-3}$	$9.0 \times 10^9 \text{ cm}^{-3}$	$3.95 \times 10^{10} \text{ cm}^{-3}$	$6.0 \times 10^{10} \text{ cm}^{-3}$
Sheath Length	1.5 cm	1.4 cm	0.9 cm	0.7 cm
Peak Sheath E-field	650 V/cm	800 V/cm	1050 V/cm	1200 V/cm
Peak bulk E-field	105 V/cm	160 V/cm	245 V/cm	300 V/cm
Ionization position	Traveling	Traveling	Stationary	Stationary
Energy deposition per molecule	N/A	0.25 eV	0.067 eV	N/A

In the 150 m/s case, the density of  $O_2(a)$ , which is produced through a low frequency electron excitation process compared to dissociation, is greatly reduced due to the rate of production saturating at 200 Td while the flow loss is dramatically increased. Neutral excited species such as  $O(^3P)$  and  $O_2(b)$  (primarily produced by a resonant reaction of  $O_2(X)$  with  $O(^1D)$ ) are produced by large cross-section processes with high threshold energies. As a result, the densities  $O(^3P)$  and  $O_2(b)$  are reduced to a lesser extent by convection losses because their production rate increases with the increase in the electric field amplitude associated with the compression of the sheath at higher flow velocities. The increase in the production rates of  $O(^3P)$  and  $O_2(b)$  with increasing flow velocity are shown in Figure 4.23b. In addition, the charged particle production rate versus flow velocity is shown in Figure 4.23a. The total production rate of electrons,

shown in Figure 4.23a, is greater than the production rates of positive ions because electrons are produced by both ionization as well as detachment.

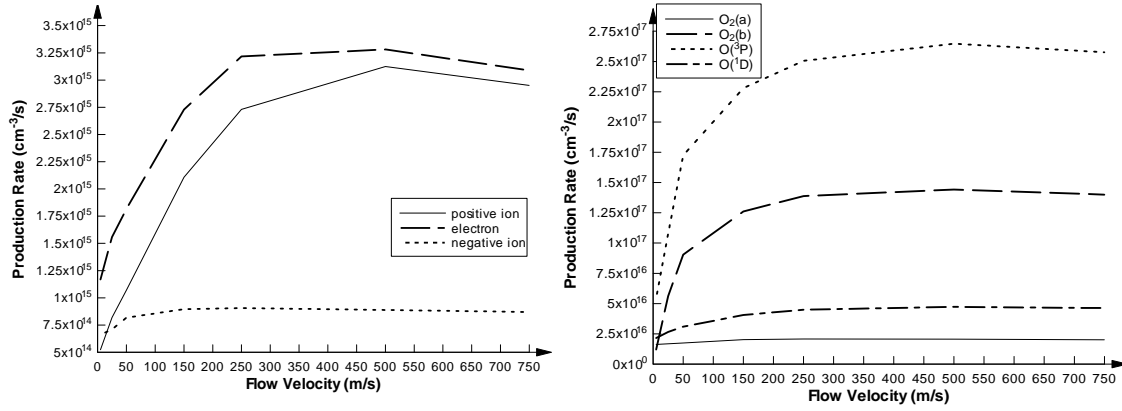


**Figure 4.23 Production Rates for (a) Charged Species (b) Neutral Excited Species in an  $\text{O}_2(\text{X})$  RF Discharge at 1000V with Flow Velocities between 5 m/s and 750 m/s**

The peak time dependent electric field in the bulk plasma increases by 65% with increasing flow velocities from 25  $\text{m/s}$  to 500  $\text{m/s}$  as shown in Figure 4.24b. As a result, the positive ion density increases with flow velocity up to 500  $\text{m/s}$ , shown in Figure 4.24a, due to the exponential dependence of ionization on the electric field amplitude. However, we see that the densities of the ions at flow velocities of 500  $\text{m/s}$  and greater decrease slightly due to convection losses which become a substantial loss mechanism for the ions. The ionization rate, at flow velocities greater than 500  $\text{m/s}$ , also slightly decreases due to lower positive ion densities in the sheath region which result in lower electric fields. The lack of increase in the ionization rate results from excited neutral species densities becoming negligible at flow velocities of 500  $\text{m/s}$  or greater. The low density of excited neutral species at higher flow velocities results in the  $\alpha$  value not increasing anymore and therefore the sheath does not decrease to less than 0.7  $\text{cm}$  (which was the sheath width of the electronegative case). Therefore, at flow velocities of greater

than 500 m/s, the discharge sheath structure and ionization rate profile become very similar to the electronegative  $O_2(X)$  RF discharge case.

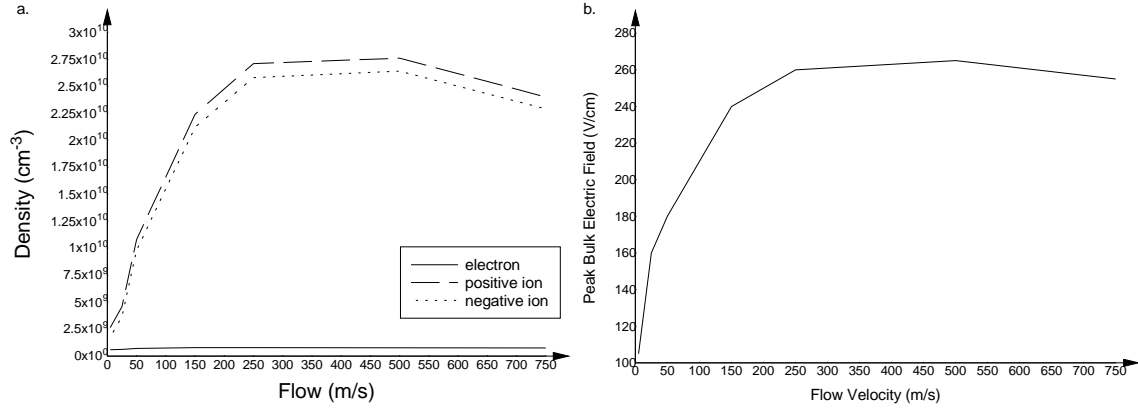


**Figure 4.24  $O_2(X)$  RF Discharge (a) Charged Species Densities (b) Peak Bulk Electric Field Amplitude with Flow Velocities between 5 m/s and 750 m/s at 1000V Applied Voltage**

From the results shown in Figure 4.25, the highest densities of  $O_2(a)$ ,  $O_2(b)$ , and  $O(^3P)$  are obtained only at low flow velocities. This occurs because the flow losses for the neutral excited species are significant compared to the production rate of those species. This result is primarily due to the small electrode length (along the direction of the flow) in this configuration and the resulting short residence time of the background gas at high flow velocities. The only excited neutral species that increase with flow velocity is  $O(^1D)$  which is quenched in reaction 1 with  $O_2(X)$  nearly instantaneously. As a result, the density of  $O(^1D)$  is determined primarily by the electric field amplitude and  $O_2(X)$  density.

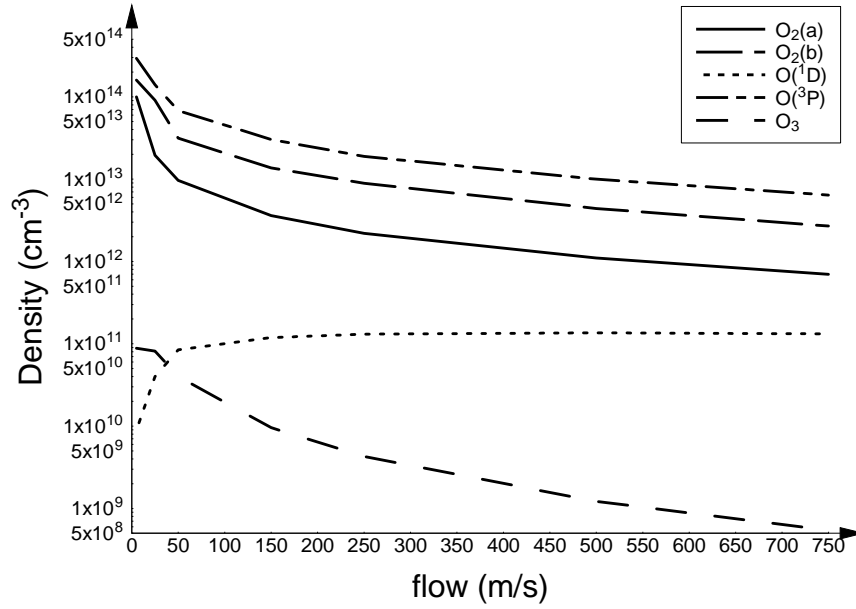


**Figure 4.25 Neutral Excited Species Densities for an  $O_2(X)$  RF Discharge at 1000V with Flow Velocities between 5 m/s and 750 m/s**

The major gain and loss mechanisms for the neutral excited species are shown in Table 4.3. Reactions were considered a major gain or loss mechanism if their reaction rates were within an order magnitude in value of the dominant gain or loss rate. Increased flow velocities generally did not change the primary loss or gain mechanism for a particular species. However, the secondary main gain mechanisms for a particular species did change with higher flow velocities due to higher densities of excited species providing additional gain terms for the species  $O_2(a)$ ,  $O_2(b)$ , and  $O(^3P)$ .

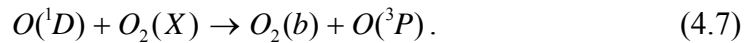


**Table 4.3 Primary Reactions that Result in Gains and Losses of Neutral Excited Species**

Flow velocity		$O_2(a)$	$O_2(b)$	$O(^3P)$	$O(^1D)$	$O_3$
5 m/s	Gain	# 35, 18	# 1, 37	# 40, 41, 1	# 41	#26, 12
	Loss	Flow	Flow, Wall	Flow, Wall	# 1, 3, 2	# 17, Flow
25 m/s	Gain	# 35, 2	# 1	1, 3, 40, 41	# 41	# 26, 12
	Loss	Flow	Flow	Flow, Wall	# 1, 3	# 17, Flow
50 m/s	Gain	# 35, 2	# 1	1, 41, 40, 3	# 41	# 26, 12
	Loss	Flow	Flow	Flow, Wall	# 1, 3	# 17, Flow
150 m/s	Gain	# 35, 2	# 1	# 1, 3	# 41	# 26, 12
	Loss	Flow	Flow	# 41	# 1, 3	# 17, Flow

<sup>1</sup>Numbers shown in table correlate to reaction equations obtained in appendix B

From Table 4.3, the secondary main gain mechanism for  $O_2(a)$ , reaction 18, which is the quenching reaction of  $O_2(b)$  by  $O(^3P)$ , is highly reduced with flow velocity due to both species decreasing in density with increased flow velocity. As a result of the quenching of  $O_2(b)$  to  $O_2(a)$  becoming insignificant at higher flow velocities, the  $O_2(a)$  total production rate does not increase with increasing flow velocity past 50 m/s as shown in Figure 4.23. For  $O_2(b)$ , direct electronic excitation becomes less significant at faster flow velocities compared to the fast rate associated with reaction 1



The excited atomic species,  $O(^1D)$ , becomes important in the production of  $O_2(b)$  due to the fast rate of the 8.4 eV dissociation reaction, which creates  $O(^1D)$ . The 8.4 eV reaction is very fast at a 1000V of applied voltage because the average electron energy during an RF cycle is approximately 6.7 eV at 150 m/s, which results in a large percentage of the electrons having enough energy to generate  $O(^1D)$ . The diminishing importance of reaction 4 (from Table 4.3) to the creation of  $O(^3P)$  is due primarily to the reaction quenching  $O(^1D)$  with  $O(^3P)$  and the density of  $O(^3P)$  having been reduced significantly at flow velocities greater than 25 m/s.

Simulation results have shown that a flowing background gas reduces the length of the active sheath and increases the electric fields in the bulk plasma due to the removal of neutral excited species that detach negative ions. The reduction in the length of the active sheath increases the electric field in the sheath and dramatically boosts the production of positive ions due to the near exponential dependence of ionization on the electric field amplitude. The production rate of neutral species, such as  $O_2(b)$ ,  $O(^3P)$ , and  $O(^1D)$  which are primarily a result of dissociation reactions, increased with flow velocity due to the compression of the sheath, resulting in the peak electric fields increasing by up to 50% in the sheath and 65% in the bulk plasma. However, the density of the neutral excited species in the discharge decreased due to increased convective losses. However, the total amount of  $O_2(b)$  and  $O(^3P)$  produced by a flowing  $O_2(X)$  background gas through the RF discharge can be increased with increasing flow velocity. This result can be advantageous especially if large fluxes of excited species are desired rather than high yield percentages relative to the background gas density. The increased

fluxes of excited neutral species from an  $O_2(X)$  RF discharge are useful for uniform chemical vapor deposition on films (Collart and others, 1995), however, it is not particularly useful for the direct production of  $O_2(a)$  for ElectriCOIL applications. The increase in positive and negative ion density production, however, has the potential to supply a second downstream discharge additional electrons and ions. This approach can allow the second discharge to operate at lower voltages for enhanced production of  $O_2(a)$  for ElectriCOIL applications or provide an independent source of ions to a second discharge which etches semi-conductors and other substrates. These potential applications are explored in further detail after the convection of the plasma and neutral excited species is investigated using a 2-D model of the RF discharge and flow tube.

### **One Dimensional $N_2(X)$ and $O_2(X)$ Gas Mixture RF Discharge Results**

In this section, we examine the effect that the addition of  $N_2(X)$  to the background gas has on the RF discharge structure and the influences of flow on the chemical kinetics, RF discharge structure, and yields of charged and excited neutral species. RF and microwave discharges in mixtures of  $N_2(X)$  and  $O_2(X)$  at moderate pressures have been studied extensively by Gordiets and others, 1995, Guerra and others, 1999, Capitelli and others, 2000. Their  $N_2(X)$  -  $O_2(X)$  discharge modeling approach used a global kinetic model combined with a one dimensional microwave discharge model, which approximated the plasma sheath near the surface of the tube with an ambipolar diffusion sheath model. The chemical kinetic model used in this investigation is based on the chemical kinetic model developed by Gordiets' and others, 1995, due to the similarity in pressures and discharge current between this investigation and Gordiets'

study. The addition of  $N_2(X)$  to a discharge has been shown by Capitelli and others, 2000, to increase the electron energy loss rate substantially over a pure  $O_2(X)$  discharge due to increased inelastic collisions in  $N_2(X)$ . The gas mixture used in our investigation is 80%  $N_2(X)$  and 20%  $O_2(X)$ , representative of sea level air. The inclusion of  $N_2(X)$  into the background gas results in a huge increase in the complexity of the heavy species chemistry and interesting changes in the response of the plasma to flow velocity.

### **$N_2(X)$ - $O_2(X)$ RF Discharge in a Stationary and 250 m/s Flow**

Several different operating conditions of the RF discharge in a flow were examined to better understand the response of the RF discharge to changing flow velocity. Similar to the  $O_2(X)$  RF discharge, when neutral excited species are included in the simulation, the flow velocity has a dramatic effect on the production of charged and neutral excited species densities in the discharge region. This is due primarily to the flow removing the excited neutral species generated by the discharge and hence altering the total detachment rates of the discharge. Figures 4.26a and 4.26b show the time-averaged charged species densities and Figures 4.26c and 4.26d show the total ionization, attachment, and detachment rates in a discharge with an RF voltage of 1000V, an electrode separation of 3 cm and flow velocities of 0 and 250 m/s. Similar to the  $O_2(X)$  RF discharge simulation, each simulation presented in this section was resolved using a 100 evenly spaced nodes and 600 time steps per RF cycle. Simulation times took between  $1.0 \times 10^{-4}$  s to  $1.0 \times 10^{-3}$  s and 1 to 3 days of wall clock time (depending on flow velocity) due to the slow evolution of the neutral species densities in achieving cyclic convergence. The ion densities,  $\alpha$  values, and average sheath length of an RF discharge

in a flow are altered by the removal of the detaching species  $O_2(a)$ ,  $O_2(b)$ ,  $O(^3P)$ ,  $N_2(A)$ ,  $N_2(X, v=6-8)$ , and  $N(^4S)$  similar to the  $O_2(X)$  RF discharge. As was observed in the case of the  $O_2(X)$  RF discharge, when large densities of negative ions (large  $\alpha$  values) are present and detachment by neutral excited species is negligible, the active RF sheath length is reduced.

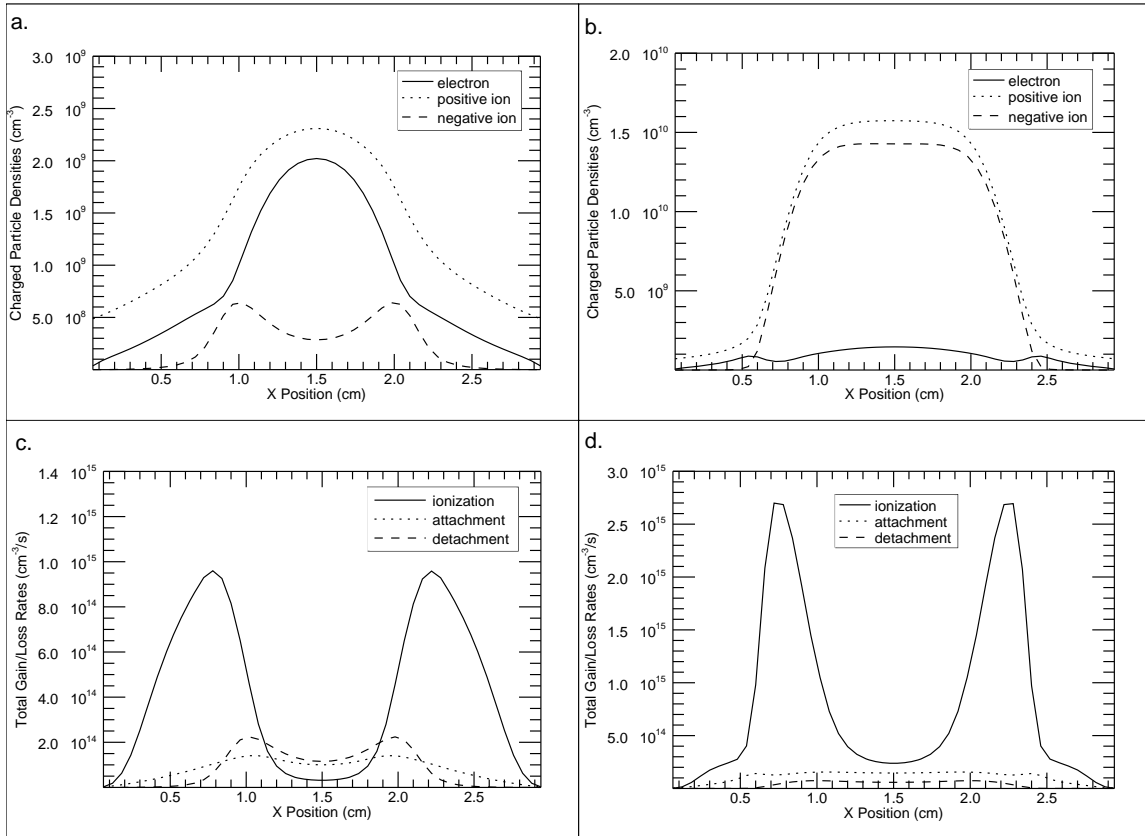
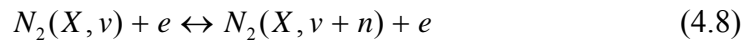


**Figure 4.26 Time Averaged Charged Species Densities in a  $N_2(X)$ - $O_2(X)$  RF Discharge in Conditions (a) Stationary (b) 250 m/s Flow (c) Bulk Loss/Gain Rates Stationary (d) Bulk Loss/Gain Rates 250 m/s Flow at 1000V Applied Voltage**

The compression of the sheath length increases the average electric field strength in the sheath region, which increases the ion flux and the time averaged electron flux to the electrode. The greater electron fluxes and electric fields result in additional Joule heating of the electrons at the edge of the sheath region. The increased Joule heating of

the electrons raises the mean energy of electrons similar to the results for an  $O_2(X)$  RF discharge. The higher electron mean energy in the sheath/pre-sheath region increases the ionization and dissociation rates and as a result the positive ion density increases with increased flow velocity as seen in Figure 4.26b. The increased ion flux and electric field result in a small increase ( $\sim 16\%$ ) of total current in the RF discharge, but nearly doubles the loss of positive ions and electrons to the electrode keeping the electron density approximately constant.

The density variations of the excited neutral species responsible for detachment are shown in appendix D. In the case of a stationary background gas,  $N_2(X, v = 6)$ ,  $O_2(b)$ ,  $N_2(X, v = 7)$ ,  $O(^3P)$ ,  $N_2(X, v = 8)$ , and  $N(^4S)$ , in order of significance, contribute the most to the detachment rate of  $O^-$ , which is the dominate negative ion species. Significant densities of  $N_2(X, v = 6 - 8)$ , shown in Figure 4.27, result in large part from stepwise electron excitation of the lower vibrational  $N_2(X, v = 1 - 3)$  states to  $N_2(X, v = 6 - 12)$  given by the equation



where the cross-section for this reaction is obtained from Polak and others, 1973,

$$\sigma(v \leftrightarrow v + n) = \sigma(0 \leftrightarrow n) / (1 + 0.05v). \quad (4.9)$$

where  $\sigma(0 \leftrightarrow n)$  is the cross-section of the electron excitation or de-excitation of  $N_2(X, v = 0)$  to  $N_2(X, v = n)$ . The direct electron excitation of  $N_2(X, v = 1 - 3)$  to higher vibrationally states results in the primary detaching species of negative ions being vibrationally excited states  $N_2(X, v = 6 - 8)$ . Detachment occurs in the fast reaction

rate of  $N_2(X, v = 6)$  with  $O^-$  given by the rate coefficient  $k_{v=6} = 2.7 \times 10^{-16} \text{ m}^3/\text{s}$  (Aleksandrov, 1978). This rate coefficient is twice as fast as the detachment rate of  $O(^3P)$  with  $O^-$  (Aleksandrov, 1978). The result that detachment by vibrational excited states dominates detachment of  $O^-$  for low ion temperature plasmas and slow flowing background gases is consistent with the results of Capitelli and others, 2000. The population of the vibrational states and the high vibrational temperature of  $T_v = 2440 \text{ K}$  (based on the ratio  $N_2(X, v = 1)$  to  $N_2(X)$ ) are on the order of the results obtained by Gordiets' and others, 1995, for their 15 mA DC discharge which was reported at  $T_v = 3000 \pm 500 \text{ K}$ . The temperature of the last vibrational state modeled is 284K indicating that the system achieved equilibrium with background gas. The increase in the slope of the state occupation curve, Figure 4.27b, at 3.1 eV or  $N_2(X, v = 11)$  is due to an increase in the V-T relaxation rate by  $O(^3P)$ .

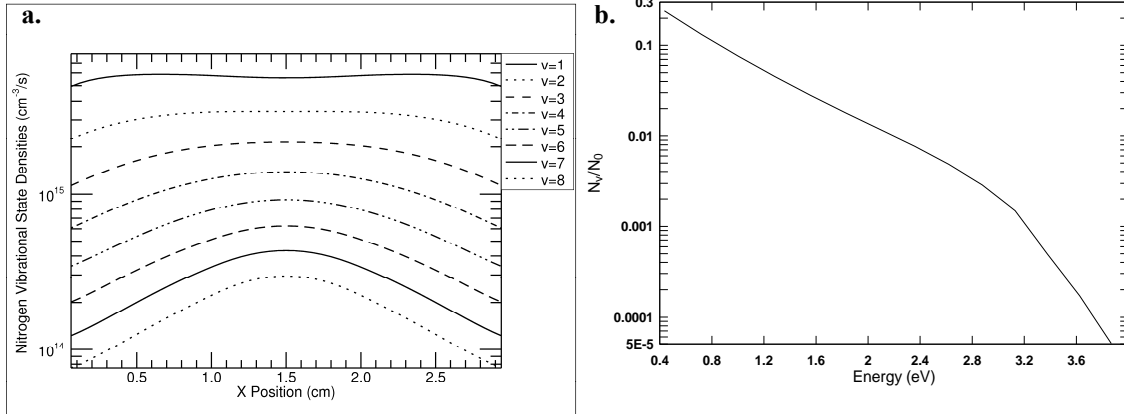


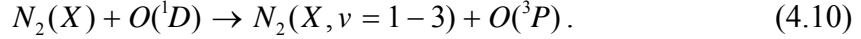
**Figure 4.27 Densities of  $N_2(X)$  Vibrational States (a)  $v = 1$  to 8 Densities Across the RF Discharge Region and (b) Ratio of the Peak Vibrational Density of the  $v = 1$  to 14 to the Background Gas Density for a Stationary  $N_2(X)$ - $O_2(X)$  Mixture Gas in a 1000V RF Discharge**

### **$N_2(X)$ - $O_2(X)$ RF Discharge in a 50 m/s Flow**

At low flow velocities ( $u_f = 50$  m/s),  $O(^3P)$ ,  $O_2(b)$ ,  $N_2(A)$ , and  $N_2(X, v = 6)$  become the primary detachers. The change in the primary detaching species from the stationary case occurs due to  $O(^3P)$ ,  $O_2(b)$ ,  $N_2(A)$ , and  $N_2(X, v = 6)$  production rates increasing with increased flow velocity, shown in Figure 4.32, where  $O_2(b)$  is created primarily by resonant reactions with  $O(^1D)$ . This result is similar to the  $O_2(X)$  RF discharge at higher flow velocities where the compression of the sheath lengths occurs due to the densities of the detaching species being reduced by flow losses. At flow velocities of 50 m/s, the dominant production mechanisms of  $O(^3P)$  are dissociation reactions resulting from the reaction of excited states  $N_2(B)$ ,  $N_2(C)$ ,  $N_2(a')$  with  $O_2(X)$  and electron impact dissociation (processes 48, 45, and 215 in Appendix C). The dominant production mechanisms for  $O_2(b)$  are quenching reactions of  $N_2(A)$  and  $O(^1D)$  with  $O_2(X)$  (processes 1 and 32 in appendix C). Processes 1, 32, 45, and 48 are heavy species reactions, however, the excited species  $N_2(A)$ ,  $N_2(B)$ ,  $N_2(C)$ , and  $O(^1D)$ , involved in reactions with  $O_2(X)$  to generate  $O(^3P)$  and  $O_2(b)$  are produced primarily by direct electron impact or by energy exchange with vibrational states  $N_2(X, v = 6 - 8)$ . The large densities of  $N_2(X, v = 6)$ , shown in Figure 4.27, result from the direct electron excitation of the more populated lower vibrational  $N_2(X, v = 1 - 3)$  states to the  $N_2(X, v = 6 - 12)$  states similar to the stationary case. The lower vibrational



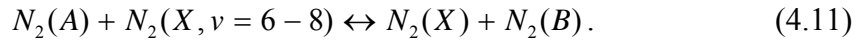
states,  $N_2(X, v = 1 - 3)$ , are populated in the quenching of  $O(^1D)$  by  $N_2(X)$  given by the reaction



The production of  $O(^1D)$  and direct electron excitation of lower vibrational states,  $N_2(X, v = 1 - 3)$ , are also both enhanced by the increased electric fields associated with a flowing background gas (previously discussed in the  $O_2(X)$  RF discharge section). These two mechanisms are responsible for the large vibrational populations at 50 m/s flow velocities.

#### **$N_2(X)$ - $O_2(X)$ RF Discharge at greater than 250 m/s Flow**

At flow velocities greater than 250 m/s,  $N_2(A)$  and  $O(^3P)$ , shown in appendix D, become the only significant detaching species. The population of  $N_2(A)$  is primarily balanced by energy exchange with vibrational states  $N_2(X, v = 6 - 8)$  given by reaction 43 and equation 4.11



The reaction rate associated with equation 4.11 is very high,  $k_{39} = 1.0 \times 10^{10} \text{ cm}^3/\text{s}$ , which results in the reaction quenching  $N_2(A)$  and  $N_2(X, v = 6 - 8)$  densities at lower flow velocities. However, as the density of  $N_2(X, v = 6 - 8)$  becomes sufficiently low at flow velocities greater than 150 m/s, equation 4.11 becomes less dominant in reducing the density of  $N_2(A)$ . The density of  $N_2(A)$  then becomes balanced only by flow losses, direct electron excitation, and fast energy exchanges of  $N_2(B)$  with  $N_2(X)$  through the reverse reaction given by equation 4.11 and reaction 42. Reaction 42 is also one of the

main production mechanisms of  $N_2(X, v=6)$  at flow velocities greater than 250 m/s.

The detachment rate of  $N_2(A)$  and  $O(^3P)$  at 250 m/s flow velocities is very small due to their reduced densities. The reduction in detachment rates at higher flow velocities results in the discharge becoming more electronegative in nature (similar to the electronegative  $O_2(X)$  RF discharge) and producing a 28% increase in the time averaged electric fields and charged species currents to the electrode seen in Figure 4.28 b and d.

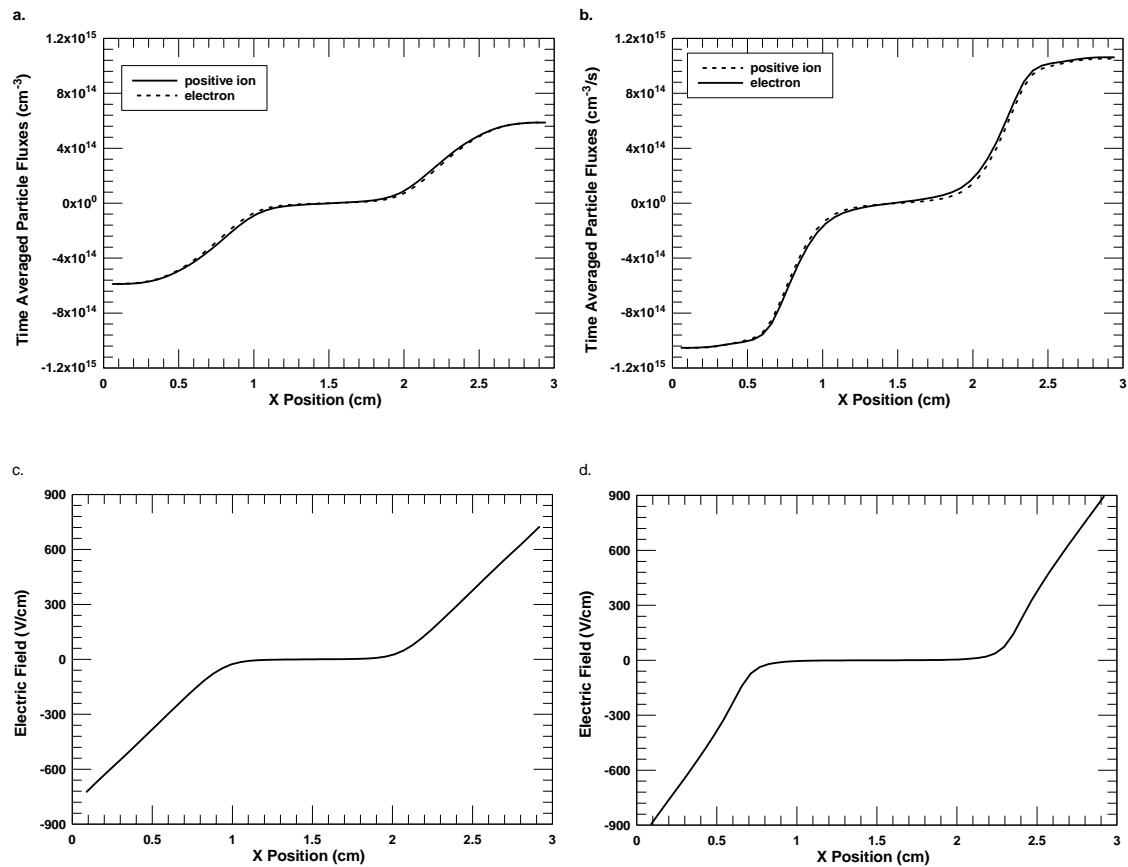


**Figure 4.28 Time Averaged Ion and Electron Flux in a  $N_2(X)$ - $O_2(X)$  RF Discharge in (a) Stationary (b) 250 m/s Flow Conditions. Time Averaged Electric Field in (c) Stationary (d) 250 m/s Flow Conditions at a 1000V Applied Voltage**

The time dependent electric fields and electron fluxes for the 0 m/s and 250 m/s cases are shown in Figure 4.29. Peaks in the electron flux in Figure 4.29b correspond to

the peaks in the electron density shown in Figure 4.25b which become prominent in the  $N_2(X) - O_2(X)$  mixture in the presence of a flow. Increases in the time dependent electric field and electron current density in the bulk plasma, shown in Figures 4.29b and 4.29d, due to flow are not as large as in the pure  $O_2(X)$  RF discharge case. The peak time dependent electric fields in the bulk plasma are  $E_B = 131$  V/cm and  $E_B = 170$  V/cm for the stationary and 250 m/s flow cases respectively. The difference is due to the lower  $\alpha$  value which results from the lower dissociative attachment rate associated with the  $N_2(X) - O_2(X)$  mixture. The lower  $\alpha$  value enables better shielding of the positive space charge of the sheath due to a larger percentage of the positive charge being shielded by electrons (described previously for the  $O_2(X)$  RF discharge comparison). The time dependent current densities in the stationary case exhibit more electropositive characteristics such as larger sheath, little ion current in the bulk plasma and lower total current through the discharge. At higher flow velocities, the current density is more electronegative in characteristic which is associated with smaller sheaths, non-negligible ion current in the bulk plasma, and larger displacement and total current. The compression of the sheath length and hence increase in the displacement and total current results in an increase in the power deposition in the discharge with increased flow velocity which was also observed in a pure  $O_2(X)$  RF discharge.

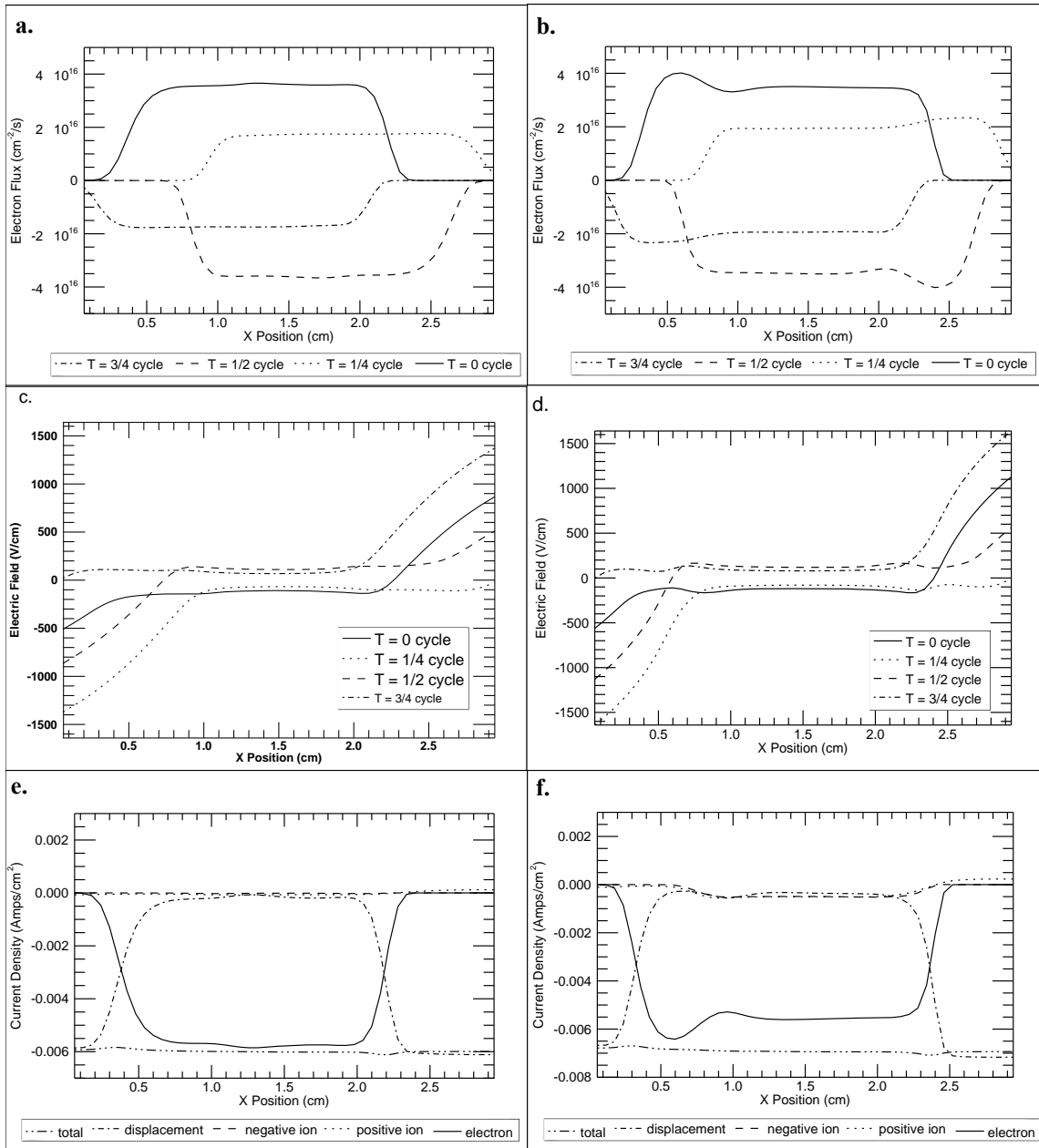


**Figure 4.29 Time Dependent Electron Current Density in a  $N_2(X)$ - $O_2(X)$  RF Discharge in (a) Stationary (b) 250 m/s flow conditions. Time Dependent Electric Field in (c) Stationary (d) 250 m/s Flow Conditions. Time Dependent Current Densities in (e) Stationary (f) 250 m/s Flow Conditions**

The effect of a wide range of flow velocities on the charged and neutral species densities is shown in Figures 4.30, 4.31, and 4.32. General trends from Figure 4.30 indicate that for velocities less than 150 m/s, the ionization rate and positive ion densities

increase with increasing flow velocity due to the sheath compression, shown in Figure 4.31. Negative ion densities also increase due to reduced detachment by excited neutral species. In the range of flow velocities between 100 m/s and 250 m/s, the ion densities remain approximately constant due to lower sheath compression and higher flow losses of charged species out of the discharge region. For flow velocities greater than 250 m/s, ion densities decrease due to the increased flow losses and no significant increase in the ionization rate. The lack of sheath compression results from detaching species densities being reduced sufficiently that the  $\alpha$  value does not increase any further. This effect is also seen in Figure 4.30 at 250 m/s where the production rate of electrons start to decrease because no additional ionization is occurring and the detachment rate has become negligible. Because detachment does not play a significant role in electron production at higher flow velocities, electrons and positive ions have essentially the same production rate at flow velocities of 500 m/s or greater.

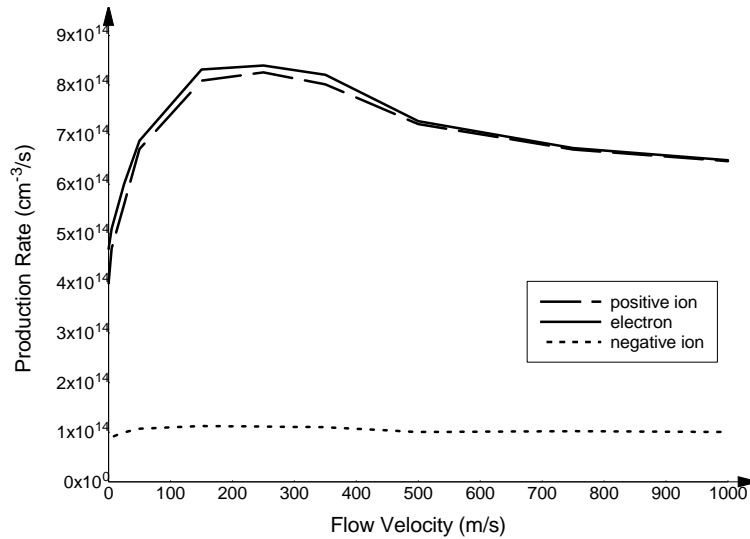


**Figure 4.30 Average Charged Species Production Rates in a Flowing  $N_2(X)$ - $O_2(X)$  Gas at Flow Velocities of 0 to 1000 m/s at a 1000V Applied Voltage**

The electron density in the discharge region for all flow conditions remains fairly constant within the discharge region regardless of the increase in the ionization rate due to the sheath length compression. The constant electron density in the discharge region is due to the increased ionization being balanced against losses associated with dissociative attachment and particle currents to the electrode which depend on the electric field amplitude in the sheath and the electron mean energy. The background gas flow velocity is negligible compared to the electron thermal velocity and there is low collisional coupling between the electrons and the background gas. These factors result in the flowing background gas having little direct effect on the electron density.

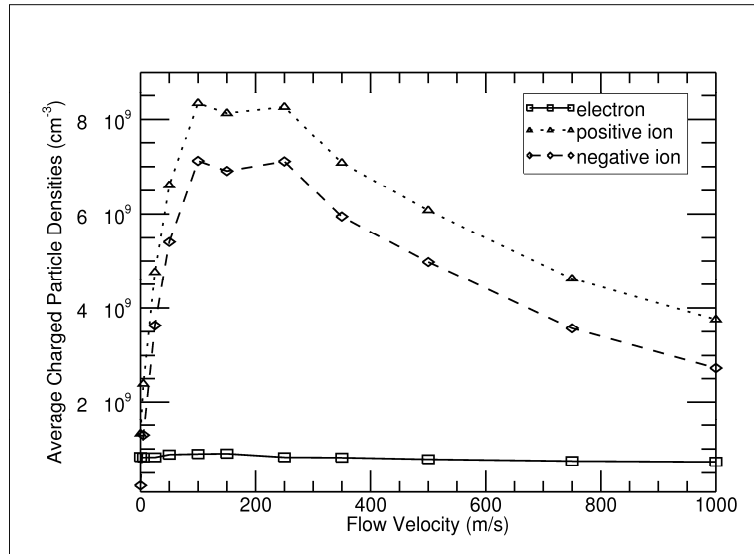


**Figure 4.31 Charged Species Densities in a  $N_2(X)$ - $O_2(X)$  Flowing Gas at Velocities of 0 to 1000 m/s at a 1000V Applied Voltage**

The total production rates averaged over the length of the discharge for the neutral excited species are shown in Figure 4.32. Dissociation and direct electron excitation

production rates for  $O(^3P)$ ,  $N_2(A)$ , and  $N(^4S)$ , increase with increasing flow velocity up to 150 m/s and then become constant or even decrease with increasing flow velocity. The total production rate of  $O(^3P)$ , shown in Figure 4.32a, decreases quickly from 0 m/s to 5 m/s. This is due to  $O(^3P)$  being created by several metastable electronic states,  $N_2(a')$  and  $N_2(B)$ , dissociating  $O_2(X)$ , through reactions 45 and 50, and  $N(^4S)$  dissociating  $NO(X)$  through reactions 116 – 119 and forming vibrationally states  $N_2(X, v = 1 - 4)$  and  $O(^3P)$ . The high densities of the electronic metastable states of  $N_2(X)$ , which create vibrationally excited states, and direct electron excitation of lower vibrational states  $N_2(X, v = 1 - 4)$  to higher vibrational states result in a large production rate of  $N_2(X, v = 6 - 7)$  when the background gas is not flowing. However, as flow velocities increase beyond 5 m/s the metastable and other vibrational states reduce in density. This results in direct electron excitation and the reaction given by equation 4.11 becoming the main producers of  $N_2(X, v = 6 - 7)$ .

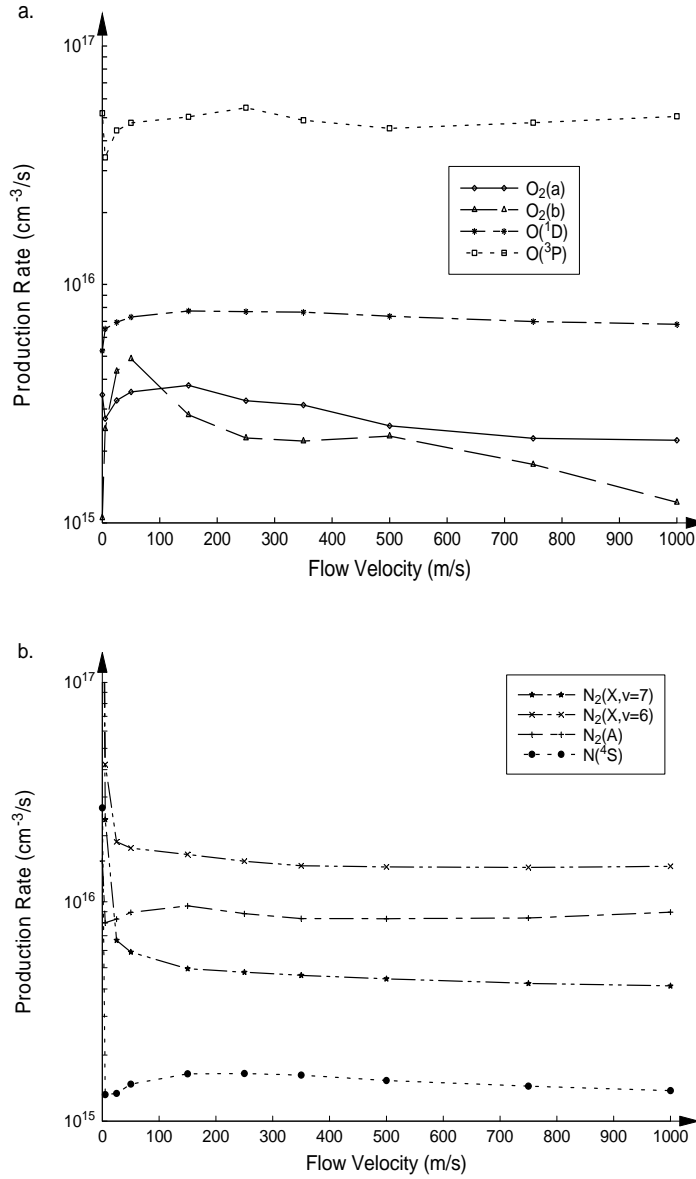


**Figure 4.32 Neutral Excited Species Production Rates in a  $\text{N}_2(X)\text{-O}_2(X)$  Flowing Gas for (a)  $\text{O}_2(X)$  species and (b)  $\text{N}_2(X)$  species at Velocities of 0 to 1000 m/s at a 1000V Applied Voltage Averaged Over the Discharge Gap**

Neutral excited species of interest, due to either being detachers or useful for material processing, are plotted as a function of flow velocity in Figure 4.33. In general, the densities of the excited species diminish with increasing flow velocity due to flow losses and the production rates, shown in Figure 4.32, being approximately constant at



flow velocities greater than 150 m/s. The  $N_2(A)$  density, however, increases as flow velocity increases from 0 m/s to 150 m/s, as seen in Figure 4.33, due to the reduction in the density of  $N_2(X, v = 6-8)$  vibrational states. The  $N_2(X, v = 6-8)$  vibrational states quench  $N_2(A)$  through the reactions given by equations 4.10 and 4.11. In Figure 4.33, we see a strong coupling between the species  $N_2(A)$  and  $N_2(X, v = 6-7)$  due to the fast reactions given by equations 4.10 and 4.11.

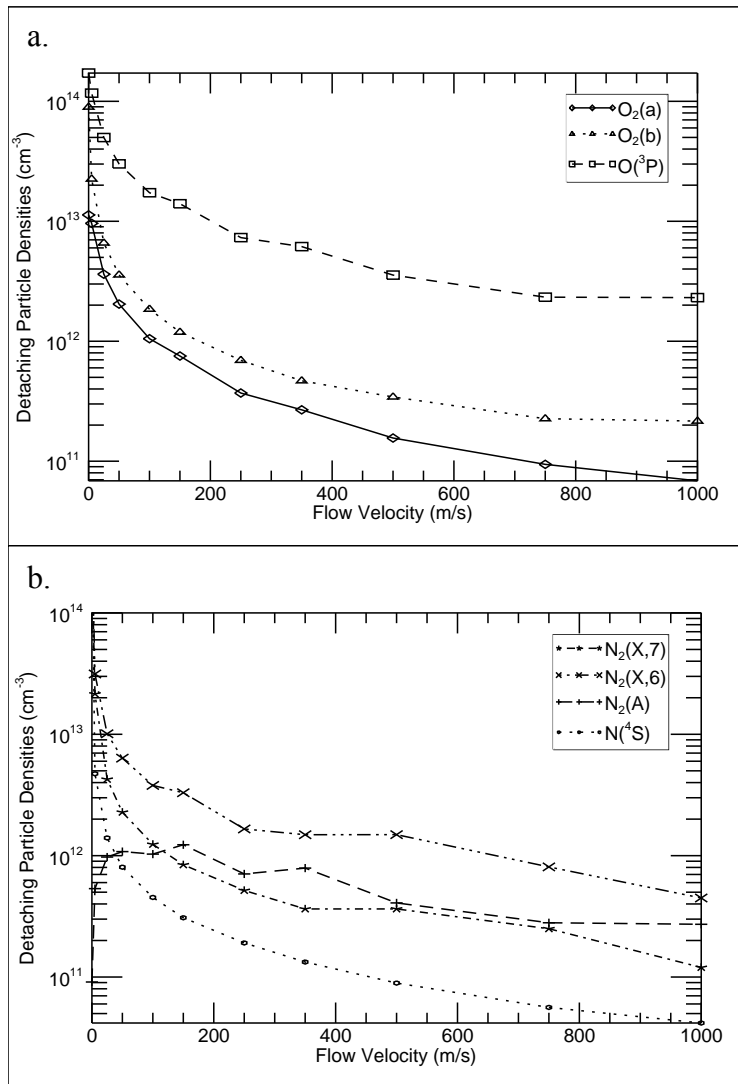


**Figure 4.33 Neutral Excited Detaching Species Densities in a  $N_2(X)$ - $O_2(X)$  Flowing Gas at Velocities of 0 to 1000 m/s in a 1000V Applied Voltage**

The increase in flow velocity also increases the power densities required to sustain the discharge. In the simulations, a constant RF voltage is maintained and the current density is allowed to vary. As the flow velocity increases, the current density and hence power required to sustain the RF discharge increases due to the increased losses of excited species which help sustain the discharge by detaching negative ions. Detachment is slightly more prevalent in an  $N_2(X) - O_2(X)$  discharges than in the  $O_2(X)$  RF discharge due to the abundance of excited species. However, in the  $N_2(X) - O_2(X)$  RF discharge, like the  $O_2(X)$  RF discharge, the role of detachment in reducing the power density requirements required to sustain the discharge is greatly diminished at higher flow velocities.

Comparing the results of  $O_2(X)$  and  $N_2(X) - O_2(X)$  RF discharges, we note that in both cases the production of negative and positive ions increases with increasing flow velocity. This is due to the compression of the active discharge sheaths associated with the increased negative ion density resulting from the convective removal of detaching neutral species. The density of the positive and negative ions, however, starts decreasing at 250 m/s which is about half the flow velocity at which the ion densities started to be reduced at in the  $O_2(X)$  RF discharge. This effect is attributed to the lower electronegativity and hence larger sheaths of the  $N_2(X) - O_2(X)$  RF discharge as well as the higher ionization threshold energy of  $N_2(X)$  and electron energy collisional loss rate associated with a  $N_2(X) - O_2(X)$  mixture. The higher electron energy loss rate reduces the overall electron mean energy and hence ionization rate in the discharge.

The densities of excited neutral species created by the RF discharge decrease with increasing flow velocity with the notable exception of  $N_2(A)$ , which at higher flow velocities becomes important at detaching negative ions. The change (with increasing flow velocity) in the importance of various neutral excited species in detaching negative ions is similar to the results from the  $O_2(X)$  RF discharge and is dependent on the production mechanism of the neutral species and the collision partners required for the reaction. Neutral excited species created by higher frequency electron processes, such as dissociation, generally do not reduce in density as quickly as species produced by lower frequency processes. However, certain excited neutral species quench other excited neutral species (such as the quenching reactions that occur between  $N_2(X, v = 6 - 7)$ ,  $N_2(A)$ , and  $N(^4S)$ ) and as a result, the primary excited species responsible for detaching negative ions changes at higher flow velocities than in the  $O_2(X)$  RF discharge.

As with  $O_2(X)$  RF discharges, the higher flow velocities are not intended for producing high relative densities of excited neutral species. However, the production rate of neutral excited species in the  $N_2(X)$  and  $O_2(X)$  mixture RF discharge increases with increasing flow velocity which creates higher neutral excited species fluxes. Higher neutral excited species fluxes are desirable for remote plasma enhanced Chemical Vapor Deposition (CVD) and etching processes that require large fluxes of neutral excited species to enhance the uniformity of deposition, photoresist removal and reactive etching (Collart and others, 1995). In the next section, the convection and decay of the plasma and excited neutral species downstream of the RF discharge region is investigated using a 2-D model of the flow tube. Results from the 2-D modeling of an  $N_2(X) - O_2(X)$

mixture show that significant densities of positive and negative ions can be convected downstream and electrons can be produced downstream of the discharge due to detachment of the negative ions by neutral excited species generated in the discharge.

### **Two Dimensional RF Discharge Results in a Flow Tube**

In this section, the results of the one dimensional simulations are extended to determine what charged and neutral species densities can be expected downstream of the RF discharge. To examine the evolution of the plasma downstream of the RF discharge, the one dimensional PFM described previously was extended to two dimensions.  $O_2(X)$  and  $N_2(X) - O_2(X)$  mixture background gases with chemical kinetic reactions were considered and the neutral and charged species densities convected downstream of the discharge are investigated. The plasma is generated by an RF discharge that is oriented perpendicular to the background gas flow in the tube as shown in Figure 4.1. The plasma is then convected downstream by the flowing background gas. In the simulation, the RF electrodes are spaced 3 cm apart and the simulation extends 15 cm downstream and 5 cm upstream of the RF discharge region. The two dimensional RF discharge simulations were run using 800 time steps or more per RF cycle on a 30 by 250 node grid in the x and y directions respectively. The small time step was required to satisfy the dielectric relaxation time step restriction,  $\Delta t < 8.0 \times 10^{-11}$  s, driven by downstream conditions. The large number of Newton-Raphson steps used for the implicit Crank-Nicholson time advance was found to be more computationally intensive than allowing the simulation time step to be less than the dielectric relaxation time. The small time steps combined with the relatively slow evolution of the neutral excited species resulted in run times of

approximately 8 to 16 weeks despite the acceleration processes developed in Chapter II. Results of the simulations indicate that a plasma with a large electron density and neutral species densities can be generated with a reasonable amount of voltage and power. In addition, chemical kinetic reactions play a significant role in producing and maintaining a large electron density downstream and causing the positive and negative ion densities to decay rapidly downstream of the RF discharge.

First, we examine the two dimensional plasma simulation considering stationary and flowing gas conditions. Initially chemical kinetics will not be included for either flow condition. Results of a two dimensional RF discharge in stationary and flowing conditions with the absence of chemical kinetics are presented to provide a basis of comparison to an RF discharge with flow included. We then examine  $O_2(X)$  and  $N_2(X) - O_2(X)$  mixture cases in a flowing background gas with the full chemical kinetics considered in a flowing background gas. The charged and neutral species densities convected downstream are investigated and compared to the results without chemical kinetics included.

Simulation results for a 1000V, 1 Torr  $O_2(X)$  RF discharge in a stationary background gas in the absence of excited neutral species are shown in Figure 4.34. The positive ion density profile shown in Figure 4.34a is nearly parabolic in the direction of the discharge current in the bulk plasma region between the electrodes. The electron density, shown in Figure 4.34a, has peaks near the electrode which is due to the field reversal phenomenon observed in the one dimensional  $O_2(X)$  RF discharges previously.

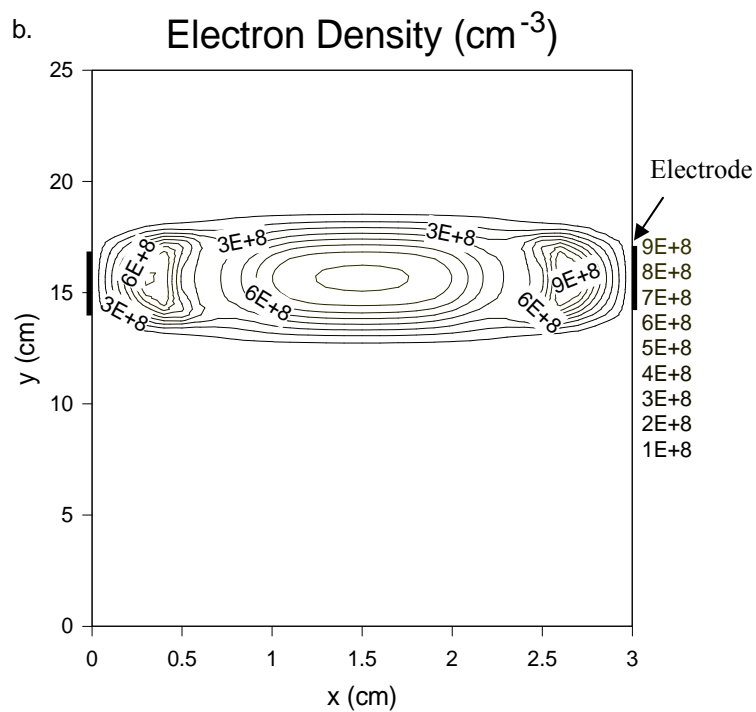
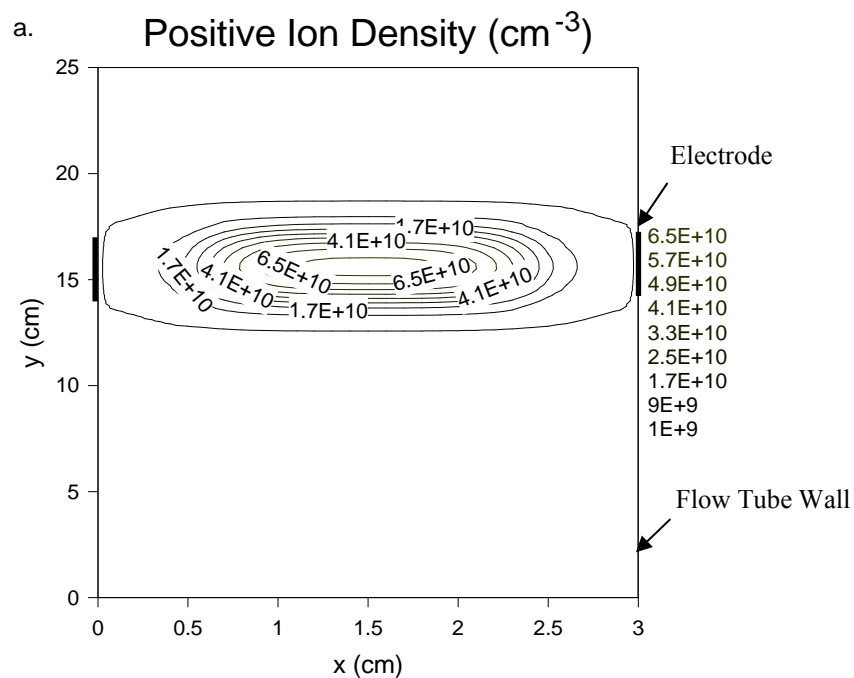


**Figure 4.34 Densities in a 2-D  $O_2(X)$  RF Discharge in a Stationary Gas (a) Positive Ion Density (b) Electron Density at a 1000V Applied Voltage and 1 Torr Pressure with No Heavy Species Chemical Kinetics**

The time dependent variations of the electric field and current density, along the centerline of the electrodes in the two dimensional discharge are essentially identical to the one dimensional results shown in the 1-D  $O_2(X)$  RF discharge results section.

Transition effects can be seen in the sheath region in the density of the electrons and ions near the interface of the metal electrode with the dielectric of the flow tube material are observed. The transverse profiles of the charged species densities are shown in Figure 4.35a. The Gaussian profile is consistent with the dominance of ambipolar diffusion.

The transverse ambipolar diffusion electric field, which keeps the electrons and negative ions contained in the discharge region, is plotted in Figure 4.35b. Due to the lack of detaching species, the  $\alpha$  value of the discharge is very high resulting in a low ambipolar electric field transverse to the RF discharge (Lieberman and Lichtenberg, 1994).

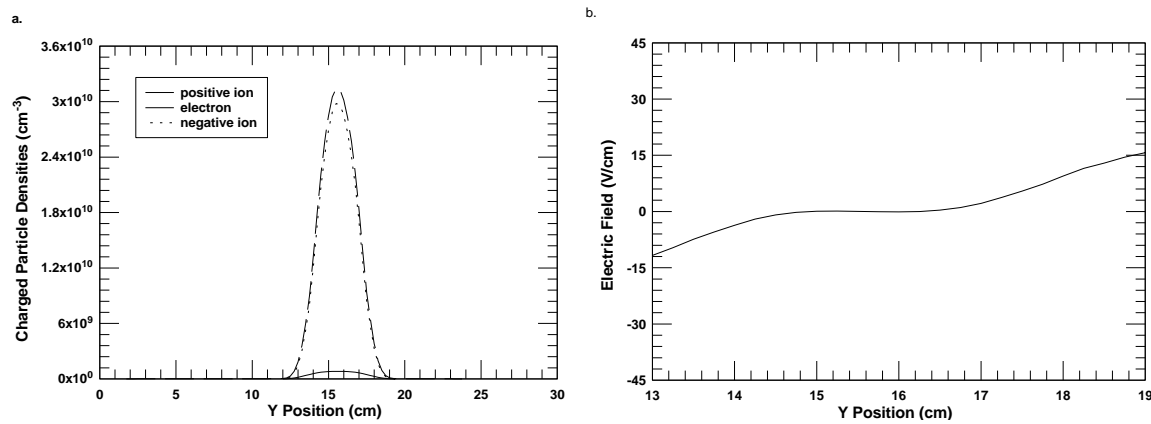


**Figure 4.35 (a) Charged Species Densities (b) Ambipolar Field of an  $O_2(X)$  RF Discharge in a Stationary Gas at 1000V and 1 Torr Pressure with No Chemical Kinetics 1-D Center Profile**

Results from the stationary two dimensional RF discharge simulation suggest that one dimensional RF discharge simulations provide adequate insight into the characteristics of the RF discharge for the parameters of interest. As a result, the stationary two dimensional case is only presented here to enable comparison between the densities and

electric fields in the flowing and stationary case. Next, we examine the effect of a flowing background gas on the RF discharge in the absence of excited neutral species and compare the results to the stationary case.

### **Electronegative $O_2(X)$ RF Discharge with Flow**

In the presence of a flowing background gas, the plasma generated by the RF discharge is convected downstream due to the collisional coupling between the background gas and the ions as shown in Figure 4.36. The collisions of the background gas with the negative ions occur frequently enough, at 1 Torr and  $\lambda_i = 1.57 \times 10^{-3}$  cm, to surmount the ambipolar potential well that normally traps the negative ions in the discharge region in the absence of flow. The peak in the positive and negative ion densities, shown in Figure 4.36a, is displaced downstream of the center of the electrodes. The ambipolar electric field transverse to the RF discharge, shown in Figure 4.37, repels the negative ions upstream (the enhanced transverse ambipolar fields do not allow the majority of the negative ions to escape discharge region) and balances the momentum transferred to the negative ions by the flowing background gas resulting in the peak of the negative ion density being displaced downstream. In Figure 4.36, the density profile of the positive ions in the center of the discharge region is also displaced slightly downstream due to collisions with the flowing background gas and lower electric fields in the center of the discharge. However, near the electrodes, the velocity of the positive ions towards the electrode is dominated by the electric field in the sheath and the flow velocity and momentum transfer of the background gas is negligible in comparison. As in the electronegative  $O_2(X)$  RF discharge case presented previously, no excited neutrals species are included in the simulation and as a result the density of the electrons outside



of the discharge region decays rapidly. The rapid decay is due to attachment processes and a lack of ionization to sustain the density resulting in a positive and negative ion plasma downstream of the discharge as seen in Figure 4.36b. Outside of the discharge region, the mean energy of the electrons decreases and densities are reduced rapidly due to both overcoming the ambipolar electric field transverse to the RF discharge and inelastic collisions in the absence of Joule heating. When the electrons are reduced to lower energies on the order of the electron affinity ( $\varepsilon = 0.43 \text{ eV}$ ) of molecular oxygen, three body attachment, instead of disassociative attachment (electron affinity to atomic oxygen is  $\varepsilon = 1.5 \text{ eV}$ ) becomes the dominant attachment mechanism (Aleksandrov, 1978). As a result of the losses associated with three-body attachment and diffusion of electrons to the wall with no production via ionization or detachment to balance these losses, the electron density downstream of the discharge becomes negligible. The poor collisional coupling between the electrons and the background gas result in minimal momentum transfer of the flowing background gas to the electrons. Therefore, collisions alone are insufficient for the electrons to surmount the ambipolar fields of the discharge and be convected downstream.

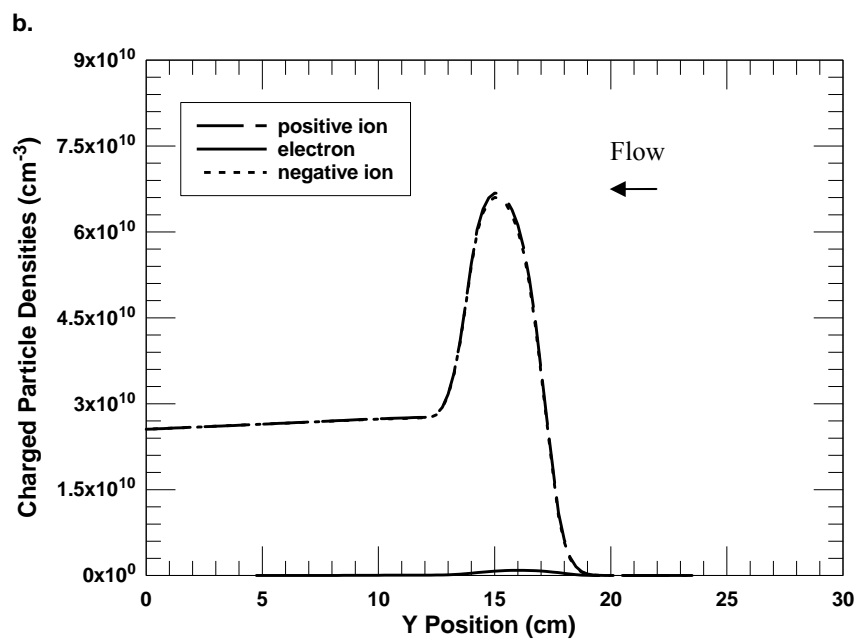
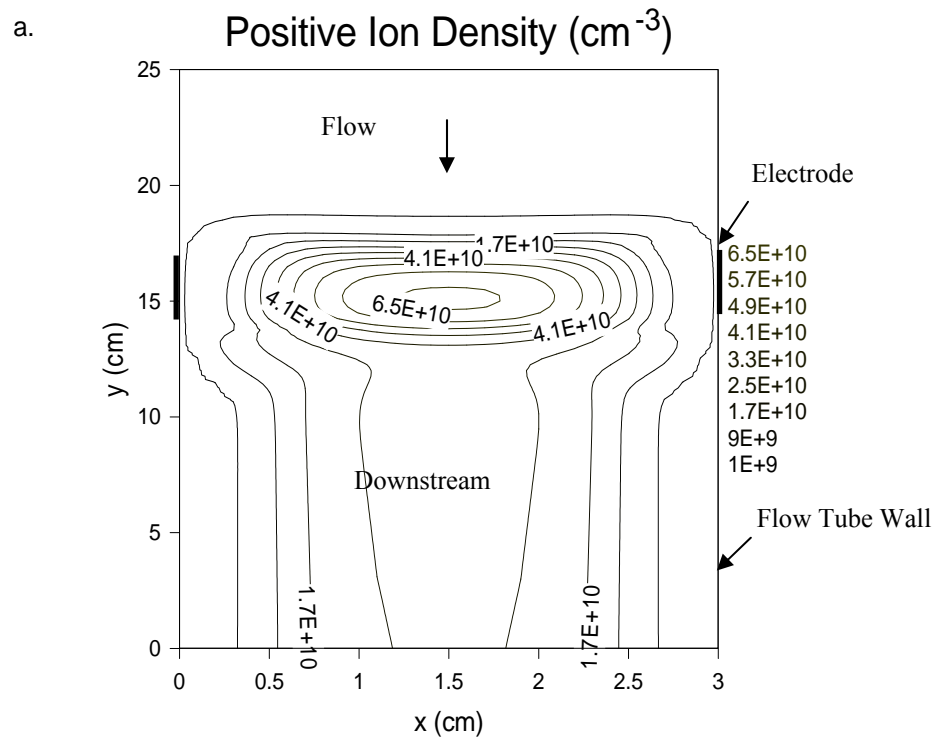


**Figure 4.36 Charged Species Densities of an  $\text{O}_2(\text{X})$  RF Discharge in a 250 m/s Flow (a) Contour Plot of Positive Ion Densities (b) 1-D Center Profile of Charged Species Densities with No Chemical Kinetics**

Due to the ambipolar fields transverse to the RF discharge repelling the negative ions, the density of the negative ions falls rapidly outside of the discharge region. Positive ion densities decay with the negative ions in the ambipolar field to maintain quasi-neutrality. The rapid decay in the negative ion density stops at about 2 cm downstream of the electrodes as shown in Figure 4.36. After the positive and negative ions are convected downstream of the ambipolar fields, their density decays very slowly due to the slow rates of recombination and ambipolar diffusion to the walls. The decay rate of the positive ions in a highly electronegative plasma can be described by the equation

$$\frac{dn_i}{dt} = -k_r n_n n_i - \frac{D_a}{\Lambda^2} n_i \quad (4.12)$$

where the ambipolar diffusion is given by  $D_a \approx 2D_i$  for large values of  $\alpha$  (Lieberman and Lichtenberg, 1994). The absence of excited neutral species makes the convection of electrons downstream of the discharge non-existent at moderate pressures of 1 Torr for any highly electronegative gas. In addition, the exclusion of neutral excited species also results in an underestimation of the decay rate of positive and negative ions downstream of the discharge.

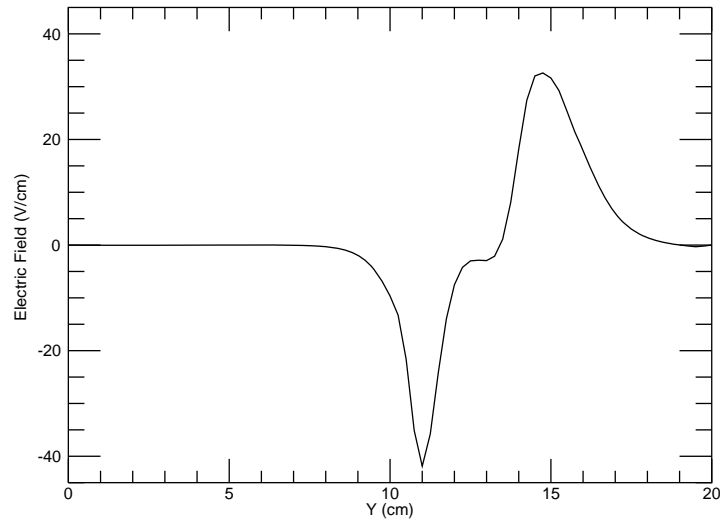


**Figure 4.37 Ambipolar Electric Field in a  $N_2(X)$ - $O_2(X)$  RF Discharge in a 250 m/s Flow at 1000V and 1 Torr Pressure with Neutral Excited Species 1-D Center Profile**

### **$O_2(X)$ and $N_2(X)$ - $O_2(X)$ RF Discharge with Excited Neutrals**

Including excited neutral species in the  $O_2(X)$  RF discharge changes both the density of the electrons and the decay rate of the positive and negative ion densities downstream of the RF discharge as shown in Figure 4.38. Due to the presence of the flowing background gas, as was observed in the 1-D case, the  $O_2(X)$  RF discharge has a large  $\alpha$  value resulting from the detaching neutral species in the discharge region not developing large enough densities to balance out the dissociative attachment reaction.

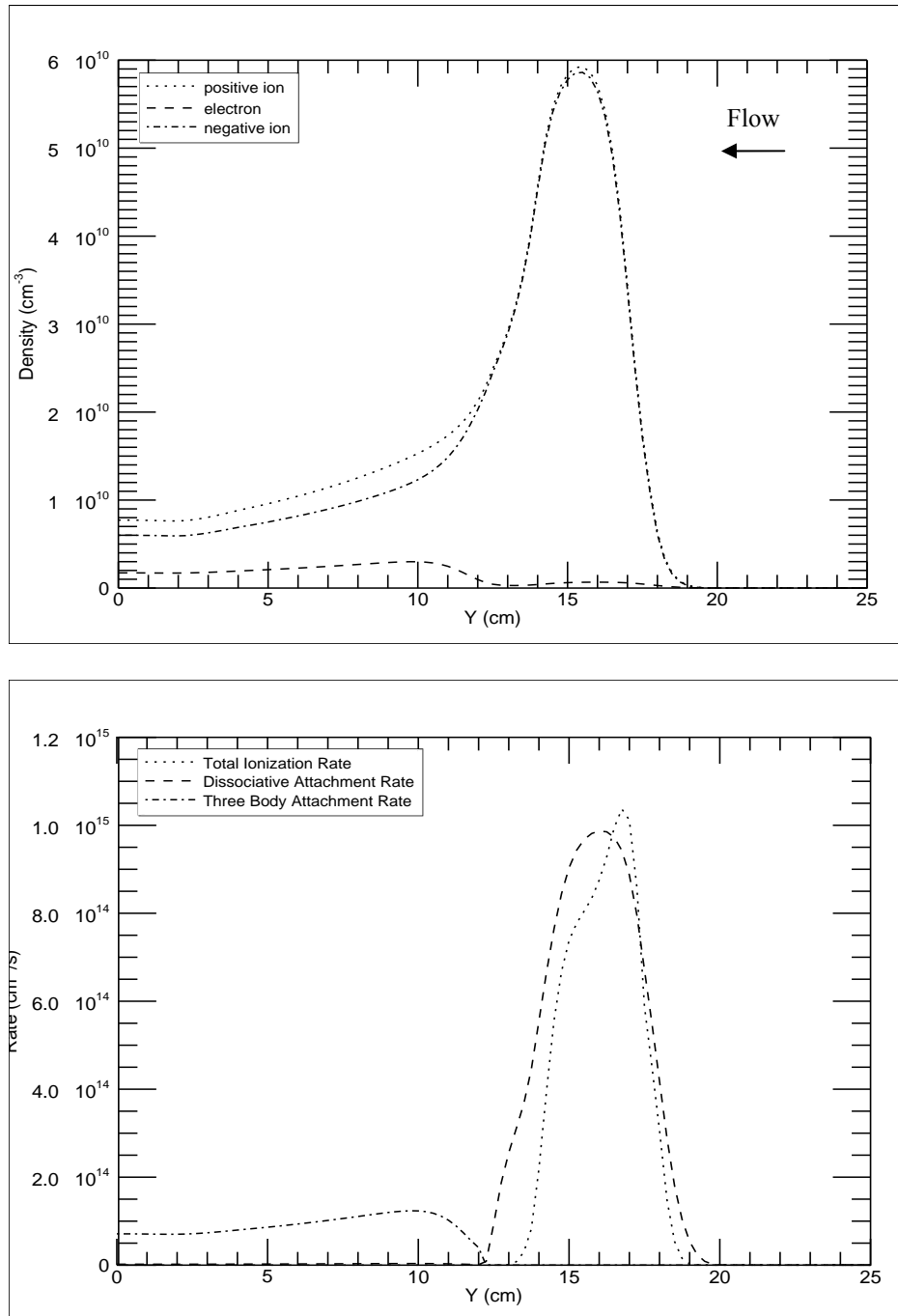


**Figure 4.38 Species Densities of an  $O_2(X)$  RF Discharge in a 250 m/s Flow at 1000V Applied Voltage 1-D Center Profile**

The neutral excited species that are responsible for detaching negative ions tend to be metastable electronic states of both  $O_2(X)$  and  $N_2(X)$ . The densities of  $O_2(a)$ ,  $O_2(b)$

and  $O(^3P)$  downstream for a pure  $O_2(X)$  RF discharge are shown in Figure 4.39.

Because of the short residence time of the background gas in the discharge region, the densities of  $O_2(a)$  and  $O_2(b)$  remain approximately constant downstream of the discharge due to their gains and losses being primarily due to slow heavy species reactions and quenching by the wall. In most laser related experiments, whose aim is to produce the maximum density of  $O_2(a)$ ,  $O(^3P)$  is the major quencher of both  $O_2(a)$  and  $O_2(b)$ . Densities of  $O(^3P)$ ,  $O_2(a)$ , and  $O_2(b)$  are low for the flow velocities considered in this study since the quenching of  $O_2(a)$  and  $O_2(b)$  by  $O(^3P)$  is unimportant: this result is consistent with the results of Zimmerman, 2003. The slight reduction in density of  $O(^3P)$  downstream of the discharge is due primarily to quenching by the wall.

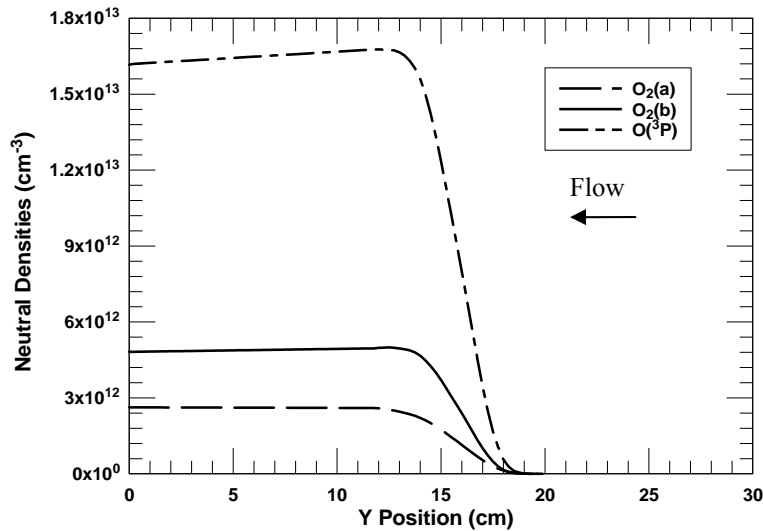


**Figure 4.39  $O_2(X)$  Species Densities in an RF Discharge in a 250 m/s Flow at 1000V Applied Voltage 1-D Center Profile**

The results shown in Figure 4.39 are reasonably consistent with the density profiles predicted by the GlobalKin model results of Zimmerman, 2003; however, Zimmerman's

flow velocities are much lower resulting in much more pronounced increases and decreases in neutral species densities within and downstream of the discharge.

After exiting the discharge region, the evolution of the charged species densities downstream is very dependent on the excited neutral species densities produced in the RF discharge. In Figure 4.39, we observe the fast decay of the positive and negative ions directly downstream of the RF discharge due to the ambipolar electric field repelling the negative ions. The negative ion densities in the presence of neutral excited species decay much more rapidly due to detachment than the previous case when neutral excited species were not included. The density of the positive ions decreases due to the decrease in the  $\alpha$  value. This results in increases in the ambipolar diffusion coefficient which is shown by Lieberman and Lichtenberg, 1994, to be

$$D_a \approx D_i \frac{1 + \gamma_n + 2\gamma_n \alpha}{1 + \alpha \gamma_n}. \quad (4.13)$$

As a result of the presence of  $O_2(a)$ ,  $O_2(b)$  and  $O(^3P)$ , the electron density increases downstream of the RF discharge due to the detachment rate remaining approximately the same and the total attachment rate decreasing downstream of the discharge. The decreasing attachment rate is due to a change from dissociative attachment to three-body attachment as the primary attaching process shown in Figure 4.40b. The combination of both the negative ion density and excited neutral species contribute to the large density of the electrons downstream of the discharge. The density decay of the electrons and positive and negative ions downstream of the ambipolar fields can be approximately described by equation 2.56 which compares precisely with the density decay profiles shown in Figure 4.40a.

Downstream of the  $O_2(X)$  and  $N_2(X)$ - $O_2(X)$  RF discharge, the dominant negative ion species eventually changes from  $O^-$  to  $O_2^-$ . The change in the negative ion identity is due to the reduction in the electron temperature downstream of the discharge, shown in Figure 4.40, which results in the three body attachment process becoming dominant. The three body attachment reactions (415 and 416 in Appendix C) at 1 Torr is much less than the dissociative attachment rate in the RF discharge region. As a result, the transition of the dominant negative ion species occurs over a longer distance than the domain of the simulation. The transition of the dominant attachment mechanism from dissociative attachment to three body attachment is shown in Figure 4.41.

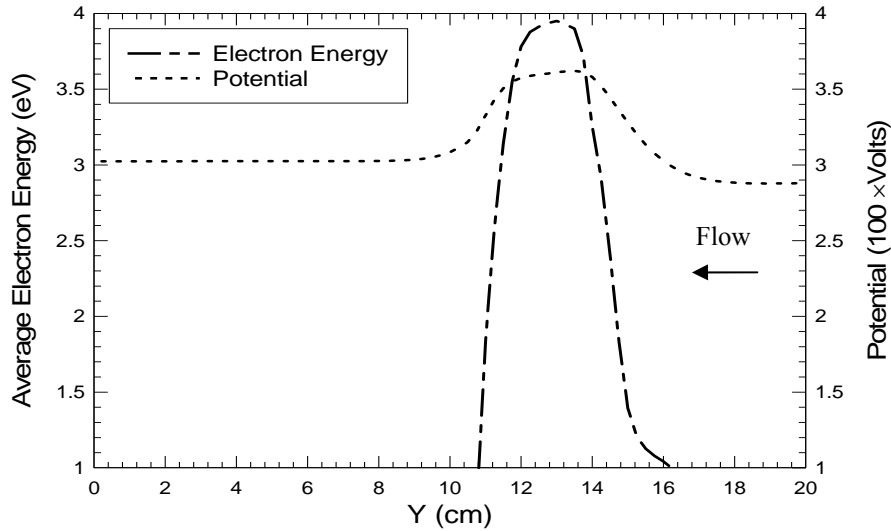


**Figure 4.40 Mean Electron Energy of  $N_2(X)$ - $O_2(X)$  RF Discharge in a 250 m/s Flow at 1000V Applied Voltage 1-D Center Profile**



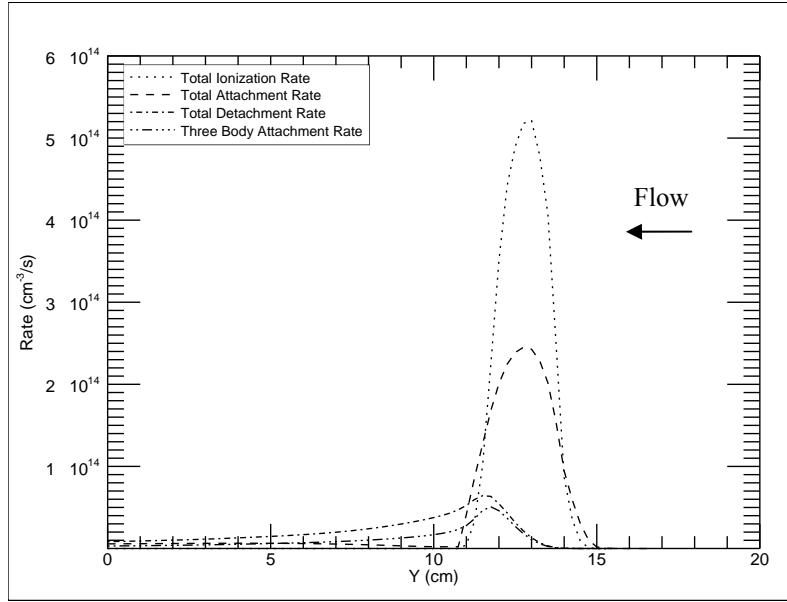


**Figure 4.41 Production Rates of a  $N_2(X)$ - $O_2(X)$  RF Discharge in a 250 m/s Flow at 1000V Applied Voltage using a 1-D Center Profile**

The presence of electrons downstream of the RF discharge is observed for both the pure  $O_2(X)$  and the  $N_2(X) - O_2(X)$  gas mixture discharges as shown in Figure 4.42. The electron densities and mean energies downstream of the RF discharge are fairly similar in both background gases.

The major difference between  $O_2(X)$  and  $N_2(X) - O_2(X)$  mixture discharges is seen in the negative and positive ion densities. The lower densities of the negative ions are due to the lower dissociative attachment rates in the  $N_2(X) - O_2(X)$  mixture versus pure  $O_2(X)$ . The lower density of positive ions is due to reduced mean electron energy resulting from increased electron inelastic collisions in an  $N_2(X) - O_2(X)$  mixture.

Another difference between the discharges in the two gases is the more peaked profile of the positive and negative ions in the discharge, which is due to the lower ionization rates of an RF discharge in an  $N_2(X) - O_2(X)$ . The lower ionization rate results in the positive

ion density not saturating before reaching the end of the discharge. The lower ionization rates are due to the higher ionization threshold energy (15.6 eV for  $N_2(X)$  versus 12.0 for  $O_2(X)$ ) and energy relaxation rate of  $N_2(X)$ .

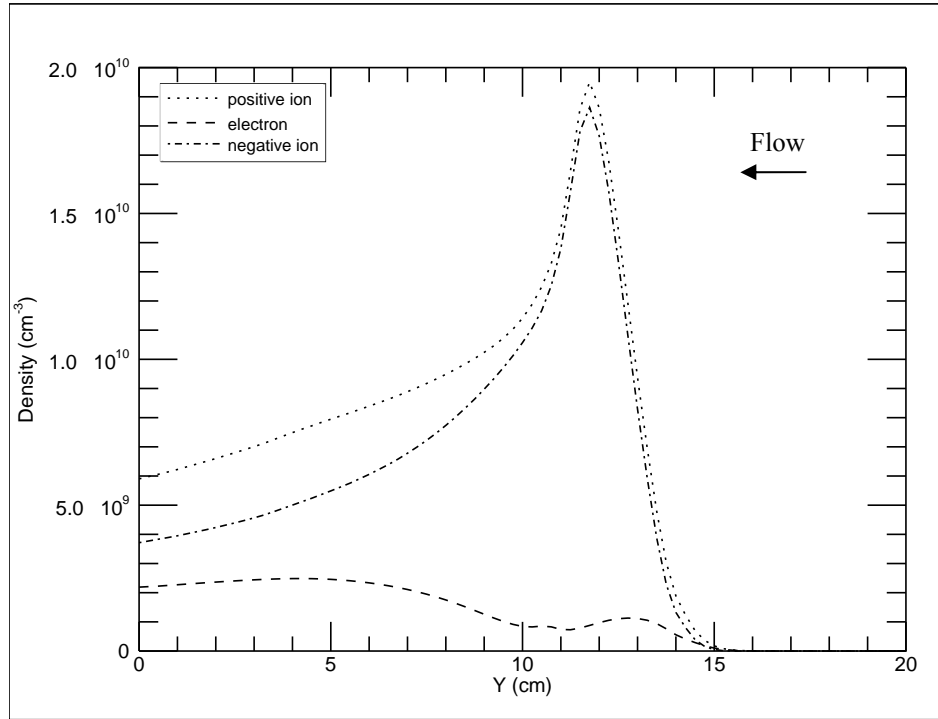


**Figure 4.42 Charged Species Densities in a  $N_2(X)$ - $O_2(X)$  RF Discharge in a 250 m/s Flow at 1000V Applied Voltage 1-D Center Profile**

The primary loss mechanisms of positive ions in a  $N_2(X)$  -  $O_2(X)$  gas mixture downstream of the RF discharge are ambipolar diffusion to the tube walls and ion-ion recombination. The negative ion density decays due to detachment and recombination reactions as well. Excited neutral species densities, depending on the species, are quenched or created in either inelastic collisions with other species or by deactivation at the wall of the flow tube. The excited neutral species primarily responsible for detaching

negative ions in a  $N_2(X) - O_2(X)$  gas mixture and maintaining the high electron densities downstream of the RF discharge are plotted in Figures 4.43 and 4.44.

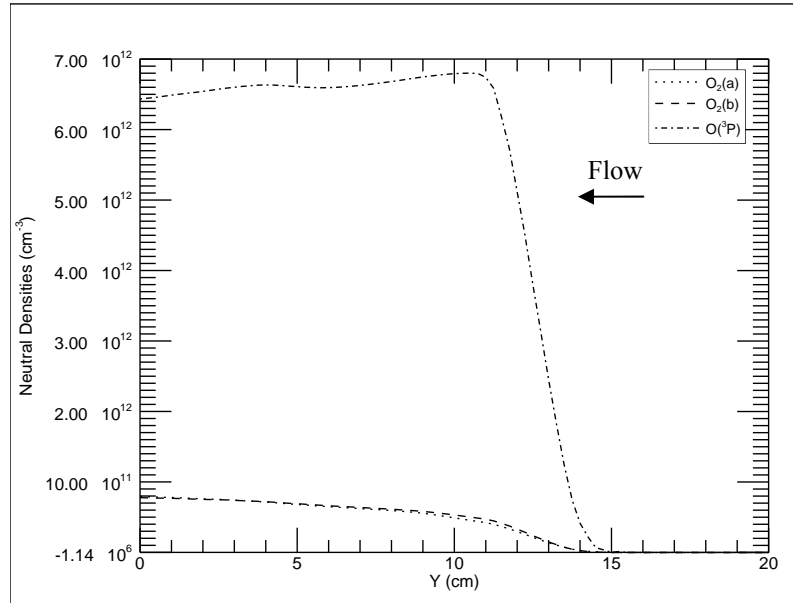
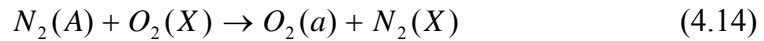


**Figure 4.43  $O_2(X)$  Species Densities in a  $N_2(X) - O_2(X)$  RF Discharge in a 250 m/s Flow at 1000V Applied Voltage 1-D Center Profile**

The densities of excited neutral species generally decay downstream of the RF discharge due to the previously mentioned loss mechanisms, however, in the case of  $O_2(a)$ ,  $O_2(b)$ , and  $N_2(X, v = 7)$ , the densities actually increase due to higher energy excited states being deactivated and producing these species. An example of such a reaction, reaction 31, is given by



which is the primary production mechanism of  $O_2(a)$  in the downstream region.

In  $O_2(X)$ , the metastable state  $O_2(a)$  is most responsible for the detachment of negative ions downstream of the RF discharge based on the excited species density and the higher detachment coefficient,  $k_a = 3.0 \times 10^{-10} \text{ cm}^3/\text{s}$ . In the  $N_2(X) - O_2(X)$  mix,

$N_2(A)$  and  $O(^3P)$  are most responsible for detachment of negative ions downstream with the detachment coefficients being  $k_A = 2.2 \times 10^{-9} \text{ cm}^3/\text{s}$  and  $k_O = 1.4 \times 10^{-10} \text{ cm}^3/\text{s}$  respectively.

Relatively high densities of vibrationally excited nitrogen,  $N_2(X, v = 6 - 8)$ , compared to what is expected are observed downstream of the discharge. The reason for the relatively high density of  $N_2(X, v = 6 - 8)$  is primarily due to the relaxation of higher vibrational states,  $v = 7 - 15$ , described by reaction 42 and the large reduction in density of  $O(^3P)$  and  $N(^4S)$  due to low residence times of the background gas. Reaction 42 specifically excites the  $N_2(X, v = 6 - 8)$  states with fast excitations by  $N_2(B)$ .  $N_2(B)$  is made through the reverse of reaction 42 and reaction 37 from  $N_2(A)$  generated in the discharge region. A primary production reaction of  $N_2(B)$  is given by



$N_2(B)$  immediately excites the vibrational states  $N_2(X, v = 6 - 8)$  through the near resonant reaction 42 given by equation 4.11. The reaction given by equation 4.15 and the reverse of reaction 42 result in the fast decay in  $N_2(A)$  downstream of the discharge, seen in Figure 4.44. The V-T coefficient and reaction rate of  $N_2(X, v = 6)$  with  $N_2(X)$  from equation 3.9 and 3.10 is  $k_{6,5} = 3.11 \times 10^{-14} \text{ cm}^3/\text{s}$  and  $1.297 \times 10^{15} \text{ cm}^{-3}/\text{s}$ , which is lower than the excitation rate of  $N_2(X, v = 6)$ ,  $5.5 \times 10^{15} \text{ cm}^{-3}/\text{s}$ , resulting from reaction 42 downstream of the discharge region. The V-T relaxation rate with atomic species, such as  $O(^3P)$  where  $k_{6,5} = 6.6 \times 10^{-14} \text{ cm}^3/\text{s}$  and  $k_{7,6} = 1.0 \times 10^{-13} \text{ cm}^3/\text{s}$ , is generally the highest for  $N_2(X)$ - $O_2(X)$  discharges (Gordiets and others, 1995), however, the low

densities of this species result in a low relaxation rate of vibrationally excited  $N_2(X)$  at fast flow velocities. This sequence of reactions and reduced V-T rates by atomic species results in a relatively large population of vibrationally excited  $N_2(X)$  downstream of the discharge. The density of  $N(^4S)$  is approximately constant downstream of the RF discharge due to the low densities of the other excited species as well as the low quenching rates and wall deactivation coefficients associated with  $N(^4S)$ .

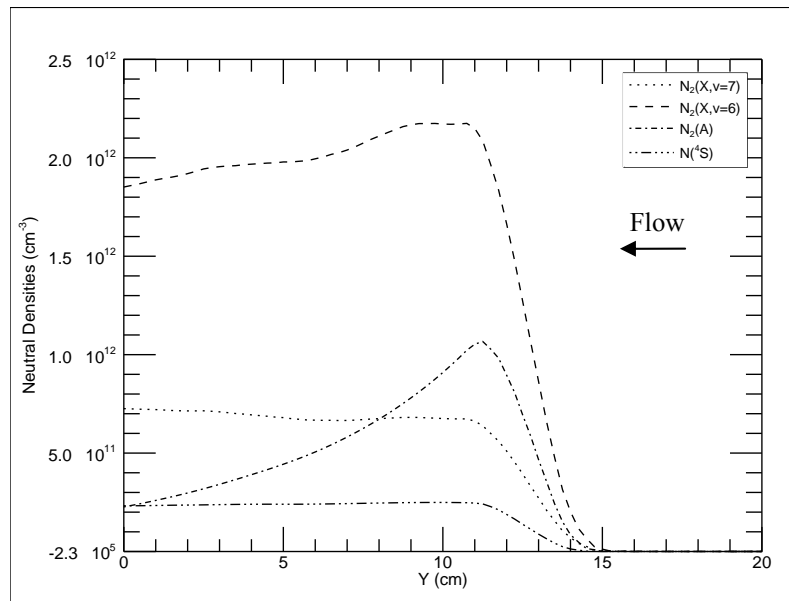


**Figure 4.44  $N_2(X)$  Species Densities in a  $N_2(X)$ - $O_2(X)$  RF Discharge in a 250 m/s Flow at 1000V Applied Voltage Using a 1-D Center Profile**

The results from the two dimensional simulations of the RF discharge in  $O_2(X)$  and the  $N_2(X)$  -  $O_2(X)$  mixture indicate that it is possible for a fast flowing background gas to convect a reasonably large density of positive and negative ions,

$n_i = 1.7 \times 10^{10} - 8.0 \times 10^9 \text{ cm}^{-3}$  depending on distance from the discharge, downstream of the RF discharge. The change in the dominant attachment process from dissociative attachment in the discharge to the slower three-body attachment process downstream

combined with the presence of excited neutral species results in an appreciable electron density downstream. This change in attachment processes results in a larger density of cold electrons downstream,  $n_e = 2.5 \times 10^9 - 2.0 \times 10^9 \text{ cm}^{-3}$  depending on distance downstream, of the RF discharge than was maintained in the discharge region,  $n_e = 8.7 \times 10^8$ , to sustain the discharge. This effect has the potential of providing an electron density downstream capable of sustaining a second discharge in the double discharge ElectriCOIL application being investigated by Pitz and others, 2004, and Hicks, 2006. The negative ions convected downstream,  $n_n = 1.55 \times 10^{10} - 6.0 \times 10^9 \text{ cm}^{-3}$ , can contribute to the second discharge's electron density supply through detachment by the neutral excited species generated by the second discharge. In addition, positive and negative ions convected downstream also produce an independent source of ions for a second discharge that can be used to etch semi-conductor and other substrate materials. For the application of producing high densities of excited molecules and atomic species, the flow velocities investigated in this section were too large compared to the length of the discharge along the flow tube. The large flow velocities resulted in low residence times of the background gas in the discharge region which did not allow sufficient time to produce large densities of neutral excited species. As was seen in the one dimensional RF discharge section, the production rate of excited neutral species produced by fast sheath driven processes, such as dissociation, increase due to the shrinking of the sheath width in the presence of a flow. This effect can potentially be utilized to produce higher quantities of neutral excited species for fast, uniform growth of materials such as  $\text{SiO}_2$  doped with  $\text{N}(^4\text{S})$ . Some production methods used to dope  $\text{SiO}_2$  with  $\text{N}(^4\text{S})$  depend less

on the density of the atomic oxygen and nitrogen species to the background gas and more on the flux of atomic species to the substrate (Ellis and Buhrman, 1998).

In the next chapter, we investigate three Langmuir probe methods for performing diagnostics on the positive ion density in a low and moderate pressure electronegative background gas. These methods are compared to standard methods used to perform diagnostics on flowing and stationary electropositive and electronegative plasmas.

Differences in the simulation and theory results are analyzed and modifications to theory are suggested to enable more accurate diagnostics of a Langmuir probe in a fast flowing electronegative background gas.

## V. Langmuir Probe in a Flowing Electronegative Plasma

To perform probe diagnostics of an electronegative plasma convected downstream of a RF discharge requires an examination and assessment of the methods currently used to analyze the current voltage characteristic of a Langmuir probe in an electropositive plasma. Due to the complexity of the probe sheath in a transitional collisional regime and the additional complexities of a flowing electronegative plasma, both a drift-diffusion fluid and Particle-in-Cell model are used to investigate the probe sheath and ion current collected by the probe. Recognizing the limitations of the validity of the drift-diffusion fluid model in lower pressure regimes ( $P < 0.1$  Torr), a PIC-MCC model was selected to evaluate the utility of a Langmuir probe and standard analysis techniques for determining the ion density of a plasma in a fast flowing, low pressure background gas. The PIC-MCC model is valid for any collisional regime; however, at higher pressures the number of collisions per time step dramatically increases the computation resources required to simulate a Langmuir probe response. Therefore, to model the  $P \sim 1$  Torr pressure regime, where the drift-diffusion fluid equations are valid, the plasma fluid model developed in Chapter II was modified to model the ion current collection of a Langmuir probe. In the following section, an overview of the basic PIC-MCC modeling methodology and computational constraints are presented. Specific aspects of the geometry and boundary conditions used to model a Langmuir probe and a comparison of the PIC-MCC results to a one dimensional time independent fluid model are presented.



## **Langmuir Probe Model Using a PIC-MCC Method**

PIC-MCC models have been used as effective tools for investigating plasma behavior and have been found to be particularly useful in analyzing inductively and capacitively coupled RF and DC discharges, cross-field devices, traveling wave tubes, and other vacuum devices (Cartwright and others, 2000) and (Kawamura and others, 2005). PIC-MCC models have been successfully employed in modeling low and moderate pressure RF discharges in either electropositive or electronegative gases and provide an excellent means of modeling spatial and temporal fluctuations of a plasma (Williams, 1997).

The underlying physical principles of the PIC-MCC model can be divided into two parts, finding the fields generated by the charged particles densities and currents and determining the motion of the charged particles produced from the fields. The fields from the charged particles are determined using Maxwell's equations or Poisson's equation, the forces on the particles due to the fields are calculated using the Newton-Lorentz equation. Momentum and energy changes due to collisions experienced by the charged particles while traveling through a background gas are determined using a Monte Carlo Collision (MCC) model. The background gas is given both a thermal and directed velocity for the purposes of determining the momentum and energy transferred between the charged particle and the background gas. Since, the number of particles in a plasma is very large, macro-particles are used to represent all the particles in the plasma. Macro-particles are single particles weighted to represent a large number of particles while still maintaining the same charge-to-mass ratio,  $q/M$ , as a single particle, resulting in the

macro-particles moving like single particles. The macro-particle positions and velocities are interpolated to a grid to create charge and current densities for use in Maxwell's equations (or Poisson's equation if modeling an electrostatic problem such as the Langmuir Probe). Using Maxwell's equations avoids the computational overhead of calculating the Coulomb interactions between the large number of particles in the simulation. Once the fields have been determined at the grid points, they are interpolated to the particles' positions, so that the forces on the particles can be calculated (Birdsall, 1985). The PIC approach described above self-consistently determines the fields, particle concentrations, charged particles distributions, and current densities of the plasma.

A spatial grid is introduced in order to determine the electric and magnetic fields or the scalar potential for the electromagnetic or electrostatic cases respectively. As a result of interpolating particle positions and velocities to the grid points and interpolating fields from the grid points to the macro-particles, the force on each particle depends on the distance to other particles (a physical force – Coulomb forces) and the particle's position within the cell (a non-physical force). Higher order interpolation and finer grids reduce non-physical forces experienced by the particles. Therefore, to achieve reasonable physical results, limitations on time step, spatial separation of the grid points, and numbers of macro-particles must be observed. For the overall discharge to be modeled accurately by the PIC-MCC method, the length of the discharge must be much larger than the Debye length  $L \gg \lambda_D$  (Birdsall, 1985). The Debye length is the distance traveled by a particle at its thermal velocity during a plasma oscillation given by

$$\lambda_D \equiv \frac{v_{th}}{\omega_p} \propto \left( \frac{T}{n} \right)^{1/2} \quad (5.1)$$

Also in order to keep the charge density of the modeled plasma from shifting by a large amount between each time step, the spatial grid spacing,  $\Delta x$ , must be smaller than the Debye length,  $\Delta x < \lambda_D$ , and the time step,  $\Delta t$ , must be less than a plasma oscillation period,  $\Delta t < \frac{2\pi}{\omega_p}$ . An additional time step constraint that also must be observed for accurate results to be achieved is the CFL condition that was discussed in chapter II and is described by equation 2.54. The CFL condition for the full solution of Maxwell's equations is given by  $\Delta t < \frac{\Delta x}{c}$ , which insures that the modeled EM wave does not skip over any cells. If the PIC simulation is electrostatic then there is no EM wave propagation and the velocity of the fastest moving particle becomes the limiting velocity for the purposes of determining the CFL condition. The accuracy of the PIC-MCC method is limited by the resolution of the MCC model, the grid spacing, time steps, and number of macro-particles. If computational resources allow the PIC modeler to meet or exceed the limits of grid spacing, time step, and number of macro-particles expressed previously then the fidelity of a PIC-MCC model is very high.

PIC-MCC models, however, do have difficulties modeling low temperature plasmas due to numerical heating (Turner, 2006). Numerical heating is caused by temporal fluctuations in the electric field due to the discrete nature and limited number of macro-particles and their random motion from cell to cell. In most plasma PIC simulations, the numerical heating is caused primarily by the electrons due to their higher thermal velocities. The fluctuating electric field in a PIC simulation, results in temporal changes of the electron temperature which cause the plasma potential to fluctuate with

time. The numerical heating causes the sheath to oscillate and the velocity of the ions entering the sheath to vary with time. The variation of the ion velocity results in a smearing of the pre-sheath/sheath transition and reduces the accuracy of the modeled sheath. Numerical heating is also more problematic for PIC codes at lower pressures because collisions with the background gas act to balance out the numerical heating of the particles providing an energy loss mechanism (Turner, 2006). In addition, for radial cylindrical geometries (the coordinate system used to model a cylindrical Langmuir probe) fewer macro-particles are present in each cell near the axis due to the decreased volume of the cell (when the density and macro-particle weighting are held constant). Lower numbers of macro-particles towards the axis result in a very noisy, numerically heated sheath for the Langmuir probe due to single particles transferring between cells. Methods of varying the weighting of the macro-particles (reducing the number of physical particles that each macro-particle represents) to keep the number of macro-particles per cell constant with changing radius results in unphysical, spurious diffusion of the lower weighted particles to the outer radius of the computational domain. Therefore, to surmount the problems associated with modeling a low pressure, cylindrical probe sheath with a reasonable amount of computational resources and accuracy required that a hybrid PIC-MCC approach be employed.

The Improved Concurrent Electromagnetic Particle-in-Cell (ICEPIC) model was used as the basis for the development of a hybrid PIC-MCC model that is presented next. The ICEPIC model is capable of being run in up to three dimensions using either a cylindrical or Cartesian geometry. The user can specify a complex geometry and system using a combination of basic shapes and multiple particle types, particle injection

methods, and boundary conditions. ICEPIC can run in either an electromagnetic mode, solving the complete set of Maxwell's equations, or electrostatic mode, solving only Poisson's equation. The electrostatic solver, which is used for the Langmuir probe model, solves Poisson's Equation using a conjugate gradient method. Particles are transported in ICEPIC using the Boris push method and the Monte Carlo Collision routine uses the null collision method (Surendra and Vahedi, 1990). ICEPIC can be run on either serial or parallel computer architectures with distributed or shared memory using MPI or PVM message passing protocols. ICEPIC has been run on up to 2048 processors simultaneously and has simulated billions of macro-particles on hundreds of millions of computational nodes for a single simulation. The next section provides an overview of the modifications that were made to ICEPIC to overcome many of the problems associated with a full PIC-MCC model in modeling a low temperature plasma sheath.

### **Hybrid PIC-MCC Model**

For a full PIC-MCC model to be stable and produce good numeric results, it must satisfy CFL and plasma oscillation time step constraints, which are on the order of  $10^{-10} - 10^{-11}$  seconds for an electrostatic problem with low energy electrons and sub-millimeter grid spacing. The ions, however, move very slowly, even in the sheath, on this time scale ( $u_{ion} \approx 10^5$  cm/s) resulting in a considerable number of time steps required to achieve a steady state result (time steps  $\approx 10^6$  from the CFL condition). Due to the time step constraints and the numeric heating problems associated with a full PIC-MCC

model, a hybrid simulation method was adopted based on an approach developed by Cartwright and others, 2000. The hybrid simulation assumes that the electrons are in Boltzmann equilibrium with the electric field of the probe sheath. The spatial Boltzmann equilibrium distribution as a function of potential difference is given by the expression

$$n(\vec{x}) = n(\vec{x}_R) \exp((V(\vec{x}) - V(\vec{x}_R)) / T) \quad (5.2)$$

where

$\vec{x}_R$  - location of the reference potential

The velocity distribution of the electrons is also in thermal equilibrium and hence has a Maxwellian velocity distribution described by the following equation:

$$n(\vec{x}, \vec{v}) = n(\vec{x}) \frac{1}{4\pi} \sqrt{\frac{2}{\pi}} \left(\frac{m}{T}\right)^{3/2} e^{-mv^2 / 2T} . \quad (5.3)$$

The Maxwell-Boltzmann particles, however, do not come to true thermal equilibrium in a system where the potential is finite at the boundaries due to the tail of the distribution existing out to an indefinite energy (Cartwright and others, 2000). As a result, the particles in the tail of the Maxwell-Boltzmann distribution near the walls can escape the bounded system yielding a truncated Maxwell-Boltzmann distribution. However, in a system where the difference between the plasma and wall potential is several multiples of the electron temperature ( $V_{plasma} - V_{probe} \gg T_e$ ), the effects of the truncated Maxwell-Boltzmann distribution on the density profile can be shown to be negligible. Therefore, equation 5.3 is integrated over the entire velocity space resulting in equation 5.2 with little impact on the accuracy of the density profile for the particles (Cartwright and others, 2000). Equation 5.2 can then be used to replace the electron density in Poisson's

equation, while the positive and negative ion density is obtained from the macro-particles in the PIC-MCC simulation. The result is given by the expression

$$\nabla^2 \Phi = -\frac{e}{\epsilon_0} (n_{PIC} - n(\vec{x}_R) \exp((V(\vec{x}) - V(\vec{x}_R)) / T)) \quad (5.4)$$

where  $n_{PIC}$  is the density of the particles accumulated on the computational grid each time step. Using the Newton-Raphson method, which was presented in Chapter II, equation 5.4 is linearized in accordance with Cartwright's approach and can be written as

$$\frac{\partial \delta(\phi^i(x))}{\partial \phi^i(x)} \phi^{i+1}(x) = -\delta(\phi^i(x)) + \frac{\partial \delta(\phi^i(x))}{\partial \phi^i(x)} \phi^i(x) \quad (5.5)$$

where

$$\frac{\partial \delta(\phi^i(x))}{\partial \phi^i(x)} = (\nabla^2 - \frac{e}{\epsilon_0 kT} n(\vec{x}_R) e^{(V^i(\vec{x}) - V(\vec{x}_R)) / T}) \quad (5.6)$$

$$\delta(\phi^i(x)) = -\frac{e}{\epsilon_0 kT} n(\vec{x}_R) e^{(V^i(\vec{x}) - V(\vec{x}_R)) / T} \quad (5.7)$$

Equation 5.5 is then finite-differenced, and solved using a standard conjugate gradient method in ICEPIC to obtain the potential and electron density at each point in the computational grid.

The convergence of this hybrid method is highly dependent on having the correct density of the Maxwell-Boltzmann species,  $n_0$ , at the reference potential. To determine this value we start with the continuity equation given by

$$\frac{dn}{dt} + \vec{\nabla} \cdot (n\vec{u}) = g - l \quad (5.8)$$

where  $g$  and  $l$  are the gain and loss terms respectively. Integration of equation 5.8 over the bounded volume results in

$$\frac{dN}{dt} + \oint_S n\vec{u} \cdot d\vec{S} = G - L \quad (5.9)$$

Here,  $N$  is the number of particles in the volume and  $G$  and  $L$  are the volumetric gains and losses of particles from the bounded system. Using an Euler integration method, the change in the number of particles is given by the expression

$$\Delta N = (G - L)\Delta t \quad (5.10)$$

In this simulation, electron density losses were restricted to losses to the wall (which is important primarily for the initial start of the simulation). The flux of electrons to the wall is calculated by obtaining the average electron density from equation 5.3 at the wall

$$\Gamma_{wall} = n(\vec{x}_{wall}) \int \vec{v} \cdot \hat{n} \frac{1}{4\pi} \sqrt{\frac{2}{\pi}} \left(\frac{m}{T}\right)^{3/2} e^{-mv^2/2T} d^3\vec{v} \quad (5.11)$$

where  $n(\vec{x}_{wall})$  is the electron density next to the wall. Integration of equation 5.11

results in the well known thermal flux to a wall given by the expression

$$\Gamma_{wall} = \frac{n(\vec{x}_{wall})v_{th}}{4} \quad (5.12)$$

From this expression the volumetric losses of electrons to the walls can be calculated by integrating the flux over the surface of the walls resulting in the following loss expression for each grid point

$$L = \sum_i \frac{n(\vec{x}_i)v_{th}}{4} \Delta S_i \quad (5.13)$$

Electron gains depend on the type of plasma being modeled. In order to maintain charge neutrality of the simulation, the gain rate of the electrons is the same as the gain rate of



the positive ions minus the negative ion gain rate. To replenish the density of the ions lost to the surfaces in the simulation, the lost ions are reinserted back into the simulated region at a location depending on the simulation set-up (the reinsertion of the macro-species into the simulation region is discussed further in the model set-up section).

The hybrid PIC-MCC method's convergence is also dependent on having a stable potential reference point. The reference potential is commonly chosen to be the plasma potential which gives physical insight into the trade off of potential for kinetic energy in the pre-sheath and sheath of the plasma. However, due to the noise of the plasma potential in the PIC method and the exponential response of the Boltzmann distribution function, the simulation was found to commonly diverge if the plasma potential is used as the potential reference. Therefore a grounded wall was used as the reference potential for the hybrid PIC method. The number density of the electrons at the reference potential,  $n(\vec{x}_R)$ , is calculated by numerically integrating the electron Boltzmann distribution function over the volume of the simulation

$$N = \oint n(\vec{x}_R) \exp((V(\vec{x}) - V(\vec{x}_R)) / T) dV \quad (5.14)$$

and then solving for the number density at the reference potential

$$n(\vec{x}_R) = \frac{N}{\oint \exp((V(\vec{x}) - V(\vec{x}_R)) / T) dV} \quad (5.15)$$

where  $N$ , the total number of electrons in the simulation, is determined from equation 5.14 (Cartwright and others, 2000).

The approach presented in this section was added to the ICEPIC computer model and allows over a two order magnitude increase in time step because the electrons are no longer moving across cells, hence the CFL condition applies to the much slower ions

which in  $O_2(X)$  have a thermal velocity of  $v_{th} = 4.74 \times 10^4$  cm/s. This method also reduces the numerical heating associated with the fast movement of the electron macro-particles from cell-to-cell which cause fluctuations of the charge density on the grid resulting time varying fields. A similar approach for investigating a flowing plasma has been used successfully by Hutchinson, 2004, for modeling a spherical Mach probe in a flowing plasma. In the next section, we compare the results of the hybrid PIC-MCC model to the pre-sheath sheath model developed in chapter I.

### **Hybrid PIC-MCC Langmuir Probe and Sheath Model Comparison**

To insure the validity of the hybrid PIC code in modeling a Langmuir probe, comparisons were made between ICEPIC and a sheath model developed by Kono, 2000. The comparison was performed in the radial direction for a cylindrical geometry in a low pressure (0.001 Torr) oxygen plasma. At lower pressures the ion inertia term of the fluid equations cannot be ignored due to the reasons stated in Chapter II, therefore the one dimensional sheath model is used in the comparison against the hybrid PIC-MCC model. In the following section, the hybrid PIC model and the pre-sheath and sheath model developed in Chapter I are compared.

The model, given by equations 1.43, 1.44, and 1.45 for the sheath and 1.50 for the pre-sheath, are compared to the results of a one dimensional, three velocity component (1-D-3v) hybrid PIC model in a cylindrical geometry. The hybrid PIC geometry is that of two concentric cylinders, with the inner cylinder having a radius of 1 cm with bias of -9 V relative to ground and a grounded outer cylinder with a radius of 7 cm. The large cylindrical inner radius of the simulation is used to reduce noise associated with the reduction in the number of macro-particles with smaller volumes near the axis of the

simulation. An electronegative plasma with the parameters:  $n_{i,0} = 5.8 \times 10^9 \text{ cm}^{-3}$ ,  $n_{e,0} = 1.0 \times 10^9 \text{ cm}^{-3}$ , negative ion to electron ratio,  $\alpha_0 = 4.8$ ,  $\sigma_i = 1.8 \times 10^{-14} \text{ cm}^2$ , and temperatures  $T_e = 2.0 \text{ eV}$ ,  $T_i = T_n = 0.025 \text{ eV}$  resulting in a Debye length of  $\lambda_D = 0.33 \text{ mm}$  was run for  $1.0 \times 10^5$  time steps. The simulation grid spacing is  $\Delta r = 0.1 \text{ mm}$  and  $3.3 \times 10^6$  and  $2.7 \times 10^6$  macro-particles were used to simulate the positive and negative ions respectively. Due to the ion mean free path being much greater than the Debye length, the plasma sheath is considered to be collisionless. Replenishment of the macro-particles lost to the surfaces in the simulation is done by reinserting the macro-particles back into the simulated region outside of the pre-sheath region with a Maxwellian thermal velocity with a uniform insertion probability over the bulk plasma per time step.

The potential difference profiles, shown in Figure 5.1, for the one dimensional sheath and hybrid PIC simulations are within two standard deviations near the wall and in the pre-sheath region (based on the variation in the hybrid PIC-MCC potential over 20 time steps shown in Figure 5.1a) for the majority of the sheath region. The two profiles only vary significantly past the transition point from the pre-sheath to the sheath region at a radius of approximately 1.12 to 1.23 cm. The difference is explained by the still present, time dependent variations of the ion density at the pre-sheath edge due to the limited number of macro-particles in each cell. The variation in the positive and negative ion densities from step to step in the PIC-MCC code is a maximum at this location as well. The potential, shown in Figure 5.1, for the two models differ at the metal surface due to the one dimensional fluid model initial conditions being based on the ion current to the surface (which are the same for both the models), not the potential at the surface.

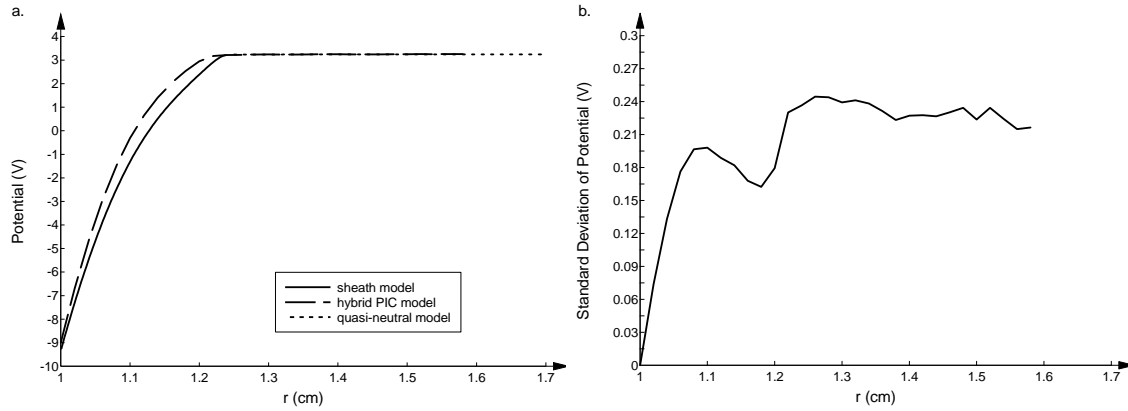


**Figure 5.1 Comparison of (a) Potential Difference and (b) Standard Deviation Profiles for the 1-D Pre-Sheath, Sheath and Hybrid PIC in the Sheath Region of a 0.001 Torr Electronegative Plasma**

The calculated electronegative Bohm velocity is  $4.5 \times 10^4$  cm/s based on the sheath edge potential from the simulation at a radius of 1.25 cm. The sheath edge is determined to be at the distance from the wall at which the quasi-neutrality of the plasma no longer exists. The positive ion velocities of the PIC and fluid models are not as close in value as the potential difference profiles, but only vary by 11.5% at the inner cylindrical surface. In addition, the accuracy of the average ion velocity value in the PIC-MCC model is more dependent on the number of macro-particles (due to the three velocity components of the distribution) in each cell than the potential which is only dependent on the number of particles in each cell (Turner, 2006). As a result the standard deviation in the positive ion velocity from the hybrid PIC-MCC model, shown in Figure 5.2b, increases substantially in the sheath region.

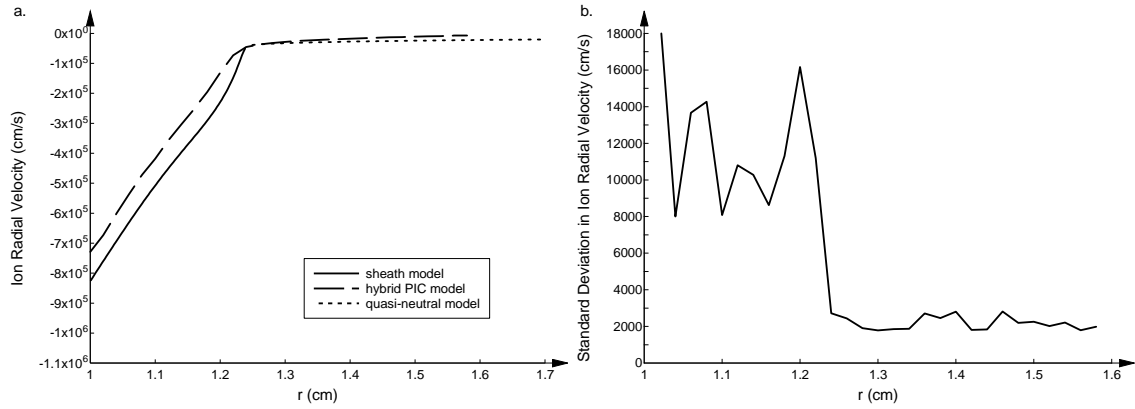


**Figure 5.2 Comparison of the 1-D Sheath, Pre-Sheath and Hybrid PIC-MCC Models (a) Positive Ion Velocity Profiles in the Sheath Region of a 0.001 Torr Electronegative Plasma and the (b) Standard Deviation in the Positive Ion Velocity Profile**

Charged particle density profiles are also different in the positive ion profiles near the transition between the pre-sheath and sheath regions at 1.17 cm to 1.25 cm shown in Figure 5.3b. However, the PIC-MCC model's average positive ion density is 5.2% greater than the fluid model near the wall which is consistent with the relationship between density and current given by the ion current continuity equation 1.43. The electron density profiles are very close in value due to the closeness of the two potential profiles and are not compared in Figure 5.3.

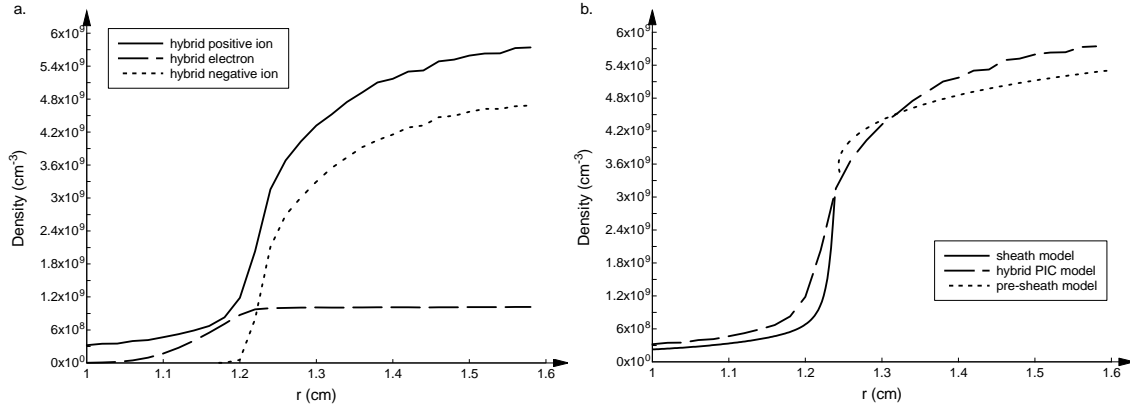


**Figure 5.3 Comparison of Density Profiles between the Hybrid PIC-MCC and Sheath Model (a) Positive and Negative Ions and Electron Densities from the Hybrid PIC-MCC model and (b) Comparison of Ion Density Profiles for a 0.001 Torr Electronegative Plasma**

The cited agreement of the one dimensional sheath and pre-sheath model and the hybrid PIC-MCC model in radial positive ion velocity, potential and positive ion density suggests that the hybrid PIC-MCC model is suitable for examining the sheath of a Langmuir probe given an adequately large number of macro-particles. The numerical noise of the PIC-MCC model, however, does not make it the ideal model for examining a steady state plasma sheath especially considering the computational resources required to obtain the low noise simulation of the sheath. It is however, an unconditionally stable and very robust kinematic modeling approach that is capable of examining an asymmetric, transitional collisional, two dimensional sheath caused by a flowing electronegative background gas. As result, it was one of the few model types capable of fully performing the investigation of a probe sheath in the required conditions without any prior assumptions. This absence of assumptions in the PIC-MCC model allows us to examine some unanticipated phenomenon resulting from the presence of negative ions in

a flowing plasma. In the next section, we review the hybrid PIC-MCC model set-up for analyzing a Langmuir probe in a flowing and non-flowing plasma.

### **Langmuir Probe Model Setup**

A cylindrical Langmuir probe with an axes orientation parallel to the flow direction is investigated using the hybrid ICEPIC model presented previously. The Langmuir probe geometry parallel to the flow is inherently symmetric around a cylindrical axis, therefore the model was restricted to two dimensions,  $r$  and  $z$  to reduce computational overhead of the model. To reduce the domain size, the outer radial wall is modeled as a mirror plane shown in Figure 5.4. Particles reflect off of the mirror plane such that the angle of reflection equals the angle of incidence and the component of the electric field normal to the mirror plane is set equal to zero. The separation between the probe and the mirror boundary of 2 cm is large enough such that there is no interference with the sheath of the probe, hence there exists a quasi-neutral plasma at a constant plasma potential between the probe and the mirror plane. This set-up is equivalent to the Langmuir probe being inserted in a large plasma of uniform density in the radial direction.

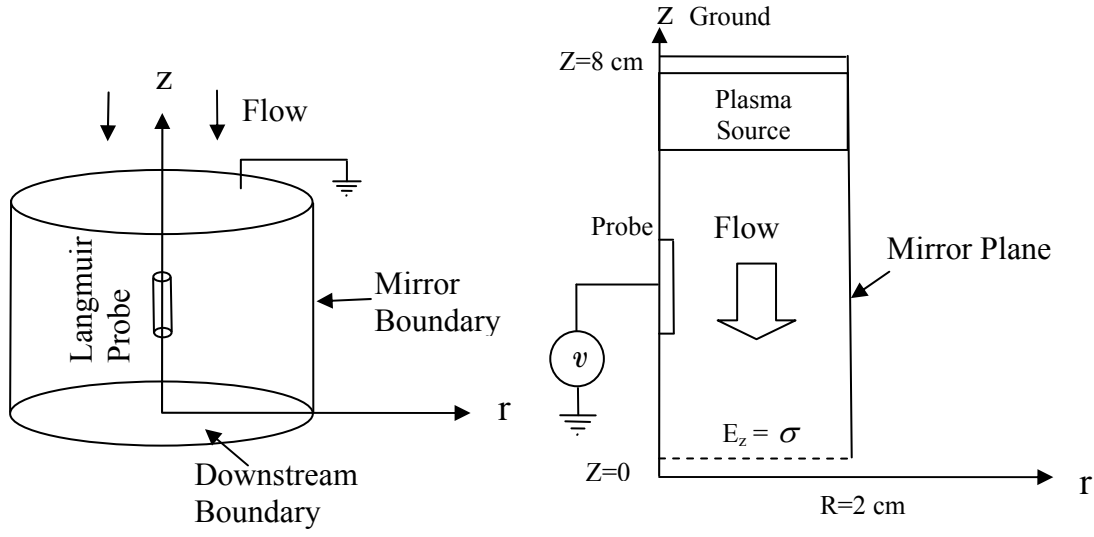


**Figure 5.4 Langmuir Probe in a Flowing Background Gas Geometry (a) Three Dimensional Cylindrical Geometry of Langmuir Probe Model and a (b) Two Dimensional  $r, z$  Slice of Langmuir Probe Model**

The model is initiated with a uniform density plasma flowing at the same velocity as the background gas. The plasma density in the tube is maintained by inserting macro-particles upstream of the probe, in the plasma source region in Figure 5.4b, simulating a source from an upstream discharge. This method reduces the computational overhead of maintaining the plasma through ionization and secondary emission and also allows more precise variation of charged particle densities to match potential experimental conditions. Inserted particles are given an isotropic, thermal velocity and if a flowing background gas is present in the simulation, the flow velocity of the background gas is added to the thermal velocity of the particles. This is done because the plasma is being generated upstream of the Langmuir probe and the ion velocity distribution is assumed to be already in equilibrium with the background gas flow velocity.



The upstream boundary in the model is a grounded metal surface that provides a potential reference for the probe. In a realistic scenario the plasma generated by the RF discharge would extend downstream beyond the simulated region, however, this requires significant computational resources. Therefore, the system is truncated to the region of interest around the probe. The downstream potential boundary condition, given by equations 2.54 and 2.57, collects the current convected downstream to generate the charge on the boundary. Since, the plasma is quasi-neutral, the net charge through the downstream boundary goes to zero on average and the electric field at the boundary is approximately zero. In addition to convective flux to the surface, the thermal diffusion of the finite temperature ions also contributes to the loss of ions to the downstream boundary. Based on Garrigues approach and the standard particle beam injection method used in ICEPIC, the positive and negative ion densities are inserted with a positive  $z$  velocity at the lower  $z$  boundary with a thermal Maxwellian distribution such that the ion velocity in the  $z$  direction has a distribution given by

$$f_z(v) = C \exp\left[-\frac{M_i}{2kT_i}(v_z + u_f)^2\right] \quad (5.16)$$

where  $C$  is the normalization constant. This approach equates the diffusive fluxes of the particles lost downstream with the particles injected at the downstream boundary in the positive  $z$  velocity such that the net flux through the downstream boundary is the convection flux (Garrigues and others, 2002). This results in the divergence of the ion flux, given by equation 2.21, being approximately zero at the downstream boundary and as a result there is no increase or decrease in the particle density. This approach is similar

to the method used to model the downstream boundary for the RF discharge model discussed in Chapter II.

The Langmuir probe simulations with or without flow are performed on a two dimensional r-z cylindrical mesh with simulation dimensions of  $z = 8$  cm and  $r = 2$  cm and cell dimensions of  $dr$  and  $dz = 0.25$  mm. Each simulation was performed on 32 processors of the NAVOCEANO BABBAGE 3,092 IBM P5+ Cluster or the Army Research Laboratory's John von Neumann 6,045 node 2.5 GHz Opteron LINUX cluster. Each simulation was composed of 30 million positive and negative ion macro-particles with equal charge weighting per macro-particle consistent with the densities  $n_i = 5 \times 10^9 \text{ cm}^{-3}$  and  $n_n = 3 \times 10^9 \text{ cm}^{-3}$ . For the hybrid PIC-MCC simulation, electron temperatures of 0.2 eV were simulated,  $r_p = 0.5$  mm, and the probe was biased to -30 V relative to ground. An electron temperature of 0.2 eV is based on balancing the energy loss and gain of super-elastic, elastic, and inelastic collisions of electrons with excited and ground state background gas based on the densities obtained in Chapter IV at 1 Torr.

The background gas pressure was varied between 0.001 and 0.01 Torr with a flow velocity of 0, 200, and 400 m/s. The positive and negative ion collision cross sections of  $\sigma_i = 1.8 \times 10^{-14} \text{ cm}^2$  and  $\sigma_n = 0.8 \times 10^{-14} \text{ cm}^2$  (the negative ion is  $O^-$ ) are used to approximate the transport in an oxygen background gas for a Maxwellian distribution of ions with  $T_i = T_n = 0.025$  eV. For low pressures and small radius probes, it is well known that the orbital motion of the ions around a cylindrical or spherical probe limit current collection. The reduction in ion current collection caused in the orbital motion limiting (OML) case by weak collisions has been predicted by theory (Sternovsky, 2004)

and studied using a polar PIC models (Cenian and others, 2005). Sternovsky, 2004, has also shown that ion charge exchange collisions are very important to current collection in the OML case; however, in the radial motion limited case there is very little difference between a charge exchange and elastic collision for the purposes of determining the ion current collected by a probe. To simplify the modeling and the analysis of the effect of pressure and flow, we restrict ourselves to the radial motion limiting case. Because the simulation is radial motion limited, the charge exchange and elastic collision cross-sections were combined into a total collision cross-section.

The threshold for convergence of the conjugate gradient method, which was used to solve Poisson's equation each time step, was such that the  $L_2$  norm was less than  $1 \times 10^{-5}$ . A simulation time step of  $dt = 1 \times 10^{-8}$  s was used and simulation time to convergence varied between  $t = 1 \times 10^{-4}$  s for a 0.001 Torr background gas pressure and  $t = 1 \times 10^{-3}$  at 0.1 Torr. Wall clock time required to achieve a steady state varied from a few hours to 3 days due to increases in collision frequency and the lower mobility of ions at higher pressures.

### **Hybrid PIC-MCC Langmuir Probe Model Results at Low Pressures**

The simulations presented in this section show the effect that increasing pressure has on a Langmuir probe sheath and the current collected by a probe in a flowing electronegative plasma. In this section, the 0.001 Torr and 0.01 Torr cases in stationary and 200 m/s flowing conditions are examined and compared against established probe theory for stationary and flowing conditions. For the low pressure 0.001 Torr stationary

and flowing cases, the ion mean free path is larger than the Debye length and therefore falls within the collisionless probe analysis regime. For the 0.01 Torr case, the ion mean free path and the Debye length are of the same order of magnitude which constitutes the transitional collisional regime.

### **Probe in a Stationary and Flowing, Collisionless Electronegative Plasma**

Starting with the stationary, collisionless case, we will examine the sheath structure and compare the sheath length with established electronegative probe theory. A contour plot of the ion density and potential profiles around a cylindrical Langmuir probe are shown in Figure 5.5. The roughness of the contour edges are due to the still present numerical noise associated with PIC simulations. In the absence of a flowing background gas, the ion density and potential contours are symmetric and approximately ellipsoidal when viewed at a 1 to 1 aspect ratio (the aspect ratio in Figure 5.5 is 10 to 1 to enable better examination of the change in the sheath). The observed shape of the probe sheath is consistent with the finite cylindrical probe theory of Kiel and Crespo, which is based on the sheath of a cylindrical Langmuir probe being ellipsoidal in nature. The simulated current collected by the probe is  $I_p = 2.83 \times 10^{-5}$  Amps.

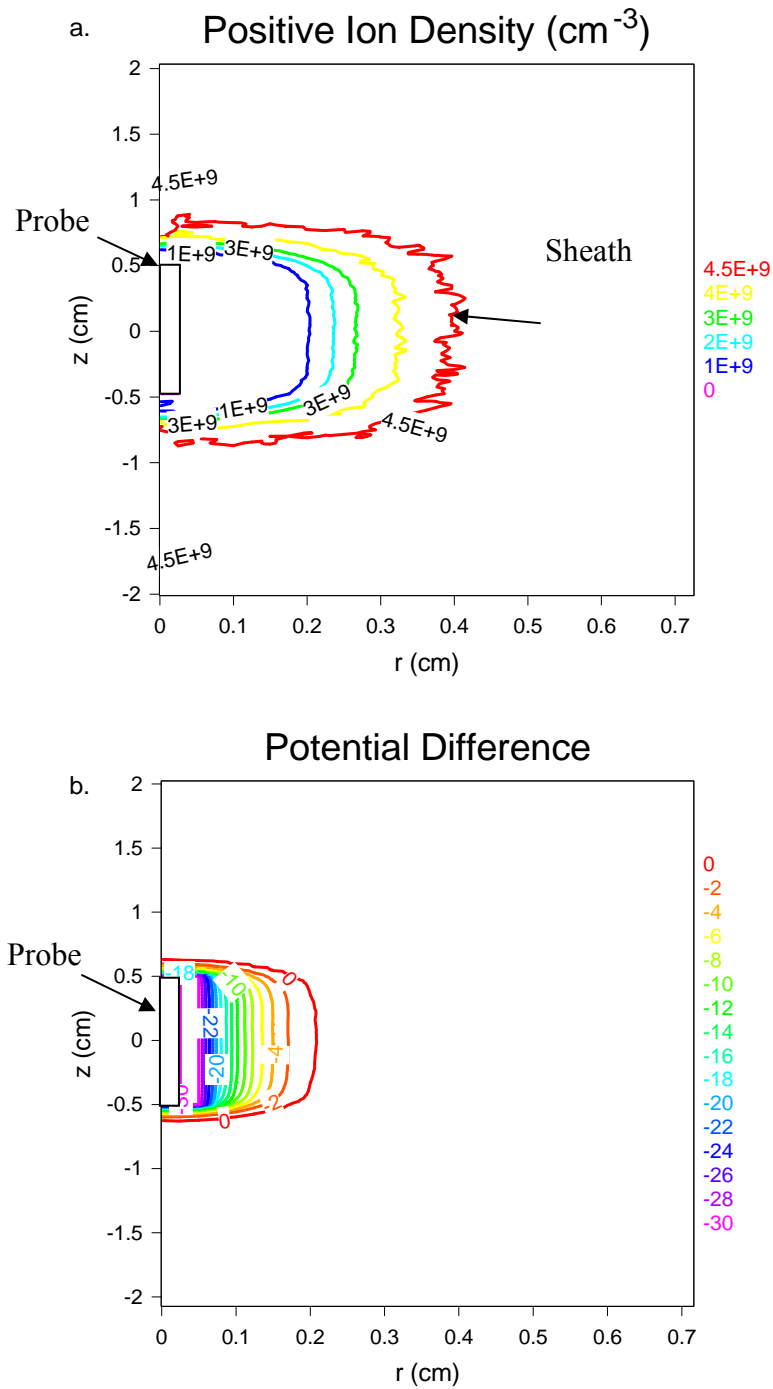


**Figure 5.5 Langmuir Probe in a 0.001 Torr Non-Flowing Oxygen Plasma (a) Positive Ion Density (b) Potential Difference**

To ensure that the model is consistent with collisionless, electronegative probe theory, we compare the simulation sheath length, determined from the end of the net positive charge region associated with the sheath, to Allen and Braithwait's, Crespo's, and Kono's sheath radius calculations. A slice of the probe sheath at its midsection, located at  $z = 4.0$  cm, is shown in Figure 5.6. From Figure 5.6b, it is shown that the net positive charge of the sheath ends at  $\sim 0.247$  cm. At this radius, we obtain a sheath edge potential of approximately 0.037 V and corresponding electronegative Bohm velocity of 49,000 cm/s. Starting with Allen and Braithwaite's method, using the collected current from the simulation, equation 1.60 for the electronegative Bohm velocity, and assuming energy conservation with cold ions, a potential drop of 0.044 V and an electronegative Bohm velocity of 51,600 cm/s in the pre-sheath region is predicted. Including the effect of warm ions by substituting the electronegative Bohm velocity into the energy conservation equation 1.65, the sheath edge potential is found to be 0.0413 V relative to the plasma potential and the electronegative Bohm velocity is 50,800 cm/s.

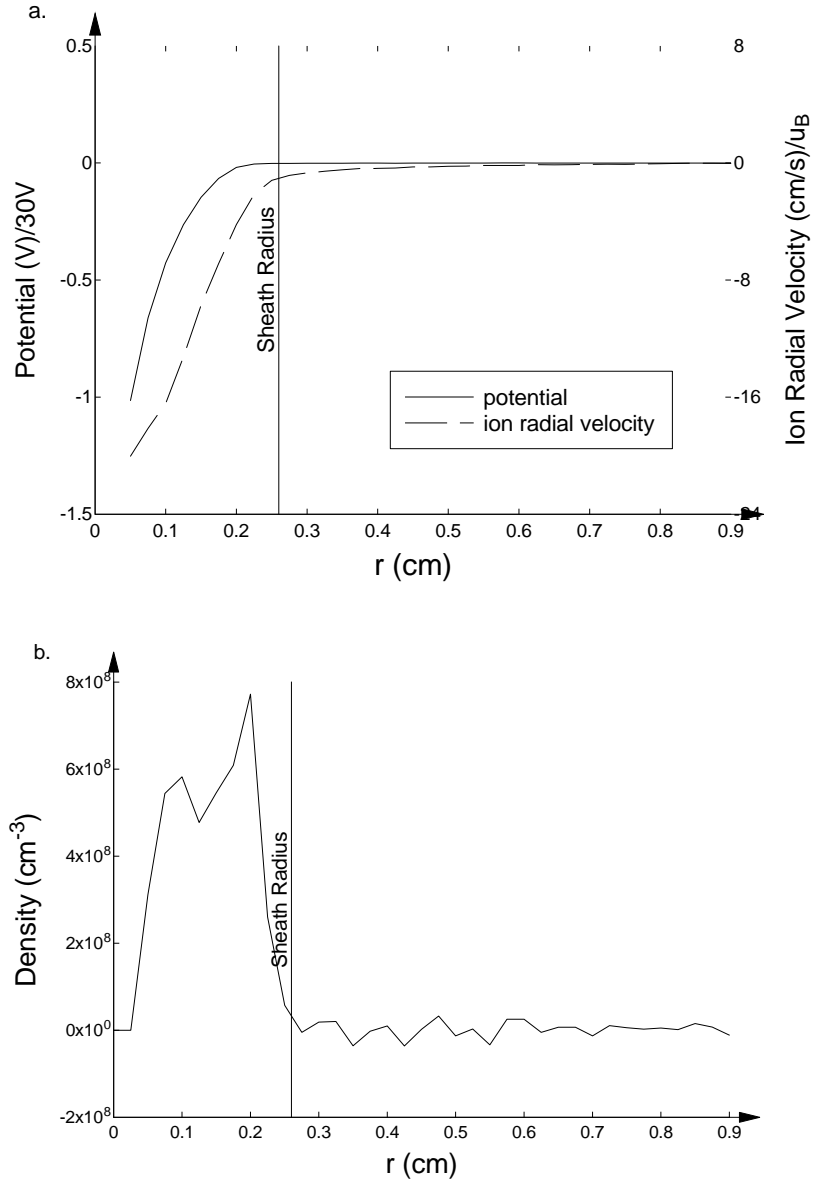


**Figure 5.6 Mid-Section Slice of the (a) Potential and Radial Ion Velocities and (b) Net Charge Density of the Langmuir Probe Sheath in 0.001 Torr Stationary Background Gas**

Using the current continuity equation, 1.43, we obtain a sheath length of 0.204 cm and 0.196 cm for cold and warm ions respectively (Allen and Braithewait, 1988). Using the more detailed analysis method of Crespo for a Langmuir probe in a collisionless electronegative plasma, results in a predicted radius of 0.233 cm. The results of the

analysis suggest that the hybrid PIC-MCC simulation approach in two dimensions is within 20% of standard electronegative probe theory suggesting that the hybrid PIC-MCC model is accurate in two-dimensions as well. Adding additional macro-particles and resolving the mesh of the simulation reduces noise as seen in Figures 5.1 and 5.2, however, the computational resources required to simulate a two dimensional system to a converged state become prohibitive even on modern super-computers.

Comparing a flowing case, 200 m/s, to the stationary case, the measured current collected by the probe,  $I_p = 2.87 \times 10^{-5}$  Amps, is approximately the same current collected by the probe in the stationary case. The lack of change in the probe current in the presence of a flow indicates that at this low of a pressure the probe is in a diffusion limited collecting regime consistent with Clements and Smy, 1969, assertions. The electric Reynold's number from equation 1.65 is  $R = 0.07414$ , which also indicates that the contribution of the convection velocity is much less than the diffusion velocity and hence the flowing plasma should have little effect on the current collected by the probe. The radial current density, shown in Figure 5.7, along the length of the probe shows only a small increase in the current to the downstream tip of the probe in the flowing versus stationary case. This result is similar to Hutchinson's, 2004, result and is associated with the focusing of ions by the sheath. This result is discussed in much greater detail later on.



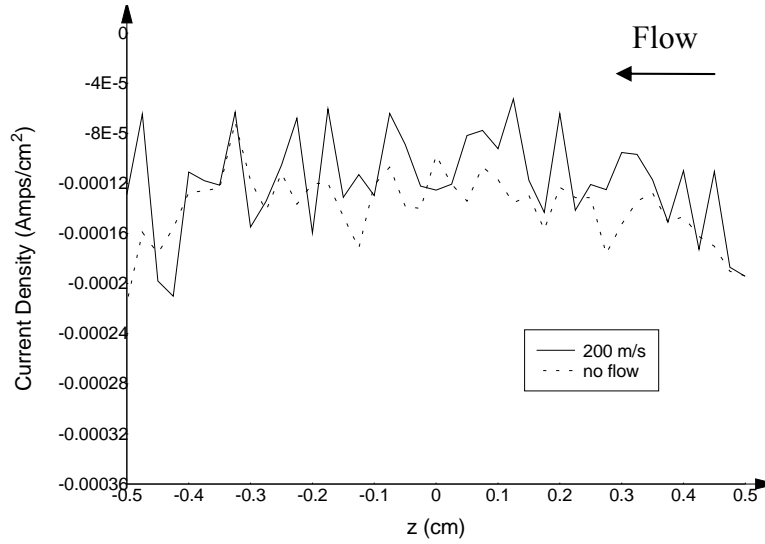


**Figure 5.7 Radial Current Density Comparisons along the Probe Length in a 0.001 Torr Oxygen Background Gas Flowing at 200 m/s and No Flow.  $z = 0$  is the Mid-Section of the Probe**

The plasma flow does induce an increasing asymmetry in the space charge surrounding the probe, shown in Figure 5.8a, even at the low pressures which is worth investigating and actually reduces the current collected by the probe for the 0.01 Torr pressure regimes.

Contour plots of the positive ion density and potential of the plasma around the probe with flow are shown in Figure 5.8. Comparing the flowing and stationary case, we note that in the flowing case ion density contours upstream of the probe are more compressed than the downstream contours, suggesting that the flowing nature of the plasma has altered the probe sheath even at very low pressures. In Figure 5.8.b, the potential difference contour lines are nearly symmetric both upstream and downstream except for the -0.2 V contour line which is compressed upstream of the probe.

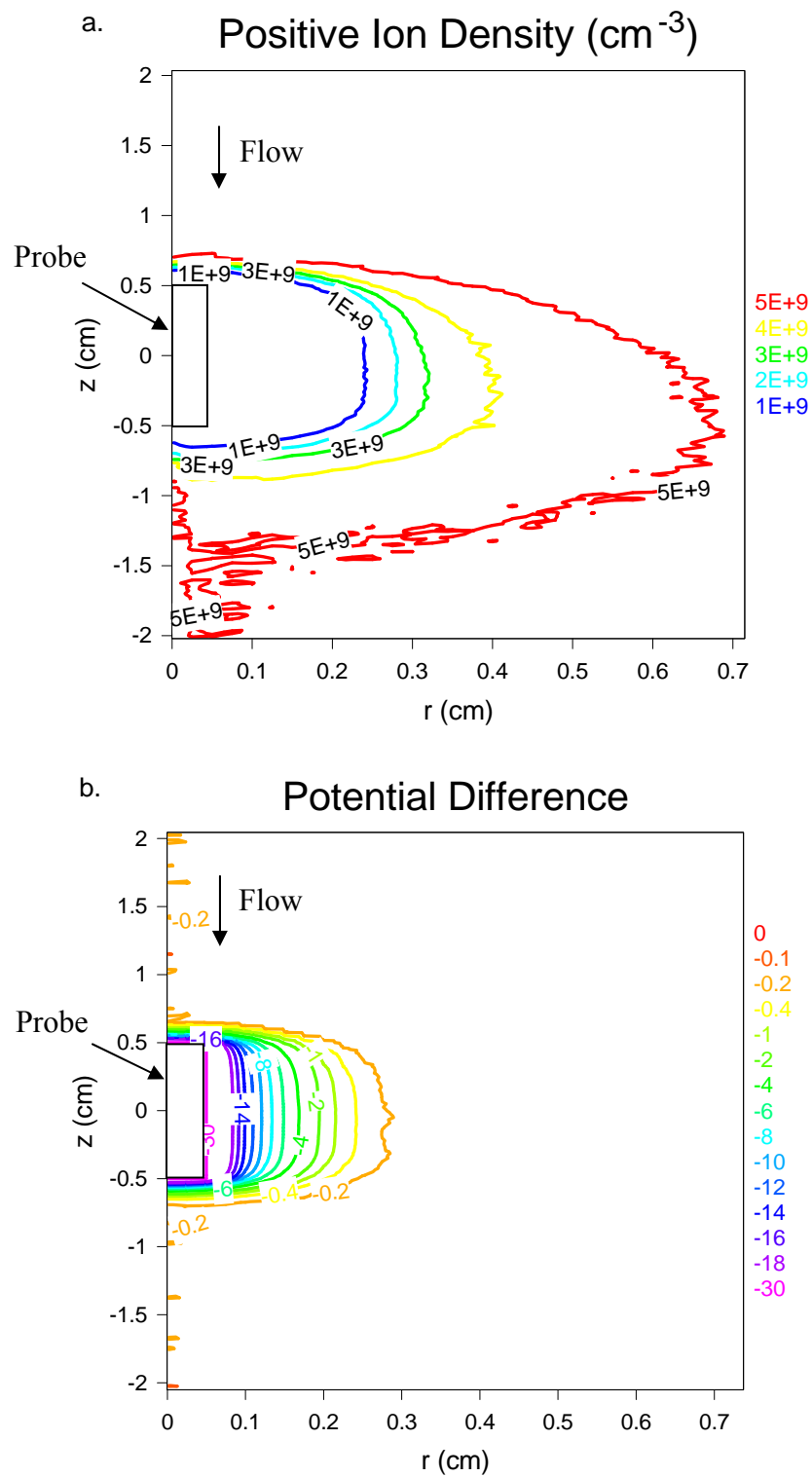


**Figure 5.8** Langmuir Probe in a 0.001 Torr Oxygen Plasma Flowing at 200 m/s (a) Positive Ion Density (b) Potential Difference

This compression in the potential of the pre-sheath upstream in the negative  $z$  direction is due to the flow lowering the acceleration requirement for the ions in the pre-sheath to attain the ion sound velocity. The lowering of the ion acceleration requirement in the  $z$  direction reduces the potential drop across the pre-sheath as was observed by McMahon and others, 2005 in his study of an infinite probe transverse to the flow in a collisionless, electropositive plasma. McMahon observed that as the convected ions reached velocities on the order of the ion thermal velocity where  $T_e = T_i$ , the pre-sheath collapses and the sheath radius and pre-sheath radius became identical. The pre-sheath layer in the 200 m/s case is still present though because the electronegative Bohm velocity of 488 m/s for  $\gamma_n = \gamma_i = 8$ ,  $\alpha_0 = 2.05$ , and  $\phi_s = 0.1$ , where  $\phi_s$  is the sheath edge potential, is still greater than the flow velocity. The reduction in the potential drop over the pre-sheath is seen in Figure 5.9, where the drop in the sheath potential is sharper upstream than downstream.

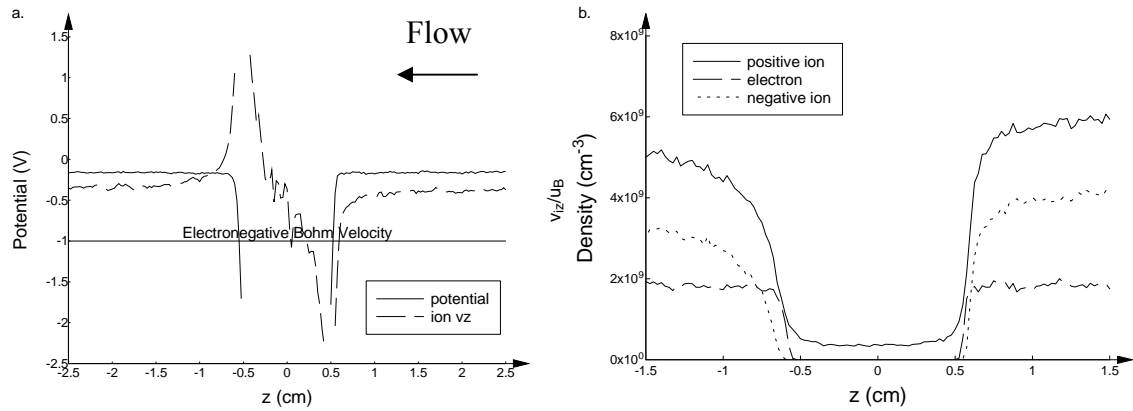


**Figure 5.9 (a) Potential and Positive Ion Velocity Profiles Normalized to the Probe Bias and Electronegative Bohm Velocity in the  $z$  Direction and (b) Particle Densities with Center Set to Middle of Probe at  $r = .15$  cm ( $r_p=0.05$  cm) from Axis in a 0.001 Torr Electronegative Plasma with the Probe Biased to -30 V**

Now comparing the potential profiles for the 200 m/s and 400 m/s flowing and stationary cases, the compression of the pre-sheath potential at 400 m/s flow is much greater than the 200 m/s case. The closeness of the flow velocity to the electronegative Bohm velocity results in the compression of the pre-sheath and the reduction in the pre-sheath length near the tip of the probe, which is observed in Figure 5.10.

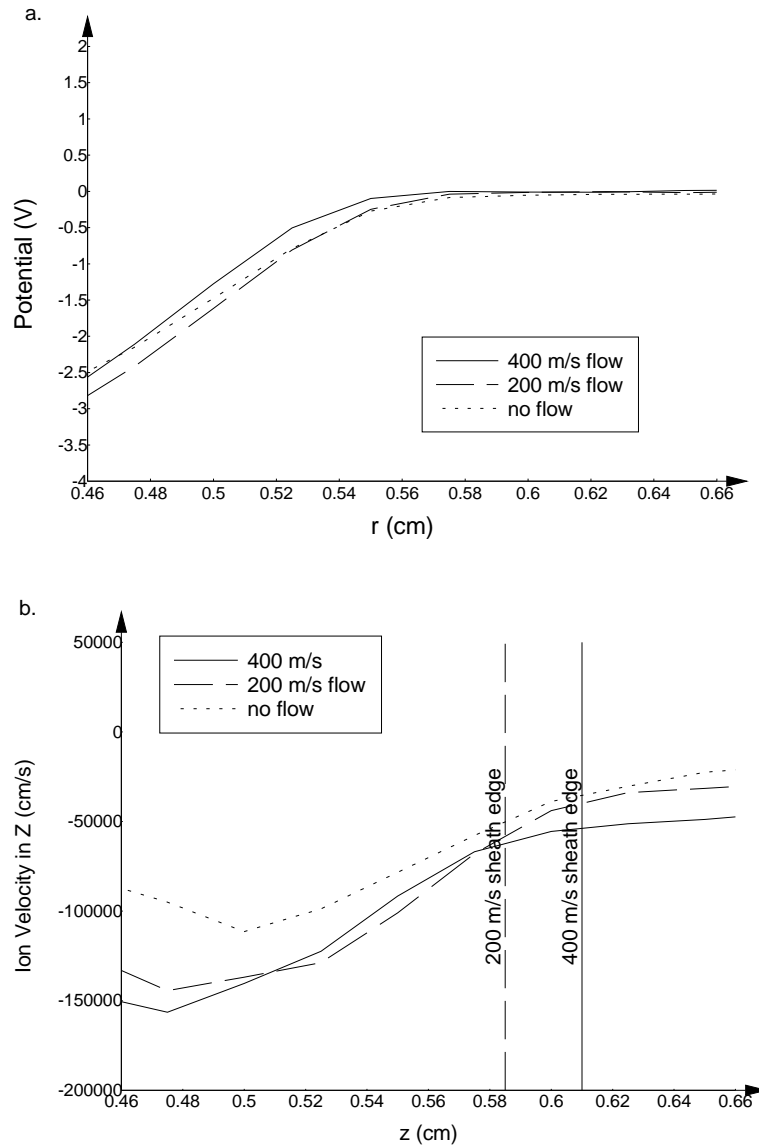


**Figure 5.10 (a) Potential and (b) Positive Ion Velocity Comparison of 400 m/s, 200 m/s and No Flow Cases using a Z-Slice in the Sheath at  $r = 0.15$  cm**

In addition to the decrease in the potential drop over the pre-sheath region, the flow of an electronegative plasma into the sheath also results in the buildup of negative ions upstream of the probe. This build up is due to the negative ions not having enough energy to penetrate the sheath field. The positive ion density then increases to maintain quasi-neutrality, while the fast electrons easily redistribute around the sheath and hence maintain the same density upstream and downstream of the probe which is shown in Figure 5.9b. The slight asymmetry introduced in the ion distribution around the probe is due to the ions flowing through the sheath which also results in a depletion of ions downstream of the probe. The previously described factors result in a  $1.3 \times 10^9 \text{ cm}^{-3}$  (22% difference in upstream versus downstream ion densities) larger density of positive ions upstream versus downstream of the probe at  $r = 0.15 \text{ cm}$  as shown in Figure 5.9b. The change in the net charge density then becomes asymmetric resulting in asymmetries in the potential and positive ion densities upstream and downstream of the probe. These results are also consistent with the electropositive, collisionless results observed by McMahon, 2005, who observed higher densities upstream of the probe with the probe axis oriented transverse to the plasma flow direction.

The region downstream of the probe, however, is not devoid of positive ions. The positive ions are able to move back into the depleted downstream region due to both diffusion and the focusing of positive ions by the edge of the pre-sheath into the region behind the probe sheath as indicated by Figure 5.11. Ions downstream of the probe at a radius greater 0.2 cm, shown in Figure 5.11, accelerate radially towards the probe due to the electric field in the pre-sheath region. Downstream ions at a radius of less than 0.2 cm accelerate upstream to the downstream tip of the probe. A similar result was also

observed by Hutchinson in his study of a spherical probe in a flowing plasma with non-zero Debye length (Hutchinson, 2003). In Hutchinson's study, the focusing by the pre-sheath resulted in the current to the downstream portion of the spherical probe being greater than the current to the upstream portion of the probe due to ion focusing. Smy and Noor, 1976, have also observed an ion focusing behavior caused by probes in high flow velocity or low ionization regimes. Smy and Noor, 1976, stated that, "at high flow velocity we see that the fields within the sheath may not be sufficient to ensure that a large portion of the ions entering the sheath do indeed reach the probe – many, in fact, will be swept on by the flow back into the plasma." The focusing effect caused by the pre-sheath region accelerating the positive ions radially towards the probe without the ions being collected at the probe surface is seen in Figure 5.11.

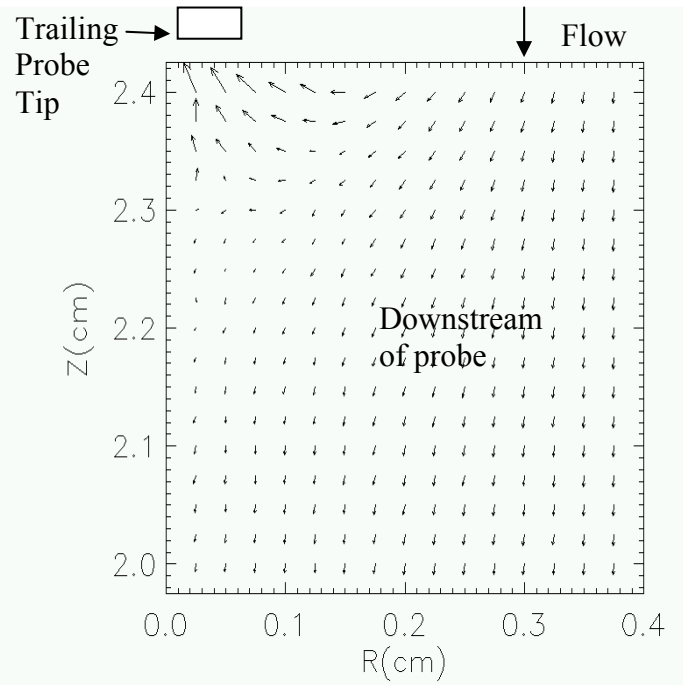


**Figure 5.11 Positive Ion Velocity Vector Plot Near Downstream Tip of the Probe with Probe Center at 3 cm**

The negative ions, however, are repelled by the probe's sheath and hence flow around the sheath of the probe leaving a void of negative ions downstream of the probe. The negative ions eventually fill in behind the positive ions through diffusion, shown in Figure 5.13, when the sheath potential of the probe shown in Figure 5.8b becomes negligible. A larger depletion region and asymmetry in the negative ion density exists in comparison with the positive ion density downstream of the probe, Figure 5.12. The repulsion, extended depletion region, and diffusion of the negative ions downstream of the probe is also observed in a vector plot of the negative ion velocities shown in Figure 5.13.

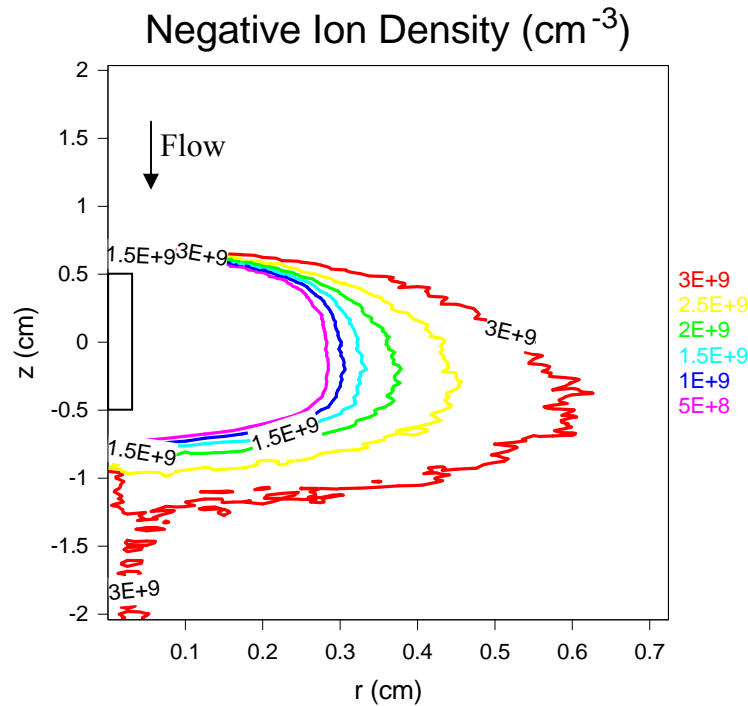


**Figure 5.12 Negative Ion Density Around a Probe in a 0.001 Torr Oxygen Plasma Flowing at 200 m/s**

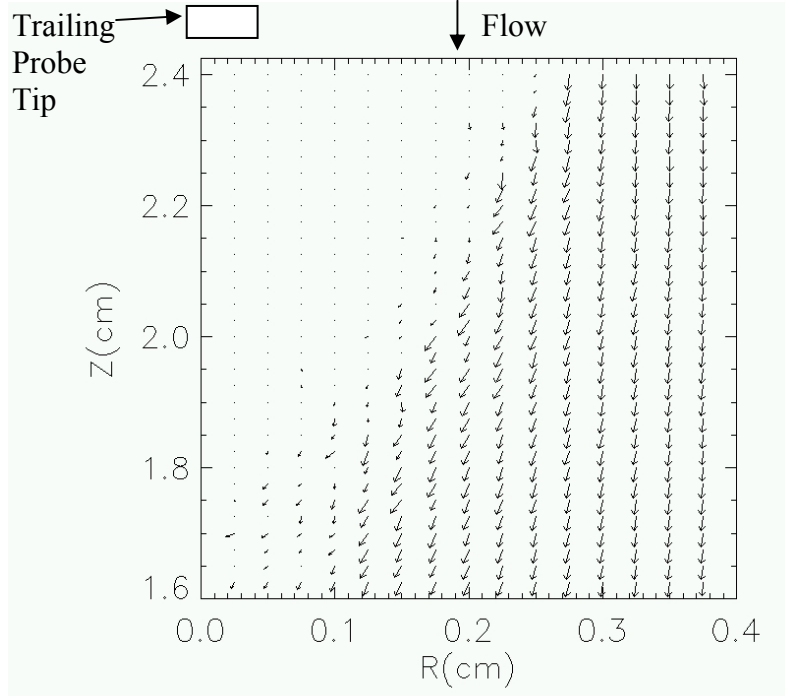


**Figure 5.13 Negative Ion Velocity Vectors Downstream of the Probe in a 200 m/s Flow at 0.001 Torr with Center of Probe at 3 cm**

The asymmetry in the density of the negative ions also has a larger radial extent than the positive ion asymmetry due to the negative ions being repelled by the sheath and pre-sheath. The sheath at the probe tip is at an oblique angle relative to the flow direction. As a result, the negative ions are reflected outwards from the tip of the sheath as shown in Figure 5.14. The negative ions beyond the sheath in the pre-sheath region of the tip can also be seen to be reflected to greater radial distances. This results in a reflected flow of negative ions moving parallel to the obliquely angled sheath near the tip of the probe until about  $r=0.245$  cm (the calculated sheath radius of the probe). When the negative ions reach the sheath edge, at  $r > 0.245$  cm downstream of the probe tip, they are



repelled by the probe's pre-sheath electric field which extends radially from the probe surface shown in Figure 5.14.

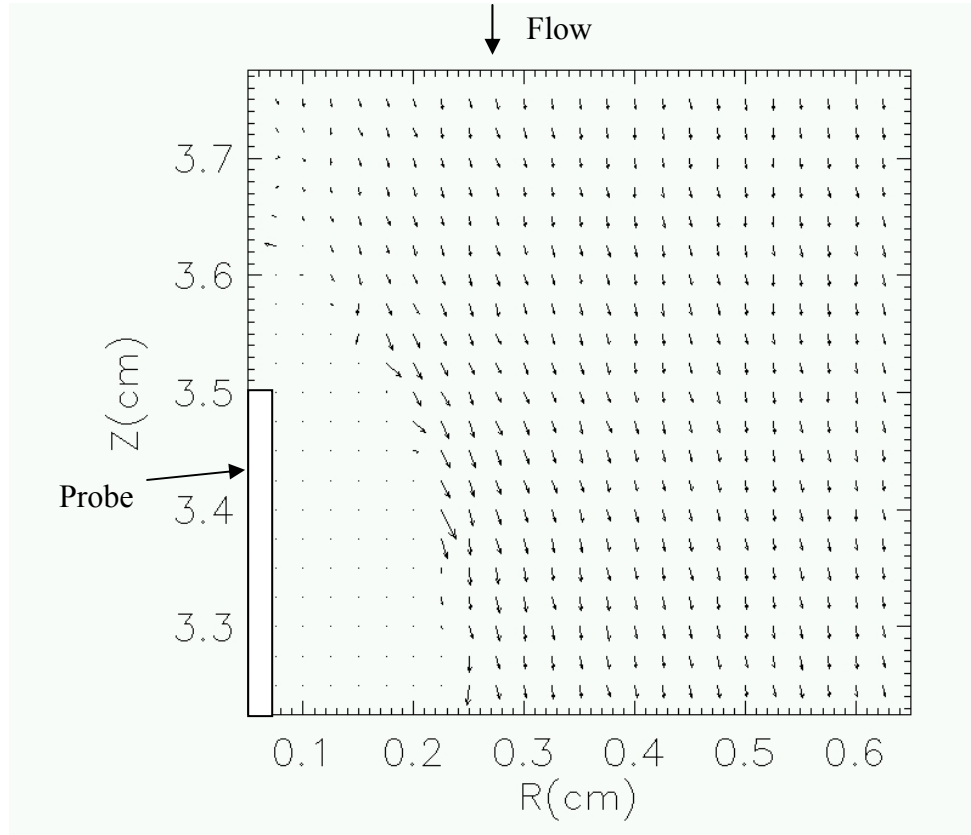


**Figure 5.14 Negative Ion Velocity Vectors at the Upstream Tip of the Probe in a 200 m/s Flow at 0.001 Torr with Center of Probe at 3 cm**

Next, we compare the sheath radius in the flowing and non-flowing cases and investigate the validity of collisionless probe theory for analyzing ion current collection in the flowing case. Figure 5.15 shows a comparison of the radial sheath potential, radial ion velocity, and net charge density for the flowing and non-flowing cases. The asymmetry in the net charge density introduced by the flowing plasma reduces the sheath radius by about 0.23 mm; however, as noted previously the collected current did not

change significantly. The sheath edge potential of 0.044 V in the pre-sheath region is predicted using Allen and Braithewait's, 1988, method. Using the current continuity equation, 1.60, the predicted sheath length of the probe is 0.204 cm. The numerical noise associated with the hybrid PIC code is on the order of the sheath edge potential making comparisons of the models in the pre-sheath difficult, but the two methods for predicting the sheath length produce reasonably close results. For the flowing case, the hybrid PIC model results in a 0.037 V drop in the pre-sheath region resulting in a sheath length of 0.27 cm compared to the 0.247 cm, which is a  $\sim 10\%$  increase in the radius in the flowing case. The reason for the slight increase observed in the sheath length in the 200 m/s flowing case over the non flowing case is explained in further detail when we examine results for the 0.01 Torr case. The results of the hybrid PIC and sheath models though different are close enough to suggest that analyzing the probe in an electronegative, moderately fast flowing plasma using a traditional electronegative probe analysis technique is not unreasonable for the 0.001 Torr pressure regime at flow velocities near 200 m/s.

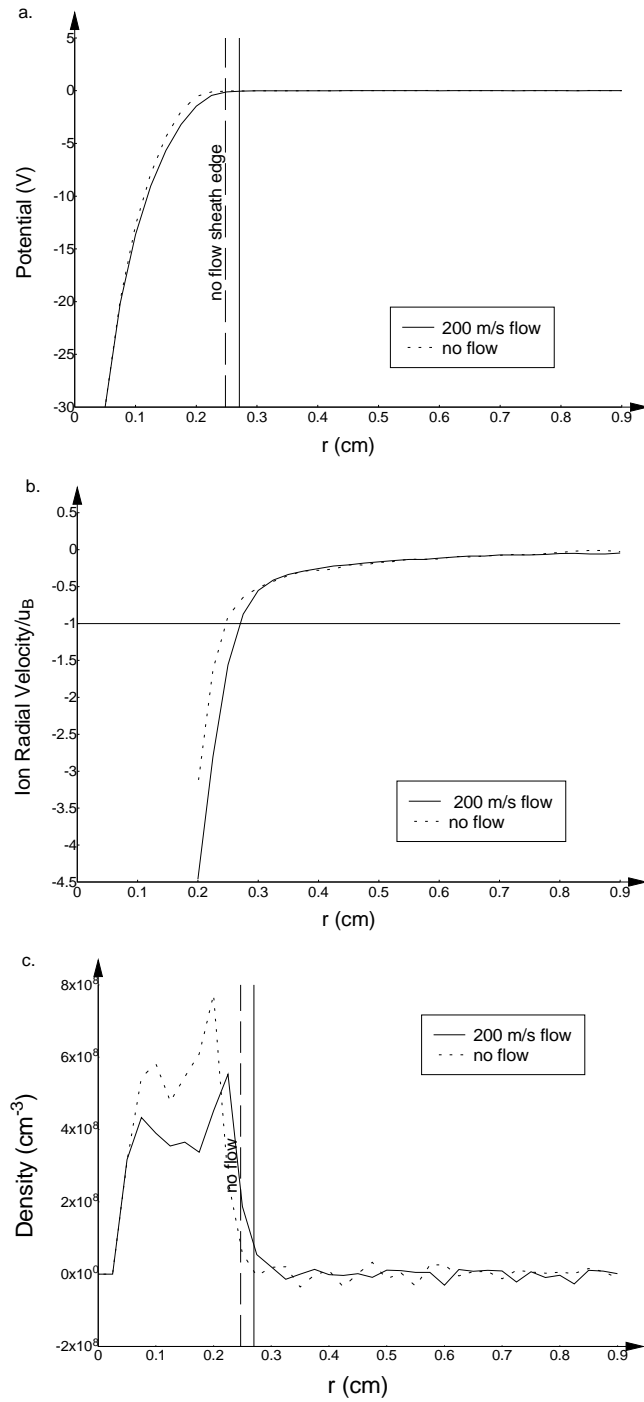


**Figure 5.15 Probe Sheath in a 0.001 Torr 200 m/s Flowing Oxygen Plasma Comparing the (a) Potential (b) Radial Ion Velocity and (c) Net Charge Density in Flowing and Non-Flowing Case using a Radial Profile at the Probe Mid Section**

Having established that there is minimal effect on the current collected by a probe for a 200 m/s flow at 0.001 Torr, we examine the sheath structure at 0.01 Torr. The ion mean free paths are now  $\lambda_i = 0.157$  cm and  $\lambda_n = 0.3536$  cm. The Debye length remains  $\lambda_D = 0.074$  cm and flow velocity remains 200 m/s. The 0.01 Torr pressure regime is now near the transitional collisional regime and the mean free path of the ions are on the order of the probe sheath length. The occasional collisions experienced by the ions as they traverse the pre-sheath and sheath are shown to alter the current collected by the probe. The currents collected by the probes in the flowing and non-flowing case are  $I_p = 2.0 \times 10^{-5}$  amps and  $I_p = 3.7 \times 10^{-5}$  amps respectively. The decrease in collected ion current in a flowing case has been observed by Kusumoto, 1992, and Smy, 1976 in experiments and by Xu, 1992, and McMahon and others, 2005, using computer models. Kusumoto, 1992, has suggested that the ion-neutral collisions in a flowing electropositive plasma (mean free path for Kusumoto's experiment  $\lambda_i = 0.2 - 0.4$  cm with  $r_p / \lambda_D \rightarrow \infty$ ) caused the sheath dimensions to decrease resulting in the reduction of the ion current collected by the probe. Results from the Hybrid PIC-MCC model which are presented next, however, suggest that the positive ions are not able to diffuse upstream to the probe sheath and hence the current collected by the probe is reduced. In addition, the following analysis of the model results show that the sheath actually expands at these pressures and flow velocities in the case of an electronegative plasma.

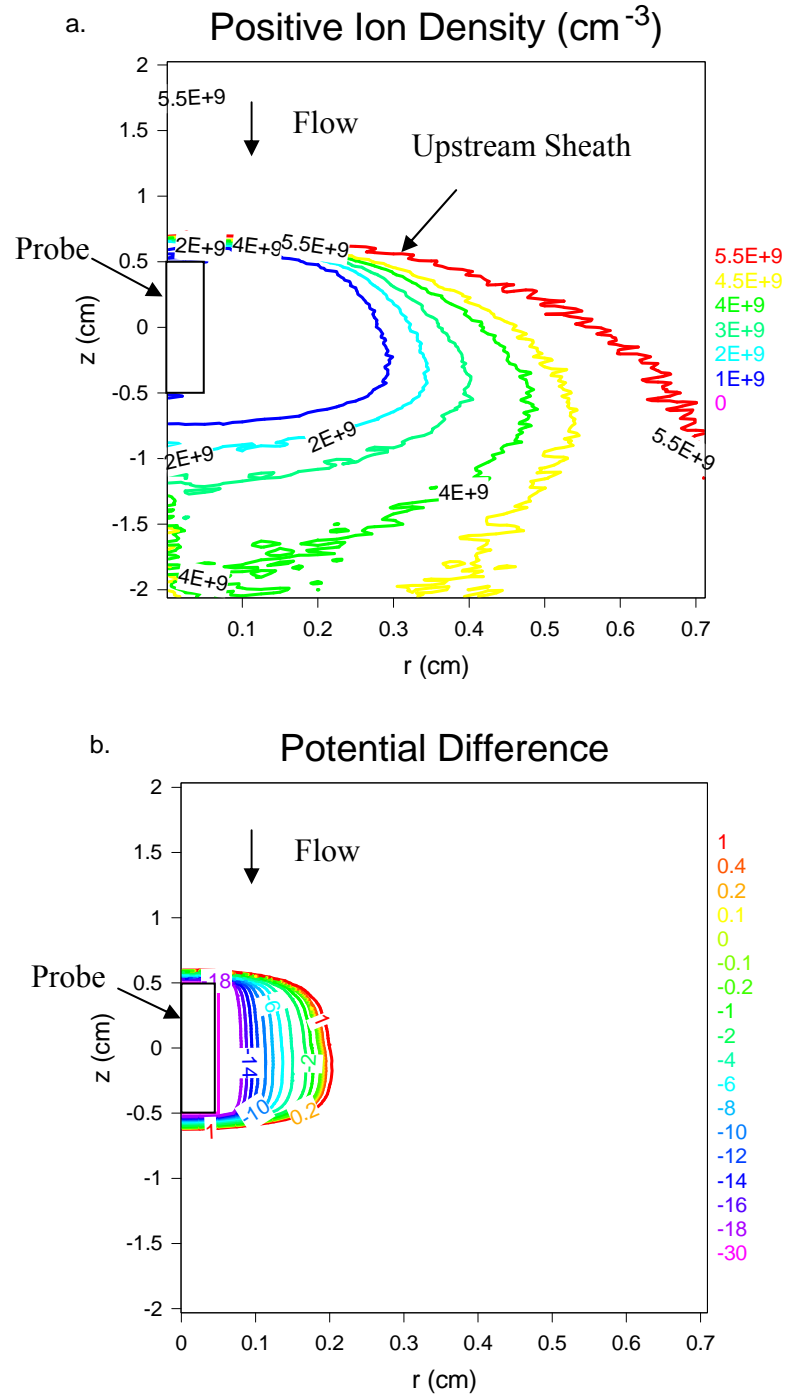


**Figure 5.16** Langmuir Probe in a 0.01 Torr 200 m/s Flowing Oxygen Plasma (a) Positive Ion Density and (b) Potential Difference

Examining the positive ion density contour plot in Figure 5.16a and comparing to the 0.001 Torr flowing case in Figure 5.8a, the spatial extent of the asymmetry in the positive ion density has increased due to collisions. In addition, the contour plots of the potential also indicate that the radial extent of the sheath has increased with respect to the non-flowing case, shown in Figure 5.17b. This result contradicts standard probe theory and the sheath length decrease with flow mechanism, suggested by Kusumoto, to explain the decrease in the measured current observed when the probe is in a flowing plasma (Kusumoto, 1992). To understand the observed growth in the sheath, we need to examine the upstream sheath and pre-sheath closely.

Examining the sheath at 0.1 cm downstream of the probe tip ( $z = 3.4$  cm in Figure 5.15), we determine the sheath radii to be 0.217 cm and 0.239 cm for the non-flowing and flowing cases respectively. The sheath length is based on the length from the probe at which the plasma becomes quasi-neutral. The electronegative Bohm velocity is  $8.55 \times 10^4$  cm/s and  $7.05 \times 10^4$  cm/s based on the potential drop at the sheath edge, which is shown in Figure 5.17. At the mid-section of the probe ( $z = 3.0$  cm in Figure 5.15), the sheath radii are shown to be 0.225 cm and 0.3 cm respectively (33% increase in the sheath radius with a 200 m/s flow). The sheath edge potential for both cases is 0.064 V.

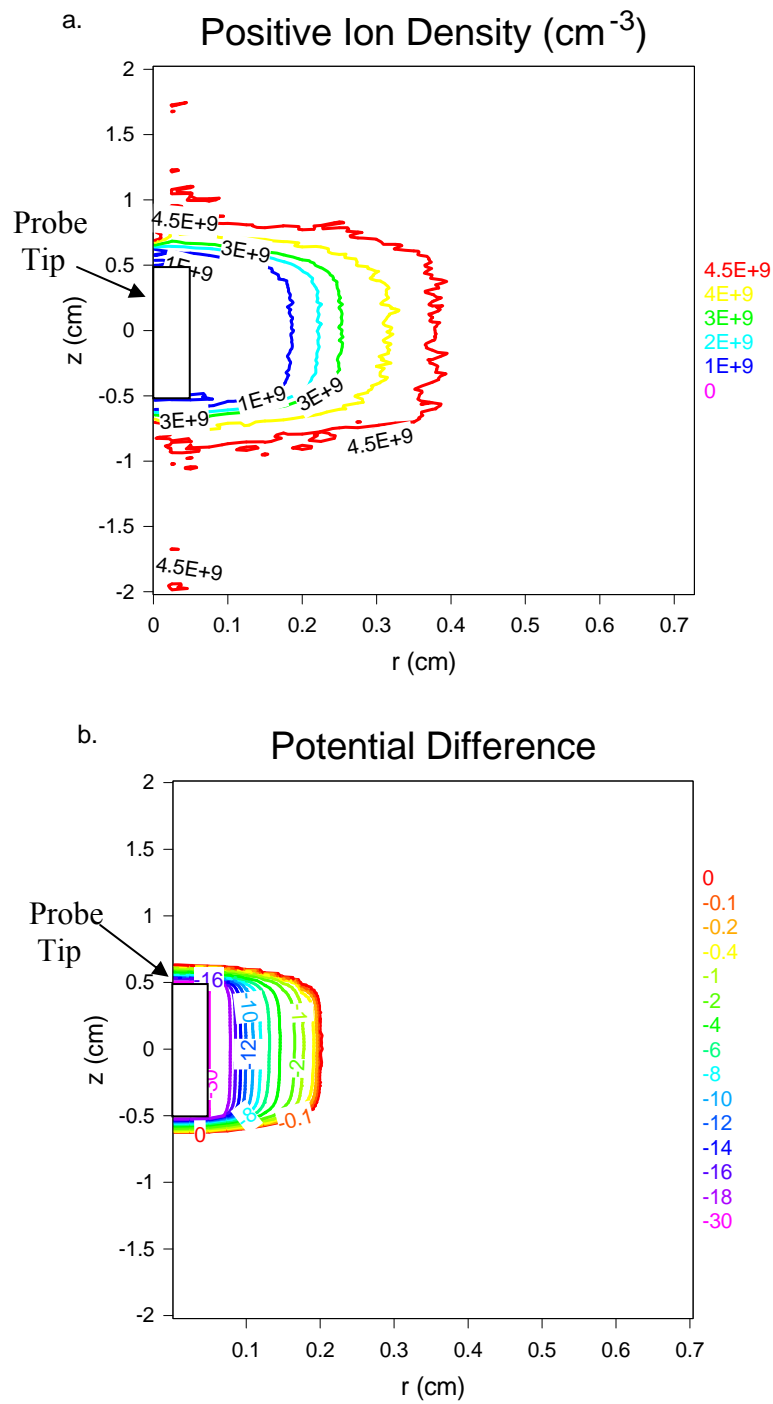


**Figure 5.17** Langmuir Probe in a 0.01 Torr Stationary Oxygen Plasma (a) Positive Ion Density and (b) Potential Difference

Figure 5.18 confirms the observation indicated by the potential contour plot of a probe in a 200 m/s flow, Figure 5.16b, that the pre-sheath near the tip of the probe is at a greater than 90 degree angle relative to the background gas flow direction. The angle of the upstream pre-sheath has very little effect on the positive ions because they are simply accelerated by the sheath to the probe surface.

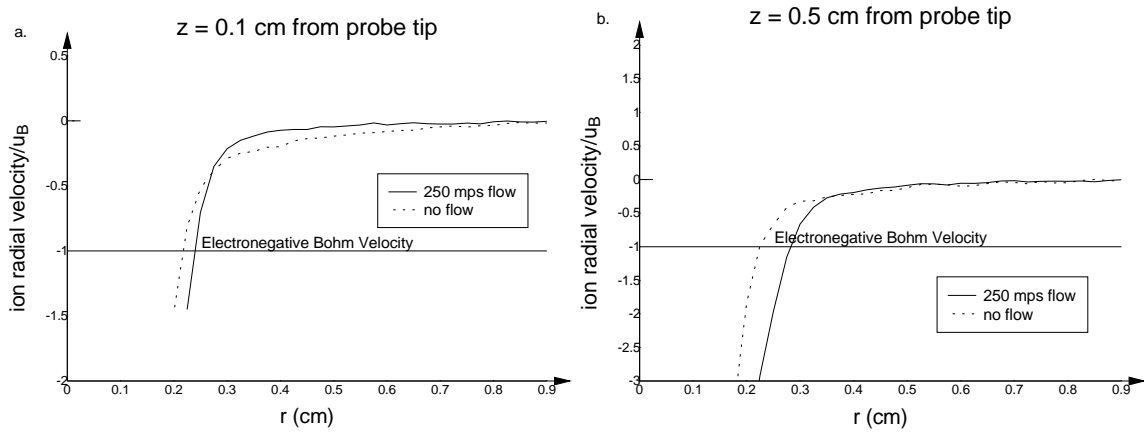


**Figure 5.18 Comparison of the Radial Ion Velocity and Sheath Radius (a)  $z = 0.1$  cm (b)  $z = 0.5$  cm from the Tip of the Probe. Ion Velocities are Normalized by the Electronegative Bohm Velocity**

The negative ions that make it to the sheath edge, however, are repelled by the electric field of the sheath and reflect off of the sheath at an angle when presented with the angled sheath at the tip of the probe as shown in Figure 5.19. Similar to the previous description for Figure 5.14, the negative ions are repelled in the pre-sheath at a larger radial distance from the probe. From Oksuz's study of a collisional plasma pre-sheath, the potential drop over the pre-sheath is higher in a collisional versus collisionless plasma due to the need to accelerate the positive ions to the electronegative Bohm velocity (Oksuz and Hershkowitz, 2006). The drag due to collisions increases the electric field requirement to accelerate the positive ions, which is consistent with the higher potential



drop over the pre-sheath potential measured in the 0.01 Torr versus 0.001 Torr case. This larger potential drop generates a higher electric field in the pre-sheath region and the negative ions are repelled to a greater distance from the tip of the probe when incident on the angled pre-sheath in the higher collisional case.

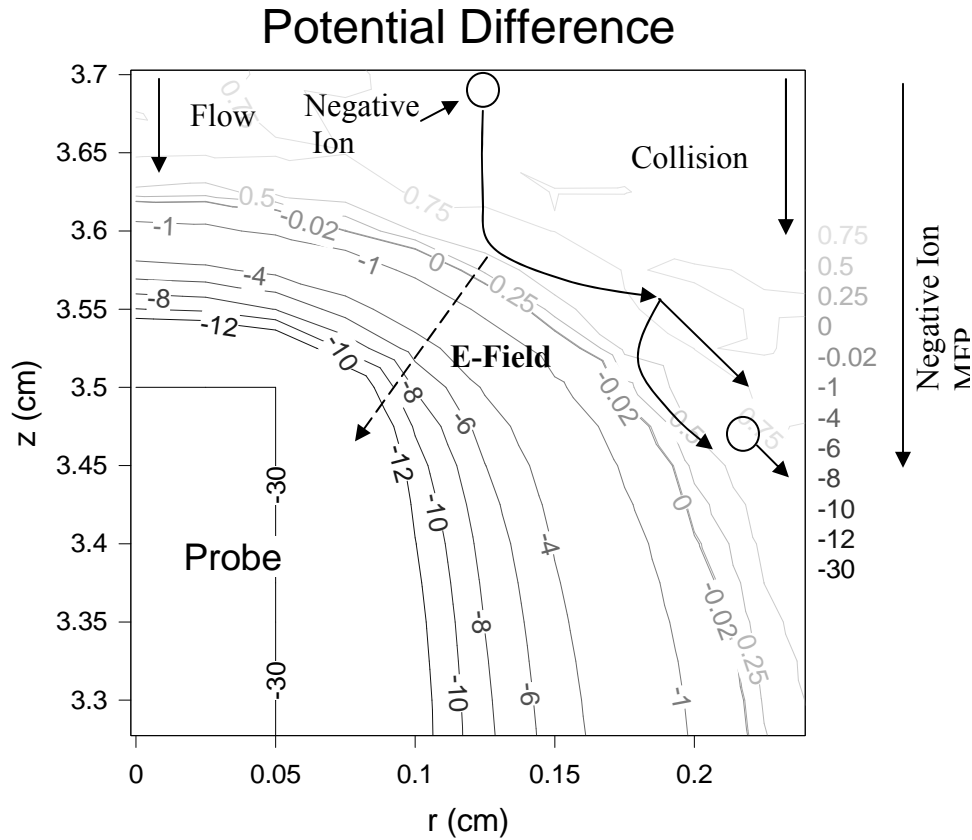


**Figure 5.19 Contour Plot of Potential Around the Probe Tip in a 200 m/s Flow at 0.01 Torr with Probe Center at  $z = 3$  cm**

A comparison of the drop in potential over the pre-sheath region for the case of a Langmuir probe in a 200 m/s flow at both 0.001 Torr and 0.01 Torr is shown in Figure 5.20. Due to the numerical noise of PIC simulations, the fluctuations in the time

averaged potential are on the order of the potential in the pre-sheath, therefore, a curve fit of the potential is used to show the potential drop over the pre-sheath.

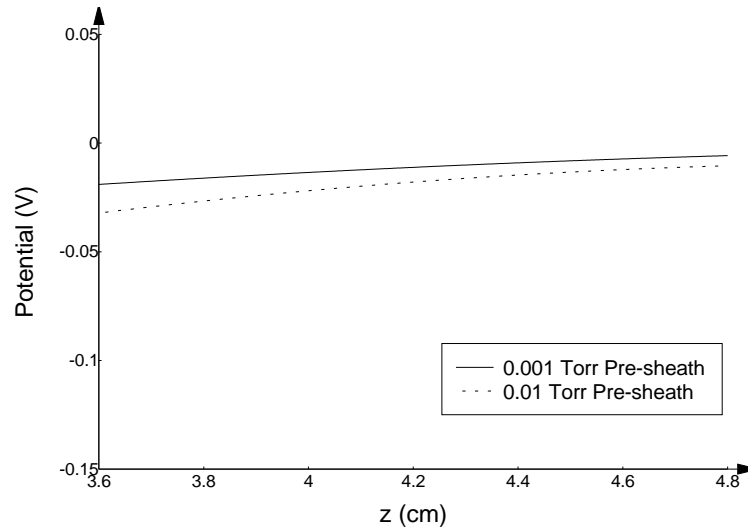


**Figure 5.20 Drop in Potential Over the Pre-Sheath at  $r=0.2$  cm**

The repulsion of negative ions further upstream by the pre-sheath potential results in a larger deflection of the negative ions and an increase in the radial extent of the negative ion depletion region. These changes in the ion densities and hence net charge density produce a larger sheath. Since, the negative ion mean free path is larger than the radial extent of the sheath, the negative ions on average travel beyond the edge of the sheath before experiencing a collision that would “push” it into the sheath as seen in Figure 5.21. In Figure 5.21 the spurious average negative ion velocity vectors that point towards the sheath are due to the low number of negative ion macro-particles in the pre-sheath region. These single negative ion macro-particles enter the sheath edge and are reflected.

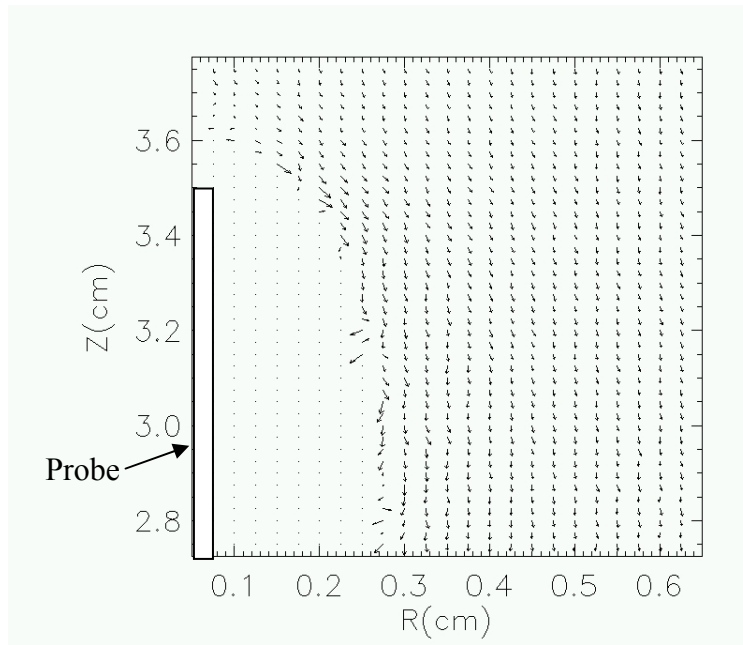


**Figure 5.21 Negative Ion Velocities Near the Tip of the Probe in a 200 m/s Flow at 0.01 Torr with Probe Center at  $z = 3$  cm**

The net charge density around the tip of the probe is shown in Figure 5.22. The pre-sheath field repelling the negative ions from the probe results in the net charge spreading out radially further in a 0.01 Torr versus a 0.001 Torr background gas as shown in Figure 5.22 a and b. Figures 5.22 a and b indicate that the sheath has also increased in radius because the edge of the sheath occurs where quasi-neutrality no longer exists.

Asymmetries in the net charge introduced by the negative ions flowing parallel to the upstream sheath edge can also be observed in Figure 5.22a.

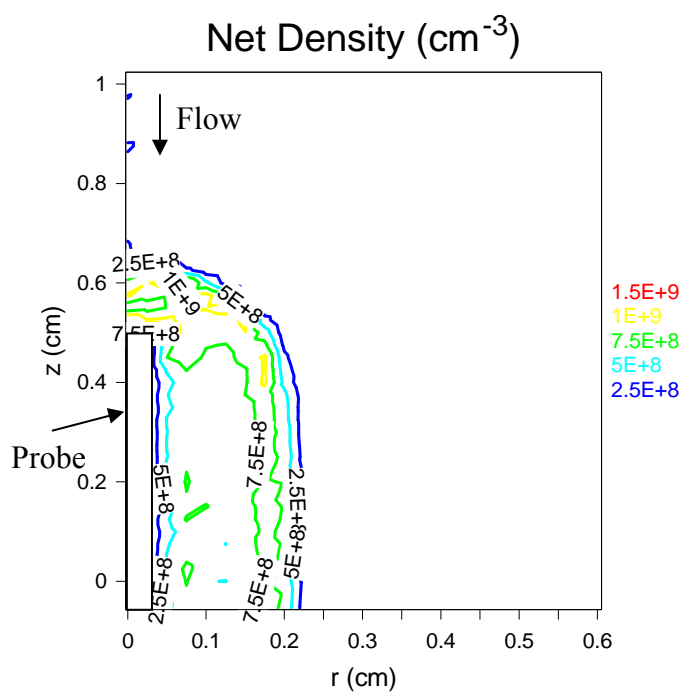
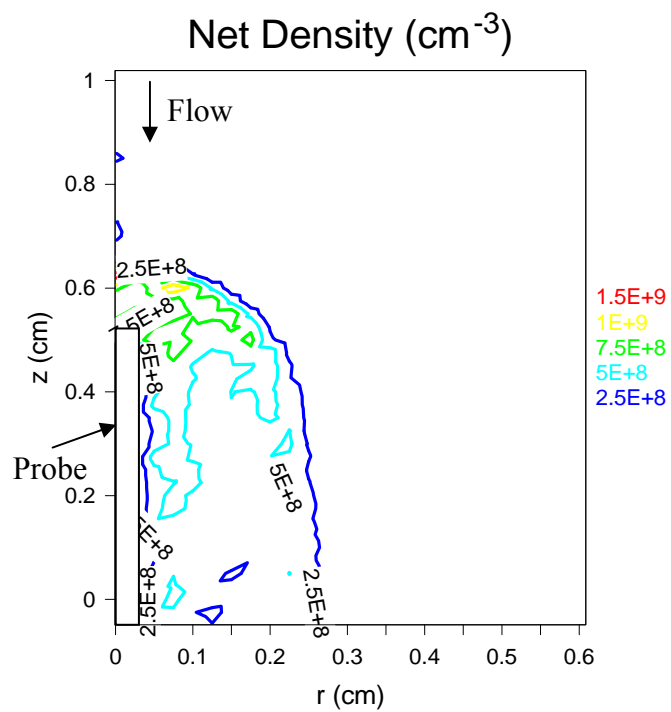
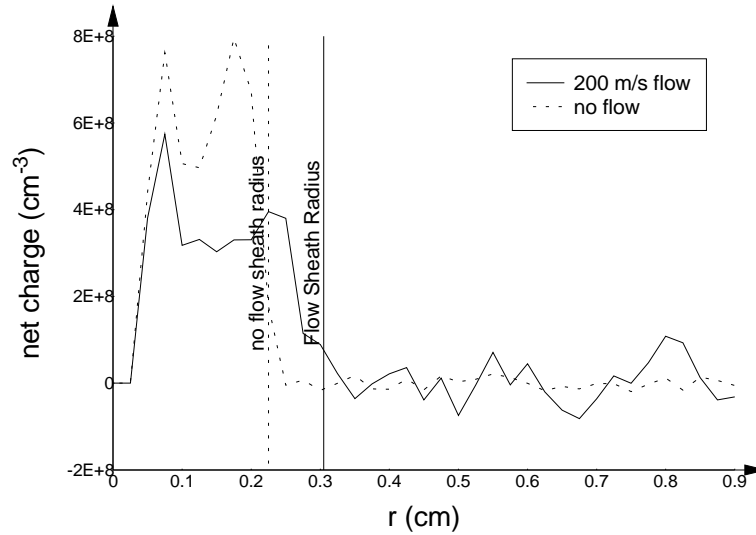


Figure 5.22 Net Charge Density Around a Probe (a) 200 m/s Flow and (b) No Flow

A mid-sectional slice, where  $z = 0$ , of the net charge near the sheath region is shown in Figure 5.23. The space charge in the flowing case extends out to approximately 0.3 cm with a lower average net charge density versus the non-flowing case. The non-flowing case has a shorter radial extent and higher net charge density resulting in a higher sheath electric field and positive ion collection current.



**Figure 5.23 Mid Sectional Profile of the Charge Density Around a Langmuir Probe in a 200 m/s Flow**

Based on Lam's electric Reynold's number criterion, where  $R = 0.7414$ , the source of current to the probe is still primarily due to diffusion of positive ions to the collecting surface. This criterion is confirmed by the observation that there is a reduction in the positive ion current, despite the increase in the sheath radius. The reduced positive ion current is due to the reduced mean free path of the positive ions combined with the flowing gas denying access to the collecting surface of the upstream probe. To provide an understanding of how the flow reduces the ion diffusion into the probe sheath and the total ion current collected by the probe, we examine the diffusion of the ions upstream

using the time independent fluid equations. Starting with the ion momentum equation, 1.45, in normalized units with ion inertia and neglecting any fields or gradients in the density results in the equation

$$u \frac{du}{dx} = \delta(u + u_f) . \quad (5.17)$$

The initial velocity of the ions upstream is approximately the thermal ion velocity in the +z direction minus the flow velocity in the -z direction. Integrating equation 5.17 using the initial ion velocity, we obtain the following equation for the distance that a group of ions with a thermal velocity in the upstream direction would travel before being stopped by collisions with the flowing background gas on average resulting in  $u \approx 0$

$$x = \frac{(v_{ith} - u_f) + u_f \log(u_f) - u_f \log(u_f + (v_{ith} - u_f))}{\delta(v_{ith} - u_f)} \quad (5.18)$$

For this pressure regime,  $x = 0.07$  cm which suggests that the surface area of the sheath that is downstream of the probe is denied a source of ions. This is due to the ions not being able to diffuse upstream. The increased pressure of 0.01 Torr also reduces the ability of the ions in the plasma flowing parallel to the probe to diffuse radially into the pre-sheath region during their trip past the probe. Therefore, the current collected in the flowing case is lower than the current collected by the probe in the non-flowing case. The alteration of the collected current by the flow is also seen in the current density collected along the length of the probe surface shown in Figure 5.24. In the 0.01 Torr pressure regime with flow, slightly more current is collected towards the upstream tip of the probe than downstream of the tip.

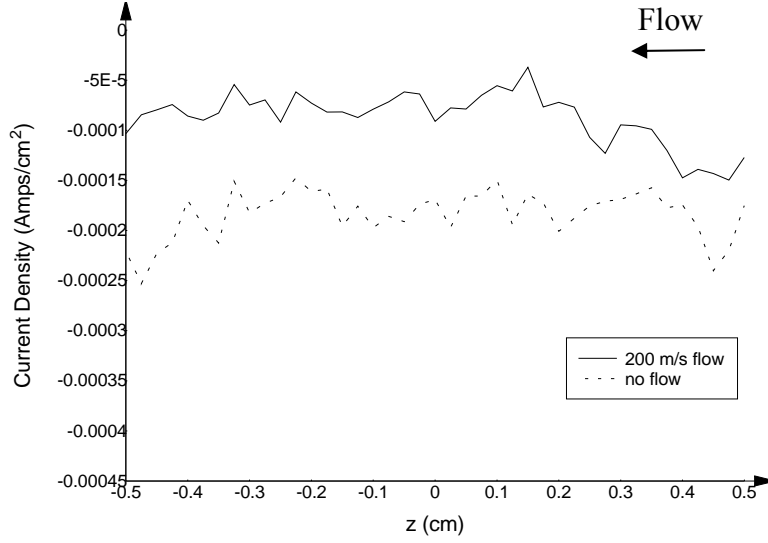


**Figure 5.24 Radial Current Density Comparisons Along the Probe Length at 0.01 Torr Flowing at 200 m/s and Stationary.  $Z = 0$  is the Mid-Section of the Probe**

The standard method for analyzing a flowing plasma in the lower pressure regimes is by using the convection-diffusion current theory given by

$$I_i = 4\sqrt{(e^2 \mu_i r_p u_f T_e) n_i L} \quad (5.19)$$

where  $L$  is the length of the probe (Smy, 1976). The convection-diffusion theory was developed for an electropositive flowing plasma, however, this study suggests that it is useful for analyzing a flowing electronegative plasma as well. Since all other aspects of the simulation remain the same, we expect the probe current to decrease with decreased mobility. Since the collecting surface of the sheath is denied to ions downstream of the probe and at large radial distances parallel to the probe, the current in the flowing case is reduced compared to the non-flowing case which is shown in Figure 5.25. This result for an electronegative plasma is consistent with the results of Kusumoto, 1973, Smy, 1976,

Xu, 1992, and McMahon and others, 2005 who investigated a probe in a flowing electropositive plasma.

From equation 5.19, the predicted current collected by the probe is  $2.04 \times 10^{-5}$  amps for the 0.01 Torr, 200 m/s flowing conditions which is essentially identical to the simulation current collected by the probe. A comparison of the hybrid PIC-MCC probe model and diffusion convection theory from 200 m/s to 800 m/s is shown in Figure 5.25. At flow velocities less than 400 m/s, the predicted current collected from the hybrid PIC-MCC probe model and convection diffusion theory are within 5% in value. At higher flow velocities of 800 m/s the convection diffusion theory current and the hybrid PIC-MCC collected differ by 18%. The reason for the observed difference at higher flow velocities is that the convection diffusion theory assumes that all positive ions that enter the sheath are collected by the probe. However, as previously noted in this section at higher flow velocities, positive ions near the sheath edge are not collected by the probe. Due to the finite length of the probe the positive ions are instead focused by the sheath field. The assumption of the convection diffusion theory that all positive ions entering the sheath were collected by the probe was noted by Smy and Noor, 1976, as a limitation to its applicability for analyzing plasmas using a probe at higher flow velocities. The hybrid PIC-MCC model results suggest that Clement and Smy's convection-diffusion theory should provide a reasonable measurement of positive ion densities from probe CVCs in an electronegative flowing plasma in the transitional collisional regime near 0.01 Torr; however, modifications need to be made to equation 5.19 for higher flow velocity cases in the transitional pressure regime. The required modifications need to



account for the fast flowing positive ions as well as the effects of negative ions which increase the sheath length and reduce the sheath electric fields observed in this study.

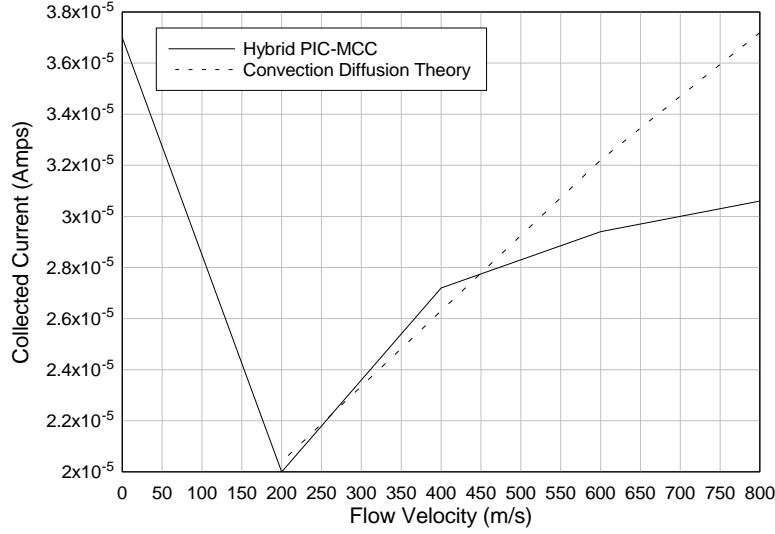


**Figure 5.25 Comparisons of Hybrid PIC-MCC Probe Model and Convection Diffusion Theory at 0.01 Torr in a Flowing Background Gas at 200 m/s to 800 m/s**

In this section, we have examined the effect of increased pressure on the sheath structure and current collected by the probe. We have found that at 0.001 Torr and flow velocities of 200 m/s that the flow has little effect on the current collected by the probe and that it is reasonable to use collisionless electronegative probe theory. This conclusion is consistent with the conclusion drawn by McMahon and others, 2005. For higher pressures, however, we found that the greater deflection of the negative ions by the pre-sheath potential due to the higher sheath edge potential drop resulted in the negative ion density being depleted to a greater extent parallel to the probe. The larger depletion region of the negative ions shifted the space charge in the probe sheath and increased the sheath radius of the probe. However, due to the lower mobility of the positive ions in this pressure regime, the radial diffusive current of the ions traveling

parallel to the probe is decreased and the diffusive ion current contribution downstream of the probe is decreased. These two effects result in the current of the 0.01 Torr case with flow being reduced with respect to the ion current collected in the 0.01 Torr non-flowing case and 0.001 Torr flowing case. Despite this increase in sheath radius caused by the negative ion deflection, Clement and Smy's diffusion-convection theory still predicted the ion current collected by the probe accurately at flow velocities less than 400 m/s. At higher flow velocities the diffusion-convection theory and the hybrid PIC-MCC results differed due to theory assuming that all ions that enter the sheath region are collected by the probe. In the next section, we investigate the effect that a flowing oxygen background gas at 1 Torr has on the sheath structure and ion current collection of a Langmuir probe.

### **Fluid Langmuir Probe Model Results at Moderate Pressures**

To explore the alteration of the sheath and the current collected by a Langmuir Probe in the 1 Torr pressure regime required a different modeling approach from the hybrid PIC-MCC method used previously. The increased ion collisions combined with an increase in convergence time of the simulation to a steady state due to the lower mobility of the ions at higher pressures results in a dramatic increase in the computational resources required to simulate the probe at higher pressures. Therefore, a modified version of the two dimensional fluid model presented in Chapter II was used to simulate the ion current collection by a Langmuir probe at 1 Torr pressures. In this section, the sheath structure around a Langmuir probe in a flowing electronegative gas is investigated and CVC's developed from the modified fluid model are analyzed and compared to the

convection limited theory of Clement and Smy, 1969 presented in Chapter I on page 41. In the 1 Torr pressure regime in  $O_2$ , Lam's electric Reynold's number,  $R = 7.414$ , is larger than 1 and  $RX^2\phi^2 = 30.45$ , therefore from equations 1.63 and 1.64 the probe should have a thick sheath and most of the current to the probe should be due to positive ions convected into the thick sheath.

The set-up for the higher pressure Langmuir probe model using the fluid model is slightly different from the PIC-MCC model due to the small domain size required for a single processor. The Langmuir probe is inherently symmetric around a cylindrical axis, therefore, the model was restricted to two dimensions,  $r$  and  $z$  to reduce computational time of the model. To reduce the computational domain size, the Langmuir probe is modeled as being in the center of a hollow metallic tube that is infinite in length with a plasma occupying the rest of the volume of the tube (see Figure 5.26).

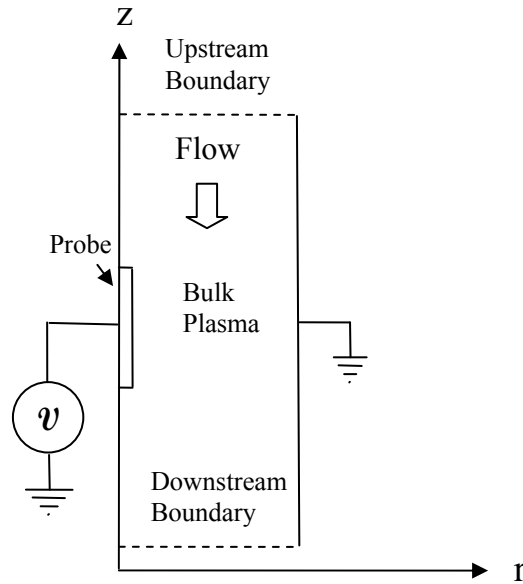


**Figure 5.26 Langmuir Probe Fluid Model Set-up**

The separation between the probe and the outer tube wall is made large enough such that the sheaths of the two surfaces do not overlap, hence there exists a quasi-neutral plasma at a constant plasma potential between the two surfaces. This is equivalent to the Langmuir probe being inserted in a large plasma of uniform density, which should approximately model a large volume flow tube. The boundary conditions for the upstream and downstream boundaries are the same as the boundary conditions used for the RF discharge model. The potential boundary condition is given by equation 2.54 and 2.57 and the boundary condition for the charged species number densities by equation 2.59.

The plasma density in the tube is maintained by reinserting any density lost to the tube or Langmuir probe surface back into the plasma volume. This method reduces the amount of computational time over maintaining the plasma through ionization and secondary emission and also allows the consideration of a wide range of charged species densities to match potential experimental conditions. In the generation region of a gas discharge, the local change in density of a charged species in a particular region is due to ionization, secondary emission, chemical kinetic reactions, or movement of charged species due to either drift or diffusion. In an electronegative discharge, an electric field exists in the bulk plasma region and as a result the charged species densities are altered fairly rapidly due to a substantial drift flux ( $\sim 1.0 \times 10^{15} \text{ cm}^{-2} / \text{ s}$  to  $1.0 \times 10^{17} \text{ cm}^{-2} / \text{ s}$ ) in the bulk plasma. Large divergences in the ion flux, associated with large ion velocities, results in a large time rate of change in the ion density according to the continuity equation. However, the plasma of interest is downstream of an RF discharge and hence

there are no internal electric fields or gain or loss mechanisms in the bulk plasma as is seen in the computational results shown in Chapter IV. Therefore, the modeled plasma density is maintained not by ionization or secondary emission, but by reinserting the charged species lost to the Langmuir probe or walls of the simulation back into the plasma in a non-intrusive way. In the case of electronegative plasmas with  $\alpha_0 < 100$ , an increase in the  $\alpha_0$  value results in an increase in the pre-sheath length (Chung, 2006). An increase in the pre-sheath length, which is many Debye lengths for 1 Torr pressures, of the probe while maintaining the same number of negative ions in a finite volume plasma has the effect of increasing the negative ion density in the bulk plasma. This is due to the negative ions being repelled by the pre-sheath electric field by both the probe and the outer wall of the simulation and hence reducing the volume that the negative ions can occupy which results in an increase in the  $\alpha_0$  value. This effect results in the simulation never coming to a steady state because the  $\alpha_0$  value and hence pre-sheath length continuously grows. To avoid having the reinserted positive ions and electrons interfere with the sheath formation and alter the  $\alpha_0$  value required an adaptive gain approach be taken. The adaptive gain term has the form

$$g = \frac{\Gamma_{wall} S}{V_{sub}} + \frac{\sum_{sub} (n_{goal} - n_k) dV_k}{V_{sub} \Delta t} \quad (5.20)$$

where  $n_{goal}$  is the goal density within the simulation volume and  $V_{sub} = \sum_{sub} V_k$  is the simulation sub volume where  $n_k \geq n_{goal}$ . If  $g > 0$ , then the charged species are only reinserted into the simulation in the volume where  $n_k \geq n_{goal}$  which is outside the pre-

sheath region. If the density of the bulk plasma grows to a large enough value such that  $g < 0$  then the gain term is turned off and there is only a loss of charged species to the simulation surfaces.

A modification to the two dimensional fluid model was required due to the relatively large time scale (relative to the dielectric relaxation time which is approximately  $10^{-10}$  s) required for the slow moving positive and negative ions to develop a steady state sheath around the Langmuir Probe. The large time scale problem is compounded by the fact that a steady state sheath must be maintained at all times as the voltage of the probe is scanned through a range of potential values. This is done to obtain a CVC which is analyzed to determine the density of the plasma based on the background theory developed in Chapter I.

Using the continuity equation and Langmuir probe model results, it can be shown that the lack of an internal electric field and chemical kinetic reactions results in a very slow alteration of ion densities in the pre-sheath region if the change in density is only due to the divergence of the ion flux. Starting with the ion continuity equation and approximating the time derivative as the change in the ion density over the change in time results in

$$\frac{dn_i}{dt} + \vec{\nabla} \cdot \vec{\Gamma}_i = S \quad (5.21)$$

$$\Delta n_i = (S - \vec{\nabla} \cdot \vec{\Gamma}_i) \Delta t \quad (5.22)$$

Based on Figure 5.28, in the pre-sheath region  $-\vec{\nabla} \cdot \vec{\Gamma} \cong -1.0 \times 10^{13} \text{ cm}^{-3}/\text{s}$  and  $S \cong 1.0 \times 10^{10} \text{ cm}^{-3}/\text{s}$ , therefore to alter the density in the pre-sheath region by

$\Delta n_i \cong 1.0 \times 10^9 \text{ cm}^{-3}$  requires a simulation time of  $\Delta t \cong 1.0 \times 10^{-2} \text{ s}$ . To achieve a stable solution when modeling the electrons using the continuity, momentum, and energy equations requires that the simulation time step be less than the dielectric time step. For moderate densities ( $n_e \cong 1 \times 10^9$ ) and low energy electrons ( $\varepsilon \leq 1 \text{ eV}$ ) the dielectric time step is approximately  $1 \times 10^{-10} \text{ s}$  in oxygen, hence the simulation needs to run for approximately 100 million time steps to converge to a steady state solution. Therefore, it was necessary to develop a modeling method which did not explicitly model the electron transport and hence could overcome the restrictions of the dielectric relaxation time stability limit.

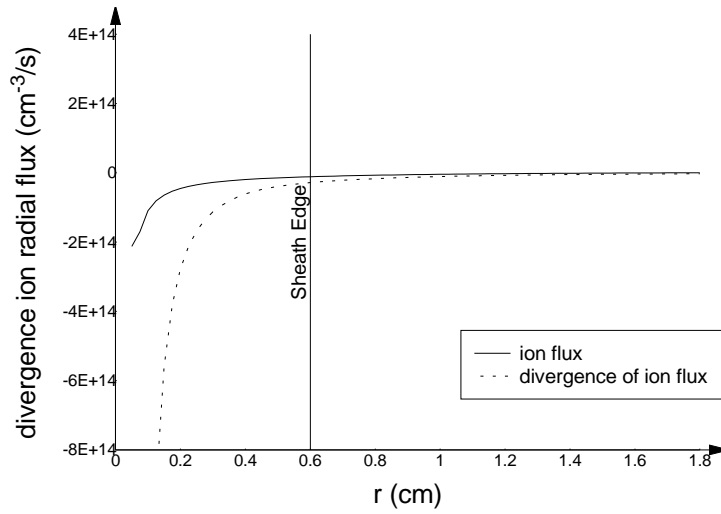


**Figure 5.27 Ion Flux and the Divergence of the Ion Flux in a Sourceless 1-D O<sub>2</sub> Probe Model with the Sheath Edge Determined using the Quasi-Neutrality Condition**

To avoid this dielectric relaxation time step limit, the time independent form of the electron momentum equation, equation 2.20, is solved for the case when the probe is

negatively biased ( $V_{probe} > 3\varepsilon_e$ ) relative to the plasma. The electron flux to the probe is negligible under those conditions (Cartwright and others, 2000), hence

$$\vec{\Gamma}_e = -n_e \mu_e \vec{E} - D_e \vec{\nabla} n_e = 0 \quad (5.23)$$

Solving for the electron density

$$\frac{\vec{\nabla} n_e}{n_e} = \frac{\mu_e}{D_e} \vec{\nabla} V \quad (5.24)$$

Substituting in equation 2.8 and integrating

$$\int_{x_R}^x \vec{\nabla} \ln(n_e) \cdot d\vec{l} = \int_{x_R}^x \frac{\vec{\nabla} V}{T_e} \cdot d\vec{l} \quad (5.25)$$

where  $x_R$  is a point located in the bulk plasma region and  $x$  is at the point of interest.

The integration results in the familiar Boltzmann relation for electrons in equilibrium with the electric field around the probe given by the expression

$$n_e(x) = n_e(x_R) \exp((V(x) - V(x_R)) / T_e). \quad (5.26)$$

Substituting Equation 5.25 into Poisson's equation results in the following expression

$$\nabla^2 V = -\frac{e}{\varepsilon_0} (n_i - n_n - n_{e,0} \exp((V - V_p) / kT_e)) \quad (5.27)$$

This equation is then finite differenced and solved along with the positive and negative ion continuity and momentum equations using a Newton-Raphson iteration scheme which was discussed in Chapter II. The modified plasma fluid model, using equation 5.26 to simulate the electron density, can now be run at time steps of  $2 \times 10^{-8}$  s.

The following simulations were performed on a single CPU computer and took 3 to 6 weeks wall clock time to converge and  $5 \times 10^{-3}$  to  $1 \times 10^{-2}$  s in simulation time depending on the flow conditions (faster convergence was achieved due to the flowing



plasma increasing flux and decreasing sheath length). Simulations were run in a 4 cm by 4 cm,  $r - z$  cylindrical grid using a  $160 \times 160$  uniform grid at resolutions of  $\Delta x = 2.5 \times 10^{-2}$  cm. The densities of the plasma are  $n_i = 5.0 \times 10^9$  and  $\alpha_0 = 1.5$ . The mobilities of the positive and negative ions in an oxygen background gas are  $\mu_i = 0.168 / P$  and  $\mu_n = 0.181 / P$ . A separate simulation was run to convergence with each bias potential to ensure a steady state sheath had been obtained. Each simulation was performed with a 1 Torr oxygen background gas with an electron temperature of 0.2 eV and positive and negative ion temperatures of 0.025 eV in equilibrium with the background gas temperature. All the plasma parameters used in the modified fluid model are the same as those used in the hybrid PIC-MCC model.

Examining the contour plot for the non-flowing case, we note that the ion density depletion region around the probe is symmetric and has a larger extent than the ion density contours for the non-flowing 0.001 and 0.01 Torr cases shown in Figures 5.8 and 5.15. In the absence of the probe sheath, the ion density is constant; hence the change in the ion density farther from the probe indicates that the sheath length is longer at 1 Torr. This result is consistent with the collisional continuum theory of Kiel, 1966, who showed that the sheath length of the probe would expand with increased collisions due to the friction force of the collisions reducing the current to the probe.



249

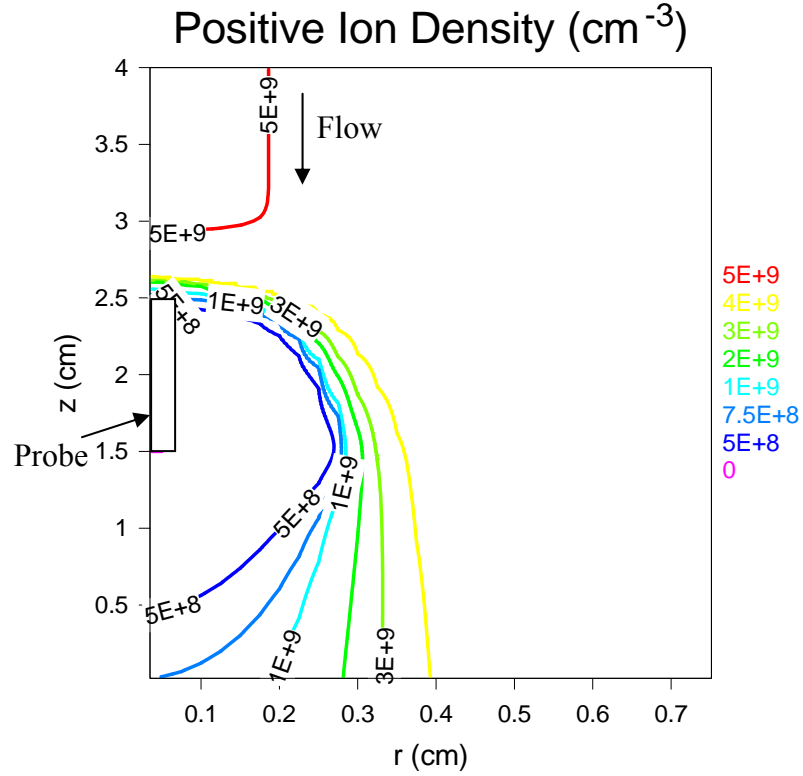


**Figure 5.29 Contour Plot of the Positive Ion Density Around a Probe in a 1 Torr Non-Flowing and Flowing Background Gas with Probe Biased to -30V**

The radial extent of the ion density depletion region in the 1 Torr case is less than the 0.01 Torr case where the ion density depletion region extends out to over 1 cm. In addition, the radius of the perturbation of the potential due to the probe in the non-flowing case at 1 Torr, shown in Figure 5.30a, is larger than in the 0.01 Torr non-flowing case. This is due to the higher collision frequency of the ions with the background gas which causes a larger drop in potential over a longer pre-sheath region (Oksuz and other, 2003). The perturbation radius of the potential caused by the probe in the flowing 1 Torr case is shown in Figure 5.29b. The perturbation radius of the potential is smaller in the flowing versus non-flowing case. This result differs from the 0.01 Torr flowing case and

the reason for the difference is mostly attributed to the much shorter mean free path of the negative ions in the 1 Torr pressure regime.

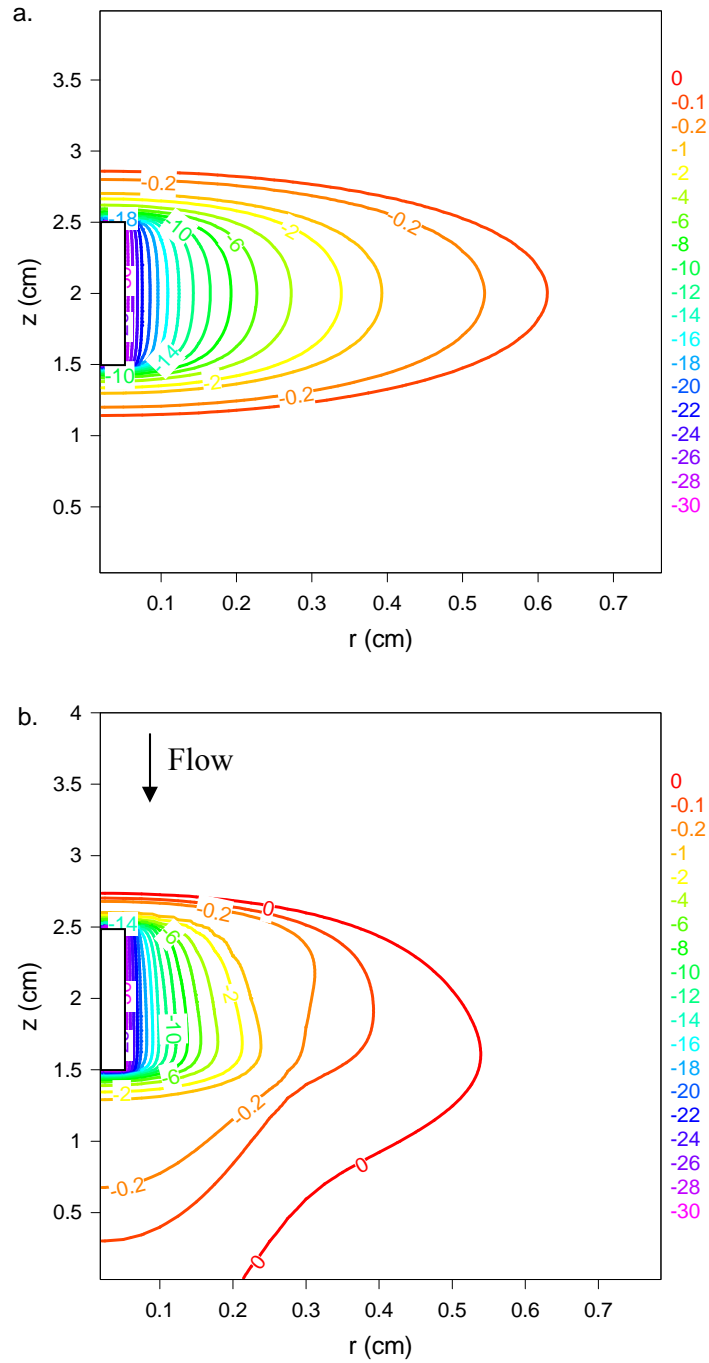


**Figure 5.30 Contour Plot of the Potential Difference Around a Probe in a 1 Torr in a (a) Stationary and (b) 250 m/s Flowing Background Gas with Probe Biased to -30V**

The deformation of the potential in the electronegative sheath in 1 Torr case is due to multiple collisions of the flowing background gas with the negative ions such that the negative ions are pushed into the upstream sheath. The multiple collisions of the flowing background gas with the negative ions act to “push” the negative ions into the sheath region. This results in a significant negative ion density at a location from the probe where the sheath electric field would normally have repelled the negative ions. This is unlike the 0.01 Torr case in which the negative ions experience collisions so infrequently that they were reflected off the pre-sheath region and traveled beyond the sheath radius before experiencing another collision on average. The “pushing” of the negative ions into the sheath by the flowing gas modifies both the sheath and pre-sheath region electric field substantially. This only occurs if the collision frequency of the negative ions with the background gas is frequent enough that multiple collisions occur during the time it takes the negative ion to be repulsed by the sheath electric field. To determine the collision frequency required to alter the probe sheath with a flow, we examine the acceleration away from the probe tip of a single negative ion by the Langmuir probe sheath based on the repelling forces of the electric field given by

$$\vec{F} = M_n \frac{d^2 \vec{x}}{dt^2} = -q\vec{E} \quad (5.28)$$

From Figure 5.30, it is apparent that the electric field strength in the probe pre-sheath varies nearly linearly with distance at the sheath edge, therefore equation 5.28 can be recast as

$$M_n \frac{d^2 x}{dt^2} = -q\beta x \quad (5.29)$$

where  $\beta$  is the linear change in the electric field strength with distance. Equation 5.29 has the same form as the ideal linear spring differential equation and as a result the negative ion repulsion frequency is given by

$$f_r = \frac{1}{2\pi} \sqrt{\frac{q\beta}{M_n}} \quad (5.30)$$

If the collision frequency of the negative ions with the background gas is greater than the frequency at which the negative ions get repulsed by the electric field in the pre-sheath then the negative ions are pushed into the pre-sheath region as is seen in Figure 5.31.

The negative ions gain additional directed energy into the sheath with each collision such that the flowing background gas gives the negative ions enough additional energy that they can even penetrate the 0.3 eV pre-sheath shown in Figure 5.31.

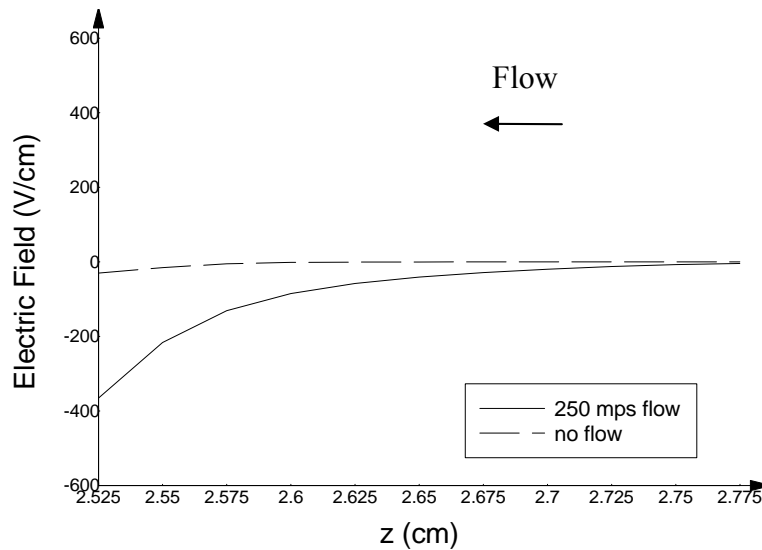


**Figure 5.31 Electric Field at the Tip of the Probe in No Flow and 250 m/s Flow Conditions at 1 Torr and -30V Bias**

Approximating the electric field as growing in strength in the sheath while approaching the probe from the bulk plasma as approximately  $E \approx 10^3 x$  V/cm, results in

the negative ion repulsion frequency from equation 5.29 being approximately  $8.68 \times 10^5$  Hz. Using a cold gas approximation, the collision frequency with the background gas is  $\nu_c = 6.44 \times 10^7 s^{-1}$  in which the flow velocity of 250 m/s instead of the thermal velocity ( $u_{flow} = 250$  m/s and  $v_{i,th} = 435$  m/s) of the background gas is used to estimate the collision frequency in the direction of the probe tip. The collision frequency even at this fairly low pressure of 1 Torr is much larger than the frequency at which the negative ions moving towards the probe are repelled by the sheath's electric field, hence the negative ions experience many collisions with the flowing background gas while being repelled by the sheath. These frequent collisions result in the negative ions being “pushed” into the pre-sheath region near the tip of the probe such that they have a higher density in the pre-sheath than the electrons as shown in Figure 5.32. The electrons unlike the negative ions are repelled by the pre-sheath electric field due to their low collisional coupling with the background gas. The presence of the negative ions in the sheath region alters the upstream sheath and pre-sheath length and changes the proportion of the potential drop between the sheath and pre-sheath regions as seen in Figure 5.32. The compression of the sheath shown on axis in the z direction in Figure 5.32 also occurs at a larger radius from the probe tip and accounts for the compression of the radial sheath of the probe. This compression of the radial sheath results in less positive ion current being collected by the probe.

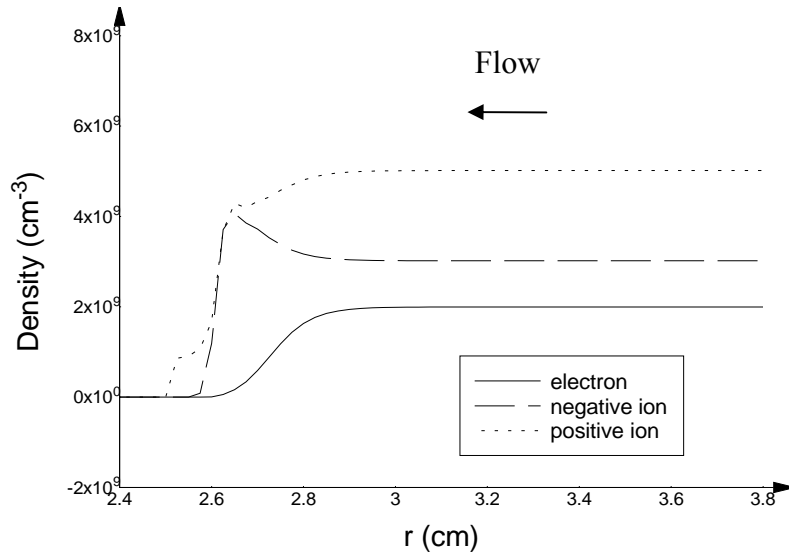


**Figure 5.32 Charged Species Densities at the Tip of the Probe ( $z = 2.5$  cm)**

Defining the sheath length near the probe tip as beginning at the point where the plasma is no longer quasi-neutral in Figure 5.33a, the sheath at the tip of the Langmuir Probe has been reduced in length from 0.38 cm to 0.2 cm due to the background gas flow. In addition, similar to the lower pressure cases, the transition in the potential from the pre-sheath to the sheath region is sharper and closer to the probe tip due to the flow reducing the acceleration requirements for the positive ions shown in Figure 5.33b (McMahon and others, 2005).



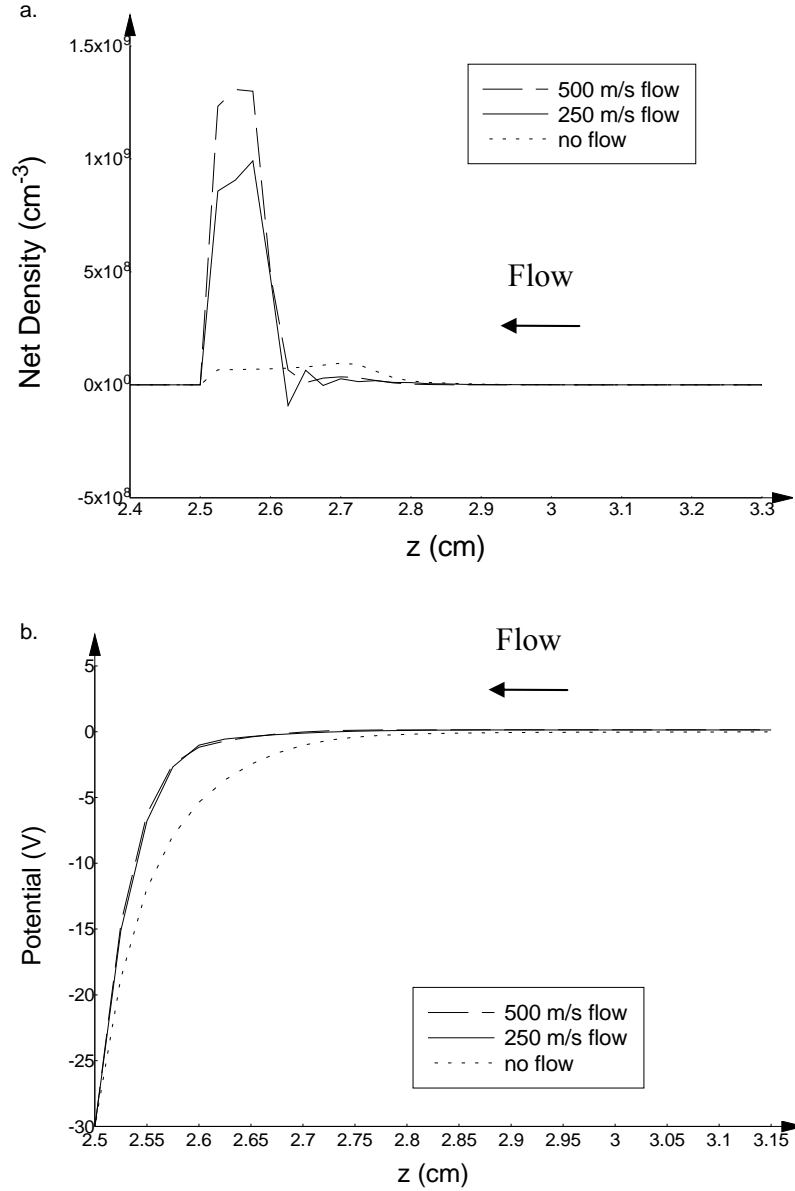


**Figure 5.33 Comparison of (a) Net Charge and (b) Potential Profiles at the Probe Tip ( $z = 2.5$  cm) in the Non-Flowing, 250 m/s, and 500 m/s Flow Cases**

Similar to the hybrid PIC-MCC model results discussed previously, the negative ions are repelled by the angled upstream sheath of the probe and travel parallel to the upstream sheath as shown in Figure 5.33. Due to the high collision frequencies with the background gas, the negative ions are not repelled by the pre-sheath at a radius greater

than  $r = 0.45$  cm unlike in the 0.01 Torr case shown in Figures 5.21 and 5.34. Similar to the pre-sheath at the tip of the probe, the upstream pre-sheath at larger radii is also compressed by the collisions of the flowing background gas with the negative ions resulting in a smaller pre-sheath and sheath radius, Figure 5.35b. As a result, the positive ion current flowing in the  $-z$  direction into the upstream sheath of the Langmuir Probe is somewhat reduced by the background gas flow, resulting in a smaller ion current collected by the Langmuir probe in a 1 Torr versus a 0.01 Torr flowing background gas.

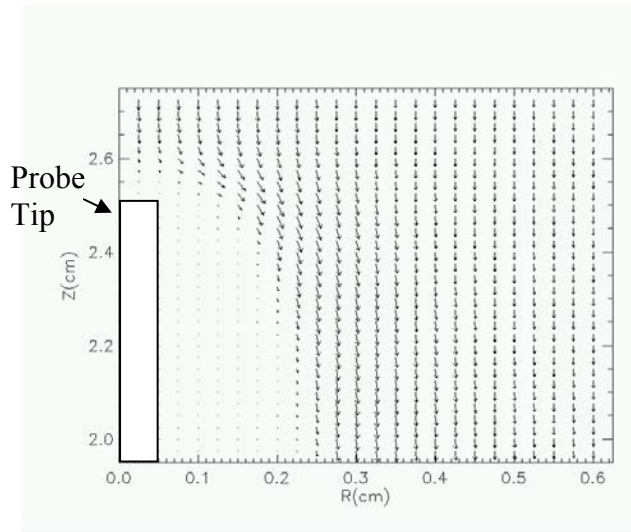


**Figure 5.34 Negative Ion Velocity Vector Plot Near Probe Tip with Probe Biased to -30V, 1 Torr, and 500 m/s Flow Velocity**

The ion current collected by the probe in a 1 Torr background gas with a 250 m/s flow at a -30 volt bias is increased by 700% over the stationary case. This dramatic increase in collected current in the flowing versus stationary case is due mainly to the reduced mobility of the ions at higher pressures which reduces diffusion of ions into the collecting surface of the probe. The flowing background gas reduces the sheath radius of the probe and hence ion collecting surface of the probe as shown in Figure 5.35, however

with a flowing background gas, the ions are convected into the upstream sheath of the probe much faster than they diffuse into the probe collecting surface in the stationary case. As a result, additional ion current is collected in the flowing case versus the stationary case even though the radial sheath is compressed. The increase in positive ion current to the probe in a flowing background gas and the dominance of the convection current over the diffusive current collected by the probe is consistent with the theory of Clements and Smy, 1969, presented in Chapter I on page 41 and is orientation independent for a thick sheath convection limited regime.

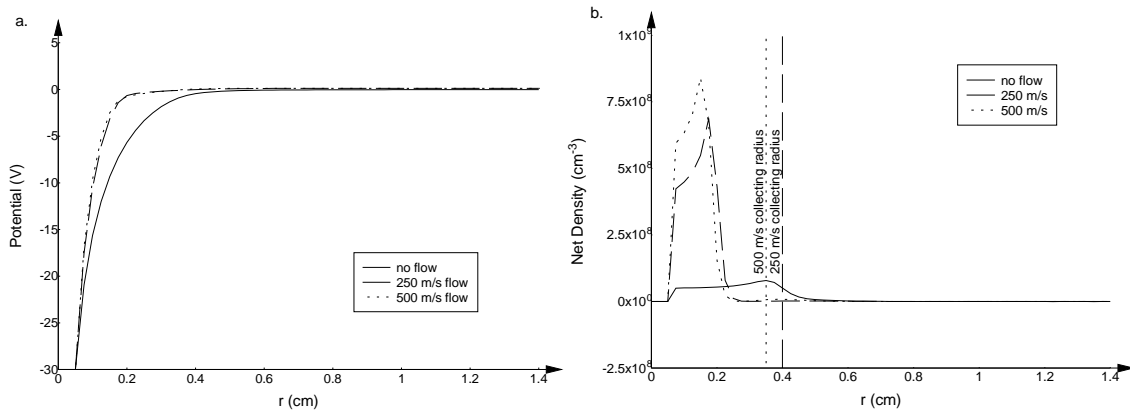


**Figure 5.35 Comparison of Radial (a) Potential Profiles and (b) Net Charge Near Tip of Probe at  $z = 2.4$  cm in a 1 Torr, -30 V Bias Oxygen Plasma in Non-Flowing, 250 m/s, and 500 m/s Flow Cases**

However, defining the location in the pre-sheath where the potential and electric field is non-zero (at approximately  $r \sim 0.0056$  m from Figure 5.28 and 5.31) as the collecting radius of a disc results in an ion collection current of  $I_p = 1.97 \times 10^{-5}$  amps (which is determined by integrating the incident flux over the surface of the disc). This collected current is much larger than the current actually collected by the probe. Since, the probe is of finite length and the ions have a substantial velocity parallel to the probe, some of the ions that enter the radial pre-sheath region do not traverse the sheath fast enough to

intercept the probe surface and are instead focused by the probe sheath as discussed in the previous section. This observation is consistent with the theory developed by Smy and Noor, 1976, which states that for fast flowing plasmas in a collisional gas the electric field would not be sufficient to collect all the high velocity ions passing through the pre-sheath and even sheath region.

At high flow velocities and low ion mobilities, the pre-sheath or sheath radius does not necessarily determine the collecting area of the probe in the convection limited regime. Therefore, we need to develop another criterion for determining this collecting area in order to compare the model results to the convection limited regime theory. To calculate the current collecting area of the probe sheath, consider that the ions at 250 m/s take approximately  $t_l = 4.0 \times 10^{-5}$  seconds to travel the length of the 1 cm probe. To determine the time required for the ions to traverse the radial probe sheath, the inverse of the ion radial velocity is integrated with respect to radius

$$t_t = \int_{r_p}^{r_c} \frac{1}{v_i(r)} dr \quad (5.31)$$

where  $v_i(r)$  is the ion radial velocity at radius  $r$ ,  $t_t$  is the time required for ions to traverse the probe sheath, and  $r_c$  is the probe collecting radius.  $r_c$  is calculated by setting the time required for the ions to travel the length of the probe, equal the time required for the ions to traverse the collecting radius ( $t_l = t_t$ ). The collecting radius versus voltage calculated by this method is shown in Figure 5.36. Also shown in Figure 5.36 is the radius at which the sheath becomes quasi-neutral at the mid-section of the probe, which is reasonably close to the calculated collecting radius of the probe in the

250 m/s case. This is due to the electric field in the sheath being much larger than in the pre-sheath, hence most of the positive ions in the sheath region are captured. In the pre-sheath, however, the electric field is small enough that the ions are not accelerated to the probe's surface before passing through the pre-sheath region. For the 500 m/s case, the pre-sheath is more compressed due to the higher collision frequency of the negative ions with the background gas. However, the quasi-neutral radius is a little larger than the collecting radius due to the higher velocity of the ions and the rapid collisions of the positive ions with the flowing background gas. These rapid collisions with the background gas force the positive ions downstream of the probe without being collected. As a result, at faster flow velocities a greater sheath electric field is required to “capture” the positive ions and hence the collecting radius is reduced in the 500 m/s versus 250 m/s flow case.

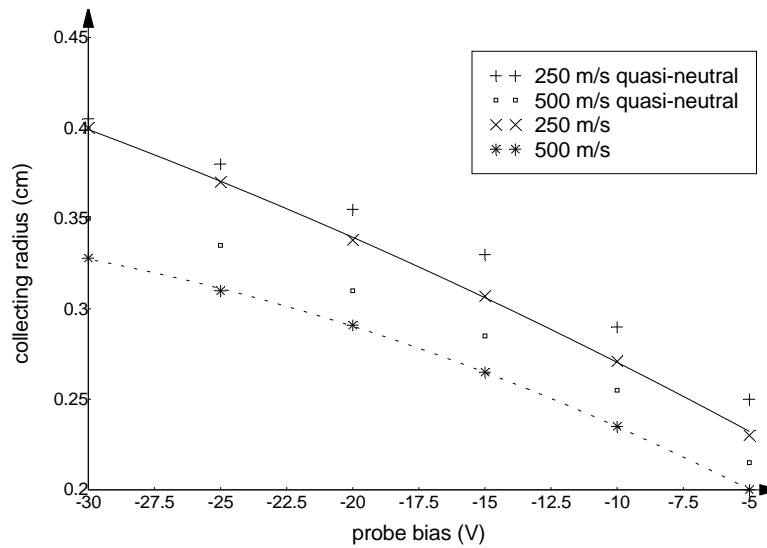


**Figure 5.36 Positive Ion Collecting Radius and Quasi-Neutral Radius as a Function of Probe Bias**

Considering the pressure regime and based on Lam's electric Reynold's number,  $R = 7.414$ , being larger than 1 and  $RX^2\phi^2 = 30.45$ , from equations 1.63 and 1.64, the probe should have a thick sheath and most of the current to the probe should be due to positive ions convected into the thick sheath. The current collected in this manner can be calculated where the collecting surface is that of a disk perpendicular to the flow

$$I_{convection} = e\pi r_c^2 n_i U_{flow} \quad (5.32)$$

which is similar to the convection limited thick sheath expression determined by Clements and Smy, 1969. The approach of Clements and Smy, 1969, used a rectangular collecting surface due to the probe having an orientation perpendicular to the flow. The positive ions flow into the collecting radius and are transported into the Langmuir probe via the large electric fields in the sheath region.

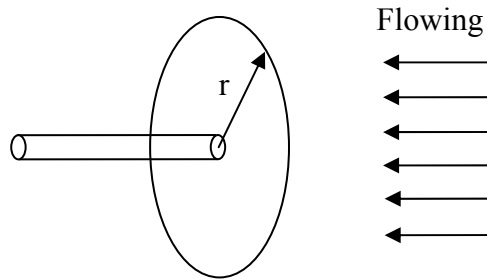


**Figure 5.37 Langmuir Probe Collection Radius for Ions Flowing into the Sheath Region**

Figure 5.38 presents a comparison of the CVC produced by the plasma fluid model with Clement and Smy's convection limited thick sheath model from Chapter I,

page 39. The currents calculated by the plasma fluid model are used to determine the probe bias that would collect the same ion current in an electropositive plasma with the same mobility and positive ion density. The results of the comparison suggest that an electronegative sheath at lower probe biases is similar to an electropositive sheath in a flow. However, as the probe bias increases, the current collecting radius of the probe in an electropositive plasma grows faster than in an electronegative plasma. As shown previously in an electronegative plasma, the negative ions can deform the sheath which results in a reduced radius for the collection of convection current by the probe. However, this cannot be verified by this study because modeling an electropositive flowing plasma required a much larger domain size due to both the sheath of the outside flow tube and the Langmuir probe being substantially larger. This resulted in a need for larger computational resources than were available to the study.

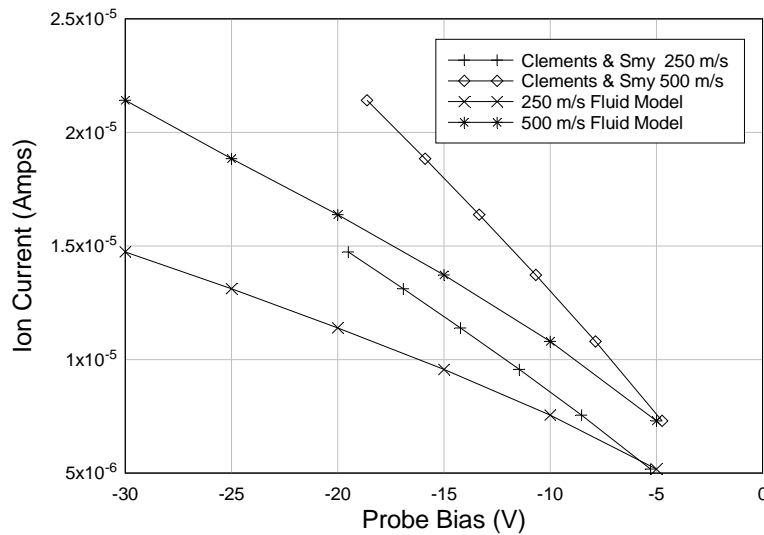


**Figure 5.38 Comparison of the Probe CVC in a Non-Flowing and Flowing Gas at Velocities of 500 m/s and 250 m/s and 0.5 mm Radius Probe**

The approach of Clements and Smy, 1969, was used to determine the positive ion density used in the fluid model simulation based on the CVC shown in Figure 5.38. The results of the analysis, shown in Figure 5.39 for a simulated ion density of  $n_i = 5.0 \times 10^9 \text{ cm}^{-3}$ , suggest that using the approach of Clements and Smy in a flowing electronegative plasma can result in up to a 50% error in positive ion density measured at higher probe biases. At lower probe biases, due to the small extent of the collecting radius of the probe, the simulation and theory agree, however, at a -5 volt bias, the probe is primarily collecting electron current making determination of the ion current collected at that probe bias problematic.

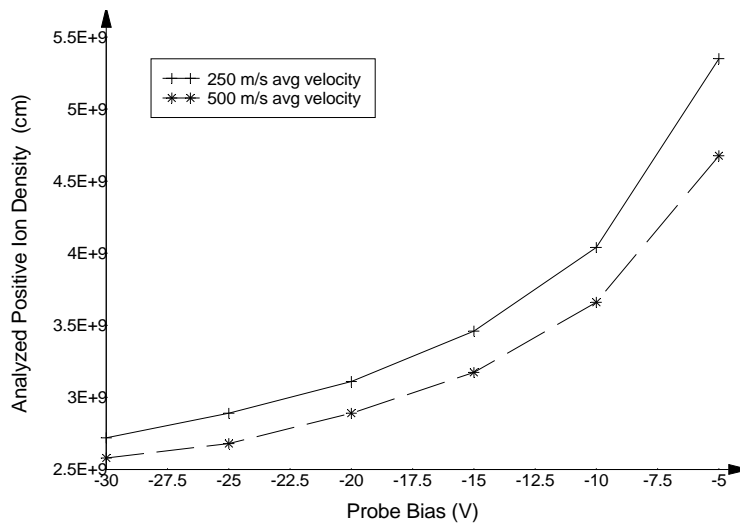


**Figure 5.39 Estimated Positive Ion Density Based on Simulated Current Collection Using Clements and Smy's Theory where  $n_i = 5.0 \times 10^9 \text{ cm}^{-3}$  in the simulation in a 1 Torr Oxygen Background Gas Flowing at 250 m/s and 500 m/s**

However, not all current collected by the Langmuir probe in this pressure regime is due to convection. Some of the collected current is due to the diffusion of the ions into the downstream collecting surface resulting from the moderate mobilities of the positive ions



at 1 Torr pressures (Clements and Smy, 1976). In the case of a stationary plasma, the radius of the pre-sheath that collects ion current is approximately constant along the length of the probe. As a result, all the positive ions that enter the pre-sheath region eventually are collected by the probe according to radial motion limited theory (Riemann, 1997). However, in the case of a probe in a flowing background gas, not all ions moving into the pre-sheath region are collected by the probe due to the axial flow of the ions moving them out of the pre-sheath region before they can be collected by the probe (Smy and Noor, 1976).

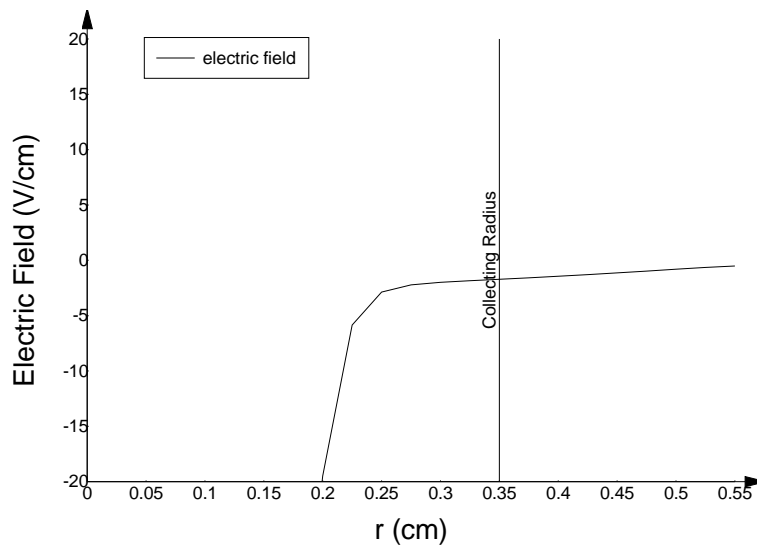


**Figure 5.40 Radial Electric Field Near the Upstream Collecting Radius for a 500 m/s Flow Case at -30V Probe Bias and 1 Torr Background Gas**

As a result, the ions that diffuse into the sheath region downstream of the upstream collecting radius of the probe, shown in Figure 5.41, have less time to be transported to the probe surface. Based on the time of flight equation, 5.32, the ions drifting into the sheath downstream of the collecting radius need to be closer to the probe to be collected. As a result, the radius of the downstream collecting surface approximately decreases

linearly with axial distance from the upstream collecting radius as shown in Figure 5.41. The linear decrease in the radius of the downstream collecting surface is due to the constant electric field along this surface and hence constant drift velocity moving the positive ions radially towards the probe as the positive ions are convected downstream.

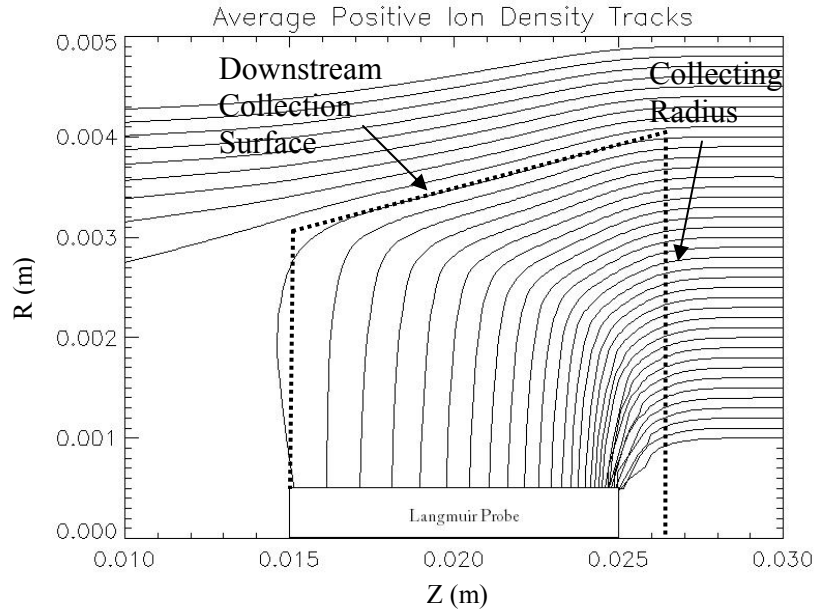


**Figure 5.41 Average Path of the Positive Ions Collected by the Probe Based on Initial Radial Distance from the Probe at 200 m/s Flow Velocities**

As suggested by the ion density paths in Figure 5.41, the current density collected along the length of the probe is strongly biased towards the upstream tip of the probe, shown in Figure 5.42. In the stationary case, the ion current density collection distribution of the probe is spread out uniformly over the probe length with only slight increases at each tip due to the stronger electric field. In the 0.01 Torr, 200 m/s flowing case, larger collection currents densities near the tip of the probe were observed, however, in the 0.001 Torr case there was no difference between the current densities at either the upstream or

downstream tip. Since the sheath is much more compressed towards the tip of the probe, this creates higher radial sheath electric field near the tip of the probe (seen in Figure 5.36) and results in the collected positive ion current being primarily at the tip of the probe in the 1 Torr pressure regime. However, also seen in Figure 5.41 and 5.42, some of the current is collected downstream of the probe tip either due to the ions being at a greater radius when incident upon the probe's upstream collecting radius or due to the drift of the positive ions into the downstream collecting surface caused by the sheath electric field.

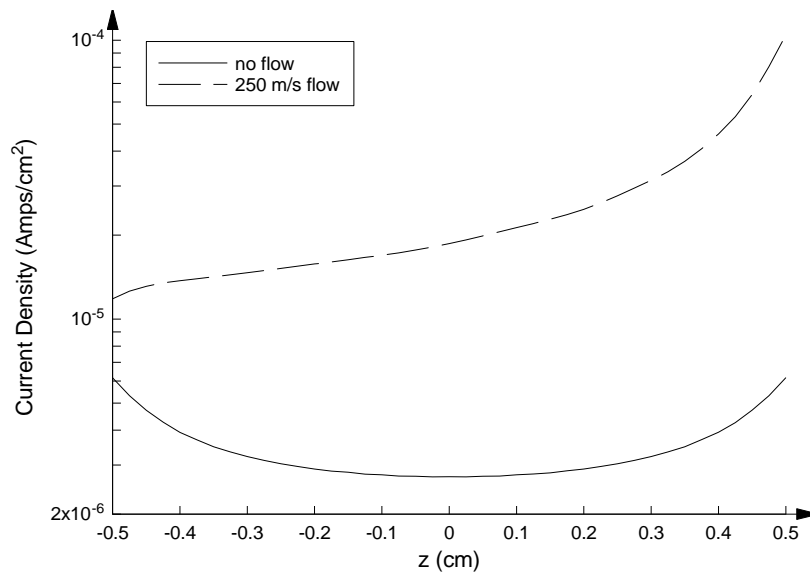


**Figure 5.42 Radial Current Density Comparisons along Length of the Probe in a 1 Torr Oxygen Plasma Flowing at 200 m/s and no flow.  $z = 0$  is the Mid-Section of the Probe**

To determine the positive ion density from the probe CVC more accurately, we need to account for the drift velocity of the positive ions into the downstream collecting surface. From the previous analysis, we can more precisely calculate the positive ion drift flux into the downstream collecting surface, shown in Figure 5.41, using the ion

radial drift flux along the downstream collecting radius. The electric field along the downstream collecting surface is due to the surface being within the probe sheath shown in Figure 5.35. Model results indicate that the ion radial drift velocity and density are approximately constant along the collecting surface as suggested by Clements and Smy, 1976. The drift current to the probe can therefore be approximated using the equation

$$I_{drift} \approx e2\pi n_i \mu_i E_c (r_c + m(z - z_s))l \quad (5.33)$$

where  $E_c$  is the electric field along the edge of the downstream collecting radius,  $z_s$  is the axial location of the upstream collecting radius, and  $m$  is the slope of the downstream collecting surface. This results in the total current collected by the probe being given by the expression

$$I_{total} = I_{convection} + I_{drift} \quad (5.34)$$

Model results shown in Figure 5.43 indicate that approximately 70% of the total current collected by the probe is due to ion convection into the collecting radius. The convection current shown in Figure 5.43 was determined from equation 5.32 and the collecting radius is shown in Figure 5.36. Approximately 30% of the ion current being collected is due to the drift of the ions into the downstream collecting surface. The large percentage of positive ion current being collected by the downstream surface is unique to placing the Langmuir probe parallel to the flow (Clements and Smy and others generally placed the probe perpendicular to the flow). The parallel orientation of the probe results in a long residence time of the positive ions traveling parallel to the downstream collecting surface allowing them adequate time to drift into the downstream collecting surface.

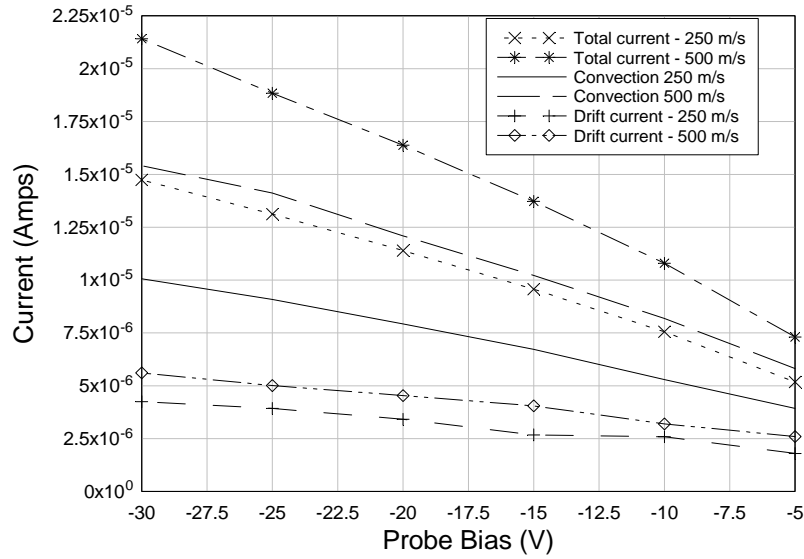


**Figure 5.43 Comparison of the Collected Current by a Probe in 250 m/s and 500 m/s Flow Conditions in a 1 Torr Oxygen Plasma Examining the Total Current, Convection Current, and Drift Current**

Using the collecting radius calculated from the fluid model along with equation 5.33 and the average electric field along the collecting surface, results in a very reasonable estimate of the current collected at the probe surface in the flowing cases shown in Figure 5.44. Differences in the approximate total positive ion current from equation 5.33 and the current incident on the probe collecting surface are due primarily to ion flux on the collecting surface not being precisely constant. The probe currents shown in Figure 5.44 also include the theoretical electron current collected by a probe based on equation 1.5 (Smy, 1976). The electron temperatures and their distribution functions downstream of the RF discharge can be measured using standard Langmuir probe analysis given by equations 1.5 and 1.6 since the background gas is room temperature according to Smy, 1976, and Menart, 2004. Smy, 1976, assumes that the collisional coupling with the background gas and it's flow velocity are negligible compared the

velocity of the electrons in the plasma and therefore stationary probe theory can be used. The theory put forth by Smy, 1976, that the electron distribution and temperature can be measured using stationary probe analysis techniques could not be examined using the simulations developed for this investigation. This is due to the assumption made in developing the probe simulation that the electrons have a Boltzmann energy distribution and do not collisionally couple with the flowing background gas.

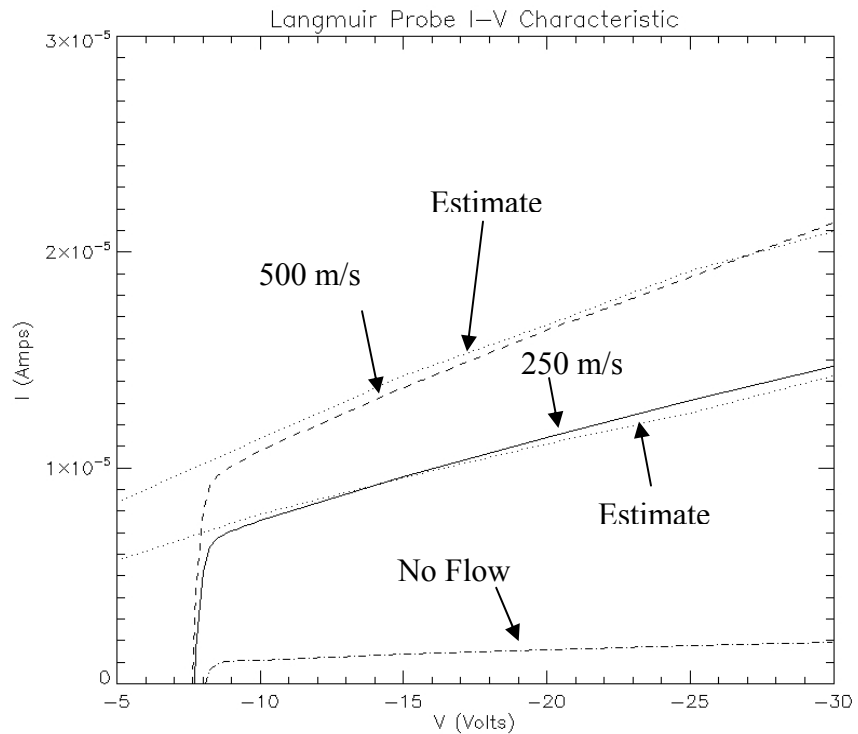


**Figure 5.44 Comparison of the Probe CVC in a 1 Torr Non-Flowing and Flowing Background Gas at 500 m/s and 250 m/s Flow Velocities between the Modified Fluid Model and Equation 5.34 using a 0.5 mm Radius Langmuir Probe**

The fluid model results suggest that the ion density can be determined using a Langmuir probe in a flowing electronegative background gas using equations 5.32, 5.33, and 5.34. However, as with any other Langmuir probe diagnostic technique the collecting radius must be known for the particular conditions of the plasma of interest.

The comparison of the Plasma Fluid Model to Clement and Smy's convection limited thick sheath theory, suggests that using the convection limited sheath theory can result in up to 50% error in the positive ion density measurements in an electronegative plasma. However, due to the complexity of the sheath equations, the necessity of describing the sheath in two dimensions, and the asymmetry of the sheath in a flowing plasma, an analytic estimation of the collecting radius was not developed in this study to analyze a probe CVC in an electronegative flowing plasma. The Plasma Fluid Model could be run over a wide parameter space of flow velocities, probe biases, and pressures to develop tables of collection radii to analyze Langmuir Probes in an electronegative flowing background gas. However, this approach for analyzing the CVC of a Langmuir probe is impractical due to the immense amount of time ( $\sim 2$  months) required for the simulation to converge to a steady state solution.

## **Conclusions**

The effect of a flowing background gas on an electronegative RF discharge and the diagnostics of the resulting plasma with a Langmuir probe have been investigated for pressures between 0.001 to 1 Torr and in flow velocities up to 750 m/s. Comparisons between the RF discharge model developed for this study and the models and experiments of Lymberopoulos and Economou, 1992, Boeuf, 1987, Boeuf and Pitchford, 1995, Gordiets and others, 1995, Graves, 1988, and Salabas and others, 2002 were very favorable. Simulation results from the RF discharge model in a stationary background gas with a 1000V applied voltage, a pressure of 1 Torr, and 3 cm gap width indicate that the detachment of negative ions by excited neutral species provides the main mechanism

for balancing the negative ion to electron ratio or  $\alpha$  value of an RF discharge in both a pure  $O_2(X)$  and  $N_2(X) - O_2(X)$  gas mixture. In a stationary or slow flowing electronegative background gas, the active sheath length of an RF discharge is increased due to larger densities of detaching excited neutral species in the discharge volume. This result is consistent with the results of Shibata and others, 1995, who showed that increased detachment rates resulted in an increase in the sheath length of the discharge. The removal of the excited neutral species by the flow has the effect of increasing the  $\alpha$  value by reducing the excited neutral species densities and hence the detachment rate of negative ions. The decrease in excited neutral species densities with flow also changes the source location of the electrons and positive ions from near the center of the discharge (where the detaching excited neutral densities are at a maximum) to near the electrodes due to the larger  $\alpha$  value and ionization reactions occurring primarily near the electrodes. The reduction in the sheath length and increase in  $\alpha$  value with increasing flow velocity also has the effect of increasing the electric field amplitude in both the sheath and bulk plasma. A factor of two reduction in sheath length has been shown in this investigation for an increase in flow velocities from 25 m/s to 500 m/s, resulting in a 50% increase in peak average electric field in the sheath and an increase of 65% in the peak electric field in the bulk plasma. The average positive and negative ion densities increase by over an order of magnitude from  $n_i = 2.64 \times 10^9 \text{ cm}^{-3}$  to  $n_i = 2.71 \times 10^{10} \text{ cm}^{-3}$  and  $n_n = 1.76 \times 10^9 \text{ cm}^{-3}$  to  $n_n = 2.58 \times 10^{10} \text{ cm}^{-3}$  when the flow velocity is increased from 5 m/s to 250 m/s at 1000V in an  $O_2(X)$  RF discharge. In an  $N_2(X) - O_2(X)$  gas mixture RF discharge, positive ion densities increase by over a factor of 6 from



$n_i = 1.3 \times 10^9 \text{ cm}^{-3}$  to  $n_i = 8.4 \times 10^9 \text{ cm}^{-3}$  and negative ions by a factor of 65 from  $n_n = 1.1 \times 10^8 \text{ cm}^{-3}$  to  $n_n = 7.1 \times 10^9 \text{ cm}^{-3}$  when the flow velocity is increased from 0 m/s to 250 m/s at a 1000V due to the larger numbers of detaching neutral species. The larger electric fields in the sheath and bulk plasma increase the ionization rate and the positive ion density in the discharge. The negative ion density increases due to the increased ionization rate and the decreased detachment rate caused by lower densities of neutral excited species. However, the electron density in both background gases remains approximately constant with increasing flow velocity in the discharge region and discharge current density increases slightly due to increased displacement current in the local sheath region. Downstream of the RF discharge, the excited neutral species detach the larger density of negative ions and produce a substantial electron density for a 250 m/s flow velocity at 1 Torr pressures investigated in this study for both a pure  $O_2(X)$  and  $N_2(X) - O_2(X)$  gas mixture. In addition, the production rate of neutral excited species, such as  $O(^3P)$ ,  $O_2(b)$  (due to the production of  $O(^1D)$ ),  $N_2(A)$ , and  $N(^4S)$ , generated by higher threshold energy reactions, such as dissociation, are increased by up to 500% with increased flow velocity. Increased excited species production rates with increasing flow velocity is useful in remote plasma enhanced chemical vapor deposition applications that require large fluxes of neutral excited species to create uniform depositions (Collart and others, 1995).

It was also shown in this investigation that decreases in the relative yield of excited neutral species and the reduction in the ambipolar diffusion coefficient (due to increased  $\alpha$  values) at higher flow velocities reduces the decay rate of negative and

positive ion densities downstream of the RF discharge. An increase in the positive and negative ion densities combined with a moderate electron density downstream make a RF discharge in a fast flowing electronegative background gas an excellent means of supplying charged species downstream to a non-self sustaining discharge. Increases in neutral excited species densities, such as  $O_2(a)$  for ElectriCOIL applications, created in a lower voltage non-self sustaining discharge would enhance detachment of the negative ions supplied downstream of the first RF discharge, resulting in additional electrons to maintain the non-self sustained discharge. Increases in available electrons to sustain the discharge reduce the maintenance electric field requirements and allow the discharge to operate at near 10 Td values which have been shown to be optimal for  $O_2(a)$  production (Hicks and others, 2006). Also relative yields of excited neutral species densities, such as  $O_2(a)$ , could be boosted if the residence time of the background gas in the second downstream discharge was increased.

The presence of negative ions in a flowing moderate pressure plasma has also been shown in this study to have a substantial effect on the sheath and positive ion current collected by a Langmuir probe. At lower pressures, the sheath extent and positive ion current collected by a probe oriented parallel to a flowing electronegative plasma and background gas at various pressures were determined using a hybrid PIC-MCC model. At a pressure of 0.001 Torr and 200 m/s flow velocity, the background gas flow was shown to have little effect on the ion current collected by the probe. This was found to be due to the ion current to the probe primarily being limited by thermal diffusion of positive ions into the pre-sheath region and the convection velocity being smaller than the

diffusion velocity. The sheath radius in this case was observed to increase by 10% due to negative ions reflecting off the angled Langmuir probe pre-sheath, resulting in a flow of negative ions parallel to the angled upstream sheath edge and away from the probe. The flow of negative ions away from the Langmuir probe spreads out the space charge in the sheath resulting in a slightly larger sheath than in the non-flowing case. Due to the relatively small increase of the sheath radius at 0.001 Torr pressures, no net increase in the current collected by the probe was realized.

At a higher pressure of 0.01 Torr and 200 m/s flow velocities, the ion current collected by the probe was reduced by 46% due to the ions downstream of the probe not being able to diffuse upstream into the probe sheath. Reduction in current collected by a probe in a flowing electropositive plasma has been observed previously in several other studies (Smy, 1972) and (Kusumoto and others, 1992). However, in the 0.01 Torr and 200 m/s flow velocity case, the sheath was observed to increase by 33% in length over the non-flowing case due to negative ions reflecting off the angled Langmuir probe pre-sheath at larger distances from the upstream pre-sheath of the probe than in the 0.001 Torr case. The increased distance from the probe at which the negative ions were reflected, in the 0.01 Torr versus 0.001 Torr case, was found to be due to an increase in the sheath edge potential drop caused by the higher collision frequency of the positive ions with the background gas. This result occurs due to  $\lambda_n$  being on the order of the probe sheath dimension. The relatively large value of  $\lambda_n$  allows the negative ions reflected by the pre-sheath to travel beyond the sheath edge without experiencing another collision. Higher collision rates with the flowing background gas, shown by the fluid model results, on average scatter the negative ions into the pre-sheath region and reduce

the spreading out of the space charge in the sheath. The simulation results of this investigation suggest that standard electronegative probe analysis methods for stationary plasmas can be used for determining the ion density of a moderate,  $\alpha \approx 1 - 4$ , electronegative 0.001 Torr case at the sub-thermal flow velocity of 200 m/s. At the higher pressure of 0.01 Torr and flow velocities between 200 m/s and 400 m/s, the analysis method for the diffusion-convection regime developed by Clements and Smy, 1976, was within 5% of the positive ion current determined by the hybrid PIC\_MCC method for the same ion density, mobility, and flow conditions. This suggests that Clement and Smy's convection-diffusion model should provide a reasonable measurement of the positive ion densities from probe CVCs in an electronegative flowing plasma in the transitional collisional regime near 0.01 Torr pressures. However, a broader study of the parameter space of flowing electronegative plasmas at lower pressures needs to be conducted to verify these results. The CVC of a probe in a flowing electronegative plasma can potentially be analyzed and ion densities determined by comparing ion current collection from a hybrid PIC-MCC model with measured current collections, however, due to the long run times and large computational resources associated with these models this approach is impractical with the current model.

At even higher background gas pressures of 1 Torr, the ion current collected by a probe oriented parallel to a flowing plasma is dominated by convection current according to simulation results from this study and the theory developed by Clements and Smy, 1969, and Lam, 1965. In the higher pressure regime of 1 Torr, unlike the lower pressure regimes, the ion current collected by the probe increases with flow velocity consistent with theory. However, in the case of an electronegative flowing plasma it was shown

that the ion convection current collected by a probe is less for a given probe bias than the ion convection current collected in an electropositive plasma. The observed decrease in the ion current collection relative to the electropositive flowing plasma was caused by the compression of the upstream collecting radius resulting from the negative ions being “pushed” into the pre-sheath region and compressing the space charge, hence reducing the length of the upstream collecting radius of the probe. This observed compression of the collecting radius was due to frequent collisions of the flowing background gas with the negative ions which resulted in the negative ions overcoming the repulsion of the pre-sheath electric field. The compression of the collecting radius and hence reduced current collection by the probe in an electronegative flowing plasma was then shown to cause the standard Langmuir probe analysis method in a convection current limited regime to underestimate the positive ion density of the plasma by up to 50% for a given probe bias shown in Figure 5.31. In addition, at 1 Torr pressures it was determined that up to 30% of the current collected by a probe is due to the drift of positive ions into the collecting surface area downstream of the convection current collecting radius. This was found to be due to the long residence time of the positive ions traveling parallel to the downstream collecting surface in the parallel probe orientation used in this study (relative to a probe orientation perpendicular to the flow which is used in several other studies). The long residence time of the positive ions traveling parallel to downstream collecting surface allows the positive ions time to drift into the region of high electric field and be accelerated to the probe surface. To account for this source of current collection, a slight modification to the collecting area theory of Clements and Smy, 1969, was developed to account for the drift of ions into the downstream collecting surface. The correction was

performed by using an angled collecting region downstream of the upstream collecting radius shown in Figure 5.32 to account for the time of flight of the ions parallel to the probe. However this correction requires a computer model to determine the collecting radius and downstream collecting surface for given plasma densities, pressure, and flow conditions.

The improved understanding and modified analysis method developed by this investigation of a Langmuir probe in a flowing electronegative plasma at moderate pressures can be used to develop a diagnostic method using a hybrid PIC-MCC or fluid model to determine the positive ion densities created by an RF discharge in a flowing electronegative background gas (given faster, parallel computers and numerical algorithms). In terms of providing charge from an upstream RF discharge to a second discharge used for producing  $O_2(a)$ , other excited neutral species, or ions for etching applications, an improved diagnostics method enables accurate measurements of the positive ion density of the plasma convected downstream. The enhanced diagnostics provide experimentalists a better measurement of the total number of electrons (due to additional electrons being produced from negative ion detachment of negative ions by neutral excited species produced in the second discharge) that are available for sustaining a second non-self sustaining discharge downstream. This improved diagnostics method should enable optimization of a second discharge for producing large yields of  $O_2(a)$  for ElectriCOIL or atomic nitrogen and oxygen for material processing applications. In addition, accurate diagnostics of the positive ions convected downstream can also be used to optimize a second discharge that independently controls the ion velocity for etching semi-conductor and other substrates. The optimization is done by determining the best

flow velocities and distance to place the second discharge downstream of the first discharge for providing the most charge density to sustain the second discharge. In addition, improved diagnostics help determine the optimal flow velocity, length, electrode separation and applied voltage of the second discharge for producing  $O_2(a)$  or other excited species. The improved diagnostics allow the experimentalist to determine how fast the charge density is being depleted by the creation of neutral excited species and the resulting current losses to the electrodes along the length of the second discharge. Knowing the decay rate of the charge density should allow better adjustment of flow velocities, discharge voltages and length to maximize production of  $O_2(a)$  or other excited neutral species.

## **Recommendations**

A more efficient method of including collisions in a PIC code has been recently developed by Nanbu and others, 2005. It has been shown that the momentum and energy transfer between the background gas and the charged particles accumulated over a period of several time steps can be applied in a single efficient calculation with less dependence of the random scattering and distributions of species in energy and velocity space (Kawamura and Birdsall, 2005). This new method has shown promise in replacing the very inefficient and numerically noisy Monte Carlo Collision methods (Turner, 2006). This approach combined with the hybrid PIC approach should enable efficient, large time step, low numeric noise simulations of a Langmuir probe and RF discharges. Combined with this method, a PIC-MCC chemical kinetic model developed by Capitelli and others, 2000, would allow a more accurate analysis of the chemical kinetics of higher frequency

discharges and lower electron energy chemical kinetics for exploring  $O_2(a)$  production of a non-self sustaining discharge in order to optimize a tandem discharge set-up for maximizing the yield of  $O_2(a)$  and other excited species. This approach also allows faster hybrid PIC-MCC simulations of a Langmuir probe in a higher pressure, flowing electronegative gas and potentially make it a practical means of analyzing Langmuir probe results.



## Appendix A. Two Dimensional Extension of the Fluid Equations

The one dimensional method of solving the fluid equations can easily be extended to two dimensions by calculating the coefficients due to the divergence of the flux by including a derivative in the y direction. The two dimensional energy flux term at the half step,  $i+1/2, j+1/2$ , can be written as

$$\vec{\Phi}_{\varepsilon, i+1/2, j+1/2}^{k, m+1} = \vec{\Phi}_{\varepsilon, i+1/2, j+1/2}^{k, m+1} \left( (n_e \varepsilon)_{i+1, j}, (n_e \varepsilon)_{i, j+1}, (n_e \varepsilon)_{i, j}, V_{i+1, j}, V_{i, j+1}, V_{i, j} \right) \quad (\text{A.1})$$

where the i index corresponds to the x direction and the j index corresponds to the y direction. The Taylor series expansion for the two dimensional energy flux term at the  $i+1/2, j+1/2$  spatial step results in

$$\begin{aligned} \delta \vec{\Phi}_{\varepsilon, i+1/2, j+1/2}^{k, m+1} = & \left( \frac{\partial \vec{\Phi}_{\varepsilon, i+1/2, j+1/2}^{k, m+1}}{\partial (n_e \varepsilon)_{i+1, j}} \right) \delta (n_e \varepsilon)_{i+1, j}^{k, m+1} + \left( \frac{\partial \vec{\Phi}_{\varepsilon, i+1/2, j+1/2}^{k, m+1}}{\partial (n_e \varepsilon)_{i, j}} \right) \delta (n_e \varepsilon)_{i, j}^{k, m+1} + \\ & \left( \frac{\partial \vec{\Phi}_{\varepsilon, i+1/2, j+1/2}^{k, m+1}}{\partial V_{i+1, j}} \right) \delta V_{i+1, j}^{k, m+1} + \left( \frac{\partial \vec{\Phi}_{\varepsilon, i+1/2, j+1/2}^{k, m+1}}{\partial V_{i, j}} \right) \delta V_{i, j}^{k, m+1} + \left( \frac{\partial \vec{\Phi}_{\varepsilon, i+1/2, j+1/2}^{k, m+1}}{\partial (n_e \varepsilon)_{i, j+1}} \right) \delta (n_e \varepsilon)_{i, j+1}^{k, m+1} + \\ & \left( \frac{\partial \vec{\Phi}_{\varepsilon, i+1/2, j+1/2}^{k, m+1}}{\partial V_{i, j+1}} \right) \delta V_{i, j+1}^{k, m+1} \end{aligned} \quad (\text{A.2})$$

Similar Taylor series expansions can be performed on the two dimensional energy equation resulting in the following coefficients to populate the matrices

$$\begin{aligned}
A_{i,j} &= \frac{\Delta t}{2\Delta x} \left( \frac{\partial \vec{\Phi}_{\varepsilon,i+1/2,j}^{k,m+1}}{\partial V_{i+1,j}} \right) \\
B_{i,j} &= \frac{\Delta t}{2\Delta x} \left\{ \left( \frac{\partial \vec{\Phi}_{\varepsilon,i+1/2,j}^{k,m+1}}{\partial V_{i,j}} \right) - \left( \frac{\partial \vec{\Phi}_{\varepsilon,i-1/2,j}^{k,m+1}}{\partial V_{i,j}} \right) \right\} \\
C_{i,j} &= -\frac{\Delta t}{2\Delta x} \left( \frac{\partial \vec{\Phi}_{\varepsilon,i-1/2,j}^{k,m+1}}{\partial V_{i-1,j}} \right) \\
D_{i,j} &= \frac{\Delta t}{2\Delta x} \left( \frac{\partial \vec{\Phi}_{\varepsilon,i+1/2,j}^{k,m+1}}{\partial (n_e \varepsilon)_{i+1,j}} \right) \\
E_{i,j} &= 1 + \frac{\Delta t}{2\Delta x} \left\{ \left( \frac{\partial \vec{\Phi}_{\varepsilon,i+1/2,j}^{k,m+1}}{\partial (n_e \varepsilon)_{i,j}} \right) - \left( \frac{\partial \vec{\Phi}_{\varepsilon,i-1/2,j}^{k,m+1}}{\partial (n_e \varepsilon)_{i,j}} \right) \right\} + \left( \frac{\partial k_L(\varepsilon)_{i,j}^{k,m+1}}{\partial \varepsilon_{i,j}} \right) N_0 \\
F_{i,j} &= -\frac{\Delta t}{2\Delta x} \left( \frac{\partial \vec{\Phi}_{\varepsilon,i-1/2,j}^{k,m+1}}{\partial (n_e \varepsilon)_{i-1,j}} \right) \\
\\ 
G_{i,j} &= \frac{\Delta t}{2\Delta y} \left( \frac{\partial \vec{\Phi}_{\varepsilon,i,j+1/2}^{k,m+1}}{\partial V_{i,j+1}} \right) \\
H_{i,j} &= \frac{\Delta t}{2\Delta y} \left\{ \left( \frac{\partial \vec{\Phi}_{\varepsilon,i,j+1/2}^{k,m+1}}{\partial V_{i,j}} \right) - \left( \frac{\partial \vec{\Phi}_{\varepsilon,i,j-1/2}^{k,m+1}}{\partial V_{i,j}} \right) \right\} \\
I_{i,j} &= -\frac{\Delta t}{2\Delta y} \left( \frac{\partial \vec{\Phi}_{\varepsilon,i,j-1/2}^{k,m+1}}{\partial V_{i,j-1}} \right) \\
\\ 
J_{i,j} &= \frac{\Delta t}{2\Delta y} \left( \frac{\partial \vec{\Phi}_{\varepsilon,i,j+1/2}^{k,m+1}}{\partial (n_e \varepsilon)_{i,j+1}} \right) \\
K_{i,j} &= 1 + \frac{\Delta t}{2\Delta y} \left\{ \left( \frac{\partial \vec{\Phi}_{\varepsilon,i,j+1/2}^{k,m+1}}{\partial (n_e \varepsilon)_{i,j}} \right) - \left( \frac{\partial \vec{\Phi}_{\varepsilon,i,j-1/2}^{k,m+1}}{\partial (n_e \varepsilon)_{i,j}} \right) \right\} \\
L_{i,j} &= -\frac{\Delta t}{2\Delta y} \left( \frac{\partial \vec{\Phi}_{\varepsilon,i,j-1/2}^{k,m+1}}{\partial (n_e \varepsilon)_{i,j-1}} \right)
\end{aligned}$$

The linearized flux or energy equations given by A.2 can then be written for each node point in the computational mesh using equation 2.46.

## Appendix B. Oxygen Reactions and Rate Coefficients

The following table is a detailed description of the major chemical kinetic reactions and their importance in the gains or losses of a particular species of oxygen averaged over a RF cycle. The first column provides a cross reference for the reaction when discussed in the body of the investigation which correlates to the reaction number within the Plasma Fluid Model. Skipped reaction numbers represent inelastic electron reactions that only resulted in an energy loss to the electron and no produced species. The second column is the chemical kinetic formula responsible for the gain or loss of a particular species, which are grouped by losses and gains to a particular species. The third column is the reaction coefficient used in the plasma fluid model.

**Table B.1 Oxygen Chemical Kinetic Reactions in the PFM**

	$O_2(X)$ Species Reactions	Reaction Coefficient	Reference
#	Losses of $O(^1D)$	$\text{cm}^3/\text{s}$ or $\text{cm}^6/\text{s}$	
1	$O_2(X) + O(^1D) \rightarrow O(^3P) + O_2(b)$	$2.56 \times 10^{-11} e^{-67/T_g}$	Eliasson and Kogelschatz, 1986
2	$O_2(X) + O(^1D) \rightarrow O(^3P) + O_2(a)$	$10^{-12} e^{-67/T_g}$	Eliasson and Kogelschatz, 1986
3	$O_2(X) + O(^1D) \rightarrow O(^3P) + O_2(X)$	$7 \times 10^{-12} e^{-67/T_g}$	Eliasson and Kogelschatz, 1986
4	$O(^1D) + O(^3P) \rightarrow 2O(^3P)$	$8 \times 10^{-12}$	Eliasson and Kogelschatz, 1986
5	$O(^1D) + O_3 \rightarrow O(^3P) + O_3$	$2.4 \times 10^{-10}$	Eliasson and Kogelschatz, 1986
6	$O(^1D) + O_3 \rightarrow 2O_2(X)$	$2.4 \times 10^{-10}$	Eliasson and Kogelschatz, 1986
7	$O(^1D) + O_3 \rightarrow O_2(X) + 2O(^3P)$	$1.2 \times 10^{-10}$	Eliasson and Kogelschatz, 1986
8	$O(^1D) + O_3 \rightarrow O_2(X) + O_2(a)$	$1.2 \times 10^{-10}$	Eliasson and Kogelschatz, 1986
	Loss of $O(^3P)$ Detachment		
9	$O^- + O(^3P) \rightarrow O_2(X) + e$	$5.0 \times 10^{-10}$	Kossyi, 1992
	Gain of $O(^3P)$ Recombination		

10	$O_2^+ + O^- \rightarrow O_2 + O$	$1.4 \times 10^{-7}$	Liebermen, 1992
	Loss of $O^-$		
11	$O_2(X) + O^- \rightarrow O_3 + e$	$5 \times 10^{-15}$	Kossyi, 1992
12	$O_2(a) + O^- \rightarrow O_3 + e$	$3.0 \times 10^{-10}$	Eliasson and Kogelschatz, 1986
	Loss of $O_2(a)$		
13	$O_2(a) + O \rightarrow O_2 + O$	$7.0 \times 10^{-16}$	Kossyi, 1992
14	$O_2(a) + O_2(X) \rightarrow 2O_2(X)$	$3.0 \times 10^{-18} e^{-300/T_g}$	Billington and Borrell, 1986
15	$O_2(a) + O_3 \rightarrow 2O_2(X) + O(^3P)$	$5.2 \times 10^{-10} e^{-2840/T_g}$	Eliasson, 1983
16	$O_2(a) + O_2(a) \rightarrow O_2(b) + O_2(X)$	$2.7 \times 10^{-17}$	Perram, 1991
17	$O_2(a) + O_3 \rightarrow 2O_2(X) + O(^3P)$	$2.3 \times 10^{-11}$	TG Slinger, 1979
	Loss of $O_2(b)$		
18	$O_2(b) + O(^3P) \rightarrow O_2(a) + O(^3P)$	$8 \times 10^{-14}$	Kossyi, 1992
19	$O_2(b) + O(^3P) \rightarrow O_2(X) + O(^1D)$	$3.39 \times 10^{-11} \left( \frac{300}{T_g} \right)^{0.1} e^{-4201/T_g}$	Kossyi, 1992
20	$O_2(b) + O_2(X) \rightarrow O_2(a) + O_2(X)$	$4.0 \times 10^{-17}$	Martin, Cohen, Schatz
21	$O_2(b) + O_2(X) \rightarrow 2O_2(X)$	$4.0 \times 10^{-17}$	TG Slinger, 1979
22	$O_2(b) + O_3 \rightarrow O_2(a) + O_3$	$6.0 \times 10^{-12}$	TG Slinger, 1979 (Izod&Wayne)
23	$O_2(b) + O_3 \rightarrow O_2(X) + O_3$	$2.5 \times 10^{-11}$	TG Slinger, 1979 (Gilpin)
24	$O_2(b) + O^- \rightarrow O_2(X) + O(^3P)$	$6.9 \times 10^{-10}$	Aleksandrov, 1978
	Gain of $O_3$		
25	$2O(^3P) + O_2(X) \rightarrow O_3 + O(^3P)$	$2.15 \times 10^{-37} \exp(+345 / T_g)$	Eliasson and Kogelschatz, 1986
26	$O(^3P) + 2O_2(X) \rightarrow O_3 + O_2(X)$	$6.4 \times 10^{-38} \exp(+663 / T_g)$	Eliasson and Kogelschatz, 1986
	Direct Electron Excitation		
27	$e + O_2(X) \rightarrow 2e + O_2^+$	$f(E / N)$	Phelps, 1985
28	$e + O_2(X) \rightarrow O^- + O(^3P)$	$f(E / N)$	Phelps, 1985
35- 36	$e + O_2(X) \leftrightarrow e + O_2(a)$	$f(E / N)$	Phelps, 1985
37-	$e + O_2(X) \leftrightarrow e + O_2(b)$	$f(E / N)$	Phelps, 1985

38			
40	$e + O_2(X) \rightarrow e + 2O(^3P)$	$f(E / N)$	Phelps, 1985
41	$e + O_2(X) \rightarrow e + O(^3P) + O(^1D)$	$f(E / N)$	Phelps, 1985
42	$e + O_2(X) \rightarrow e + O(^3P) + O(^1D)$	$f(E / N)$	Phelps, 1985
43	$e + O_2(a) \rightarrow 2e + O_2^+$	$f(E / N)$	Phelps, 1985, Capitelli, 2000
44	$e + O_2(a) \rightarrow O^- + O(^3P)$	$f(E / N)$	Burrow, 1973
51- 52	$e + O_2(a) \leftrightarrow e + O_2(b)$	$f(E / N)$	Fournier, 1984
54	$e + O_2(a) \rightarrow e + 2O(^3P)$	$f(E / N)$	Phelps, 1985, Capitelli, 2000
55	$e + O_2(a) \rightarrow e + O(^3P) + O(^1D)$	$f(E / N)$	Phelps, 1985, Capitelli, 2000
56	$e + O_2(a) \rightarrow e + O(^3P) + O(^1D)$	$f(E / N)$	Phelps, 1985, Capitelli, 2000
57	$e + O(^3P) \rightarrow 2e + O^+$	$f(E / N)$	Itikawa and Ichimura, 1990
58	$e + O(^3P) \rightarrow O^-$	$f(E / N)$	Itikawa and Ichimura, 1990
59- 60	$e + O(^3P) \leftrightarrow e + O(^1D)$	$f(E / N)$	Itikawa and Ichimura, 1990
66	$e + 2O_2(X) \rightarrow O_2(X) + O_2^-$	$f(E / N)$	Itikawa and Ichimura, 1990

## Appendix C. Nitrogen and Oxygen Reactions and Rate Coefficients

The following tables are a detailed description of the major chemical kinetic reactions and their importance in the gains or losses of a particular species of molecular nitrogen and molecular oxygen. The first column provides a cross reference for the reaction when discussed in the body of the investigation which correlates to the reaction number within the Plasma Fluid Model. Skipped reaction numbers represent inelastic electron reactions that only resulted in an energy loss to the electron and no produced species due to a fast deactivation rate. The second column is the chemical kinetic formula responsible for the gain or loss of a particular species, which are grouped by losses and gains to a particular species. The third column is the reaction coefficient used in the plasma fluid model.

**Table C.1 Nitrogen Chemical Kinetic Reactions in the PFM**

Reaction Number	Pure $N_2(X)$ Species Reactions	Rate Coefficient ( $cm^3 / s$ ) or ( $cm^6 / s$ )	Table C.3
	Electronic State Interactions		
29	$N_2(A) + N(^4S) \rightarrow N_2(X) + N(^4S)$	$2.0 \times 10^{-12}$	1
30	$N_2(A) + N(^4S) \rightarrow N_2(X) + N(^2P)$	$4.0 \times 10^{-11} \left( \frac{T}{300} \right)^{2/3}$	2
34	$N_2(A) + N_2(X) \rightarrow 2N_2(X)$	$3.0 \times 10^{-16}$	3
37	$2N_2(A) \rightarrow N_2(X) + N_2(B)$	$3.0 \times 10^{-10}$	4
38	$2N_2(A) \rightarrow N_2(X) + N_2(C)$	$1.5 \times 10^{-10}$	5
47	$N_2(C) + N_2(X) \rightarrow N_2(a') + N_2(X)$	$1.0 \times 10^{-11}$	6
49	$N_2(a') + N_2(X) \rightarrow N_2(B) + N_2(X)$	$1.9 \times 10^{-13}$	7
52	$N_2(a') + N_2(A) \rightarrow e + N_2^+ + N_2(X)$	$1.5 \times 10^{-11}$	8
53	$2N_2(a') \rightarrow e + N_2^+ + N_2(X)$	$1.0 \times 10^{-11}$	8
54	$N_2(a'') + N_2(X) \rightarrow 2N_2(X)$	$1.0 \times 10^{-14}$	9
	Direct Electron Excitation of $N_2(X)$		
240	$e + N_2(X) \rightarrow 2e + N_2^+(X)$	$f(E / N)$	10

242-263	$e + N_2(X) \leftrightarrow e + N_2(v=1-15)$	$f(E/N)$	10
290-386	$e + N_2(v) \leftrightarrow e + N_2(v')$	$f(E/N)$	10
265-266	$e + N_2(X) \leftrightarrow e + N_2(A)$	$f(E/N)$	10
269-271	$e + N_2(X) \leftrightarrow e + N_2(B)$	$f(E/N)$	10
274	$e + N_2(X) \leftrightarrow e + N_2(B)$	$f(E/N)$	10
275-276	$e + N_2(X) \leftrightarrow e + N_2(a')$	$f(E/N)$	10
277-278	$e + N_2(X) \leftrightarrow e + N_2(a)$	$f(E/N)$	10
279	$e + N_2(X) \rightarrow e + N_2(a')$	$f(E/N)$	10
280-281	$e + N_2(X) \leftrightarrow e + N_2(C)$	$f(E/N)$	10
283-284	$e + N_2(X) \leftrightarrow e + N_2(a'')$	$f(E/N)$	10
286-289	$e + N_2(X) \rightarrow e + 2N(^4S)$	$f(E/N)$	10
290-386	$e + N_2(X, v) \leftrightarrow e + N_2(X, v')$	$f(E/N)$	8
387-410	$e + N_2(v=1-6) \rightarrow e + 2N(^4S)$	$f(E/N)$	48
415	$e + 2O_2(X) \leftrightarrow O_2^- + O_2(X)$	$f(E/N)$	11
416	$e + O_2(X) + N_2(X) \leftrightarrow O_2^- + N_2(X)$	$f(E/N)$	11
	Vibrational Chemical Kinetics		
39-41	$N_2(A) + N_2(6-8) \rightarrow N_2(B) + N_2(0-2)$	$1.0 \times 10^{-10}$	12
42-44	$N_2(B) + N_2(0-2) \rightarrow N_2(A) + N_2(6-8)$	$1.0 \times 10^{-10}$	8
131-132	$N_2(A) + N_2(14-15) \rightarrow N_2(X) + 2N(^4S)$	$4.6 \times 10^{-12}$	8
135-199	$N(^4S) + N_2(v) \rightarrow N(^4S) + N_2(v')$	equation 3.9	14
417-641	$N_2(v) + N_2(v') \rightarrow N_2(v-1) + N_2(v'+1)$	equation 3.4	13
702-716	$N_2(v) + N_2(X) \rightarrow N_2(v-1) + N_2(X)$	equation 3.9	14
131-132	$N_2(A) + N_2(14-15) \rightarrow N_2(X) + 2N(^4S)$	$4.6 \times 10^{-12}$	8

**Table C.2 Nitrogen, Oxygen, and Nitrous Oxide Chemical Kinetic Reactions in the PFM**

#	Reaction	Rate Coefficient	Table C.3
	Electronic State Interactions		
27	$N_2(A) + O(^3P) \rightarrow NO(X) + N(^2D)$	$7.0 \times 10^{-12}$	15
28	$N_2(A) + O(^3P) \rightarrow N_2(X) + O(^1S)$	$2.1 \times 10^{-11}$	15
31	$N_2(A) + O_2(X) \rightarrow N_2(X) + O_2(a)$	$2.0 \times 10^{-13}$	16
32	$N_2(A) + O_2(X) \rightarrow N_2(X) + O_2(b)$	$2.0 \times 10^{-13}$	6
33	$N_2(A) + O_2(X) \rightarrow N_2O(X) + O(^3P)$	$2.0 \times 10^{-14}$	16
35	$N_2(A) + NO(X) \rightarrow NO(X) + N_2(X)$	$6.9 \times 10^{-11}$	17
36	$N_2(A) + N_2O(X) \rightarrow NO(X) + N_2(X) + N(^4S)$	$1.0 \times 10^{-11}$	18
48	$N_2(C) + O_2(X) \rightarrow N_2(X) + 2O(^3P)$	$3.0 \times 10^{-10}$	19
50	$N_2(a') + O_2(X) \rightarrow N_2(X) + 2O(^3P)$	$2.8 \times 10^{-11}$	12, 19
51	$N_2(a') + NO(X) \rightarrow N_2(X) + N(^4S) + O(^3P)$	$3.6 \times 10^{-11}$	12, 19
55	$2N(^4S) + N_2(X) \rightarrow N_2(A) + N_2(X)$	$1.7 \times 10^{-39}$	20-23
56	$2N(^4S) + O_2(X) \rightarrow N_2(A) + O_2(X)$	$1.7 \times 10^{-39}$	20-23
57	$2N(^4S) + NO(X) \rightarrow N_2(A) + NO(X)$	$1.7 \times 10^{-39}$	20-23
58	$2N(^4S) + O(^3P) \rightarrow N_2(A) + O(^3P)$	$1.0 \times 10^{-38}$	20-23
59	$3N(^4S) \rightarrow N_2(A) + N(^4S)$	$1.0 \times 10^{-38}$	20-23
60	$2N(^4S) + N_2(X) \rightarrow N_2(B) + N_2(X)$	$2.4 \times 10^{-39}$	20-23
61	$2N(^4S) + O_2(X) \rightarrow N_2(B) + O_2(X)$	$2.4 \times 10^{-39}$	20-23
62	$2N(^4S) + NO(X) \rightarrow N_2(B) + NO(X)$	$2.4 \times 10^{-39}$	20-23
63	$2N(^4S) + O(^3P) \rightarrow N_2(B) + O(^3P)$	$1.4 \times 10^{-38}$	20-23
64	$3N(^4S) \rightarrow N_2(B) + N(^4S)$	$1.4 \times 10^{-38}$	20-23
65	$O_2(a) + N(^4S) \rightarrow NO(X) + O(^3P)$	$2.0 \times 10^{-14}$	19
66	$O_2(a) + N_2(X) \rightarrow O_2(X) + N_2(X)$	$3.0 \times 10^{-21}$	19
67	$O_2(a) + NO(X) \rightarrow O_2(X) + NO(X)$	$2.5 \times 10^{-11}$	49
68	$O_2(b) + N_2(X) \rightarrow O_2(a) + N_2(X)$	$1.7 \times 10^{-16}$	50
69	$O_2(b) + NO(X) \rightarrow O_2(a) + NO(X)$	$6.0 \times 10^{-14}$	51, 52
70	$2O(^3P) + O_2(X) \rightarrow O_2(X) + O_2(X)$	$1.0 \times 10^{-38}$	23, 24
71	$2O(^3P) + O_2(X) \rightarrow O_2(a) + O_2(X)$	$7.0 \times 10^{-40}$	23, 24
72	$2O(^3P) + N_2(X) \rightarrow O_2(X) + N_2(X)$	$2.5 \times 10^{-40}$	23, 24
73	$2O(^3P) + N_2(X) \rightarrow O_2(a) + N_2(X)$	$7.0 \times 10^{-40}$	23, 24
74	$3O(^3P) \rightarrow O_2(X) + O(^3P)$	$3.6 \times 10^{-42}$	23, 24



75	$3O(^3P) \rightarrow O_2(a) + O(^3P)$	$7.0 \times 10^{-40}$	23, 24
76	$2O_2(a) + O_2(X) \rightarrow 2O_3$	$1.0 \times 10^{-37}$	53
77	$N(^2D) + O(^3P) \rightarrow N(^4S) + O(^1D)$	$4.0 \times 10^{-13}$	16, 26
78	$N(^2D) + O_2(X) \rightarrow NO(X) + O(^3P)$	$5.2 \times 10^{-12}$	27
79	$N(^2D) + N_2(X) \rightarrow N_2(X) + N(^4S)$	$6.0 \times 10^{-15}$	18, 19
80	$N(^2D) + NO(X) \rightarrow N_2(X) + O(^3P)$	$1.8 \times 10^{-10}$	18, 28
81	$N(^2D) + N_2O(X) \rightarrow N_2(X) + NO(X)$	$3.5 \times 10^{-12}$	18, 29
82	$N(^2P) + N(^4S) \rightarrow 2N(^4S)$	$1.8 \times 10^{-12}$	12
83	$N(^2P) + O(^3P) \rightarrow N(^4S) + O(^1D)$		8
84	$N(^2P) + O_2(X) \rightarrow NO(X) + O(^3P)$	$1.0 \times 10^{-12}$	30
85	$N(^2P) + N_2(X) \rightarrow N_2(X) + N(^4S)$	$2.6 \times 10^{-15}$	31
86	$N(^2P) + NO(X) \rightarrow N_2(X) + O(^3P)$	$3.0 \times 10^{-11}$	32
87	$O(^1S) + O(^3P) \rightarrow O(^1D) + O(^1D)$	$5.0 \times 10^{-11}$	62, 31
88	$O(^1S) + N(^4S) \rightarrow O(^3P) + N(^4S)$	$1.0 \times 10^{-12}$	32
89	$O(^1S) + O_2(X) \rightarrow O_2(X) + O(^3P)$	$4.0 \times 10^{-12}$	33
90	$O(^1S) + N_2(X) \rightarrow N_2(X) + O(^3P)$	$1.0 \times 10^{-17}$	34
91	$O(^1S) + O_2(a) \rightarrow 3O(^3P)$	$3.2 \times 10^{-11}$	35, 36
92	$O(^1S) + O_2(a) \rightarrow 2O(^3P) + O(^1D)$	$1.1 \times 10^{-10}$	35, 36
93	$O(^1S) + O_2(a) \rightarrow O(^1D) + O_2(b)$	$2.9 \times 10^{-11}$	35, 36
94	$O(^1S) + NO(X) \rightarrow NO(X) + O(^3P)$	$8.0 \times 10^{-10}$	37, 38
95	$O(^1S) + O_3 \rightarrow 2O_2(X)$	$6.0 \times 10^{-10}$	37
96	$N(^4S) + NO(X) \rightarrow N_2(X) + O(^3P)$	$1.8 \times 10^{-11}$	39
97	$N(^4S) + O_2(X) \rightarrow NO(X) + O(^3P)$	$3.2 \times 10^{-13}$	40
98	$N(^4S) + O_3 \rightarrow NO(X) + O_2(X)$	$2.0 \times 10^{-16}$	41
99	$2N(^4S) + N_2(X) \rightarrow N_2(X) + N_2(X)$	$8.3 \times 10^{-34}$	19, 23, 40
100	$2N(^4S) + O_2(X) \rightarrow N_2(X) + O_2(X)$	$1.9 \times 10^{-33}$	19, 23, 40
101	$3N(^4S) \rightarrow N_2(X) + N(^4S)$	$8.3 \times 10^{-34}$	19, 23, 40
102	$2N(^4S) + O(^3P) \rightarrow N_2(X) + O(^3P)$	$4.98 \times 10^{-34}$	19, 23, 40
103	$2N(^4S) + NO(X) \rightarrow N_2(X) + NO(X)$	$8.3 \times 10^{-34}$	19, 23, 40
104	$2N(^4S) + N_2(X) \rightarrow N_2(X) + N_2(X)$	$2.7 \times 10^{-34}$	19, 23, 40
105	$2O(^3P) + N(^4S) \rightarrow O_2(X) + N(^4S)$	$6.2 \times 10^{-32}$	23, 42

106	$3O(^3P) \rightarrow O_2(X) + O(^3P)$	$2.5 \times 10^{-31}$	23, 42
107	$2O(^3P) + NO(X) \rightarrow O_2(X) + NO(X)$	$6.8 \times 10^{-33}$	23, 42
108	$O(^3P) + N(^4S) + N_2(X) \rightarrow NO(X) + N_2(X)$	$1.03 \times 10^{-32}$	19, 23, 40
109	$O(^3P) + 2N(^4S) \rightarrow NO(X) + N(^4S)$	$1.03 \times 10^{-32}$	19, 23, 40
110	$O(^3P) + N(^4S) + O_2(X) \rightarrow NO(X) + O_2(X)$	$1.03 \times 10^{-32}$	19, 23, 40
111	$2O(^3P) + N(^4S) \rightarrow NO(X) + O(^3P)$	$1.03 \times 10^{-32}$	19, 23, 40
112	$O(^3P) + N(^4S) + NO(X) \rightarrow 2NO(X)$	$1.03 \times 10^{-32}$	19, 23, 40
113	$O^- + N(^4S) + NO(X) \rightarrow e + NO(X)$	$2.6 \times 10^{-10}$	43
114	$O^- + N_2(A) \rightarrow e + O(^3P) + N_2(X)$	$2.2 \times 10^{-9}$	44
115	$O^- + N_2(B) \rightarrow e + O(^3P) + N_2(X)$	$1.9 \times 10^{-9}$	45
116 - 119	$N(^4S) + NO(X) \rightarrow O(^3P) + N_2(X, v = 2 - 5)$	$4.5 \times 10^{-12}$	46, 47 branch ing ratios
120 - 123	$N_2(X) + O(^1D) \rightarrow O(^3P) + N_2(X, v = 1 - 4)$	$7.5 \times 10^{-12}$	46, 47 branch ing ratios
124 - 126	$O^- + N_2(X, v = 6 - 8) \rightarrow e + O(^3P) + N_2(X)$	$2.7 \times 10^{-10}$	44 branch ing ratios
	$O_2(X)$ , $NO(X)$ and $N_2(X)$ V-V and V-T		
127 - 130	$O(^3P) + N_2(X, v = 12 - 15) \rightarrow NO(X) + N(^4S)$	$6.9 \times 10^{-12}$	53
133	$O(^3P) + O_2(X, v = 1) \rightarrow O(^3P) + O_2(X)$	$4.5 \times 10^{-15}$	46, 47
134	$O(^3P) + NO(X, v = 1) \rightarrow O(^3P) + NO(X, v = 1)$	$6.5 \times 10^{-11}$	46, 47
642 - 671	$O_2(X) + N_2(X, v) \leftrightarrow O_2(X, v = 1) + N_2(X, v - 1)$	$1.7 \times 10^{-13}$	46, 47
672 - 701	$NO(X) + N_2(X, v) \leftrightarrow NO(X, v = 1) + N_2(X, v - 1)$	$1.3 \times 10^{-14}$	46, 47
717 - 731	$O_2(X) + N_2(X, v) \rightarrow O_2(X) + N_2(X, v - 1)$	$3.15 \times 10^{-6}$	46, 47

732 - 746	$NO(X) + N_2(X, v) \rightarrow NO(X) + N_2(X, v - 1)$	$2.96 \times 10^{-6}$	46, 47
747 - 763	$O(^3P) + N_2(X, v) \rightarrow NO(X) + N_2(X, v - 1)$	$1.2 \times 10^{-13}$	46, 47

**Table C.3 References for Tables C.1 and C.2**

Reference Number	Reference
1	Gillmore and others, 1969
2	Flagan and others, 1972
3	Clark and Setser, 1980
4	Hays and Oskam, 1973
5	JPCRD, 1988
6	Calear and Wood, 1971
7	Dreyer and others, 1974
8	Gordiets and others, 1995
9	Golubovsky and Telezhko, 1984
10	Phelps and Pitchford, 1985
11	Hunter and Christophoruo, 1984
12	Slovetski, 1980
13	Keck and Carrier, 1965
14	Gordiets and others, 1986
15	Piper, 1982
16	Iannuzzi and others, 1982
17	Zhao and Setser, 1988
18	Black and others, 1959
19	Kossyi and Kostinsky, 1992
20	Delcroix and others, 1976
21	Becker et al, 1972
22	Partridge and others, 1988
23	Krivososova and others, 1987
24	Baulch, 1976
25	Fredrick and others, 1977
26	Davenport and others, 1976
27	Husain and others, 1974
28	Donovan and Husain, 1970
29	Black and others, 1975
30	Husain, 1977
31	Slanger and Black, 1976
32	Felder and Young, 1972

33	Slanger and others, 1972
34	Levine, 1985
35	Slanger and Black, 1981
36	Kenner and Ogryzlo, 1982
37	London, and others, 1971
38	Filseth and others, 1972
39	Benson and others, 1975
40	Baulch and others, 1973
41	Stief and others, 1979
42	Baulch and others, 1976
43	McDaniel and others, 1970
44	Aleksandrov, 1978
45	Sabadil and others, 1980
46	Gordiets and Ricard, 1993
47	Nahorny and others, 1994
48	Phelps, 1991
49	Yaron and others, 1991
50	Choo and Leu, 1985
51	O'Brien and Myers, 1970
52	Becker and others, 1971
53	Capitelli and others, 2000

**Table C.4 Wall Loss Probabilities in a Nitrogen – Oxygen Mix**

Excited Species	$\gamma$
$N_2(X, v) \rightarrow N_2(X, v - 1)$	$7 \times 10^{-3}$
$N_2(A) \rightarrow N_2(X)$	1
$N_2(a') \rightarrow N_2(B)$	1
$O_2(a) \rightarrow O_2(X)$	$2 \times 10^{-5}$
$O_2(b) \rightarrow O_2(X)$	$2 \times 10^{-2}$
$N(^2D) \rightarrow N(^4S)$	1
$N(^2P) \rightarrow N(^4S)$	1
$O(^1D) \rightarrow N(^3P)$	1
$O(^1S) \rightarrow N(^3P)$	1

## Appendix D. Neutral Species Densities in a Nitrogen-Oxygen Mixture

The current densities and excited neutral species density profiles for  $N_2(X)$  -  $O_2(X)$  mixtures are shown in Figures D.1 and D.2 in stationary and 250 m/s flow conditions. Similar to the current densities for  $O_2(X)$ , 0 flow velocity conditions For both conditions the excited neutral species densities reduce towards the electrodes due to quenching by the walls. Local minimums in the density profiles occur towards the center of the density profiles due to electronic state interactions with other excited neutral species. The local minimum in the 250 m/s flow case also occur due to the neutral particle production location occurring nearer the sheath edge because of the higher electric fields. As the species diffuse towards the center of the discharge it is removed by the flow resulting in a lower density towards the center of the discharge.

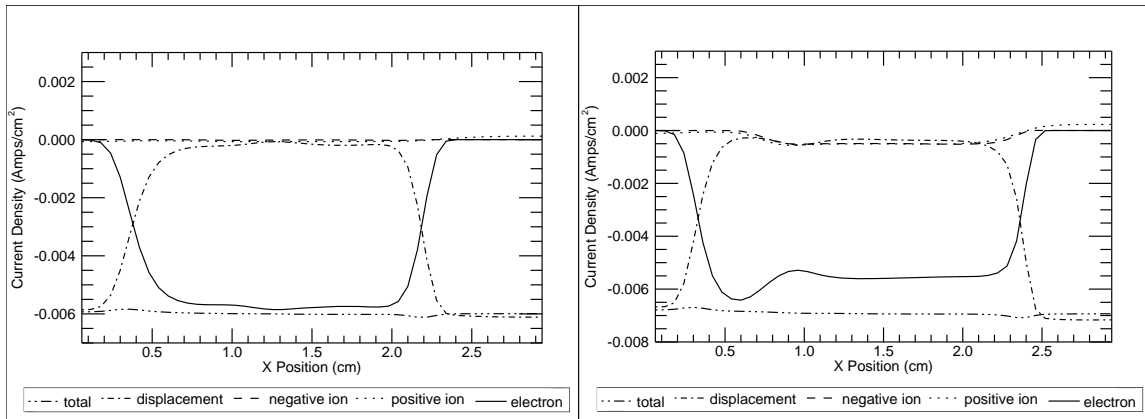


**Figure D.1 Time Dependent Current Densities in a  $N_2(X)$ - $O_2(X)$  RF Discharge at 1000V in (a) Stationary (b) 250 m/s Flow Conditions**

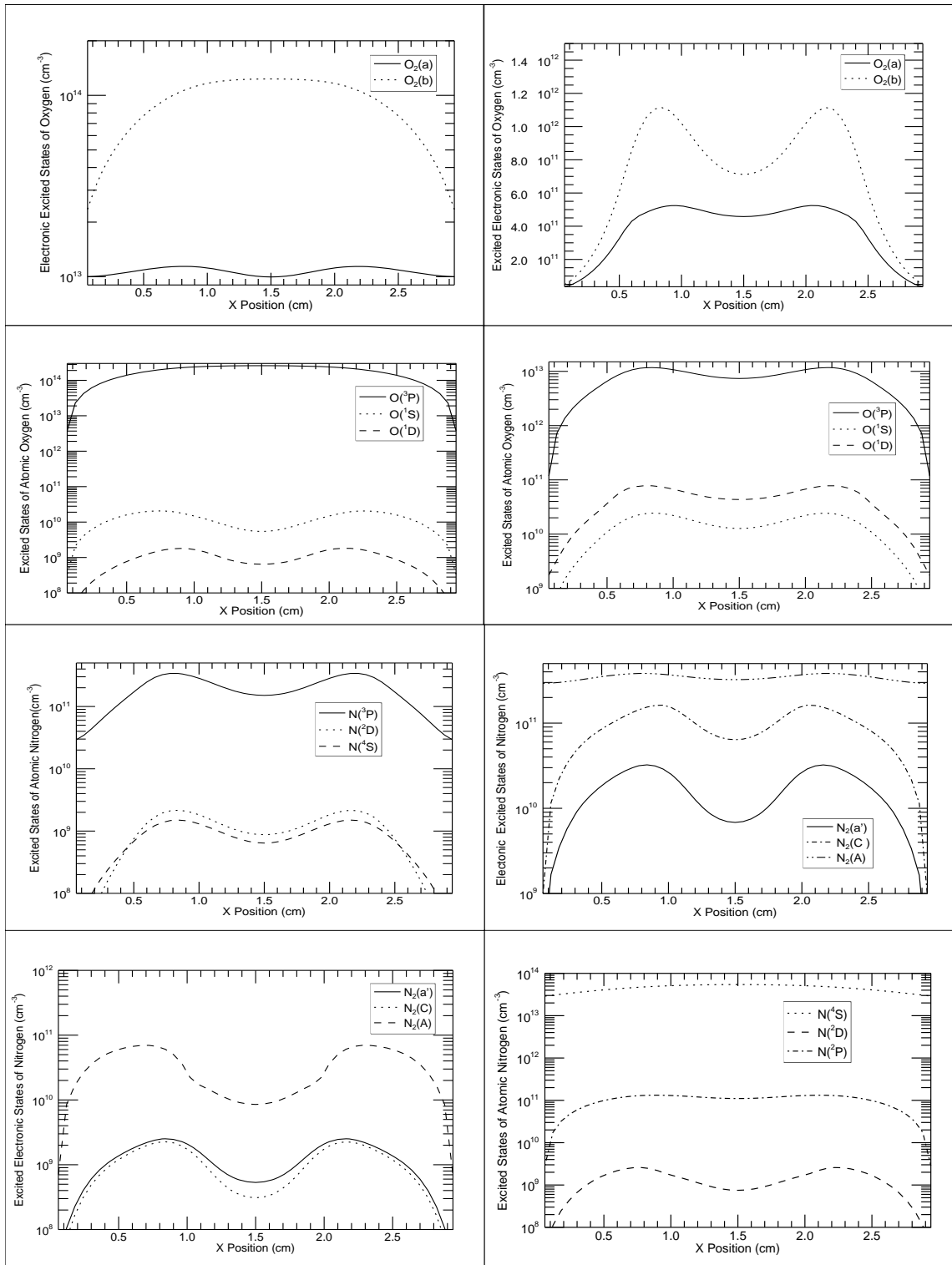


**Figure D.2 Density Profiles of Excited Neutral Species Produced in a  $N_2(X)-O_2(X)$  RF Discharge 1000V at 0 and 250 m/s Flow Velocities**

## Bibliography

- Akishev, Yu. S., A.V Demianov, and I. V Kochetov, Teplofis. Vis. Temp., 20: 818-827 (1982).
- Aleksandrov, N. L. and A.M Konchakov, "The Effects of Vibrational Excitation on the Rate of Attachment of Electrons to O<sub>2</sub> Molecules in a Gas Discharge," Moscow Technical Physics Institute, 22 (2): 254-257 (1984)
- Aleksandrov, N. L., "Electron Detachment from O<sup>-</sup> and O<sub>2</sub><sup>-</sup> ions in Excited Molecules in an Air Discharge," Sov. Phys. Tech. Tech Phys, 23 (7): 806-808 (1978).
- Allen, J.E., R.L.F. Boyd, and P. Reynolds, Proc. Phys. Soc. (London) B70: 297 (1957).
- Allen, J.E., "The plasma boundary in electronegative gases," 31<sup>st</sup> EPS Conference on Plasma Phys. London, Vol. 28G (2004).
- Amemiya, H., K. Ogawa, T. Suzuki, and M. Endou, "Optogalvanic study of a negative ion plasma in a hollow cathode discharge in oxygen," J. Phys. Appl. Phys., 26: 2174-2183 (1993).
- Amemiya, H., B. M. Annaratone, and J. E. Allen, "The collection of positive ions by spherical and cylindrical probes in an electronegative plasma," Plasma Sources Sc. Tech., 8: 179-190 (1999).
- Andrews J. G., and Swift-Hook D. T., "Spherical probe in a flowing plasma," J. Phys. A: Gen. Phys., 4: 142-158 (1971).
- Baulch, D. L., D.D Drysdale, J. Duxbary, and S. L. Grant, Eds., Homogeneous Gas Phase Reactions of the O-O Systems, CO, O, H Systems and Sulphur-Containing Species, no. 3. London: Butterworths, 1976.
- Baulch, D. L., D. D. Drysdale, and D. C. Horne, Eds., Homogeneous Gas Phase Reactions of the H<sub>2</sub>, N<sub>2</sub>, O<sub>2</sub> systems, no. 2. London: Butterworths, 1973.
- Becker, K. H., W. Groth, and U. Schurath, "The quenching of metastable O<sub>2</sub>(a<sup>1</sup>Δ<sub>g</sub>) and O<sub>2</sub>(b<sup>1</sup>Σ<sub>g</sub><sup>+</sup>) molecules," Chem. Pys. Lett, 8: 259-262 (1971).
- Bennet, E. J., "Time dependent Boltzmann Equation in the Two-term Approximation Solver", Wright-Patterson AFB, OH, 1997.
- Benson, S. W., D. M. Golden, R. W. Woolfolk, and R. W. Lawrence, "Estimation of rate constant as a function of temperature for reactions X+YZ ↔ XY + Z, X + Y + M



- XY + M and X + YZ + M  $\leftrightarrow$  XYZ + M, where X, Y, and Z are atoms, Hydrogen, Nitrogen, Oxygen,” Int. J. Chem. Kinet. Symp.1: 399-440 (1975).
- Billington, A. P. and P. Borell, “The low temperature quenching of singlet molecular oxygen  $O_2(a^1\Delta_g)$ ,” J. Chem. Soc. Faraday Trans., 82: 963-970 (1986).
- Birdsall, C. K. and B. A. Langdon, Plasma Physics via Computer Simulation. New York: McGraw-Hill Book Company, 1985.
- Black, G., T. C. Slanger, G. A. St. John, and B. A. Young, “Vacuum Ultraviolet Photolysis of N<sub>2</sub>O, Deactivation of N(2D),” J. Chem. Phys., 51(1): 116, (1969)
- Boeuf, J.-P., “Numerical model of rf glow discharges,” Phys. Rev. A., 35 (6): 2782-2892, (1987).
- Boeuf, J.-P., Ph Belenguer, and T. Hbid, “Plasma species interactions,” Plasma Sources Sci. Technol., 3: 407-417, (1994).
- Boeuf, J.-P., and Pitchford, L. C. “Two-dimensional model of a capacitively coupled rf discharge and comparisons with experiments in the Gaseous Electronics Conference reference reactor,” Phys. Rev. E, 51 (2): 1376-1391 (1995).
- Bohm, D. Characteristics of Electrical Discharges in Magnetic Fields. New York: McGraw-Hill, 1949.
- BOLSIG, “Boltzmann solver for the SIGLO-series 1.0,” CPA Toulouse & Kinema Software (1996).
- Braginsky, O. V., A. S. Kovalev, D. V. Lopaev, “Discharge singlet oxygen generator for oxygen-iodine laser: I. Experiments with rf discharges at 13.56 and 81 MHz” J. Phys. D: Appl. Phys., 39: 5183-5190.
- Burrow, P. D., “Dissociative Attachment from the  $O_2(a^1\Delta_g)$  State,” J. Chem. Phys., 59 (9): 4922-4931 (1973).
- Cacciatore, M. and G. D. Billing, ”State-to-State Vibration-Translation and Vibration-Vibration Rate Constants in H<sub>2</sub>-H<sub>2</sub> and HD-HD Collisions,” J. Phys. Chem., 96: 109 (1992).
- Cacciatore, M., Capitelli M., and Gorse C. ”Non-equilibrium dissociation and ionization of nitrogen in electrical discharges,” Chem. Phys., 60: 141 (1982).
- Cacciatore, M., "Vibrational Energy Exchanges Between Diatomic Molecules of Relevance to Atmospheric Chemistry" in Molecular Physics and Hypersonic Flows, Ed. M. Capitelli, NATO ASI Series, vol. 482 series C, Kluwer Academic Publishers, 1996.

- Calear, A. B. and P. M. Wood, "Rates of Energy Transfer from  $N_2(A^3\Sigma_u^+)$  to Various Molecules," Trans. Faraday Soc., **87** (6): 272-288 (1971).
- Cao De Zhao and D. W. Setser, "Energy transfer reaction of  $N_2(A^3\Sigma_u^+)$  to  $SO$  and other diatomic and polyatomic molecules," J. Phys. Chem., **92** (5): 1169-1178 (1988).
- Capitelli M., Ferreira C. M., B. F. Gordiets, and A. I. Osipov, Plasma Kinetics in Atmospheric Gases. New York: Springer-Verlag, 2000.
- Carroll, D.L., Verdeyen, J.T., Zimmerman, J., Skorski, L., and Solomon, W.C., "Recent Electrodynamics Modeling of the ElectriCOIL System," AIAA Paper 2003-4030: (2003a).
- Carroll, D.L., Verdeyen, J.T., King, D.M., Woodard, B., Skorski, L., Zimmerman, J., and Solomon, W.C., "Modeling of the ElectriCOIL System," IEEE J. of Quantum Electronics, **39** (9): 1150-1159 (2003b).
- Cartwright, K. L., J. P. Verboncoeur, and C. K. Birdsall, "Nonlinear hybrid Boltzmann-particle-in-cell algorithm." Phys. of Plasmas, **7** (8): 3253-3264 (2000).
- Cenian A., A. Chernukho, A. Bogaerts, R. Gijbels, C. Leys, "Species-in-cell Monte Carlo modeling of Langmuir probes in an Ar plasma," J. Appl. Phys. **97**: 123310-123320 (2005).
- Chen, F. F. Plasma Diagnostic Techniques. New York: Academic Press. Chapt. 4, pp. 113-200, 1965.
- Choo, K. Y. and M. T. Leu, "Rate constants of the quenching of metastable  $O_2(^1\Sigma_g^+)$  molecules," Int. J. Chem. Kinet., **17**: 1155-1167 (1985).
- Chung, P. M., L. Talbot, and K. J. Touryan, Electric Probes in Stationary and Flowing Plasmas: Theory and Application. New York: Springer-Verlag, 1975.
- Clark, W. G. and D. W. Setser, "Energy transfer reaction of  $N_2(A^3\Sigma_u^+)$  quenching by hydrogen halides, methyl halides, and other molecules," J. Phys. Chem., **84**: 2225 (1980).
- Clements, R. M. and P. R. Smy, "Electrostatic-probe studies in a flame plasma," J. of Appl. Phys., **40** (11): 4553-4567 (1969).
- Clements, R. M. and P. R. Smy, "Ion current from a collision-dominated flowing plasma to a cylindrical electrode surrounded by a thin sheath," J. of Appl. Phys., **41** (9): 3745-3758 (1970).

- Clements, R. M. and P. R. Smy, "Transition from diffusion-convection to sheath-convection of a cold lanmuir probe in a moving compressible plasma," J. of Phys., **14**: 1001-1008 (1981).
- Collart, E. J. H., J.A. G. Baggerman and R. J. Visser, "On the role of atomic oxygen in the etching of organic polymers in a radio-frequency oxygen discharge," J. Appl. Phys. **78** (1): 47-54 (1995).
- Davenport, J. E., T. G. Slanger, and G. Black, "The Quenching of  $N(^2D)$  by  $O(^3P)$ ," J. Geophys. Res., **81**: 12-16 (1976).
- Delcroix, J. L., C. M. Ferreira, and A. Ricard, in Principles of Laser Plasmas, G. Bekefi, Ed. New York: Wiley, 1976, Ch. 5.
- Donkó, Z., P. Hartmann, and K. Kutasi, "On the reliability of low pressure dc discharge modeling," Plasma Sources Sci. Technol., **15**: 178-186 (2006)
- Donovan, R. J., and D. Husain, "Recent Advances in the Chemistry of Electronically Excited Atoms," Chem. Rev., **70**: 489-516 (1970).
- Dreyer, J. W., D. Perner, and C. R. Roy, "Rate Constants for the Quenching of  $N_2(A^3\Sigma_u^+, v = 0 - 8)$  by  $CO$ ,  $CO_2$ ,  $NH_3$ ,  $NO$  and  $O_2$ ," J. Chem. Phys., **61**: 3164 (1974).
- Elaissi, S., M. Yousfi, H. Helali, S. Kaxxix, K. Charrad and M. Sassi, "Radio-frequency electronegative gas discharge behaviour in a parallel-plate reactor for material processing," Plasma Devices and Operations, **14** (1): 27-45 (2006).
- Eliasson, B., "Electrical Discharge in Oxygen. Part 1: Basic Data and Rate Coefficients," Tech. Rep. KLR 83-40C. Brown Boveri, 1993.
- Felder, W. and R. A. Young, "Quenching of  $O(^1S)$  by  $O(^3P)^*$ ," J. Chem. Phys., **56**: 6028 (1972).
- Ferreira, C. M., G. Gousset, and M. Touzeau, "Quasi-Neutral Theory of Positive Columns in Electronegative Gases," J. Phys. D: Appl. Phys., **21**: 1403-1413 (1988).
- Fiala, A., L. C. Pitchford, and J. P. Boeuf, "Two dimensional, hybrid model of low-pressure glow discharge," Physical Review E, **49**(6) : 5607-5622 (1994).
- Filseth, S. V., F. Stuhl, and K. H. Welge, "Collisional deactivation of  $O(^1S)$ ," J. Chem. Phys., **57**: 4046 (1972).

- Flagan, R.C., and J. P. Appleton, "Excitation mechanisms of the Nitrogen first positive and first negative radiation at high temperature," J. Chem. Phys., 56: 1163 (1972).
- Fournier, G., Cinetique de L'Oxygen en Milieu Plasma. Editions de Physique, Paris France: 1984.
- Franklin, R. N., and J. Snell, "Modeling discharges in electronegative gases," J. Phys. D: Appl. Phys., 32 : 2190-2196 (1999).
- Franklin, R. N., "The plasma-wall boundary region in negative-ion-dominated plasmas at low pressures," Plasma Sources Sc. Techol., 9 : 191-198 (2000a).
- Franklin, R. N. and J. Snell, "Are the oscillations found in electronegative plasmas at low pressure an artifact?," J. Phys D: Appl. Phys., 33 (16): 1990-1995 (2000b).
- Franklin, R. N., "COMMENT: Is oxygen a detachment-dominated gas or not?," J. of Phys D: Appl. Phys., 33 (22): 1 (2000c).
- Franklin, R. N., "The role of  $O_2(a^1\Delta_g)$  metastables and associative detachment in discharges in oxygen," J. Phys D: Appl. Phys., 34 (12): 1834-1839 (2001a).
- Franklin, R. N., "A critique of models of electronegative plasmas," Plasma Sources Sci. Technol. 10 : 162-184 (2001b).
- Franklin, R. N. and J. Snell, "The plasma-sheath transition with a constant mean free path model and the applicability of the Bohm criterion," Phys. Plasmas, 8 (2): 643-647 (2001c).
- Franklin, R. N., "What significance does the Bohm criterion have in an active collisional plasma-sheath?," J. of Phys D: Appl. Phys., 35 (18): 2270-2273 (2002).
- Franklin, R. N., "There is no such thing as a collisionally modified Bohm criterion," J. of Phys D: Appl. Phys., 36 (22): 2821-2824 (2003).
- Franklin, R. N., "Where is the 'sheath edge'?", J. of Phys D: Appl. Phys., 37(9): 1342-1345 (2004).
- Frederick, J. E. and D. W. Rusch, "On the Chemistry of Metastable Atomic Nitrogen in the F Region Deduced from Simultaneous Satellite Measurements of the 5200 Angstrom Airglow and Atmospheric Composition," J. Geophys. Res., 82: 3509-3517 (1977).
- Fujii, H. "COIL in Japan," AIAA Paper 94-2419 Colorado Springs, CO, 1994

- Gilmore, F. R., E. Bauer, and J. W. Mc.Gowan, "A Review of Atomic and Molecular Excitation Mechanisms in Non-equilibrium Gases Up To 20000K," J. Quant. Spectros. Radiant. Transfer **9**: 157 (1969).
- Golubovsky, Yu. B., and V. M. Telezhko, Teplofis. Vis. Temp. **22** (1): 15 (1977).
- Gordiets, B. F., A. I. Osipov, and L. A. Shelepin., Kinetic Process in Gases and Molecular Lasers. Russia : 1986.
- Gordiets, B. F. and A. Ricard, "Production of *N*, *O* and *NO* in N<sub>2</sub>-O<sub>2</sub> flowing discharges," AIAA Journal, **36** (9): 1643-1651 (1998).
- Gordiets, B. F. and C. M. Ferreira, "Self-Consistent Modeling of Volume and Surface Processes in Air Plasma," AIAA Journal, **36** (9): 1643-1651 (1998).
- Gousset, G., C. M. Ferreira, M. Pinhero, P. A. Sa, M. Touzeau, M. Vialle, and J. Loureiro, "Electron and heavy-species kinetics in the low pressure oxygen positive column," J. Phys. D: Appl. Phys., **24**: 290-300, (1991).
- Graves, D. B. and T. E. Nitschke, "A Comparison of Species in Cell and Fluid Model Simulations of Low Pressure Radio Frequency Discharges," J. Appl. Phys., **76** (10): 5646-5660 (1994).
- Graves, David B., "Fluid model simulations of a 13.56-MHz rf discharge: Time and space dependence of rates of electron impact excitation," J. Appl. Phys. **62** (1): 1987.
- Guerra, V., E. Galiaskarov, and J. Loureiro, "Dissociation mechanisms in nitrogen discharges," Chem. Phys. Let., **371**: 567-581 (2003).
- Hagelaar, G. J. M., and G. M. W. Kroesen, "Speeding up fluid models for gas discharges by implicit treatment of the electron energy source term," J. Comput. Phys., **159**: 1 (2000).
- Hall, R. I. and S. Trajmar, "Scattering of 4.5 eV electrons by ground  $O_2(X^3\Sigma_g)$  state and the metastable  $O_2(a^1\Delta_g)$  oxygen molecules," J. Phys. B: Atom. Molec., Phys., **8** (12): L293-L296 (1975). Hays, G. N., and H. J. Oskam, "Reaction Rate Constant for 2N<sub>2</sub> , " J. Chem. Phys., **59** :6088-6091 (1973).
- Hays, G. N., and H. J. Oskam, "Reaction rate constant for  $2N_2(A^3\Sigma_u^+) \rightarrow N_2(C^3\Pi_u) + N_2(X\Sigma_g^+, v' > 0)(E)$  , " J. Chem. Phys., **59**: 6088-6091 (1973).
- Hershkowitz, N., "How Langmuir probes work," in *Plasma Diagnostics*, Vol. 1, ed by O. Auciello and D. L. Flamm, New York: Academic Press, 1989.

- Hicks, A., S. Tirupathi, Yu. Utkin, N. Jiang, W. R. Lempert, J.W. Rich, I. V. Adamovich, K. Galbally-Kinney, W. J. Kessler, W. T. Rawlins, P. A. Mulhall, and S.J. Davis, "Gain Measurements in a Non-Self-Sustained Electric Discharge Pumped Oxygen-Iodine Laser Cavity", AIAA Paper 2006-3754, 37<sup>th</sup> AIAA Plasmadynamics and Lasers Conference, June 2006, San Francisco, CA
- Hoegy, H. R. and L. E. Wharton, "Current to a moving cylindrical electrostatic probe," J. Appl. Phys. **44**: 5365-5367 (1973).
- Horn R.A. and C. R. Johnson, "Norms for vectors and matrices" Ch. 5 in Matrix Analysis. Cambridge, England: Cambridge University Press, 1990.
- Husain, D., "The Reactivity of Electronically Excited Species," Ber.Bunsen-Ges. Phys. Chem., **81**(2): 168-177 (1977).
- Husain, D., S. K. Mitra, and A. N. Young, "Kinetic study of electronocally excited mitrogen atoms  $N(^2D, ^2P)$  by attenuation of atomic resonance radiation in vacuum ultraviolet," J. Chem. Soc. Faraday Trans., **70**: 1721-1731 (1974).
- Hutchinson, I. H., "Sphere in Flowing Plasma with non-zero Debye Length the unmagnetized Mach Probe part 2," 30th EPS Conference on Contr. Fusion and Plasma Phys., **27**: (2003).
- Iannuzzi, M. P., J. B. Jeffries, and F. Kaufman, "Product channels of the  $N_2(A^3\Sigma_u^+) + O_2$  interaction," Chem. Phys. Lett., **87** (6): 570-574 (1982).
- Itikawa, Y. and A. Ichimura, "Collisions of Electrons and Photons with Atomic Oxygen," J. Phys. Chem. Ref. Data, **19** (3): 642-643 (1990).
- Ivanov, V. V., K. S. Klopovsky, D. V. Lopaev, A. T. Rakhimov and T. V. Rakhimova, "Experimental and Theoretical Investigation of Oxygen Glow Discharge Structure at Low Pressures," IEEE Trans. Plasma Sci. **27**: 1279-1287 (1999).
- Keck, J. and G. Carrier, "Diffusion Theory on Non Equilibrium Dissociation and Recombination," J. Chem. Phys., **43**: 2284-2298 (1965).
- Kenner, R. D. and E. A. Ogryzlo, "A direct determination of the rate constant for quenching of atomic oxygen  $O(^1S)$  by molecular oxygen  $O_2(a^1\Delta_g)$ ," J. Photochem., **18**(4): 379 (1982).
- Kiel, R. E. and C. H. Su, "Continuum Electrostatic Probe Theory for Large Sheaths on Spheres and Cylinders," J. Appl. Phys., **40** (9): 3668-3673.

- Kiel, R. E. "Continuum Theory of Electrostatic Probes," J. Appl. Phys., **37** (13): 4907-4910. Kossyi, I. A., A. Y. Kostinsky, A. A. Matveyev, and V. P. Silakov, "Kinetic Scheme of the non-equilibrium discharge in nitrogen-oxygen mixtures," Plasma Sources Sci. Technol., **1**: 207-220 (1992).
- Kinema Research Associates, "SIGLO-RF: PC version 1.0" Kinema Software
- Kono A., "Formation of an oscillatory potential structure at the plasma boundary in electronegative plasmas," J. Phys. D: Appl. Phys., **32**: (1999) pp. 1357-.
- Kono, A., "Complex sheath formation around a spherical electrode in electronegative plasmas: a comparison between a fluid model and a species simulation," J. Phys. D: Appl. Phys., **34**: 1083-1095 (2001).
- Kossyi, I. A., A. Y. Kostinsky, A. A. Matveyev, and V. P. Silakov, "Kinetic Scheme of the non-equilibrium discharge in nitrogen-oxygen mixtures," Plasma Sources Sci. Technol., **1**: 207-220 (1992).
- Kouznetsov I. G., Lichtenberg A. J., and Lieberman M. A., "Internal sheaths in electronegative discharges," J. Appl. Phys. **86**, (8): 4142-4154 (1999).
- Krivososova, O. E., S. A. Losev, V. P. Nalivaikov, Yu K. Mukoseev, and O. P. Shalatov, Plasma Chemistry **14** : 3-31 (1987) B.M. Smornov, Ed. Moscow: Energizdat,
- Kurata, M. Numerical Analysis for Semiconductor Devices. Lexington, MA: Heath Pub., 1982.
- Kushner, M. J., "Modeling of magnetically enhanced capacitively coupled plasma sources: AR discharges," J. Appl. Phys., **94**(3) : 1436-1447 (2003).
- Kwok, D. T. K., M. M. M. Bilek, D. R. McKenzie, T. W. H. Oates, and P. K. Chu, "Disturbance of langmuir probe at the steady-state sheath boundary in a drifting plasma," IEEE Transactions Plasma Science, **32**(2) : 422-428 (2004).
- Laher, R. R. and F. R. Gilmore, "Updated Excitation and Ionization Cross Sections for Electron Impact on Atomic Oxygen," J. Phys. Chem. Ref Data, **19** (1) : 277-305 (1990).
- Lam. S. H., "A general theory for the flow of weakly ionized gases," AIAA Journal, **2**(2) : 256-262 (1964).
- Levine, J. S., "The Photochemistry of Atmosphere," 1<sup>st</sup> Ed., New York: Academic Press., 1985, Ch. 1.

- Lichtenberg, A.J., M.A. Lieberman, I.G. Kouznetsov, "Transitions and scaling laws for electronegative discharge models," Plasma Sources Sci. Technol., **9**: 45-61 (2000).
- Lichtenberg, A. J., V. Vahedi, and M.A. Liberman, "Modeling electronegative plasma discharges," J. Appl. Phys., **75**: 2339 (1994).
- Lieberman, M. A. and A. J. Lichtenberg, Principles of Plasma Discharges and Materials Processing. New York: John Wiley and Sons, 1994.
- London, G., R. Gilpin, H. I Schiff, and K. H. Welge, "Collisional deactivation of  $O(^1S)$  by  $O_3$  at room temperature," J. Chem. Phys., **54**: 4512 (1971).
- Luginsland, John W. and Robert E. Peterkin, "A virtual Prototyping Environment for Directed-Energy Concepts," Computing in Science and Engineering, April 2002: 42-49
- Lymberopoulos, D. P. and D. J. Economou, "Fluid Simulations of Glow Discharges: Effect of Metastable Atoms in Argon," J. Appl. Phys. **73** (8): 3668–3679 (1992).
- Lymberopoulos, D. P., and D. J. Economou, "Two-dimensional simulation of polysilicon etching with chlorine in a high density plasma reactor," IEEE Trans. Plasma Sci., **23**, 573 (1995).
- Malter L. and E. O. Johnson, "A Floating Double Probe Method for Measurements in Gas Discharges," Phys. Rev. **80** (1): 58 - 68 (1950).
- McMahon J. C., Xu G. Z., and J. G. Laframboise, "The effect of ion drift on the sheath, presheath, and ion-current collection for cylinders in a collisionless plasma," Phys. of Plasmas **12**: 062109-1-062109-20 (2005).
- Morales, C. R., J. I. Fernandez Palop, S. Borrego del Pino, and J. Ballesteros, "Analytical fit of the I-V characteristic for cylindrical and spherical probes in electronegative plasmas," J. Appl. Phys., **96**(9): 4777-4795 (2004).
- Mott-Smith, H. M. and I. Langmuir, The Collected Works of I. Langmuir Vol. 4. New York: Pergamon Pub., 1961; originally published in Phys. Rev. **28**, 727 1926.
- Nahorny, J., D. Pagnon, M. Touzeau, M. Vialle, B. Gordietz, and C. M. Ferreira, "Experimental and Theoretical Investigation of a  $N_2 - O_2$  Flowing Glow Discharge," J. Phys. D: Appl. Phys.: (1994).
- Nitschke, T. E. and D.B. Graves, "A comparison of species in cell and fluid model simulations of low-pressure radio frequency discharges," J. Appl. Phys. **76**: 5646 (1994).



- O'Brien, R. J. and G. H. Myers, "Direct flow measurements of  $O_2(b^1\Sigma_g^+)$  quenching rates," J. Chem. Phys. **53** (10): 3832 (1970).
- Panda, S., D. J. Economou, and M. Meyyappan, "Effect of metastable oxygen molecules in high density power-modulated oxygen discharge," J. Appl. Phys., **87**(12) : 8323-8333 (2000).
- Paranjpe, Ajit P. Studies of Gas Discharges for Dry Etching Modeling and Diagnostics. Ann Arbor, MI: University Microfilms International, 1990.
- Paranjpe, Ajit P., Ph.D. thesis, Stanford University, 1989 (un-published).
- Phelps, A. V. University of Colorado JILA Information Center Report 28. 1985
- Phelps, A.V., and L.C. Pitchford, University of Colorado JILA Information Center Report No. 26. Phys. Rev. A **31**: 2932-2948 (1985).
- Phelps, A. V., "Cross Sections and Swarm Coefficients for Nitrogen Ions and Neutrals in  $N_2$  and Argon Ions and Neutrals in Ar for Energies from 0.1 eV to 10 keV," J. Phys. Chem Ref. Data, **20** (30): 557-573 (1991).
- Pinheiro, M. J., G. Gousset, A. Granier, and C. M. Ferreira, "Modeling of low-pressure surface wave discharges in flowing oxygen: I. Electrical properties and species concentrations," Plasma Sources Sci. Technol. **7**: 524-536 (1998).
- Piper, L. G., "The excitation of  $O(^1S)$  in the reaction between  $N_2(A^3\Sigma_u^+)$  and  $O(^3P)$ ," J. Chem. Phys., **77** (2): 2373-2377 (1982).
- Piper, L. G., "State-to-state  $N_2(A^3\Sigma_u^+)$  energy pooling reactions II. The formation and quenching of  $N_2(B^3\Pi_g, v'=12)$ ," J. Chem. Phys., **88** (11): 6911-6921 (1988).
- , "State-to-state  $N_2(A^3\Sigma_u^+)$  energy pooling reactions I. The formation and quenching of  $N_2(C^3\Pi_u)$  and Herman infrared system," J. Chem. Phys., **88** (1): 231-239 (1988).
- Pitz, G., M. Lange, and G. P. Perram, "Singlet oxygen kinetics in a double microwave discharge." Proceedings of SPIE, Vol. 5448 (2004).
- Polak, L. S., P. A. Sergeev, and D. I. Slovetski, Chimia Vis Energii, **7**: 387 (1973).
- Polak, L. S., P. A. Sergeev, and D. I. Slovetski, Teplofis Vis Temp., **15** (1):15 (1977).

- Punset C., J.-P. Boeuf, and L. C. Pitchford, "Two-dimensional simulation of an alternating current matrix plasma display cell: Cross-talk and other geometric effects," J. of Appl. Phys. **83** (4): 1884-1897 (1999).
- Raizer, Yuri P. Gas Discharge Physics. New York: Springer-Verlag, 1991.
- Raizer, Yuri P. Radio-Frequency Capacitive Discharges. London: CRC Press, 1994.
- Revel, I., L. C. Pitchford, and J. P. Boeuf, "Calculated gas temperature profiles in argon glow discharges," J. Appl. Phys. **88** (5): 2236-2242, (2000).
- Riemann, K.-U., "The Bohm criterion and the field singularity at the sheath edge," Phys. Fluids B: Plasma Phys., **1** (4): 961-963 (1989).
- Riemann, K.-U., "The Bohm criterion and sheath formation," J. Phys. D: Appl. Phys. **24** (4): 493-518 (1991).
- Riemann, K.-U., "Comments on the Bohm criterion and sheath edge for finite Debye Length," Phys. Plasmas **4**: 4158 (1997a).
- Riemann, K.-U., "The influence of collisions on the plasma sheath transition," Phys. Plasmas, **4** (11): 4158-4166 (1997b).
- Riemann, K.-U., "Comment on "On the consistency of the collisionless sheath model"" Phys. Plasmas **9**: 4427 (2002).
- Riemann, K.-U., "Kinetic analysis of the collisional plasma-sheath transition," J. Phys. D: Appl. Phys. **36**(22): 2811-2820 (2003).
- Rockwood, S. D., "Elastic and Inelastic Cross Section for Electron-Hg Scattering from Hg Transport Data," Phys Rev A **8**: 2348 (1973)
- Salabas A., Gousset G., and Alves L. L., "Two-dimensional fluid modelling of charged species transport in radio-frequency capacitively coupled discharges," Plasma Sources Sci. Technol. **11**: 448-465 (2002).
- Sato, N. and Y. Shida, "Effect of Gas Flow on RF Plasmas," Jpn. J. Appl. Phys. **38**: 4426-4439 (1999).
- Scharfetter, D.L., and H. K. Gummel, IEEE Trans El Devices **ED-16**: 64 (1969).
- Schmiedberger J., S. Hirahara, Y. Ichinoche, M. Suzuki, W. Masuda, Y. Kihara, E. Yoshitani and H. Fujii. SPIE, **32**: 4184 (2001).
- Schott, L., Electrical probes in Plasma Diagnostics. New York: Wiley, 1968.

- Shibata, M., N. Nakano, and T. Makabe, "O<sub>2</sub> rf discharge structure in parallel plate reactor at 13.56 MHz for material processing," J. Appl. Phys. **77** (12): 6181-6187 (1995).
- Shibata, M., N. Nakano, and T. Makabe, "A novel sustaining mechanism in capacitively coupled radio frequency plasma in oxygen," J. Appl. Phys., (37): 4182-4196 (1998).
- Slanger, T. G., B. G. Wood, and G. Black, "The Temperature dependence of  $O(^1S)$  quenching by  $O_2^*$ ," Chem. Phys. Lett., **17**: 401-403 (1972).
- Slanger, T. G. and G Black, " $O(^1S)$  Quenching by  $O(^3P)^*$ ," J. Chem. Phys., **64**: 3763-3766 (1976).
- Slanger, T. G. and G. Black, "Interactions of  $O_2(b^1\Sigma_g^+)$  with  $O(^3P)$  and  $O_3$ ," J. Chem. Phys., **70**: 3434-3438 (1979).
- Slanger, T.G. and G Black, "The product channels in quenching of  $O(^1S)$  by  $O_2(a^1\Delta_g)$ ," J. Chem. Phys., **75**: 2247-2251 (1981).
- Slovetski, D. I., Mechanisms of Chemical Reactions in the Nonequilibrium Plasma. Moscow: Nauka, Russia: 1980.
- Smy, P. R., "The use of Langmuir probes in the study of high pressure plasmas," Advances in Physics **25** (5): 517-529 (1976).
- Smy, P. R. and A. I. Noor, "High-pressure Langmuir probe in a weak flowing plasma or a plasma sheath," J. of Appl Phys. **47** (4): 1327-1340 (1976).
- Stafford, D.S., and Kushner, M.J., "Simulation of O<sub>2</sub>(1-delta) Yields in Mixtures of O<sub>2</sub> and Inert Gases in Low Pressure Plasmas," 56th Gaseous Electronics Conference (2003).
- Sternovsky Z., "The effect of ion-neutral collisions on the weakly collisional plasma-sheath and the reduction of the ion flux to the wall," Plasma Sources Sci. Technol. **14**: 32-35 (2005).
- Stief, L. J., W. A. Payne, J. H. Lee, and J. V. Michael, "The Reaction  $N(^4S) + O_3$ : an upper limit for the rate constant at 298 K," J. Chem. Phys., **70** (11): 5241-5243 (1979).
- Stoffels, Stoffels, Vender, Kando, Kroesen, and Hoog, "Negative ions in a radio-frequency oxygen plasma," Phys. Rev. E **51** (3): 2425-2436 (1995).

- Su, C. H. and S. H. Lam, "Continuum Theory of Spherical Electrostatic Probes," Physics of Fluids 6 (10): 1479-1491 (1963).
- Surendra M., and M. Dalvie, "Moment analysis of rf parallel-plate-discharge simulations using the species-in-cell with Monte Carlo collisions technique," Phys. Rev. E 48: 3914 (1993).
- Thorton, John A. "Comparison of Theory and Experiment for Ion Collection by Spherical and Cylindrical Probes in a Collisional Plasma," AIAA Journal 9 (2): 342-344.
- Tonks and I. Langmuir The Collected Works of I. Langmuir Vol. 5. New York: Pergamon Pub., 1961; originally published in Phys. Rev. 34, 876 1929.
- Turner, M. M., "Kinetic properties of species-in-cell simulations compromised by Monte Carlo collisions," Physics of Plasma, 13 : 033506-1-033506-10 (2006).
- Vahedi, Vahid Modeling and Simulation of RF Discharges Used for Plasma Processing. Ann Arbor, MI: University Microfilms International, 1993.
- Vahedi, V. and M. Surendra, "A monte carlo collision model for the species-in-cell method: application to argon and oxygen discharges," Computer Physics Communications, 87: 179-198 (1995).
- Vanderslice J. T. and S. Weissman, On the theory of Vibrational Energy Exchange. Maryland Univ College Park Inst for Molecular Physics, 1962 (AD-0276257).
- Ventzek, P. L., R. J. Hoekstra, and M. J. Kushner, "Two-dimensional modeling of high plasma density inductively coupled sources for materials processing," J. Vac. Sci. Technol. B 12: 461 (1994).
- Verboncoeur J. P., V. Vahedi, and M. V. Alves PDP1, PDC1, PDS1 Plasma Device 1 Dimensional Bounded Electrostatic Codes. Berkeley, CA: Regents of University of California, 1990.
- Verdeyen J. T., D. M. King, D. L. Carroll, and W. C. Solomon. SPIE, 4631, 154, (2002).
- Wayne, R. P., Singlet O<sub>2</sub>, Vol. 1, A. A. Frimer, Ed. Boca Raton, FL: CRC Press: 1985.
- Williams, P.F. (ed.), Plasma Processing of Semiconductors. Netherlands: Kluwer Academic Publishers, 1997.
- Xu, G. Z., Ph.D. thesis, York University, 1992.

Yaron, M., A. von Engel, and P. H. Vidaud, "The collisional quenching of  $O_2^*(a^1\Delta_g)$  by  $NO$  and  $CO_2$ ," Chem. Phys. Lett., **37**(1): 159 (1976).

Zimmerman, J.W., Skorski, L.W., Solomon, W.C., Kushner, M.J., Verdeyen, J.T., and Carroll, D.L., "Electrodynamic modeling of the ElectriCOIL system," SPIE 4971: 81-86 (2003).

REPORT DOCUMENTATION PAGE				Form Approved OMB No. 074-0188	
<p>The public reporting burden for this collection of information is estimated to average 1 hour per response, including the time for reviewing instructions, searching existing data sources, gathering and maintaining the data needed, and completing and reviewing the collection of information. Send comments regarding this burden estimate or any other aspect of the collection of information, including suggestions for reducing this burden to Department of Defense, Washington Headquarters Services, Directorate for Information Operations and Reports (0704-0188), 1215 Jefferson Davis Highway, Suite 1204, Arlington, VA 22202-4302. Respondents should be aware that notwithstanding any other provision of law, no person shall be subject to a penalty for failing to comply with a collection of information if it does not display a currently valid OMB control number.</p> <p><b>PLEASE DO NOT RETURN YOUR FORM TO THE ABOVE ADDRESS.</b></p>					
1. REPORT DATE (DD-MM-YYYY) 12-07-2007		2. REPORT TYPE Doctoral Dissertation		3. DATES COVERED (From – To) July 2002 – Nov 2007	
4. TITLE AND SUBTITLE  INVESTIGATION OF RADIO FREQUENCY DISCHARGES AND LANGMUIR PROBE DIAGNOSTIC METHODS IN A FAST FLOWING ELECTRONEGATIVE BACKGROUND GAS				5a. CONTRACT NUMBER	
				5b. GRANT NUMBER	
				5c. PROGRAM ELEMENT NUMBER	
6. AUTHOR(S)  Lockwood, Nathaniel, P., DR-III, DAF				5d. PROJECT NUMBER	
				5e. TASK NUMBER	
				5f. WORK UNIT NUMBER	
7. PERFORMING ORGANIZATION NAMES(S) AND ADDRESS(S) Air Force Institute of Technology Graduate School of Engineering and Management (AFIT/EN) 2950 P Street, Building 640 WPAFB OH 45433-7765				8. PERFORMING ORGANIZATION REPORT NUMBER  AFIT/DS/ENP/DSP-04J	
9. SPONSORING/MONITORING AGENCY NAME(S) AND ADDRESS(ES) N/A				10. SPONSOR/MONITOR'S ACRONYM(S)	
				11. SPONSOR/MONITOR'S REPORT NUMBER(S)	
12. DISTRIBUTION/AVAILABILITY STATEMENT  APPROVED FOR PUBLIC RELEASE; DISTRIBUTION UNLIMITED.					
13. SUPPLEMENTARY NOTES					
14. ABSTRACT <p>Discharges in a flowing background gas are used to produce charged and excited species for numerous applications including etching semiconductors and pumping gas discharge lasers (Pinhero and others, 1998). The effect of a flowing background gas on the charged and excited neutral species generation by an RF discharge in a flow tube and the diagnostics of the resulting plasma with a Langmuir probe have been investigated for pressures between 0.001 to 1 Torr and flow velocities up to 1000 m/s. This investigation was performed using a fluid method coupled to a chemical kinetic model and a hybrid Particle-In-Cell/Monte Carlo Collision modeling method based on the approaches of Boeuf, 1987 and Cartwright and others, 2000. A factor of two reduction in the sheath length was realized for an increase in flow velocity from 25 m/s to 500 m/s. This resulted in an increased average ionization rate and factor of ten increases in positive and negative ion densities, while the electron densities remained approximately constant. At pressures less than 0.01 Torr, existing probe theory was adequate for performing diagnostics, however, at pressures of 1 Torr convection limited probe theory underestimated the positive ion density of the flowing electronegative plasma by up to 50%.</p>					
15. SUBJECT TERMS <p>Plasma Diagnostics, Langmuir Probes, Plasma Sheath, Plasma Devices, Model Theory, Ion Density, RF Discharge, Gas Discharge, Flowing Electronegative Plasma, RF Discharge, Electrostatic Probe, Gas Breakdown, Gas Flow</p>					
16. SECURITY CLASSIFICATION OF:			17. LIMITATION OF ABSTRACT	18. NUMBER OF PAGES	19a. NAME OF RESPONSIBLE PERSON
a. REPORT	b. ABSTRACT	c. THIS PAGE			19b. TELEPHONE NUMBER (Include area code)
U	U	U	UU	327	William F. Bailey (ENP)  (937) 255-3636, ext 4501; e-mail: William.Bailey@afit.edu